CHARACTERIZATION OF PROPERTIES AND SPATIOTEMPORAL FIELDS OF MINERAL AEROSOL AND ITS RADIATIVE IMPACT USING CALIPSO DATA IN CONJUNCTION WITH A-TRAIN SATELLITE AND GROUND-BASED OBSERVATIONS AND MODELING

A Dissertation
Presented to
The Academic Faculty

by

HYUNG JIN CHOI

In Partial Fulfillment
of the Requirements for the Degree
Doctor of Philosophy in the
School of Earth and Atmospheric Sciences

Georgia Institute of Technology
August 2011

CHARACTERIZATION OF PROPERTIES AND SPATIOTEMPORAL FIELDS OF MINERAL AEROSOL AND ITS RADIATIVE IMPACT USING CALIPSO DATA IN CONJUNCTION WITH A-TRAIN SATELLITE AND GROUND-BASED OBSERVATIONS AND MODELING

Approved by:

Dr. Irina Sokolik, Advisor
School of Earth and Atmospheric Sciences
Georgia Institute of Technology

Dr. Viatcheslav Tatarskii
School of Earth and Atmospheric Sciences
Georgia Institute of Technology

Dr. Judith Curry
School of Earth and Atmospheric Sciences
Georgia Institute of Technology

Dr. Olga Kalashnikova
Jet Propulsion Laboratory
NASA

Dr. Josef Dufek
School of Earth and Atmospheric Sciences
Georgia Institute of Technology

Date Approved: May 16, 2011

ACKNOWLEDGEMENTS

I wish to acknowledge my advisor, Dr. Irina Sokolik, for her guidance and support in mentoring me throughout my five years at Georgia Tech. I would also like to thank Dr. Curry, Dr. Dufek, Dr. Kalashnikova, and Dr. Tatarskii for agreeing to serve on my thesis committee. I am very grateful for the support received from Republic of Korea army and the NASA funded in part for the research in this dissertation. I would like to thank my family and friends for their encouragement in completing this dissertation, and finally I would like to acknowledge my wife and best friend, Su Jeong Lee. I would not have finished this thesis without her love and assistance.

TABLE OF CONTENTS

LIST OF TABLES

LIST OF FIGURES

LIST OF SYMBOLS AND ABBREVIATIONS

α_{O^3}	Ozone volume absorption coefficient
β_m	Molecular Volume Backscatter Coefficient
β_p	Particulate Volume Backscatter Coefficient
β_{532}	Attenuated Backscatter Coefficient at 532 nm
$\beta_{532,layer}$	Layer-integrated Attenuated Backscatter Coefficient at 532 nm
$\beta_{532,\mathrm{I}}$	Perpendicular Attenuated Backscatter Coefficient at 532 nm
$\beta_{532,\mathrm{II}}$	Parallel Attenuated Backscatter Coefficient at 532 nm
β_{1064}	Attenuated Backscatter Coefficient at 1064 nm
$\beta_{1064,layer}$	Layer-integrated Attenuated Backscatter Coefficient at 1064 nm
χ_{layer}	Layer-integrated Attenuated Total Color Ratio
$\delta_{v,layer} = \beta_{\mathrm{I},layer} / \beta_{\mathrm{II},layer}$	Layer-integrated lidar volume depolarization ratio at 532 nm
$\delta_{p,layer}$	Layer-integrated lidar particulate depolarization ratio at 532 nm
ε'	Aspect Ratio
Φ	Radiant flux (W)
$\gamma(\theta)$	Volume scattering function ($m^{-1}sr^{-1}$)
η	Parameterization describing multiple scattering by particles
λ	Wavelength
ν	Wavenumber (cm^{-1})
ρ	Density
ϖ	Single scattering albedo

θ	Angle
σ_g	Geometric standard deviation
$\sigma_m(z) = S_m \beta_m(z)$	Molecular Volume Extinction Coefficient
$\sigma_p(z) = S_p \beta_p(z)$	Particulate Volume Extinction Coefficient
$\tau_p(0,z)$	Particulate Optical Depth
$\xi = G_A C$	Lidar system parameter
ω	Solid angle
a,b,c	Ellipsoid semiaxes
C	Lidar calibration coefficient
C_{sca}	Scattering Coefficient
C_{abs}	Absorption Coefficient
C_p	Specific heat at constant pressure
E	Irradiance (Wm^{-2})
E_0	(average) Laser energy for a single or averaged profile
ΔF	Radiative forcing
F	Net flux
F_ν	Spectral net flux
$F^\uparrow$	Upward flux
$F^\downarrow$	Downward flux
$g, \langle \cos\theta \rangle$	Asymmetry parameter
G_A	Amplifier gain
I	Radiative Intensity (wsr^{-1})
k	Imaginary part of the complex index of refraction

$\tilde{k}$	Wavenumber ($2\pi/\lambda$)
m	Complex index of refraction
n	Real part of the complex index of refraction
n_{el}	Electronic transition component of n
$n(r)$	Number size distribution (m^{-4})
N_0	Total particle concentration (cm^{-3})
$P(z)$	Backscattered signal power detected from range z from the lidar
$P(\theta)$	Scattering phase function
r	Particle radius
r_g	Median radius
S_{11}	Element 1,1 of Stokes scattering matrix
S_M	Molecular Extinction-to-Backscatter Coefficient
S_a	Particulate Extinction-to-Backscatter Coefficient
T	Temperature
$T_M^2(0,z)$	Molecular Two-way Transmittance between the lidar and range z
$T_{O^3}^2(0,z)$	Two-way Ozone Transmittance between the lidar and range z
$T_P^2(0,z)$	Particulate Two-way Transmittance between the lidar and range z
v	Volume
z	Height

ACE-Asia	Aerosol Characterization Experiment in Asia
AERONET	AErosol RObotic NETwork
AIRS	Atmospheric Infrared Sounder

AMMA	African Monsoon Multidisciplinary Analysis
AOD	Aerosol Optical Depth
ARIES	Airborne Research Interferometer Evaluation System
ARM	Atmospheric Radiation Measurement
ASPEN	Atmospheric Sounding Processing Environment
ATR	Attenuated Total Reflectance
BOA	Bottom of the Atmosphere
BT	Brightness Temperature
BTD	Brightness Temperature Difference
CAD	Cloud-Aerosol Discrimination
CALIPSO	Cloud-Aerosol Lidar and Infrared Pathfinder Satellite Observation
CALIOP	Cloud-Aerosol Lidar with Orthogonal Polarization
DDA	Discrete Dipole Approximation
DISORT	Discrete Ordinate Radiative Transfer
FDTD	Finite Difference Time Domain
GCM	General Circulation Model
HERA	Hybrid Extinction Retrieval Algorithm
IGOM	Improved Geometric Optics Method
IR	Infrared
MODIS	Moderate Resolution Imaging Spectroradiometer
MODTRAN	MODerate resolution atmospheric TRANsmission
NCAR	National Center for Atmospheric Research
NCDC	National Climatic Data Center
NIR	Near Infrared
NWP	Numerical Weather Prediction

OMI	Ozone Monitoring Instrument
OPAC	Optical Properties of Aerosols and Clouds
PRIDE	Puerto Rico Dust Experiment
SAMUM	Saharan Mineral Dust Experiment
SAP	Spectral Aerosol Profile
SCA	Scene Classification Algorithm
SHADE	Saharan Dust Experiment
SST	Sea Surface Temperature
SWIR	Shortwave Infrared
TIR	Thermal Infrared
TOA	Top of the Atmosphere
VFM	Vertical Feature Mask
VIS	Visible

SUMMARY

Atmospheric mineral aerosol (or dust) plays an important role in the Earth's system. However, quantification of dust impacts has long been associated with large uncertainties because of the complex nature of mineral aerosol. A better understanding of the properties and spatiotemporal distribution of atmospheric dust on the regional and global scales is needed to improve predictions of the impact that dust radiative forcing and heating/cooling rates have on the weather and climate. The Cloud-Aerosol Lidar and Infrared Pathfinder Satellite Observation (CALIPSO) mission provides unique measurements of vertical profiles of aerosols and clouds and their properties during day and nighttime over all types of surfaces. This information has the potential to significantly improve our understanding of the properties and effects of aerosol and clouds.

This dissertation presents the results of a comprehensive analysis of CALIPSO lidar (version 2 and version 3.01) data in conjunction with A-Train satellite and ground-based observations aimed at characterizing mineral aerosol in East Asia and other major dust sources. The specific objectives were to characterize the spatial distribution and properties of atmospheric dust in the dust source regions using new CALIOP (version 3.01) data in conjunction with satellite MODIS, OMI, and CloudSat data and ground-based meteorological and lidar data; investigate changes in the vertical distribution and properties of dust during mid- and long-range transport; perform a modeling of the optical properties of nonspherical dust particles, and assess the radiative forcing and heating/cooling rates of atmospheric dust by performing radiative transfer modeling

constrained by satellite data in major dust source regions.

Our research revealed significant biases in CALIPSO version 2 data, especially in the presence of dense dust plumes and dust-cloud mixed scenes. Aerosol optical depth (AOD) retrieved from CALIOP backscatter profiles was unrealistically low in many instances. Analyses on the new version 3.01 data show significant improvements in a discrimination between dust and clouds and more accurate retrievals of the aerosol extinction profiles and AOD.

Dust events observed by CALIPSO in the world's major dust source regions and downwind were analyzed on a case-by-case basis in the springs from 2007-2010. The main focus was on dust sources in East Asia and contrasting the regional features of Asian dust to those of dusts in Central Asia, India, Arabian Peninsula, Australia, USA, and Northern Africa. Some important similarities between regional dusts were found. The particulate (aerosol) linear depolarization ratio (δ_p) exhibit high values (up to 0.3-0.35) in all dust source regions and in many instances downwind. This finding shows the importance of dust nonsphericity not only for fresh emitted particles but also for aged ones, stressing the need to account for dust nonsphericity in the models and passive remote sensing. The particulate color ratio (χ_p) tends to decrease with height in dust plumes in the source regions. This is most likely due to vertically varying proportion of fine and coarse dust particles.

To aid in the retrievals and in the interpretation of CALIOP data, we have performed intensive optical simulations aimed at examining the extent to which the microphysical properties of dust particles affect the aerosol optical characteristics used in lidar remote sensing (e.g., lidar ratio, particulate depolarization, single scattering albedo).

Optical modeling was performed by merging the T-matrix method and the Improved Geometric Optics Method (IGOM) enabling us to account for fine and coarse particles. Constrained by recent microphysical data, modeling results show that representing dust particles by a mixture of spheroids can reproduce some CALIPSO and ground-based lidar observations. We found that δ_p at the 532 nm lidar wavelength has relatively low sensitivity to particle size distribution. In contrast, the lidar ratio S_a varies in a wide range. This finding questions the applicability of a fixed S_a value adopted in the CALIPSO algorithm.

Radiative transfer modeling with CALIPSO dust vertical profiles representative of different regions was performed to assess the radiative forcing and heating rates. We found a positive forcing of dust at the top of the atmosphere (TOA) over all dust sources at high Sun angle. However, a negative forcing was found for low Sun angle, with the exception of dust source regions with high (0.3-0.35) surface albedo (e.g., Northern Africa). In the transported areas, the vertical distribution of aerosol and clouds and their optical properties are the major controlling factors, with the predominantly positive radiative forcing of dust above clouds.

CHAPTER 1

INTRODUCTION

Diverse regions around the world are prodigious sources of mineral aerosol (or dust). Lifted into the atmosphere by winds, mineral aerosol plays an important role in the Earth's climate system (Sokolik et al., 2001, Otto et al., 2007, IPCC, 2007). Dust particles can scatter and absorb shortwave and longwave radiation that can cause either a positive or a negative radiative forcing, leading to a warming or cooling of the climate system (Sokolik et al., 2001, Takemura et al., 2002, Otto et al., 2007, IPCC, 2007). In addition, the radiative heating/cooling occurring in the dust layer affects the atmospheric temperature profile and thus air- and thermo-dynamics of clouds and precipitation (Alpert et al., 1998, Quijano et al., 2000). For instance, it has been suggested that the presence of dust may cause a stabilizing effect on the temperature lapse rate. Karyampudi and Carlson (1988) showed that radiative heating by Saharan dust contributes to maintaining a warmer and deeper Saharan Air Layer (SAL) over the ocean, to enhancing the strength of the midlevel easterly jet, and to reducing the convection within the equatorial zone. On the mesoscale, dust radiative heating rates can affect the evolution of a dust storm, leading to stronger surface frontogenesis (Chen et al., 1994). Consequently, knowledge of radiative heating rates by mineral aerosols may be decisive to better predictions of the dynamics associated with dust transport (Miller et al., 2006, Lau et al., 2006). However, there are large uncertainties in the assessments of radiative impacts of mineral dust at regional and global scales because direct observations of the effect of desert aerosols on heating rates are scarce.

Passive satellite sensors (such as MODIS (Moderate Resolution Imaging Spectroradiometer), MISR (Multi-angle Imaging SpectroRadiometer), and OMI (Ozone Monitoring Instrument)) have helped to constrain the direct radiative forcing of aerosols at the top of the atmosphere (Yu et al., 2005). However, these sensors are of limited use both for constraining the profile of radiative heating/cooling rates in the aerosol or cloud layers and for detecting dust over the arid and semi-arid regions where the surface reflectance is very high. The Cloud-Aerosol Lidar and Infrared Pathfinder Satellite Observation (CALIPSO) satellite, launched on 28 April 2006, provides a new capability for studying aerosol and clouds. A key component of CALIPSO is a two-wavelength, polarization sensitive backscatter lidar called CALIOP (Cloud-Aerosol Lidar with Orthogonal Polarization). The global extent of CALIOP's vertically resolved aerosol and cloud measurements during day- and nighttime over heterogeneous bright surfaces has the potential to provide new insights into the roles of aerosols and clouds in the Earth's climate system. Knowledge of the aerosol vertical profile is particularly important because aerosol residence time, and thus radiative impact, increase significantly when aerosol is lofted high above the boundary. The vertical distribution of dust aerosols determines the indirect effect of dust on cloud microsphysics and controls the radiative forcing and heating/cooling rates of dust.

To date, a number of published papers have used CALIPSO data in dust-related studies For example, Huang et al. (2007) analyzed an Asian dust episode that was transported over the Tibetian Plateau in the summer of 2006. Several studies used CALIPSO data to characterize the long-range transport of dust (Z. Liu et al., 2008, Generoso et al., 2008, Huang et al., 2008, Uno et al., 2009, and Badarinath et al., 2010).

Z. Liu et al. (2008) and Generoso et al. (2008) analyzed the properties of Saharan dust, while Huang et al. (2008) and Uno et al. (2009) examined Asian dust episodes. Badarinath et al. (2010) investigated the long-range transport of dust over the Arabian Sea and India region. A height-resolved global distribution of dust aerosols from the first year of CALIPSO observations (June 2006-May 2007) was investigated by D. Liu et al. (2008). They reported that the mean top height of dust layers in spring is the highest over the Taklimakan and Gobi deserts and suggested that these two major dust sources are related to long-range transport in the spring season. For a dust episode observed by CALIPSO, Huang et al. (2009) calculated the dust radiative forcing and heating rate over the Taklamakan Desert by using the Fu-Liou radiative transfer model. They suggested that the maximum daily mean value of heating rate is up to 5.5 K/day at 5 km and the averaged daily mean values of net dust radiative forcing are 44.4 W/m^2 at the top of the atmosphere (TOA) and - 41.9 W/m^2 at the surface.

Collectively, past studies demonstrated the capability of CALIPSO lidar data, although they considered only limited cases of short duration dust episodes in isolated regions. More importantly, they all use the version 2 data, the very first CALIPSO product that has been lacking a comprehensive evaluation and validation. Recently, our study and others demonstrated significant biases in CALIPSO version 2 data, especially in dust-laden conditions (Z. Liu et al., 2009, Chen et al., 2010). The major problems include erroneous classification of dust layers as clouds and misclassification of aerosol types (see Chapter 2). For instance, Chen et al. (2010) demonstrated that CALIPSO misclassified about 43% of dense dust layers as clouds over the Taklamakan Desert. In June 2010, a new revised version 3.01 of CALIPSO data was released which potentially

has higher quality products and in addition includes several new aerosol products (such as particulate depolarization and color ratios) that were not part of the previous version 2 data. These new products are of special interest for dust studies, given that dust particle nonsphericity is readily detected by the particulate depolarization, and the color ratio is sensitive to coarse particles. Based on some test results, Z. Liu et al. (2010) showed significant improvements in the discrimination of dense aerosol layers in the new version 3.01 data compared to version 2. However, prior to using the new CALIOP data, it is critical to comprehensively examine the performance of improved and new aerosol products in the presence of dust and clouds. The main focus of research presented in this dissertation was to conduct an in-depth, comprehensive analysis of all available (2006-2010) CALIPSO products focusing on East Asia and the world's other major dust sources. The goal was to determine both strengths and weaknesses of CALIPSO data and then use them for characterizing region-specific properties, spatiotemporal distribution, and radiative impacts of mineral aerosol.

To begin with the analysis of dust, we first examined in detail a procedure for retrieving aerosol properties from the CALIPSO level 1B data, contrasting retrievals of version 2 and version 3.01 data in dust-laden conditions. This work helps to confirm the reliability of the latest level 2 version 3.01 data, as well as to identify the major sources of errors. One of the critical issues in the CALIOP aerosol retrieval algorithm is an assumption about some aerosol optical characteristics (such as scattering phase function and lidar ratio S_a). Many studies (e.g., Kalashnikova et al., 2005, Dubovik et al., 2006, Mishchenko et al., 2003) modeled the dust optical characteristics for passive remote sensing, but only a few studies modeled the optical properties needed for lidar remote

sensing (Wiegner et al., 2009, Yang et al., 2007). Despite the recent progress in computational optical modeling, calculation of the dust optical properties still remains a challenging problem. The main problems arise from the complex nature of mineral aerosol that exhibits a wide variety of morphologies, composition and sizes (Weinzierl et al., 2009, Mishchenko et al., 2007, Sokolik et al., 2001). An added complication is the high variability of dust properties between different dust sources due to aging (i.e., physical and chemical changes of dust particles during the transport in the atmosphere). To aid in the retrievals and the interpretation of CALIOP data, we performed extensive optical simulations to examine the extent to which the variation of microphysical properties of dust particles affect the optical characteristics used in lidar remote sensing. Our research goes beyond the previous optical modeling studies by incorporating recent data on particle shapes, composition and size distributions. To cover a wide range of dust particle sizes, two optical methods (the T-matrix method and the improved geometric optics method (IGOM) were merged in a unified code. We also computed the optical characteristics of nonspherical dust particles required for radiative forcing and heating rates calculations and used them along with CALIPSO data to assess the regional radiative impact of mineral aerosol.

Overall, the main goal of this study is to improve the understanding of the properties and spatiotemporal distribution of mineral aerosol and to assess associated radiative impacts in region-specific dust sources and downwind by leveraging the new CALIPSO data. To achieve this goal, the specific objectives are as follows: 1) characterize the spatial distribution and properties of atmospheric dust in the dust source regions using new CALIOP data in conjunction with A-Train satellite multi-sensor

observations (MODIS, OMI, and CloudSat) and ground-based meteorological and lidar data; 2) investigate changes in the vertical distribution and properties of mineral dust during mid- and long-range transport; 3) perform a modeling of the optical properties of nonspherical dust particles to aid in the retrievals and in the interpretation of CALIOP data; and 4) assess the radiative forcing and heating/cooling rates of atmospheric dust by performing radiative transfer modeling constrained by satellite data in major dust source regions.

The organization of the thesis is shown in Figure 1.1. Chapter 2 examines a procedure for retrieving dust properties from the CALIPSO level 1B data and the performance of CALIPSO in dust-laden conditions in order to verify the reliability of using the latest level 2 version 3.01 data. To achieve the goal, we examined the spatiotemporal characteristics of CALIPSO and the procedure of CALIOP aerosol retrievals. Based on the understanding of the aerosol retrieval procedure, this study investigates the problems of previous version 2 products and compares the results of version 2 products with those of new version 3.01 products in dust-laden conditions, especially in dust-cloud mixed scenes. Finally, this study discusses the improvement of version 3.01 data and the added parameters of version 3.01 used in this study.

Chapter 3 describes the development of a technique for performing computations of dust optical characteristics used in lidar remote sensing and radiative transfer modeling. This technique merges two different approaches, the T-matrix and IGOM (Improved Geometric Optics Method), to provide an improved capability to represent the broad range of sizes and composition of nonspherical dust particles in optical modeling. Using the new technique, we performed an in-depth modeling analysis of the particulate

depolarization ratio (δ_p) and lidar ratio (S_a) at 532 nm used in CALIOP retrievals considering representative dust microphysical data. We also modeled the optical characteristics needed for radiative transfer calculations such as extinction coefficient, single scattering albedo (ω_0), and asymmetry parameter (g). This study focuses on how dust microphysical properties (size, composition, and morphology) and their variations during the dust lifecycle in the atmosphere affect the lidar aerosol observations and retrievals.

Chapter 4 presents the comprehensive characterization of Asian dust events during the spring season of 2007-2010 within the dust sources and downwind areas through analysis of CALIPSO data that was performed in conjunction with independent satellite and ground-based observations. The research included the examination of vertical distributions of dust aerosol and their changes during the transport. The CALIPSO aerosol products (AOD, particulate depolarization ratio and color ratio) were examined and interpreted in the context of dust physical properties. This chapter also presents the results of the radiative forcing and heating/cooling rates of Asian dust that were computed using a modified version of the SBDART (Santa Barbara DISORT Atmospheric Radiative Transfer) code and constrained by CALIPSO and other satellite data.

Chapter 5 presents analyses of dust events in the world's major dust source regions based on the new version 3.01 CALIPSO data. The focus was to identify the similarities and region-specific differences in the vertical distribution and properties of dust in the considered regions (Taklamakan Desert, Gobi Desert, Thar Desert, Central Asia, Mojave Desert, Australia Desert, Arabian Peninsula, and Northern Africa). The

impact of regional dust on the radiative forcing and heating/cooling was also examined. For this analysis, we examined individual CALIPSO tracks in each region of interest during the dust (spring) seasons, selected several representative cases, and then performed detailed analyses of CALIPSO data on a case-by-case basis. We also estimated dust characteristics averaged over each source region in order to facilitate intercomparison between source regions. Finally, we calculated the radiative forcing and heating/cooling rates of dust in each source region.

Chapter 6 provides a summary of the study and makes suggestions for further research in the field.

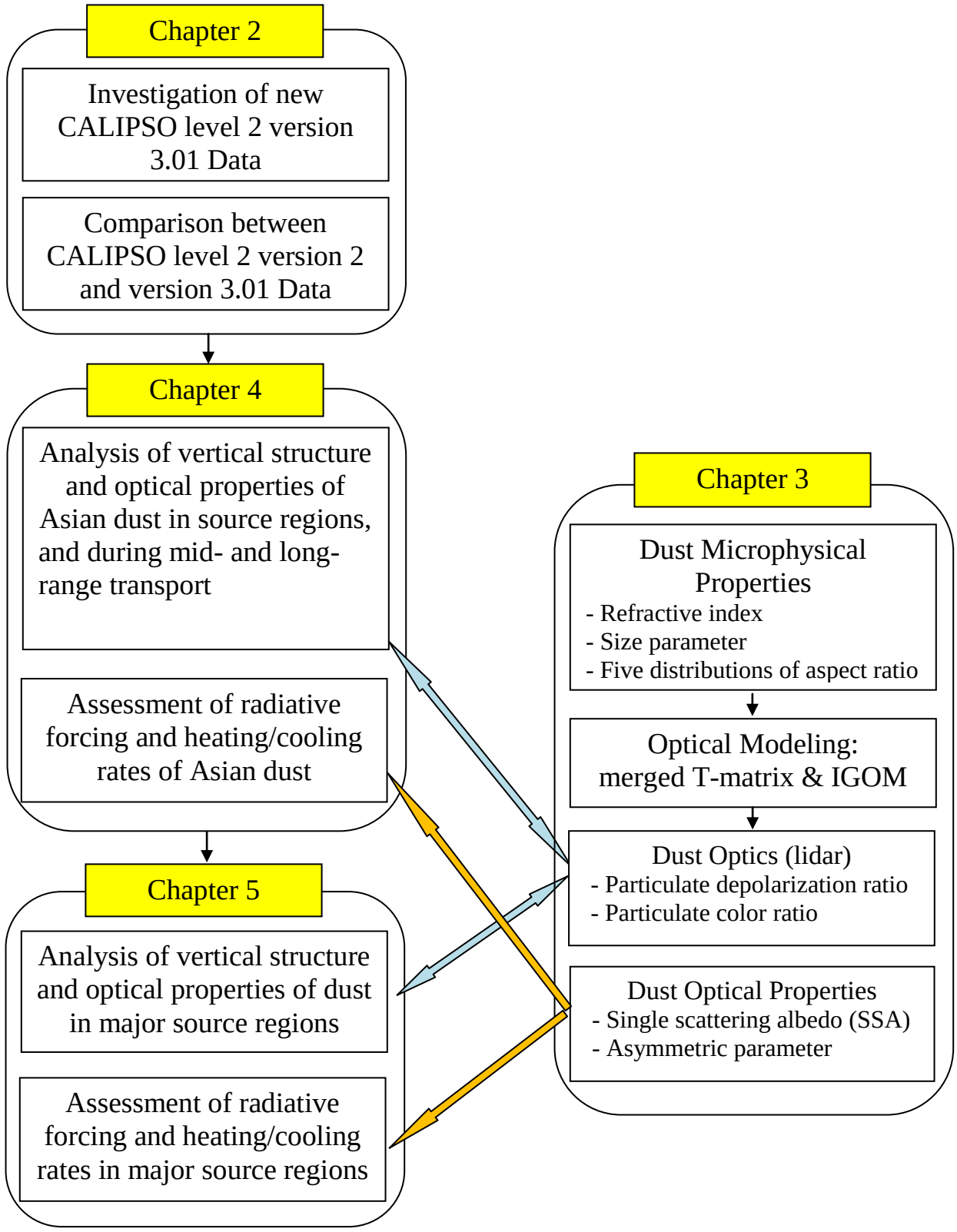

Figure 1.1 Schematic diagram of the thesis organization and performed research.

CHAPTER 2

EXAMINATION OF A PROCEDURE FOR RETRIEVING AEROSOL PROPERTIES FROM THE CALIPSO LIDAR AND ITS PERFORMANCE IN DUST-LADEN CONDITIONS

2.1 Introduction

The CALIPSO satellite has been providing a new capability for studying aerosols since launched on April 28, 2006. The capabilities of detecting aerosol layers and examining aerosol optical properties enable one to better quantify the radiative impact of aerosols on the atmosphere. In particular, radiative heating/cooling rates caused by dust can play a key role in atmospheric dynamics and thermodynamics and thus must be taken into account to adequately predict the overall impact of dust on weather and climate. The first version of CALIPSO data (called version 2) was released in January 2008 and used by the researchers in dust studies. Recently, a new version 3.01 of CALIPSO data was released in June 2010 which has significant changes to the aerosol retrieval algorithms, as well as includes several new aerosol products such as particulate depolarization and color ratio that are of great interest to dust studies. Before any study can begin using CALIPSO data, it is very important to establish confidence in the CALIPSO aerosol products and identify biases in dust-laden conditions.

The goal of this chapter is to examine a procedure for retrieving aerosol properties from the CALIPSO level 1B data and the performance of CALIPSO in dust-laden conditions analyzing both the version 2 and version 3.01 data sets. To achieve this goal,

we first examined the major CALIPSO retrieval algorithms and recent revisions. Based on an understanding the CALIPSO aerosol retrieval procedure, we then investigate the problems of previous version 2 products and compares the results of version 2 products with those of new version 3.01 in dust-laden conditions, especially dense dust plumes and dust-cloud mixed scenes. Finally, we discuss the improvement of version 3.01 data and the added parameters of version 3.01 used in this study.

Section 2.2 briefly describes the main components of CALIPSO and lidar spatiotemporal resolutions. Section 2.3 shows the procedure of aerosol extinction retrieval from lidar backscatter measurements. Section 2.4 presents the problems of version 2.01 and the results of a comparison between the previous and new data versions. Finally, Section 2.5 summarizes and discusses the study.

2.2 Overview of CALIPSO and CALIOP

CALIPSO is a joint NASA-CNES satellite mission designed to provide measurements aimed at improving our understanding of the role of aerosols and clouds in the climate system. CALIPSO has three instruments: the Cloud-Aerosol Lidar with Orthogonal Polarization (CALIOP), the Wide Field Camera (WFC), and an Imaging Infrared Radiometer (IIR), three channels in the infrared window region. The CALIOP, the primary instrument on the CALIPSO satellite (Winker et al., 2006, 2007), is designed to acquire vertical profiles of an elastic backscatter at two wavelengths (1,064 nm and 532 nm) from a near nadir-viewing geometry.

The CALIPSO flies as a part of the Afternoon constellation of satellites (called A-train) which consist of Aqua, CloudSat, CALIPSO, Parasol, and Aura. These satellites

have an afternoon crossing time close to the mean local time of the "lead" satellite, Aqua (1:30 p.m.); thus, the name, "A (short for "afternoon") Train". CALIPSO is behind Aqua by one to two minutes and separated from CloudSat by ten to fifteen seconds. Small differences in time enable one to utilize and compare the data from three satellites all together. The CALIPSO satellite was launched to a low earth sun-synchronous orbit at a 705-km altitude. CALIOP, an active remote sensor, enables one to observe aerosols during the nighttime and to compare the characteristics of the vertical distributions and optical properties of aerosols during the daytime with those during the nighttime. To illustrate, Figure 2.1 shows the orbit of CALIPSO over the Taklamakan Desert during the daytime and the nighttime for fourteen days in the spring 2007. As shown in Figure 2.1, one of the problems in CALIPSO is its narrow footprint. If CALIPSO does not pass through the dust feature, it cannot detect any aerosols even if a dust storm has occurred over the Taklamakan Desert.

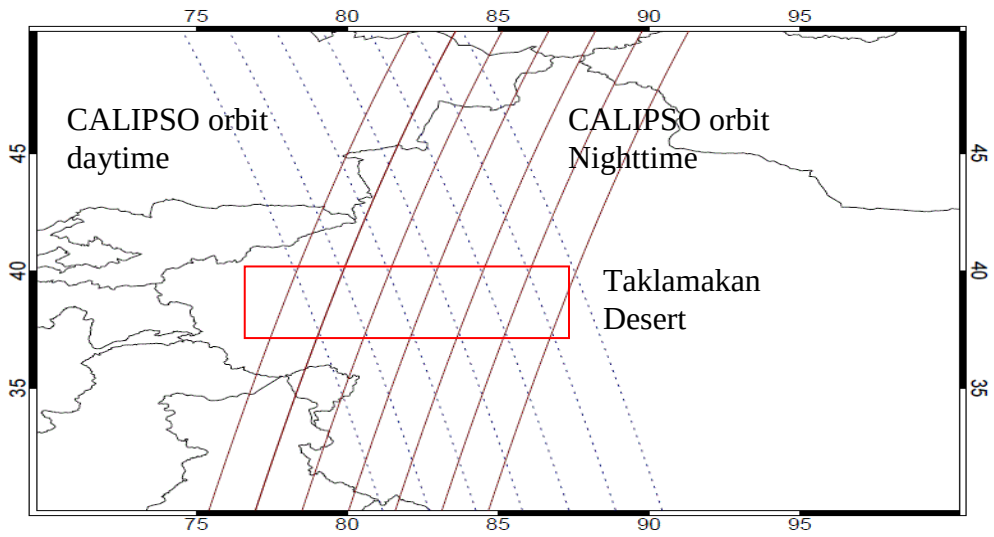

Figure 2.1 Orbits of CALIPSO over the Taklamakan Desert for fourteen days during the spring of 2007.

The diameter of the CALIPSO footprint is 70 m, and its footprint spacing is 333 m. Therefore, Level 1 data have a horizontal resolution of 333 m and a vertical resolution of 30 m between an altitude of -0.5 km and 8 km. Level 2 aerosol data retrieved from level 1 data have a lower horizontal resolution, depending on the horizontal averaging. The vertical resolution of the level 2 data is 60 m between -0.5 km and 20 km and 180 m between 20 km and 30 km for 5-km aerosol profile data, however, level 2 layer data provide the values of detected features up to eight features. The resolutions of CALIOP data are listed in Table 2.1.

Currently, CALIPSO science data products are available at Levels 1 and 2. The data products described in detail in the *CALIPSO Data Products Catalog ATBD* (PC SCI 503) are archived and distributed by the Atmospheric Science Data Center (ASDC) http://eosweb.larc.nasa.gov/PRODOCS/calipso/table_calipso.html. The latest version 3.01 of Level 2 aerosol data was released in June 2010. This study uses Level 2 CALIOP aerosol layer products.

Table 2.1 Resolution of CALIOP level 1 and 2 data.

Level 1					
Altitude Region		Vertical Resolution		Horizontal	Profiles
Base (km)	Top (km)	532 nm	1064 nm	Resolution	Per 5-km
30.1	40.0	300 m	-	5000 m	1
20.2	30.1	180 m	180 m	1667 m	3
8.2	20.2	60 m	60 m	1000 m	5
-0.5	8.2	30 m	60 m	333 m	15
-2.0	-0.5	300 m	300 m	333 m	15

Level 2				
5-km Aerosol Profile Data				
Altitude Region		Vertical	Horizontal	Profiles
Base (km)	Top (km)	Resolution	Resolution	Per 5-km
20	30	180 m	5000 m	15
-0.5	20	60 m	5000 m	15
5-km Aerosol Layer Data				
Altitude Region		Vertical Resolution	Horizontal Resolution	Profiles Per 5-km
Detected feature altitude (top / base)		No resolution (max 8 layers)	5000 m	15

2.3 Algorithm Outline

2.3.1 CALIOP Level 2 Algorithm

The retrieval of aerosols from CALIPSO level 1 data is a multi-step process, involving three different algorithms: the Selective Iterated Boundary Locator (SIBYL), Scene Classification Algorithms (SCA), and Hybrid Extinction Retrieval Algorithms (HERA).

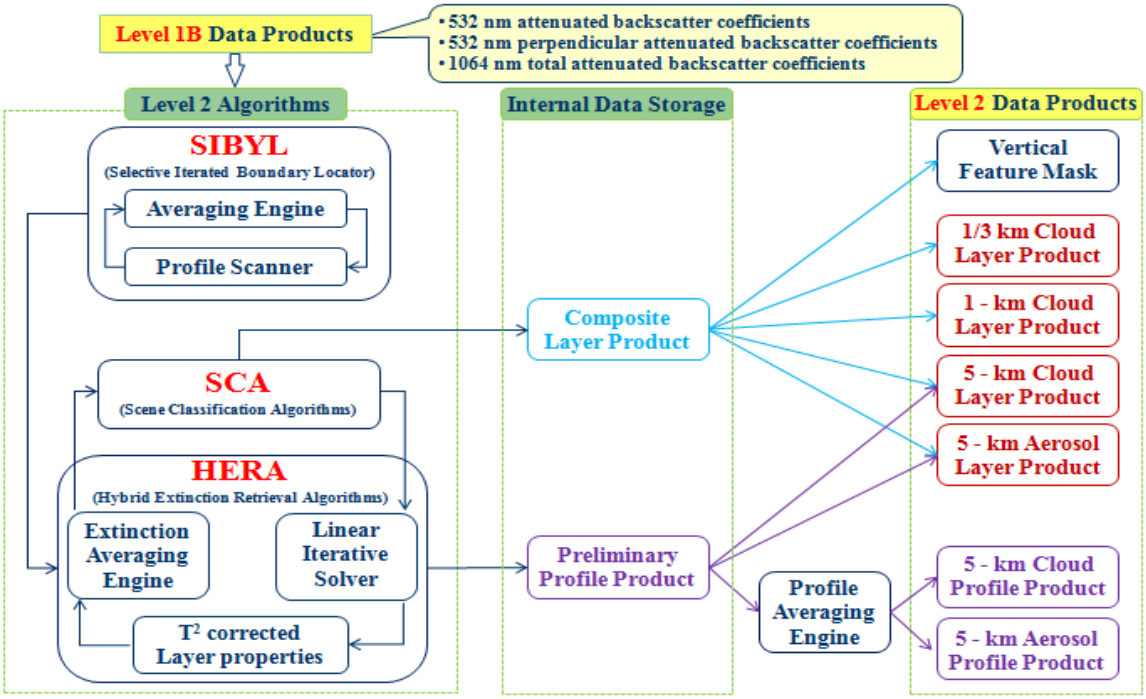

Figure 2.2 Flow chart of the level 2 algorithms of CALIPSO.

2.3.1.1 Selective Iterated Boundary Locator (SIBYL) Algorithm

The first stage of data processing employs the SIBYL algorithm to detect all of the features within a given orbit. In this algorithm, the consecutive profiles of the

attenuated backscatter in level 1 data are averaged over horizontal resolutions of 5, 20, and 80 km and vertical resolutions of 0.5 km for all altitude bins. In the averaging engine, 5-km, 20-km, and 80-km indicate a primarily averaging, an intermediate, and a maximum horizontal averaging distance, respectively. The averaging of consecutive profiles in an averaging engine helps one to improve signal-to-noise ratios (SNRs). Upon the completion of the construction, the profile scanner, a threshold algorithm, is used to scan each profile for the presence of aerosol layers, clouds, and surface returns, and the algorithm provides information about both the top and the base of the layers. The information about the top and base altitudes, the latitude, and the longitude are reported in the level 2 layer products (see further detail in CALIPSO ATBD Part 2: Feature Detection and Layer Properties Algorithms).

2.3.1.2 Scene Classification Algorithms (SCA)

On the basis of the information provided by SYBIL, the SCA determines whether the detected region is a feature or not, as shown in Figure 2.3. If the region is an atmospheric feature, the SCA examines the elevation of the feature. For the elevated feature, the lidar ratio is calculated by the transmittance-constraint method (Fernald et al., 1972, Young, 1995). After this computation, both the elevated and non-elevated features will be determined as types of clouds or aerosols using five parameters: the mean attenuated backscatter at 532 nm, the 1064/532 layer-integrated attenuated backscatter ratio, the midlayer altitude, the volume depolarization ratio, and the latitude. This algorithm, called Cloud Aerosol Discrimination (CAD), uses a multi-dimensional probability density function (PDF). The range of CAD score, f, from PDFs is from -100

to 100, and if the value of f is below 0, a feature is classified as aerosol. The absolute value of f shows the confidence of classification, that the low values of CAD are denoted as features with low confidence in the vertical feature mask. After the CAD algorithm, with three parameters (i.e., observed backscatter strength, the depolarization ratio, and the International Geosphere-Biosphere Programme (IGBP) surface types), the aerosol will be further classified as sub-type features (i.e., clear air, cloud, aerosol, stratospheric layer, surface, subsurface, totally attenuated, and no/low confidence), which called as Aerosol subtyping. The goal of aerosol subtyping algorithm, one of the SCA, is to estimate and assign the value of the aerosol extinction-to-backscatter ratio (called lidar ratio S_a) within 30% of the uncertainty.

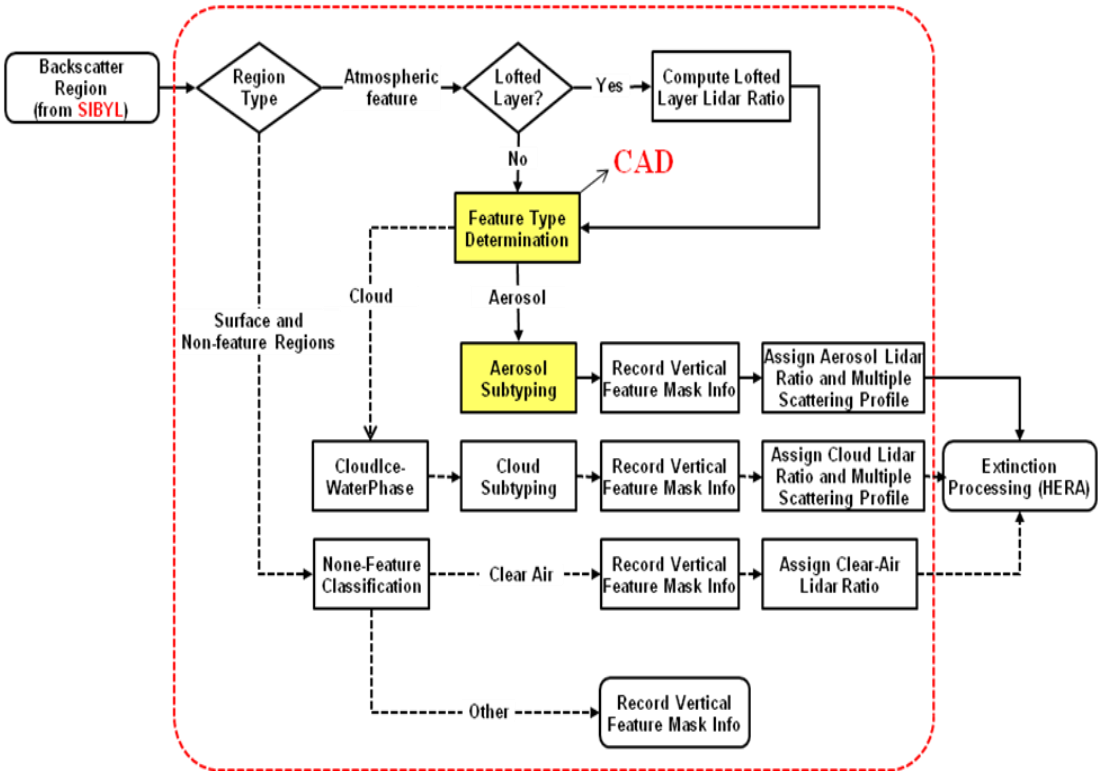

Figure 2.3 Flow chart of the SCA algorithms of CALIPSO.

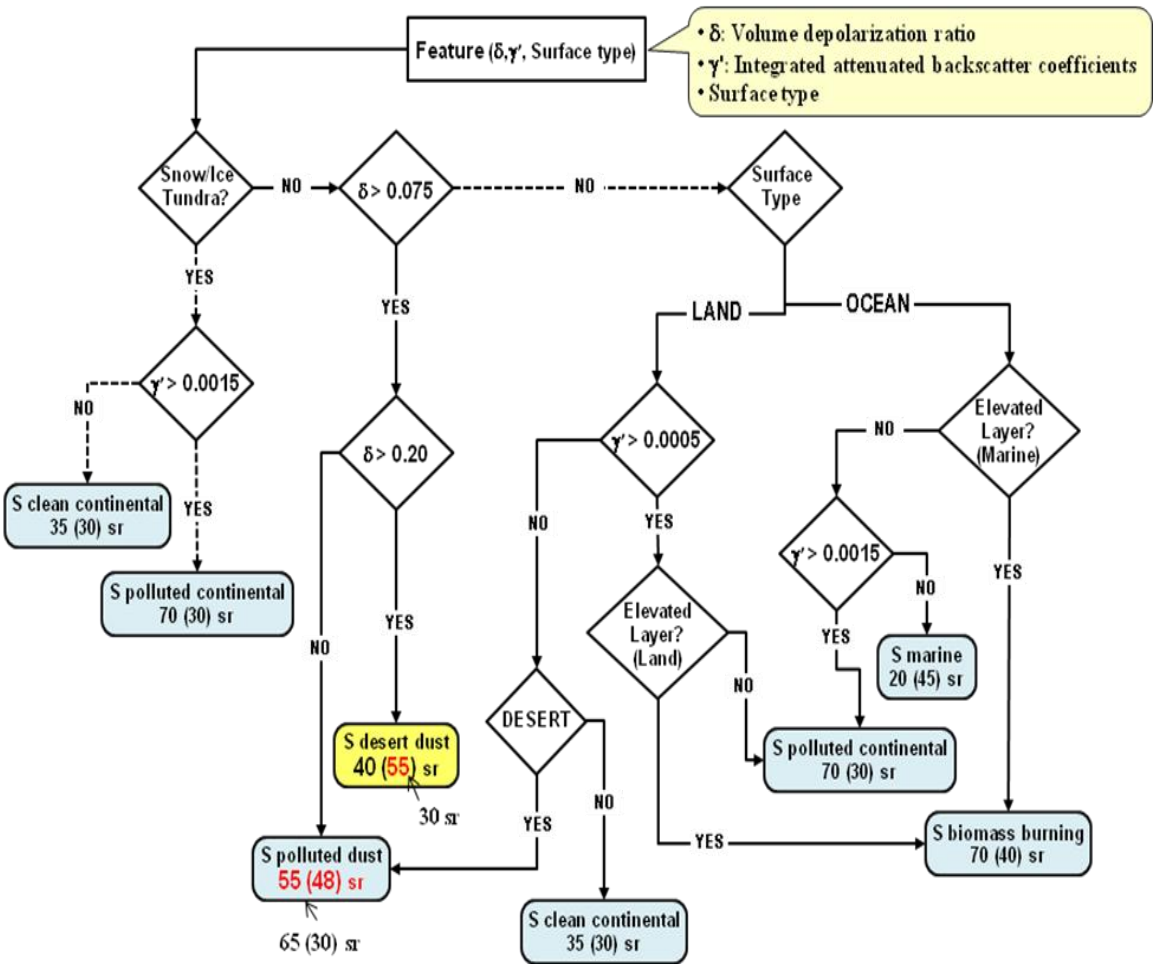

Figure 2.4 Flow chart of the aerosol subtyping algorithm.

The classified results are recorded in the vertical feature mask, and the SCA assigns the aerosol lidar ratio and the multiple scattering profiles for extinction processing in the HERA. If the feature is non-elevated, a lidar ratio is chosen based on the classified feature type in the SCA, but if the feature is lifted and a lidar ratio can be calculated using the transmittance method, the calculated lidar ratio is adopted.

2.3.1.3 Hybrid Extinction Retrieval Algorithms (HERA)

The initial lidar ratio from the SCA is applied to extinction retrieval processing in the HERA. With the retrieved extinction profiles, the total optical depth of each feature is computed and averaged, and the average is compared with the measured values, which are pre-measured from the reduction in the clear air signal from the SIBYL. The lidar ratio is adjusted when the values differ by more than the threshold value (Young & Vaughan, 2009), and then the detected layer is solved so that if falls within the error range of 30%. For the extinction retrieval processing, CALIPSO uses a forward iterative solution, which is a combination of two solutions, such as a two-component analytical solution developed by Fernald et al. (1972), Fernald (1984), and Klett (1985) and iterative solutions developed by Elterman (1964). As shown in Table 2.2, many studies used the forward iterative solutions (the near field) for retrieving the aerosol products rather than the backward iterative solutions (the far field). While the backward iterative solutions are stable (Klett, 1981,Young and Vaughan, 2009), these solutions are often problematic for CALIOP since usually it is not easy to select accurate far-field boundary conditions confidently, especially in the case of reduced SNR which happens during daytime (Young and Vaughan, 2009). Thus Young and Vaughan (2009) suggested the forward iterative solutions (Elterman, 1966) and solutions of Platt (1973, 1979) for the multiple scattering parameters. CALIPSO retrieving algorithms have also been applying these solutions for the extinction retrieval algorithm.

Table 2.2 Past studies of dust aerosol that used CALIPSO data

Studies	Region / Time	Data products (Related to CALIOP)	Algorithms
		Asian Dust	
Eguchi et al. (2009)	Asian dust/ 5-15 May 2007	- Total extinction coefficients - Particle depolarization ratio	Fernald's inversion (1984) -Forward solutions
Hara et al. (2008)	Taklimakan dust/ July-September 2006/ 2007	- Dust extinction coefficient (Derived using Fernald's inversion) - Vertical profiles of dust extinction coefficient	Fernald's inversion (1984) -Forward solutions
Hara et al. (2009)	Asian dust/ 21-31 May 2007	- Dust extinction coefficient (Derived using Fernald's inversion) - Averaged vertical profiles of the dust extinction coefficient (Derived using Fernald's inversion) - Color ratio at 532 nm and 1064 nm - Particulate depolarization ratio	Fernald's inversion (1984) -Forward solutions
Huang et al. (2007)	Tibetan dust/ June-September 2006	- Total attenuated backscattering intensity at 532 nm - Vertical profiles of total 532 nm attenuated backscattering intensity and depolarization ratio - Frequency distribution of the depolarization ratio and the color ratio	
Huang et al. (2008)	Taklimakan dust/ 26-31 July 2006	- 532 nm total attenuated backscatter coefficients - Volume depolarization ratio - Dust aerosol optical depth - Dust aerosol extinction coefficient - Averaged vertical profiles of the dust extinction coefficient (derived using Fernald's inversion)	- Hu et al. (2006)'s method in the retrieve of the AOD
Kim et al. (2008)	Asian dust/ 14,30 Sep, 24 Oct, 25 Nov 2006, 12 Jan, 21 Feb 2007	- Apparent scattering ratio at 532 nm - Vertical profiles of aerosol extinction coefficient at 532 nm - Backscatter-to-extinction ratio (lidar ratio)	- Klett method (1981, 1985) for the aerosol extinction coefficients - Berthier et al. (2006)'s method for the lidar ratio

Table 2.2 (continued)

Studies	Region / Time	Data products (Related to CALIOP)	Algorithms
		Asian Dust (continued)	
Sugimoto et al. (2009)	Asian dust/ 23 July 2006	- Extinction coefficient at 532 nm	Fernald's inversion (1984) -Forward solutions -Two-wavelength
Uno et al. (2008)	Asian dust/ 5-8 May 2007	- Dust extinction coefficient (Derived using Fernald's inversion) - Averaged vertical profiles of the dust extinction coefficient (Derived using Fernald's inversion)	Fernald's inversion (1984) -Forward solutions
Z. Liu et al. (2008)	Tibetan dust/ Spring in 2007	- Attenuated backscatter coefficients at 532 nm - Volume depolarization ratio - Backscatter color ratio	
		African Dust	
Generoso et al. (2008)	Saharan dust/ 30 June-6 July 2006, 13-17 February 2007	- Attenuated backscatter profiles at 532 nm - Time series of attenuated backscatter profiles at 532 nm (From August 2006 to February 2007)	Wang et al. (2007)'s method in the retrieve of the CALIOP data
Z. Liu et al. (2008)	Sahara dust/ 18, 19, 20 August 2006	- Optical depth at 532nm, - 1064 nm & 532 nm lidar ratio, - Optical depth ratio, - Color ratio, - Particulate depolarization ratio, - Retrieved backscatter coefficients at 532/1064 nm - 1064/532 Backscatter ratio	Fernald's inversion (1984) - Two-wavelength - Opaque water cloud
Z. Liu et al. (2010)	North Africa (12°-30°N; 30°W-35°E)/ June 2006-December 2008)	- Effective Lidar Ratio (ELR) - Multiple scattering factor	Two-way transmittance

2.3.2 Retrieval of Profiles of Particulate Backscatter and Extinction

This section introduces the retrieval of profiles of both the particulate backscatter and the extinction for the level 2 data of CALIPSO. Retrieval is a process carried out by the HERA. The two-component lidar equation can be expressed as (Young and Vaughan, 2009):

$$P(r) = \frac{1}{r^2} E_0 G_A C\left[\beta_M(r) + \beta_P(r)\right] T_M^2(0,r) T_{O_3}^2(0,r) T_p^2(0,r), \tag{2.1}$$

where

$P(r)$ is the detected backscattered signal from range r from the lidar,

E_0 is the laser energy for a single or averaged profile,

G_A is the amplifier gain,

C is the lidar calibration coefficient,

β_M is the molecular volume backscatter coefficient,

$T_M^2(0,r) = \exp\left[-2\int_0^r \sigma_M(r')dr'\right]$ is the molecular two-way transmittance between the lidar and range z,

$\sigma_M(r) = S_M \beta_M(r)$ is the molecular volume extinction coefficient,

S_m is the molecular extinction-to-backscatter (or lidar) ratio,

$T_{O_3}^2(0,r) = \exp\left[-2\int_0^r \alpha_{O_3}(r')dr'\right]$ is the ozone two-way transmittance,

$\alpha_{O_3}(r')$ is the ozone volume absorption coefficient,

β_p is the particulate (aerosol) volume backscatter coefficient,

$T_P^2(0,r) = \exp\left[-2\eta(r)\tau_P(0,r)\right]$ is the particulate two-way transmittance,

$\eta(r)$ is a parameterization describing multiple scattering by particles,

$\tau_P(0,r) = \int_0^r \sigma_P(r')dr' = \sum_{j=0}^{n-1} S_{P_j} \int_{r_j}^{r_{j-1}} \beta_p(r')dr'$ is the particulate optical depth between the lidar and range r,

$\sigma_p(r) = S_p\beta_p(r)$ is the particulate volume extinction coefficient, and

S_p is the particulate extinction-to-backscatter (or lidar) ratio.

With the deletion of the background and offset from the lidar signal, we can rearrange Eq. (1) to provide the attenuated backscatter. Since the attenuated backscatter value depends on atmospheric quantities and ranges, we obtain profiles of the attenuated backscatter signal corrected for ozone transmittance as follows:

$$\beta'(0,r) = [\beta_M(r) + \beta_P(r)]T_M^2(0,r)T_p^2(0,r) = \frac{[P(r) - P_0]r^2}{E_0 G_A C T_{O_3}^2(0,r)}. \quad (2.2)$$

2.4 Comparison of CALIOP Data from Versions 2 and 3.01

2.4.1 Problems in CALIOP Version 2 Data

Our analyses of version 2 products in dust-laden conditions revealed significant errors, especially in the case of very dense dust layers and dust-cloud mixed scenes. Very opaque dust layers over and close to the dust source areas were often misclassified as clouds due to the similarity of scattering properties between the dense dust layers and the optically thin clouds in the 3D PDFs algorithm. This misclassification causes the AOD to be underestimated. Another problem leading to the underestimation of the AOD is that the base altitude of aerosol layers is misidentified in cases of optically thick and highly absorbing aerosol layers. A good example illustrating this problem is the case of

CALIPSO daytime track on March 30, 2007, over the Gobi Desert. Figure 2.5 shows both features of the total attenuated backscatter and vertical feature mask from version 2 (left) and version 3.01 (right). In the algorithm of version 2, very dense dust plumes between 38N and 46N and below ~4 km were classified as clouds, but the algorithm in version 3 classified them correctly as dust plumes. The reason for misclassification of dust layers in version 2 is that the intensity of the lidar signal completely weaken over these layers (the surface signal was not detected at all), and therefore, the optical depth should be larger than ~3 (Liu et al., 2009). These optical properties are similar to the expected values for clouds in the CAD algorithm (Liu et al., 2009). However, the reported optical depth of opaque layers in version 3.01 indicates only the upper portion of the layer where the lidar signal can be measured. About one-fifth of the cloud layers and a few very dense aerosol layers are identified to be opaque. In these cases, CALIOP cannot determine the true layer base, and aerosol layer products cannot identify those opaque layers. When the solution is physically possible, aerosols can be retrieved about 99% successfully (CALIPSO ATBD, 2010). This improvement in the CAD algorithms of version 3 enables one to use new level 2 data with higher confidence. In addition to the confidence of the vertical feature mask, the AOD in Figure 2.6 shows a difference between versions 2 and 3.01, which illustrates the improvement of AOD in version 3.01.

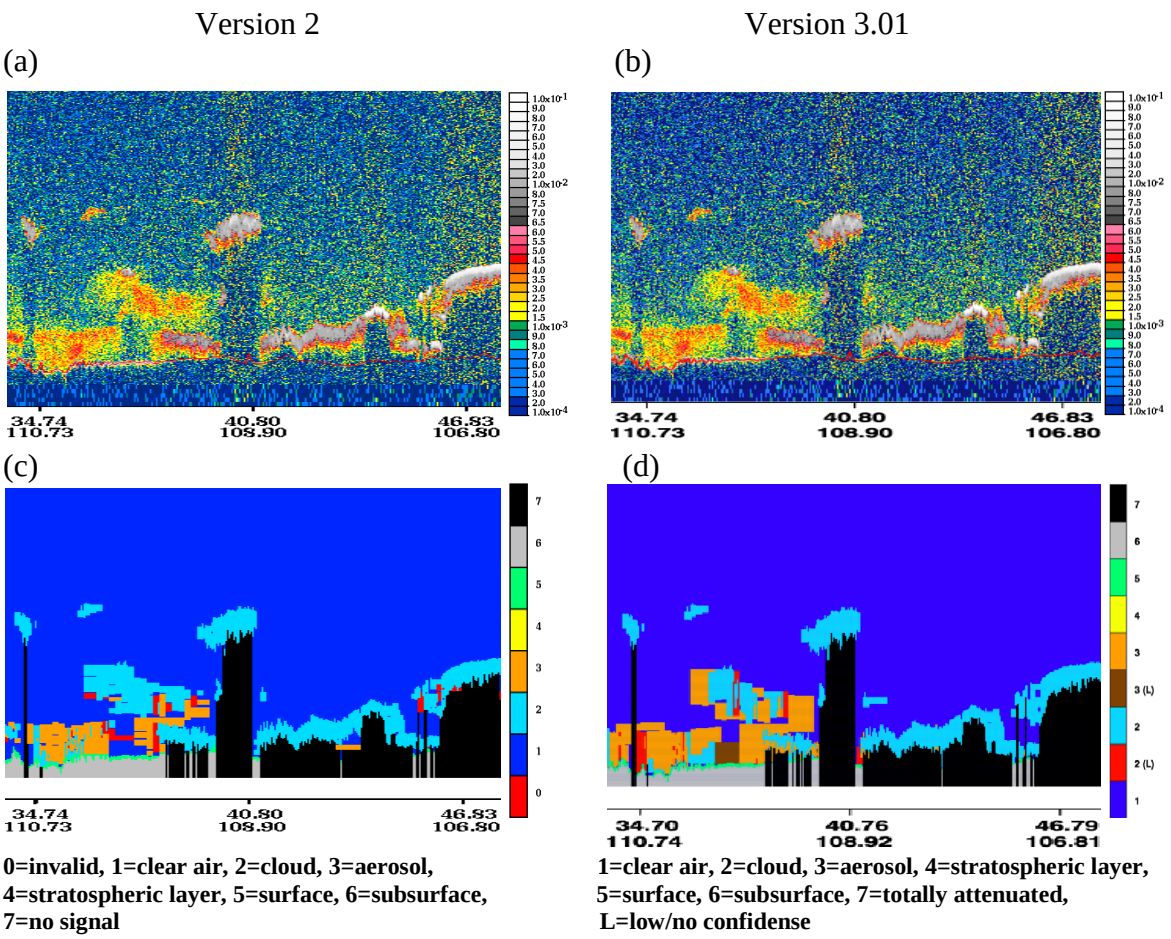

Figure 2.5 Total attenuated backscatter coefficients of (a) version 2 and (b) version 3.01 and the vertical feature mask of (c) version 2 and (d) version 3.01 over the Gobi Desert on March 30, 2007.

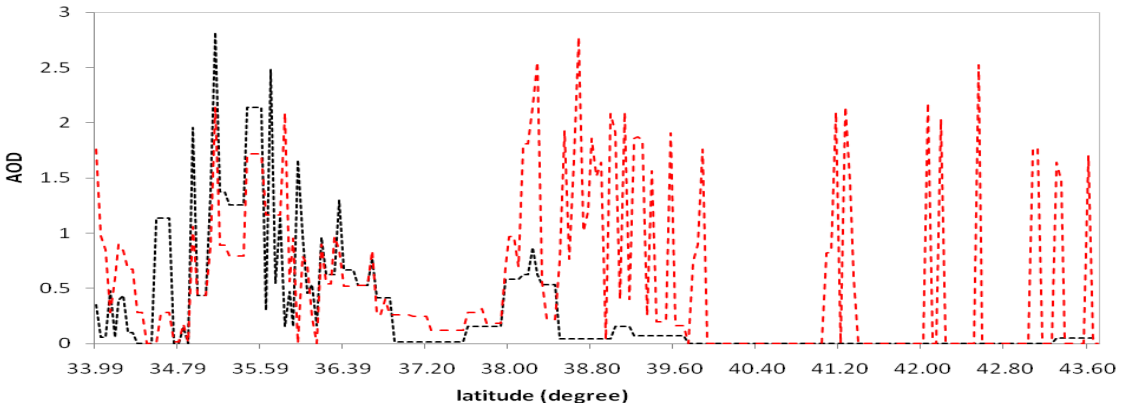

Figure 2.6 Aerosol optical depth of version 2 (black) and version 3.01 (red) over the Gobi Desert on March 30, 2007.

2.4.2 Improvements in Level 2 Version 3.01 Data

A data quality statement on the release of the CALIPSO Lidar Level 2 Cloud and Aerosol Profile Products Version 3.01 in June 2010 shows an improvement over the previous versions of 2. The algorithm for the dust retrieval was improved in four major ways: (1) aerosol and cloud level 2 profile data have the same horizontal resolution of 5 km, as shown in Figure 2.2; (2) the use of five diagnostic parameters instead of three diagnostic parameters in the CAD algorithm enables one to better distinguish clouds and aerosols, showing good results in the vertical feature mask; (3) adding the aerosol layer base extension algorithm into the SIBYL algorithm enables more accurate estimates of AOD; and (4) the lidar ratios in the two aerosol models (i.e., desert dust and polluted dust) in version 3.01 differ from those in version 2. The dust lidar ratio in version 3.01 is 55 sr at 1064 nm, which is larger than 30 sr at 1064 nm in version 2. The lidar ratios of polluted dust are 55 sr at 532 nm and 48 sr at 1064 nm in version 3.01, which are 65 sr at 532 nm and 30 sr at 1064 nm in version 2. The extinction-to-backscatter ratio (S_a) is a key parameter for retrieving the aerosol extinction and thus the optical depth from CALIPSO level 1 data. The value of S_a depends on several microphysical properties such as size distribution, shape, and composition. Chapter 3 of this study will show the relationship between S_a and these microphysical properties. In addition, new particulate parameters (i.e., the particulate depolarization ratio and the particulate color ratio) are added in version 3.01. Table 2.3 summarizes the differences and improvements between versions 2 and 3.01, and Table 2.4 shows the CALIOP version 3.01 data of interest to the study.

Table 2.3 Comparison of CALIPSO data version 2 vs. version 3.01.

Parameters	Version 2	Version 3.01
Vertical Feature Mask	Based on 3-D PDFs - Mean attenuated backscatter at 532 nm - 1064/532 layer-integrated attenuated backscatter ratio (or total color ratio) - Midlayer altitude	Based on 5-D PDFs - Mean attenuated backscatter at 532 nm - 1064/532 layer-integrated attenuated backscatter ratio (or total color ratio) - Midlayer altitude - Volume depolarization ratio - Latitude
	Classification of 8 types: Invalid, clear air, cloud, aerosol, stratospheric layer, surface, subsurface, no signal (totally attenuated)	Classification of 9 types: Clear air, cloud, cloud(L), aerosol, aerosol (L), stratospheric layer, surface, subsurface, totally attenuated, L=low/no confidence
Aerosol Type	Based on the following parameters: - Observed backscatter strength - Depolarization ratio - IGBP surface types	Based on the following parameters: - Observed backscatter strength - Depolarization ratio - IGBP surface types
	Classification of 9 types / (assigned S_a at 532/1064 nm) - Not applicable - Clean marine (20/45 sr) - Dust (40/30 sr) - Polluted continental (70/30 sr) - Clean continental (35/30 sr) - Polluted dust (65/30 sr) - Smoke (70/40 sr)	Classification of 9 types / (assigned S_a at 532/1064 nm) - Not applicable - Clean marine (20/45 sr) - Dust (40/55 sr) - Polluted continental (70/30 sr) - Clean continental (35/30 sr) - Polluted dust (55/48 sr) - Smoke (70/40 sr)
Aerosol Optical Depth (AOD)	Based on forward solution	Based on forward solution includes the aerosol layer base extension algorithm
Volume Depolarization Ratio (δ_v)	Direct measurement Quality depends on the accuracy of the top and base identification	Direct measurement Quality depends on the accuracy of the top and base identification
Particulate Depolarization Ratio (δ_p)	-	Post-extinction quantity Quality - SNR of the backscatter measurements in parallel and perpendicular - Accuracy of two-way transmittance estimates
Particulate Color Ratio (χ_p)	-	Post-extinction quantity Quality - Accuracy of layer top/base altitudes - SNR of the backscatter data - Success of the HERA profile solver

Red font shows changed or new parameters in version 3.01.

Table 2.4 CALIOP version 3.01 data products of interest to this study.

Processing Level	Symbol	Characteristics
Level 1B	$\beta'_{532,Total}$	532 nm total attenuated backscatter coefficients
	$\beta'_{532,\perp}$	532 nm perpendicular attenuated backscatter coefficients
	β'_{1064}	1064 nm total attenuated backscatter coefficients
Level 2 5-km Aerosol Layer	$\gamma'_{532,column}$	Column Integrated Attenuated Backscatter 532
	$COD_{532.column}$	Column Optical Depth Cloud 532
	$AOD_{532.column}$	Column Optical Depth Aerosol 532 (1064)
	γ'_{532}	Integrated Attenuated Backscatter 532 (1064)
	$\delta_{v,layer}$	Integrated Volume Depolarization Ratio
	$\chi'_{v,layer}$	Integrated Attenuated Total Color Ratio
	AOD_{532}	Feature Optical Depth 532 (1064)
	$\delta_{p,layer}$	Integrated Particulate Depolarization Ratio
	$\chi'_{p,layer}$	Integrated Particulate Color Ratio
Level 2 5-km Aerosol Profile	$\gamma'_{532,profile}$	Total (Perpendicular) Backscatter Coefficient 532
	$\gamma'_{1064,profile}$	Backscatter Coefficient 1064
	$\sigma_{532,profile}$	Extinction Coefficient 532 (1064)
	$\delta_{p,profile}$	Particulate Depolarization Ratio Profile

Red font indicates new parameters in version 3.01.

2.5 Summary

This chapter examined a procedure for retrieving aerosol properties from the CALIPSO level 1B data and the performance of CALIPSO in dust-laden conditions to confirm the reliability of the latest level 2 version 3.01 data. The CALIPSO lidar retrieval is a multi-step process that includes the correction of lidar signals for instrumental effects; the detection and classification of atmospheric and surface features; the classification of the aerosol types; and, finally, the retrieval of the backscatter and extinction profiles of aerosol layers and their optical depth. The process is performed at multiple horizontal resolutions. As a result, the aerosol extinction retrieval is affected by all preceding steps. We examined relevant retrieval procedures, including SIBYL, SCA, CAD, Aerosol subtyping, and HERA, along with analyses of CALIPSO products in dust-laden conditions to determine the sources of biases in previous version 2 data and the performance of new version 3.01 data. We found that version 2 data were most prone to error in the case of dense dust layers and dust-cloud mixed scenes. The new version 3.01 data showed an improved capability to discriminate between clouds and aerosols by implementing the 5D PDFs instead of 3D PDFs algorithm used in version 2 data. In addition, AOD values of version 3.01 data show more accurate results than version 2 thanks to the aerosol layer base extension algorithm added to SIBYL. AODs values were also affected by changes in the lidar ratio used for dust retrievals: version 3.01 data were generated using different lidar ratios for dust at 1,064 nm and polluted dust at 532 nm and 1,064 nm as shown in Table 2.3. The effect of these changes in lidar ratios will be further addressed in Chapter 3. Through many improvements of aerosol retrieving algorithm, version 3.01 data show more accurate data than previous version 2. Overall, our analyses

show that the latest level version 3.01 CALIPSO data provide more reliable information and hence are more appropriate for dust studies. However, our analyses also revealed the remaining sources of uncertainty or error that must be accounted for in dust studies (see further discussion in Chapters 3 and 4). Some major sources are the following: a) having two aerosol types - "dust" and "polluted dust" (see Table2.3) - does not capture the full variability of dust properties; b) low signal-to-noise ratio of the CALIOP lidar leads to the misclassification or lack of aerosol layer identification, especially near the land surface, that limits applicability of CALIPSO data for studying weak dust episodes; c) biases in daytime CALIOP attenuated backscatter profiles; d) the effect of multiple scattering, especially in dense dust plumes; and finally, e) cloud contamination still may be a factor leading to erroneous vertical features classification. Given the complexity of space lidar observations and various issues pertinent to aerosol (and dust in particular) retrievals, to fully benefit from CALIPSO lidar capabilities would require an integration of CALIPSO data with independent satellite and ground-based observations. A methodology for performing such integrative data analyses and its application to regional dust studies are presented in Chapters 4 and 5.

CHAPTER 3

MODELING AND ANALYSIS OF DUST OPTICAL PROPERTIES FOR USE IN LIDAR REMOTE SENSING

3.1 Introduction

One of the critical issues of the CALIOP aerosol retrieval algorithm is an assumption about several aerosol optical characteristics (such as lidar ratio S_a) that are required by lidar retrievals. Currently, the CALIPSO retrieval algorithm uses a fixed value S_a = 40 sr for dust regardless of the source region and transported distances (see Chapter 2). Many past experimental and modeling studies, however, demonstrated that S_a varies in dust-laden conditions depending on the microphysical properties of dust particles such as size, composition, and shape. Better understanding of how variations of dust microphysical properties occurring during the dust lifecycle in the atmosphere can affect S_a is of great importance for accurate retrievals of the aerosol extinction profile and aerosol optical depth from CALIPSO lidar measurements. On the other hand, CALIPSO lidar provides unique information on the particulate linear depolarization ratio δ_p that potentially can be used to detect nonspherical dust particles (since δ_p = 0 for spheres) and characterize the dust aging, especially changes in particle shapes. Thus, it is important to examine the behavior of both lidar optical characteristics S_a and δ_p, considering the representative dust microphysical properties in the source regions and downwind. This motivated us to perform intensive optical simulations aimed at examining the extent to which the microphysical properties of dust particles affect the aerosol optical characteristics used in lidar remote sensing. We also modeled the single scattering albedo

and asymmetry parameter, both of which are required in radiative transfer calculations of the dust radiative impact. Chapter 3 presents the results of this modeling study.

Despite the recent progress in the development of computationally fast numerical methods for optical modeling, calculation of the optical characteristics of mineral aerosol remains a challenging problem. The main reasons stem from the complex nature of dust particles whose shapes exhibit a wide variety of morphologies and sizes span over the wide range. It has been well recognized that the Mie theory, which gives accurate optical properties of spheres and is widely used in remote sensing applications, is not applicable to dust particles, especially for lidar remote sensing applications. Given the complexity of dust morphologies and limited data to reconstruct actual 3D shapes, the majority of studies approximate dust by a mixture of spheroids and employ the T-matrix technique to compute optical properties of dust-like mixtures (Mishchenko et al., 2007, Wiegner et al., 2009). This method relies not only on one critical assumption that optical properties of a mixture of dust particles can be reproduced by a mixture of spheroids, but it also involves a number of other important assumptions related to defining the aspect ratio of prolate and oblate spheroids, its change with size, and the proportion of spheroids with different aspect ratios in fine and coarse mode particles (Dubovik et al., 2006, Wiegner et al., 2009). As an example, Figure 3.1(b) illustrates how an actual dust particle can be approximated by a spheroid, which is defined by an axis ratio ε, the ratio of the horizontal semi-axis (b) to the rotational semi-axis (a) as shown in Figure 3.1(b). It is apparent that in reality, dust shapes are more complex. An alternative approach for dust optical modeling has been suggested by Kalashnikova and Sokolik (2002, 2004). This approach is based on the Discrete Dipole Approximation (DDA) method. Although DDA allows

computing the optical properties of a particle of any shape and composition, the method is very computationally expensive compared to the T-matrix method and, what is even more critical, the data on 3D shapes of dust particles are currently very limited. Thus, if the T-matrix method would be able to reproduce the lidar observations, then the more complicated DDA approach will not be needed for CALIPSO. We examine this issue by performing a detailed optical modeling with T-matrix method in relation to CALIPSO and ground-based lidar observations. In addition, due to the narrow size parameter range of the T-matrix method, some studies used the improved geometric optics method (IGOM) for coarse particles (Yang et al., 2007).

(a) (b)

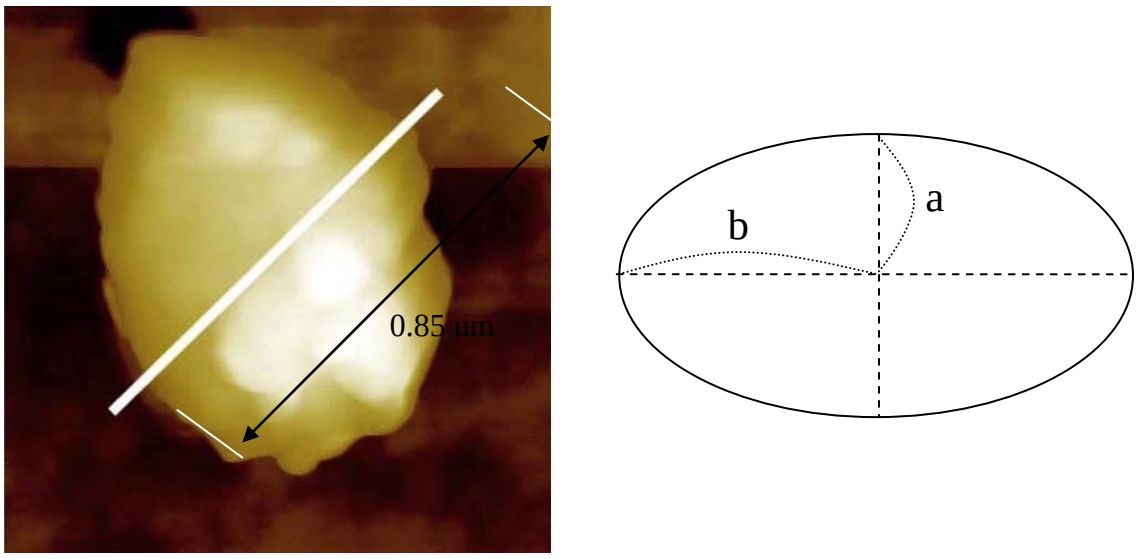

Figure 3.1 (a) Atomic Force Microscopy (AFM) image of a dust particle (from Chou et al., 2008) and (b) spheroid with axis ratio ε =b/a.

The goals of this study are to perform an intensive modeling of the optical properties of nonspherical dust particles to aid in the retrievals and in the interpretation of CALIOP data. To perform modeling over the required broad range of dust particle sizes, we developed a unified code by merging the T-matrix method and IGOM method, which is called TM/IGOM hereafter. The next section introduces the T-matrix and IGOM methods and the TM/IGOM. Section 3.3 describes the selection of microphysical parameters used in optical modeling. In Section 3.4, the results of optical modeling are discussed and compared to measurements. Lastly, Section 3.5 summarizes the main findings.

3.2 Development of a Unified Code by Merging the T-matrix Method and the IGOM Method

This section briefly introduces T-matrix and IGOM codes employed in our study. Then we show how the unified code TM/IGOM was developed and used to compute the optical characteristics of dust mixtures.

3.2.1 T-matrix Method

The T-matrix method originally developed by Waterman (1971) is an exact approach for computing the scattering and absorption properties of nonspherical, rotationally symmetric particles (e.g., spheroids). We employed a code of the T-matrix technique developed by Mishchenko and Travis (1994) which is publicly available at http://www.giss.nasa.gov/staff/mmishchenko/t_matrix.html.

The scattering matrix expresses the transformation of the Stokes vector of the incident beam, I_0, Q_0, U_0, and V_0, into the Stokes vector of the scattered beam, P, provided that both Stokes vectors are defined with respect to the scattering plane

$$\begin{bmatrix} I \\ Q \\ U \\ V \end{bmatrix} = \frac{C_{sca} n_0 dv}{4\pi R^2} P \begin{bmatrix} I_0 \\ Q_0 \\ U_0 \\ V_0 \end{bmatrix}, \tag{3.1}$$

where n_0 is the particle number density, R is the distance from the small-volume element dv to the observation point, and I, Q, U, and V are the Stokes parameters of scattered radiation. The scattering phase matrix P is defined as follows:

$$P = \begin{bmatrix} P_{11} & P_{12} & 0 & 0 \\ P_{12} & P_{22} & 0 & 0 \\ 0 & 0 & P_{33} & -P_{34} \\ 0 & 0 & P_{34} & P_{44} \end{bmatrix}, \tag{3.2}$$

The phase function P_{11} satisfies the normalization

$$\frac{1}{2}\int_0^{\pi} d\Theta \sin\theta \, P_{11}(\Theta) = 1, \tag{3.3}$$

The asymmetry parameter of the phase function is defined as

$$g = <\cos\Theta> = \frac{1}{2}\int_{-1}^{1} d(\cos\Theta) P_{11}(\Theta)\cos\Theta, \tag{3.4}$$

An efficient approach for the computations of rotationally symmetric particles with random orientation is to expand the elements of the scattering matrix as follows:

$$P_{11} = \sum_{l=0}^{l_{max}} \alpha_1^l P_{00}^l(\cos\Theta), \tag{3.5}$$

where α_1^l is the expansion coefficients and $P_{00}^l(\cos\Theta)$ are Legendre polynomials. $P_{00}^l(x) = P_l(x)$, and thus the equation above is the expansion of the phase function in Legendre polynomials. $<\cos\Theta>$ is derived by using the orthogonality property of spherical functions,

$$<cos\Theta> = \alpha^1_1 / 3, \tag{3.6}$$

The absorption cross section σ_{abs} per particle is defined as the difference between the extinction σ_{ext} and scattering σ_{sca} cross sections

$$\sigma_{abs} = \sigma_{ext} - \sigma_{sca}, \tag{3.7}$$

where the extinction and scattering cross sections are averaged over the uniform orientation distribution of a nonspherical particle and can be written in terms of the transition matrix T as follows:

$$\sigma_e = -\frac{2\pi}{k^2} Re \sum_{n=1}^{n_{max}} \sum_{m=-n}^{n} [T^{11}_{mnmn} + T^{12}_{mnmn}], \tag{3.8}$$

$$\sigma_s = \frac{2\pi}{k^2} \sum_{n=1}^{n_{max}} \sum_{m'=1}^{n_{max}} \sum_{m=-n}^{n} \sum_{m'=-n'}^{n'} \sum_{i=1}^{2} \sum_{j=1}^{2} \left| T^{ij}_{mnm'n'} \right|^2. \tag{3.9}$$

The basic principle of T-matrix consists of the expansion of scattered fields and the incident electromagnetic field in vector spherical wave functions. In T-matrix, the expansion coefficients of the incident field are transformed into those of scattered filed, which allows T-matrix to be used in the computation of any scattering characteristic of nonspherical particles. The T matrix elements are not dependent on the incident and scattering fields but depend only on the size parameter, refractive index, and shape of the scattering particle, and on the orientation of the scattering particle with respect to the reference frame. The T-matrix method is applied to size parameters ($x = 2\pi r_v/\lambda$) ranging from 0.5 to 50. This is another limitation of the T-matrix method with the limited types of particle shapes (such as spheroids, cylinder, and Chebyshev shapes).

3.2.2 IGOM Method

The IGOM is a hybrid algorithm based on the principles of geometric optic and electromagnetic wave theory. In particular, this method employs the ray-tracing technique to compute the near-field on the scattering particle surface. The corresponding far-field is obtained by mapping the near-field to its counterpart in the radiation zone on the basis of electromagnetic wave theory. The basic formulation of the IGOM can be found in two studies of Yang and Liou (1996, 2009). To increase the computational efficiency of the IGOM, the Monte Carlo method is applied to the ray-tracing technique and a simplified algorithm is used to account for the ray-spreading effect associated with mapping the near-filed to the far-field. An IGOM numerical code used in our study was provided by Dr. P.Yang.

In the IGOM code, the phase matrix can be written as

$$P_{11}^{r,t}(\theta) = 2\pi \int_0^{\pi} \left[S_{11}(\theta,\theta_t)\widetilde{P_{11}^{r,t}}(\theta_t) + S_{12}(\theta,\theta_t)\widetilde{P_{12}^{r,t}}(\theta_t) \right] sin\theta_t d\theta_t, \qquad (3.10)$$

where $\widetilde{P_{11}^{r,t}}(\theta_t)$ and $\widetilde{P_{12}^{r,t}}(\theta_t)$ are the (1,1) and (1,2) elements of the phase matrix. The factors, S_{11} and S_{12}, are related to the ray spreading effect (Yang and Liou, 1996) caused by the finite cross sections of the rays (see Yang and Liou (1996, 2009) for the detailed expressions of factors S_{11} and S_{12}).

Once the scattering matrix is determined, it is straightforward to compute the scattering phase matrix that relates the scattered stoke parameters to their incident counterparts. Eq. (11) accounts for the phase interferences among geometric optics rays and diffraction

$$\begin{bmatrix} S_2 & S_3 \\ S_4 & S_1 \end{bmatrix} = \begin{bmatrix} S_2 & S_3 \\ S_4 & S_1 \end{bmatrix}_{ray} + \begin{bmatrix} S_2 & S_3 \\ S_4 & S_1 \end{bmatrix}_{dif}, \qquad (3.11)$$

However, the effect of phase interferences on scattering pattern is negligible for polydisperse systems which consist of nonspherical particles with random orientation (Yang and Liou, 2009). Accordingly, the phase matrix can be simplified as

$$P = \frac{\sigma - \sigma_a}{2\sigma - \sigma_a} P_{ray} + \frac{\sigma}{2\sigma - \sigma_a} P_{dif}, \tag{3.12}$$

where P_{ray} is the contributions from geometric optics rays and P_{dif} from diffraction. Both P_{ray} and P_{dif} in Eq. (12) are normalized as follows:

$$\frac{1}{2}\int_0^{\pi} \mathrm{P_{ray}}(\Theta)\sin\theta d\Theta = 1 \quad \text{and} \quad \frac{1}{2}\int_0^{\pi} \mathrm{P_{dif}}(\Theta)\sin\theta d\Theta = 1, \tag{3.13}$$

The total extinction efficiency Q_e is given by

$$Q_e(a,b,k,m) = Q_{e,IGOM}(a,b,k,m) + \overline{Q_{e,edge}}(a,b,k), \tag{3.14}$$

where $Q_{e,IGOM}(a,b,k,m)$ is calculated by the IGOM, and $\overline{Q_{e,edge}}(a,b,k)$ is the mean edge contribution to the extinction efficiency, given by Fournier and Evans (1991) as follows:

$$\overline{Q_{e,edge}}(a,b,k) = \frac{\int_0^1 Q_{e,edge}(\mu,a,b,k)\left[\mu^2 + (a/b)^2(1-\mu^2)\right]^{1/2} d\mu}{\int_0^1 \left[\mu^2 + (a/b)^2(1-\mu^2)\right]^{1/2} d\mu}, \tag{3.15}$$

Yang et al. (2007) point out that both extinction and absorption efficiencies are underestimated in the IGOM computation. Therefore, Nussenzveig and Wiscombe (1980) averaged the absorption efficiency over a size parameter interval $\Delta x \sim \pi$ and suggested a mean absorption efficiency as follows:

$$Q_a = Q_{a,GOM} + Q_{a,a.e.} + Q_{a,b.e.}, \tag{3.16}$$

where $Q_{a,GOM}$ represents the geometric optics term. $Q_{a,a.e.}$ and $Q_{a,b.e}$, are the analytical expressions presented by Nussenzveig and Wiscombe (1980) based on the CAM theory, and refer to the above-edge and below-edge contributions, respectively. The extinction σ_e and scattering σ_e cross sections are given by

$$\sigma_e = Q_e A \quad \text{and} \quad \sigma_s = Q_s A \,. \tag{3.17}$$

where the projected area (A) is one quarter of the surface area (S) (Vouk, 1948). The surface area of a spheroid, given by Beyer (1981), is written as

$$s = \begin{cases} 2\pi b^2 + \pi \frac{a^2}{\varepsilon} ln \frac{1+\varepsilon}{1-\epsilon} & \text{for oblate spheroids} \\ 2\pi b^2 + 2\pi \frac{ab}{\varepsilon} sin^{-1}\epsilon & \text{for prolate spheroids,} \end{cases} \tag{3.18}$$

where a is the length of the semi-axis of rotation, b is the equatorial semi-axis, and ε is the eccentricity of the spheroid. The relationship between the parameters can be given as follows:

$$\varepsilon = \text{sqrt}\,(a^2 - b^2) / a. \tag{3.19}$$

The IGOM method is valid for a size parameter range ($x = 2\pi\, r_v/\lambda$) from 20 to 800.

3.2.3 Testing the Unified TM/IGOM Method

Testing of the unified code was performed by examining modeling results of T-matrix and IGOM in the common size parameter range. First of all, it is important to set up a size parameter between T-matrix and IGOM because they employ different definitions. The equal-volume-sphere radius r_v in T-matrix can be related to the size parameter (x) as follows:

$$x = 2\pi\, r_v / \lambda, \tag{3.20}$$

$$r_v = 50\lambda / 2\pi, \tag{3.21}$$

$$V = (4/3)\pi r_v^{\,3}\,, \tag{3.22}$$

$$a = ((3V\varepsilon') / (4\pi))^3\,, \tag{3.23}$$

$$b = a / \varepsilon', \tag{3.24}$$

$$\text{XSIZE} = 2\pi(2b) / \lambda\,. \tag{3.25}$$

where λ is the wavelength (μm), V is the volume, a is the length of the longer axis of spheroid in IGOM, b is the length of the rotational axis in IGOM, and ε' is the aspect ratio ($\varepsilon' = \varepsilon$ for oblate spheroids and $\varepsilon' = 1/\varepsilon$ for prolate spheroids), and XSIZE is the size parameter in the IGOM method.

The equal-volume-sphere radius r_v can be related to the equal-surface-area-sphere radius r_s with values of a and b in eq. (3.23) and (3.24) as follows:

$$r_s = \text{sqrt}\,(S/4\,\pi). \tag{3.26}$$

For example, the size parameter (x) of 50 corresponds to r_s = 5.393 μm in T-matrix and XSIZE = 70.205 μm in IGOM at 660 nm for a spheroid with the aspect ratio of 1.7. For example, Figure 3.2 shows comparison of the scattering phase function computed with IGOM and T-matrix. This case is for r_s = 5.393 μm in T-matrix, XSIZE = 70.205 μm in IGOM, and aspect ratio = 1.7, and the refractive index of 1.53 + i0.008. Excellent agreement between the two phase functions computed with T-matrix and IGOM is apparent.

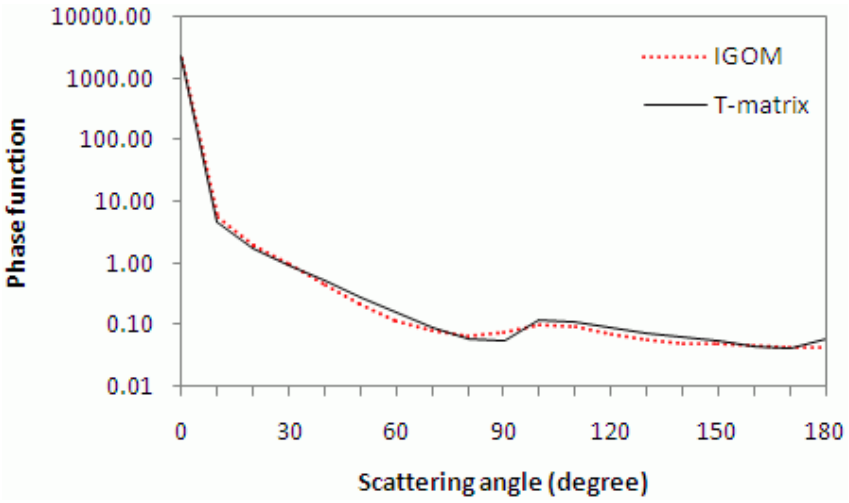

Figure 3.2 Scattering phase function computed at 660 nm for refractive index of 1.53+i0.008, size parameter of 50, and aspect ratio of 1.7.

In the unified TM/IGOM code, computations are performed with either T-matrix or IGOM depending on the parameter space. In Figure 3.3 solid line shows the boundary of size parameter (x) at each aspect ratio, separating the usage of T-matrix and IGOM at 532 nm.

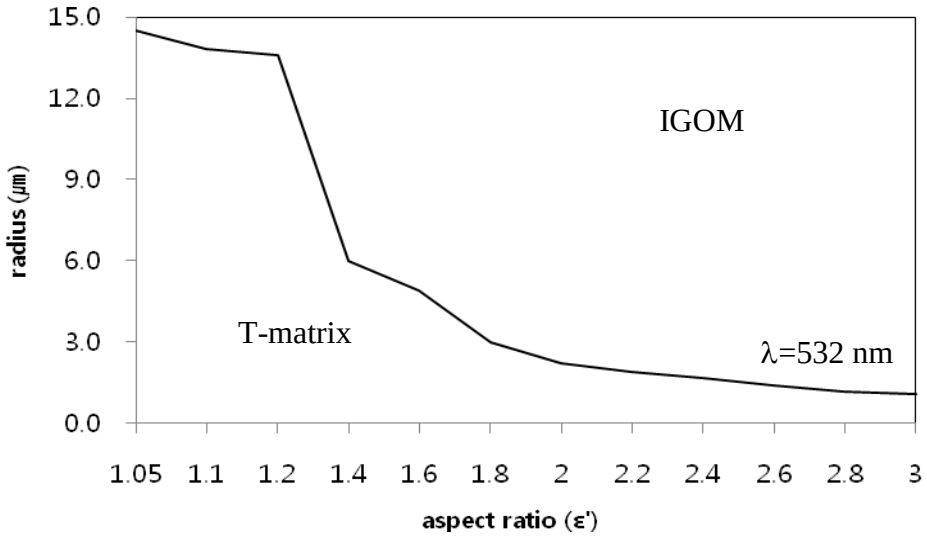

Figure 3.3 Range of the equal-surface-area-sphere radius (r_s) with the application of T-matrix method (below the boundary curve) and IGOM (above) at 532 nm.

3.2.4 Approach to Computing Optical Properties of Dust Particles

In this study, we model the following optical characteristics: scattering coefficients β_s, extinction coefficients β_e, asymmetry parameter g, single scattering albedo ω_0, the phase function of $P_{11}(180°)$ and the scattering phase matrix element $P_{22}(180°)$ at the scattering angle of 180°, aerosol lidar ratio S_a, and aerosol linear depolarization ratio δ_p. They are defined as follows

$$\beta_s = \frac{\int_{r_1}^{r_2} Q_s(r)A(r)n(r)dr}{\int_{r_1}^{r_2} A(r)n(r)dr}, \tag{3.27}$$

$$\beta_e = \frac{\int_{r_1}^{r_2} Q_e(r)A(r)n(r)dr}{\int_{r_1}^{r_2} A(r)n(r)dr}, \tag{3.28}$$

$$\omega_0 = \frac{\beta_s}{\beta_e}, \tag{3.29}$$

$$g = \frac{\int_{r_1}^{r_2} g(r)Q_s(r)A(r)n(r)dr}{\int_{r_1}^{r_2} Q_s(r)A(r)n(r)dr}, \tag{3.30}$$

$$P_{11} = \frac{\int_{r_1}^{r_2} P_{11}(r)Q_s(r)A(r)n(r)dr}{\int_{r_1}^{r_2} Q_s(r)A(r)n(r)dr}, \tag{3.31}$$

$$P_{22} = \frac{\int_{r_1}^{r_2} P_{22}(r)Q_s(r)A(r)n(r)dr}{\int_{r_1}^{r_2} Q_s(r)A(r)n(r)dr}, \tag{3.32}$$

$$S_a = \frac{4\pi}{\omega_0 P_{11}(180°)}, \tag{3.33}$$

$$\delta_p = \frac{P_{11}(180°) - P_{22}(180°)}{P_{11}(180°) + P_{22}(180°)}. \tag{3.34}$$

where n(r) is the particle size distribution.

3.3 Selection of Dust Microphysical Parameters

To construct representative dust mixtures for optical modeling, we examined data provided by several recent field experiments (e.g., ACE-Asia, PRIDE, AMMA, and SAMUM) as well as laboratory measurements (e.g., Lafon et al., 2006). Here we briefly introduce these measurements and explain how they were used to constrain the size distribution, composition and refractive indices, and aspect ratio distribution of spheroids.

3.3.1 Particle Composition and Refractive Index

The particle composition, which determines a refractive index, is acquired from the laboratory generated samples of dust aerosols and atmospheric dust samples (Sokolik and Toon, 1999; Lafon et al., 2006). For the internal mixture of 2% hematite and 98% kaolinite, Sokolik and Toon (1999) suggested a refractive index of 1.52+0.0058i. Lafon et al. (2006) modeled the optical properties of iron oxide-clay aggregates with non-absorbing mineral species (i.e., quartz and calcite) and light-absorbing species (i.e., black carbon and kaolinite) based on mineralogical composition measurements of Asian and Saharan dust aerosols. They gave that the range of the real part of the refractive index of kaolinite-containing aggregates between 1.5 and 1.6 in the visible spectrum. Based on data from the 2006 SAMUM field campaign, Kandler et al. (2008) suggested that mineral dust consists of silicates, carbonates, and quartz, and based on this compositional information, they determined the range of the real part of refractive index from 1.5 to 1.6 and the imaginary part around 0.003 ± 0.0005 at the 530 nm wavelength. Petzold et al. (2008) reported that the real part of the refractive index from 1.55 to 1.56, and the imaginary part from 0.0016 to 0.0042 at 550 nm. Heinold et al. (2008) suggested a range

of 1.53 to 1.56 for the real part and 0.0015 to 0.0085 for the imaginary part at the wavelength of 537 or 550 nm. Based on these studies, we selected the real part of the imaginary index in the range between 1.52 and 1.56, and the range from 0-0.006 for the imaginary part at the 532 nm lidar wavelength.

3.3.2 Particle Size Distribution

The Aerosol Characterization Experiment in Asia (ACE-Asia) measurements show that particle size distributions of mineral dust have two size modes in the radius in the range 0.05 to 6.0 μm (Arimoto et al., 2006, Seinfeld et al., 2004). The Puerto Rico Dust Experiment (PRIDE) experiment reported that the bimodal particle distribution had a maximum radius close to 5 μm. Chou et al. (2008) used the three-modal lognormal distribution in the radius range of 0.01 to 5 μm based on the African Monsoon Multidisciplinary Analysis project (AMMA) measurements. Wiegner et al. (2009) fitted the particle size distribution with the four-modal lognormal distribution in the radius range of 0.05-10 μm based on observations from the Saharan Mineral Dust Experiment (SAMUM). For version 2 inversion products of AERONET, Dubovik et al. (2006) applied the bimodal lognormal distribution with the radius between 0.05 to 15 μm.

In our modeling, we represented the dust particle size distribution by a bimodal lognormal function to explicitly account for fine and coarse modes:

$$n(r) = \sum_{i=1}^{2} \frac{1}{\sqrt{2\pi}\,\ln\sigma_i r} \exp\left[-\left(\ln r - \ln r_{gi}\right)^2 \Big/ 2\ln^2 \sigma_i \right]. \tag{3.35}$$

where r is the radius of the equal-surface-area-sphere, r_{gi} the geometric mean radius of the ith mode, and σ_i the geometric standard deviation of the ith mode. Based on measurements, we considered particle sizes in the radius range from 0.1-1.0 μm with r_{g1}

= 0.5 μm and $\ln\sigma^2$ = 0.5 for the fine mode (i=1) and the radius from 0.1 to 15 μm with r_{g2} = 1.0 μm and $\ln\sigma^2$ = 0.5 for the coarse mode (i=2). For a sensitivity study, we also considered size distributions having a maximum radius 6 μm and a median radius of 2.0 μm for the coarse mode.

Despite various differences in reported dust size distributions, there is a common consensus that coarse particles are most abundant in dust sources and their relative fraction decreases during transport (Maring et al., 2003). The presence of coarse dust particles strongly affects the light scattering and its variations must be taken into account (Munoz et al., 2007, Nousiainen et al., 2011). For instance, Kalashnikova et al. (2005) modeled the optical properties of dust particles by varying the proportion of the fine and coarse particles and proposed representative mineral dust composition-size-shape types with the combination of the fine and coarse modes. We investigated the effect of coarse dust particles on the optical properties by varying the proportion of fine and coarse modes, which helps to demonstrate relative contribution of each size mode to dust optical properties as well as possible changes in optical properties during transport. Accordingly, we changed the proportion of fine and coarse particles as follows:

Case 1: 30% fine mode + 70% coarse mode

Case 2: 50% fine mode + 50% coarse mode

Case 3: 70% fine mode + 30% coarse mode

3.3.3 Particle Aspect Ratio Distribution

Several recent studies provided direct measurements of the aspect ratio of dust particles as a function of size. We used these data along with the aspect ratio distributions

that are commonly being used in remote sensing to examine the effect of a certain aspect ratio distribution on lidar optics. Table 3.1 compares five distributions considered in our study. Mixture 1 (denoted by M1) represents the case of equally weighted aspect ratios from 1.2 to 3.0. Mixture 2 (M2) is similar to M1 but represents aspect ratios from 1.05-3. Mixture 3 (M3) is based on measurements of the aspect ratio from SAMUM for Saharan dust (Wiegner et al., 2009), and mixtures 4 (M4) and 5 (M5) are based on data reported by Okada et al. (2001) for Asian dust. In addition, we considered the dust mixtures consisting of only prolate spheroids (denoted by P), oblate spheroids (O), or 50% each type (PO).

Table 3.1 Aspect ratio distributions of dust particles used in optics modeling.

Aspect ratio(ε')		1.05	1.1	1.2	1.4	1.6	1.8	2.0	2.2	2.4	2.6	2.8	3.0
M1				0.1	0.1	0.1	0.1	0.1	0.1	0.1	0.1	0.1	0.1
M2		0.083	0.083	0.083	0.083	0.083	0.083	0.083	0.083	0.083	0.083	0.083	0.083
M3	Fine			0.535	0.289	0.108	0.040	0.015	0.007	0.003	0.001	0.001	0.001
	Coarse			0.103	0.234	0.218	0.157	0.101	0.065	0.041	0.027	0.018	0.026
M4				0.335	0.319	0.179	0.087	0.042	0.020	0.009	0.005	0.002	0.001
M5		0.141	0.173	0.230	0.219	0.123	0.060	0.029	0.014	0.006	0.003	0.001	0.001

3.4 Results and Discussion

The constructed mixtures were used to perform a detailed modeling of S_a, δ_p, ω_0, and g, and the results were evaluated against observations to the extent possible.

3.4.1 Effect of Aspect Ratio Distribution

Tables 3.2 and 3.3 show the values of S_a, δ_p, ω_0, and g at 532 nm for the case 1 (70% coarse mode and 30% fine mode) computed for the three mixtures (P, O, and PO) for all five aspect ratio distributions. The fine mode is in the radius range from 0.1-1.0 μm, r_{g1} = 0.5 μm and $\ln\sigma^2$ = 0.5, and the coarse mode is from 0.1-15 μm, r_{g2} = 1.0 μm, and $\ln\sigma^2$ = 0.5.

For comparisons, Table 3.4 lists observations of S_a and of δ_p performed under different dust conditions. Based on measurements presented in Table 3.4, dust episodes often show the depolarization ratio of above 0.28 and the lidar ratio of between 35 and 60 sr. Comparing Table 3.2 and Table 3.4, it is noted that only some mixtures can reproduce observations: M1_O (Mixture 1 with oblate spheroids only), M2_O (Mixture 2 with oblate spheroids only), M3_PO (Mixture 3 with 50% oblate and prolate spheroids), M3_P (Mixture 3 with prolate spheroids only), M4_P (Mixture 4 with prolate spheroids only), and M5_P (Mixture 5 with prolate spheroids only).

Table 3.2 Modeled particulate linear depolarization ratio δ_p and lidar ratio S_a at 532 nm for three cases (O: oblate spheroid, P: prolate spheroid, PO: 50% each) of five shape distributions (M1-M5) of dust particles. Each case consists of fine mode 30% and coarse mode 70%. The size range from 0.1 to 1 μm with r_g = 0.5 μm and $\ln\sigma^2$ = 0.5 for fine mode and from 0.1 to 15 μm with r_g = 1.0 μm and $\ln\sigma^2$ = 0.5 for coarse mode).

		Depolarization ratio (δ_p)				Lidar ratio (S_a)			
	n	1.52		1.56		1.52		1.56	
	k	0.003	0.006	0.003	0.006	0.003	0.006	0.003	0.006
M1	O	0.311	0.299	0.285	0.272	46.3	63.9	41.4	56.5
	P	0.229	0.233	0.200	0.200	75.4	97.9	63.6	82.9
	PO	0.270	0.266	0.242	0.236	61.1	80.9	52.5	69.7
M2	O	0.301	0.283	0.272	0.253	40.9	56.1	36.0	49.3
	P	0.245	0.241	0.207	0.202	64.7	84.3	54.3	71.1
	PO	0.273	0.262	0.239	0.228	52.8	70.2	45.1	60.2
M3	O	0.264	0.258	0.251	0.241	30.3	41.0	26.4	35.7
	P	0.278	0.285	0.242	0.246	49.8	66.8	42.4	57.1
	PO	0.271	0.271	0.247	0.243	40.1	53.9	34.4	46.4
M4	O	0.271	0.267	0.264	0.256	21.1	28.2	18.5	24.6
	P	0.293	0.309	0.258	0.268	34.3	46.3	29.5	40.1
	PO	0.282	0.288	0.261	0.262	27.7	37.2	24.0	32.4
M5	O	0.265	0.248	0.246	0.226	18.0	24.7	15.4	21.0
	P	0.303	0.302	0.254	0.251	27.0	36.8	22.8	31.3
	PO	0.284	0.275	0.250	0.239	22.5	30.7	19.1	26.1

- n is the real part of refractive index and k is the imaginary part of refractive index.

Table 3.3 Same as Table 3.2 but for the modeled single scattering albedo ω_0 and asymmetry parameter g.

		Single scattering albedo (ω_0)				Asymmetric parameter (g)			
	n	1.52		1.56		1.52		1.56	
	k	0.003	0.006	0.003	0.006	0.003	0.006	0.003	0.006
M1	O	0.8898	0.8244	0.8875	0.8216	0.7579	0.7847	0.7439	0.7724
	P	0.8887	0.8225	0.8870	0.8205	0.7813	0.8007	0.7711	0.7928
	PO	0.8892	0.8235	0.8872	0.8211	0.7696	0.7927	0.7575	0.7826
M2	O	0.8889	0.8227	0.8868	0.8201	0.7591	0.7851	0.7455	0.7731
	P	0.8881	0.8212	0.8864	0.8191	0.7787	0.7986	0.7681	0.7900
	PO	0.8885	0.8219	0.8866	0.8196	0.7689	0.7918	0.7568	0.7816
M3	O	0.8853	0.8169	0.8829	0.8140	0.7410	0.7706	0.7268	0.7585
	P	0.8860	0.8177	0.8841	0.8152	0.7623	0.7857	0.7498	0.7759
	PO	0.8857	0.8173	0.8835	0.8146	0.7517	0.7782	0.7383	0.7672
M4	O	0.8840	0.8143	0.8818	0.8117	0.7398	0.7690	0.7258	0.7572
	P	0.8849	0.8153	0.8831	0.8132	0.7583	0.7804	0.7433	0.7709
	PO	0.8844	0.8148	0.8825	0.8125	0.7490	0.7747	0.7345	0.7641
M5	O	0.8842	0.8143	0.8823	0.8120	0.7478	0.7747	0.7345	0.7633
	P	0.8849	0.8151	0.8831	0.8128	0.7607	0.7827	0.7462	0.7726
	PO	0.8846	0.8147	0.8827	0.8124	0.7543	0.7787	0.7404	0.7680

- n is the real part of refractive index and k is the imaginary part of refractive index.

Table 3.4 Lidar ratio S_{532} at 532 nm and the particle depolarization ratio δ_p reported from observations.

Source Region (Campaign)	Layer (km)	S_{532}	δ_p	Lidar (References)
Asian Dust - Source Region				
Beijing	12 days averaged	40.7±7.8	0.142± 0.042	Raman lidar (Xie et al., 2008)
Gobi , Beijing	PBL[a]	35±5		Raman lidar (Tesche et al., 2007)
Asian Dust - Transported Area				
Anmyeon Island, South Korea		45.5±8.6	0.26±0.1	Raman lidar (Noh et al., 2007)
Tokyo .Japan	4-4.6	43.1±7	0.2	UV-Raman lidar / Nd:Yag laser (Murayama et al., 2004)
Tokyo (ACE-Asia)	> 3.6	45-60	0.3-0.35	Mie backscatter lidars (Murayama et al., 2003)
Tsukuba / Tokyo, Japan		42-55		HSRL[b]/Raman lidar (Liu et al., 2002)
Nagoya / Tsukuba, Japan	2-8 4-7	46±5 (40-60)	0.2-0.33	Nd: Yag laser (Sakai et al., 2002)
Saharan Dust - Source Region				
North Africa		36.4/38.5 ±9.2[c]	0.3-0.32	Nd: Yag laser_CALIOP (Liu et al., 2010)
Quarzazate (SAMUM)	<6	50-60	0.32	Raman lidar (Muller et al., 2009; Freudenthaler et al., 2008)
Quarzazate (SAMUM)	< 4.5	41-60	0.28-0.32	HSRL[b] (Esselborn et al., 2008)
Saharan Dust - Transported Area				
Potenza (SAMUM)	2-6.5	55-60		EARLINET[d] (Muller et al., 2009)
Tito Scalo, Potenza	2.5-5.9 (mean)	37		Raman lidar (Mona et al., 2006)
Leipzig, Germany			0.1-0.25	EARLINET[d] (Muller et al., 2007)

a. Planetary boundary layer (PBL)
b. High-Spectral-Resolution Lidar (HSRL)
c. Effective Lidar Ratio (median / mean values)
d. European Aerosol Research Lidar Network (EARLINET)

3.4.2 Effect of Size Distribution and Composition

To investigate the sensitivity to size distribution, we fix the range of fine mode and change the range of coarse mode. The black solid lines in Figures 3.4 and 3.5 show the results for the size range of 1-15 μm, r_g = 1 μm and $\ln\sigma^2$ = 1,. Similarly, the black dotted lines display the results when the size range is changed from 1-15 μm to 1-6 μm. The red solid lines show modeled values when the median radius r_g is changed from 1.0 μm to 2.0 μm for the size range of 1-15 μm and the red dotted lines for the size range of 1-6 μm.

Figure 3.4 and 3.5 show that the change of size range from 1-15 μm to 1-6 μm only slightly affects the values of S_a, δ_p, ω_0, and g at 532 nm. However, the change of r_g from 1.0 μm to 2.0 μm, however, causes a noticeable increase in S_a and g, but results in a decrease in ω_0. These results indicate that the size range above the particle radius of 6 μm has little impact on dust optical properties the 532 lidar wavelength for considered median radii (1μm and 2 μm) of coarse mode. However, the value of median radius itself is important.

When the real part of the refractive index was varied from 1.52 to 1.56, δ_p and g decreased down to 0.05 and 0.017, respectively while S_a and ω_0 increased up to 9.7 and 0.0028, respectively. When the imaginary part increases from 0.003 to 0.006, S_a and g increase while ω_0 decreases and there is no certain pattern of δ_p. This result implies that changes in the imaginary part of refractive index do not have noticeable impact on the particle depolarization ratio, δ_p.

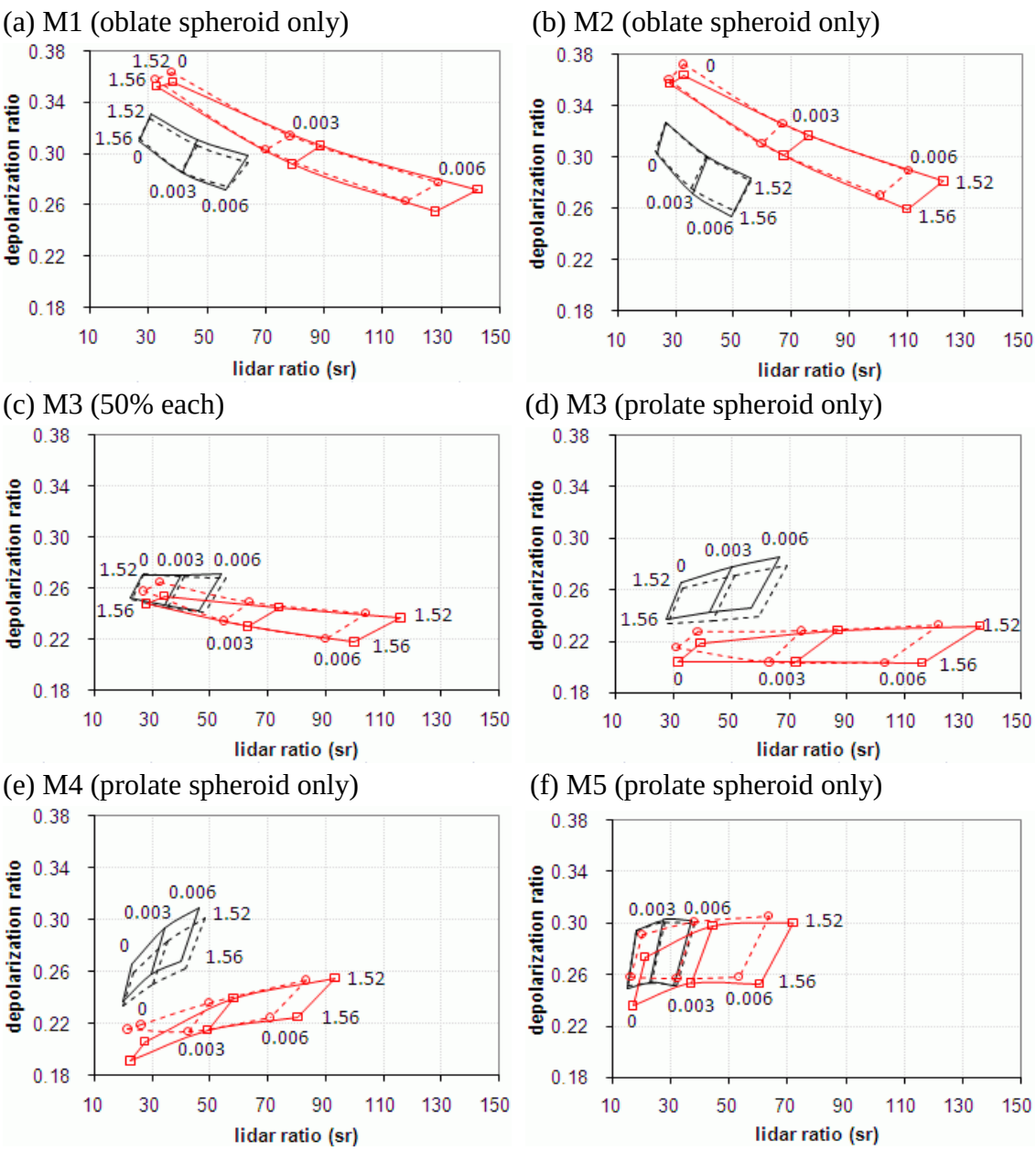

Figure 3.4 Lidar ratio and linear depolarization ratio computed for different refractive indices and aspect ratio distributions of dust particles for (a) mixture 1, (b) mixture 2 (oblate spheroid only), (c) mixture 3 (50% each), (d) mixture 4, (e) mixture 5, and (f) mixture 6 (prolate spheroid only) for 70% coarse and 30% fine modes at 532 nm (fine mode: $0.1 \leq r \leq 1$ μm with $r_g = 0.5$ μm, coarse mode: $0.1 \leq r \leq 15$ μm (solid line)/ $0.1 \leq r \leq 6$ μm (dotted line) with the median radius of 1 μm (black line)/ 2 μm (red line)) ($\ln\sigma^2 = 0.5$ is fixed for each mode).

(a) M1 (oblate spheroid only)

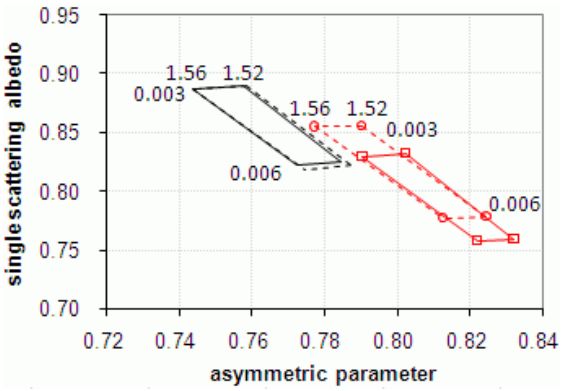

(b) M2 (oblate spheroid only)

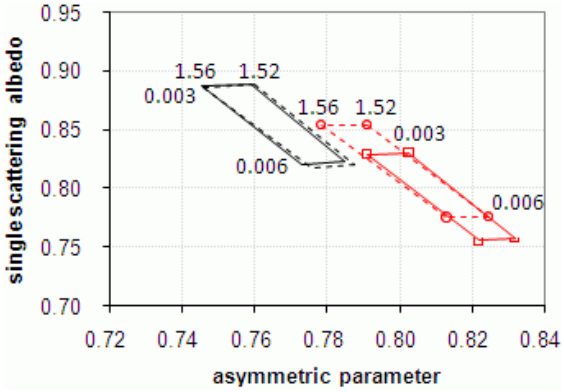

(c) M3 (50% each)

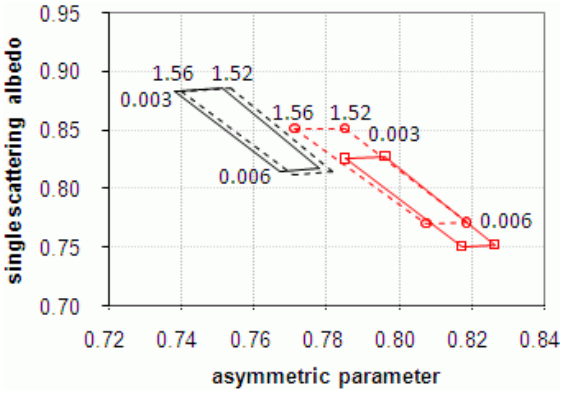

(d) M3 (prolate spheroid only)

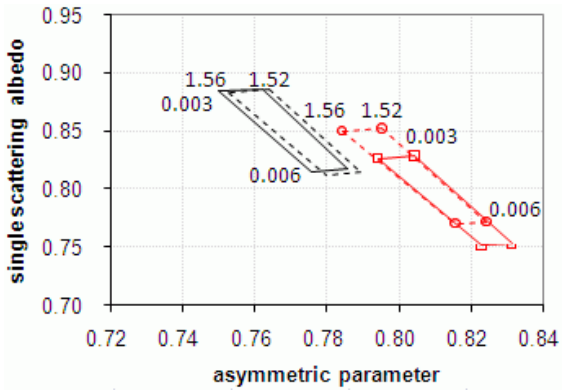

(e) M4 (prolate spheroid only)

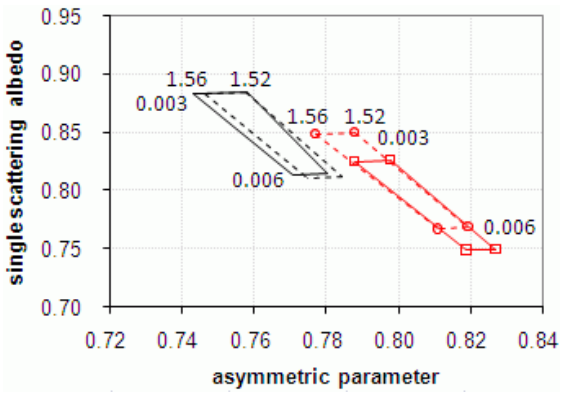

(f) M5 (prolate spheroid only)

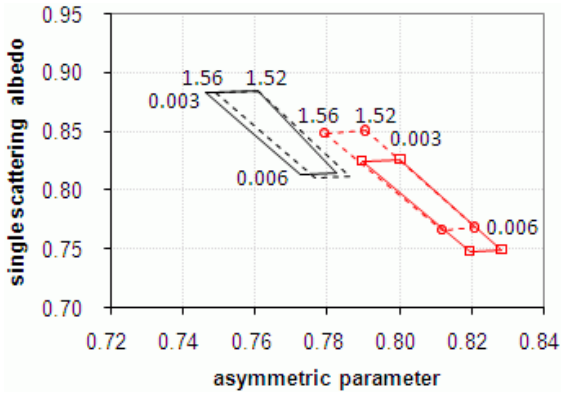

Figure 3.5 Same as Figure 3.4, but for the single scattering albedo and asymmetry parameter.

3.4.3 Effect of Coarse Dust Particles

In Figure 3.6, the black solid line represents the case 1 (70% coarse mode + 30% fine mode), the blue dotted line is for the case 2 (50% each), and the red dotted line is for the case 3 (30% coarse mode + 70% fine mode) for the selected mixtures shown in Table 3.2. Examining Figure 3.6, one can see that among all the cases, case 1 has the largest lidar ratio value, which decreases from case 2 to case 3. The largest difference between case 1 and 3 reaches ΔS_a=26.4 sr. However, no specific pattern can be seen in the behavior of δ_p. If one considers that δ_p remains constant during the dust transport, as was done by Liu et al.(2008), then the M1 oblate spheroid mixture appears to give the best-fit aspect ratio distribution for the refractive index of 1.52 + i0.003, as shown in Figure 3.6(a) where δ_p is about 0.31 as reported by Liu et al. (2008). In this figure, δ_p, S_a, ω_0, and g at 532 nm (for refractive index of 1.52 + i0.003) have the values of 0.311/ 46.8 sr/ 0.8897/ 0.7578 for the case 1, 0.309/ 42.3 sr/ 0.9085/ 0.7416 for the case 2, and 0.308/ 37.8 sr/ 0.9273/ 0.7253 for the case 3, respectively. This result shows that the value of δ_p rarely changes, while S_a and g decrease, and ω_0 increase with the decreasing fraction of coarse dust particles. The trend of g and ω_0 are similar with the other mixtures (see Figure 3.7). This result is also in good agreement with the HSRL measurements of lidar ratios on May 19 and June 3, 2006 as shown in the Fig. 3.8 of Wiegner et al. (2009). Figure 3.8 shows that lidar ratios decrease from 50.3 ± 2.2 sr (at 3.25 km) to 47.0 ± 2.4 sr (at 4.85 km) on May 19 and from 46.2 sr (below around 2.5 km) to 38 sr (at 3.8 km) on June 3, 2006. To reproduce the lower lidar ratio (38 sr) at 3.8 km, Wiegner et al. (2009) used a higher imaginary part of the refractive index. Tuning the imaginary part had no justification since no systematic changes in dust composition with altitude were observed.

Our modeling results offer an alternative explanation. Results demonstrate that the lidar ratios decrease from 46.8 sr (case 1) to 37.8 sr (case 3) for the M1 oblate spheroid mixture with the refractive index of 1.52 + i0.003. Thus, the vertical decrease of lidar ratio on June 3 2006 can be best explained by the decrease of large dust particles with altitude.

The fact that δ_p remains almost constant with the decreasing fraction of coarse particles implies that this parameter has a relatively low sensitivity to size distribution. Therefore, we believe that the conclusions of Liu et al. (2008), that δ_p remained constant during transport of an African dust episode of 2006 because of little changes in the dust size distribution, are questionable.

Another important finding is a decrease of S_a with the decreasing faction of the coarse mode. Therefore, varying lidar ratio values must be considered in CALIOP retrievals instead of fixed S_a value used in version 2 and 3.01 data. Furthermore, variations in the values of ω_0 and g also suggest that different values of ω_0 and g will need to be considered over the dust source and remote areas in satellite retrievals and radiative forcing modeling.

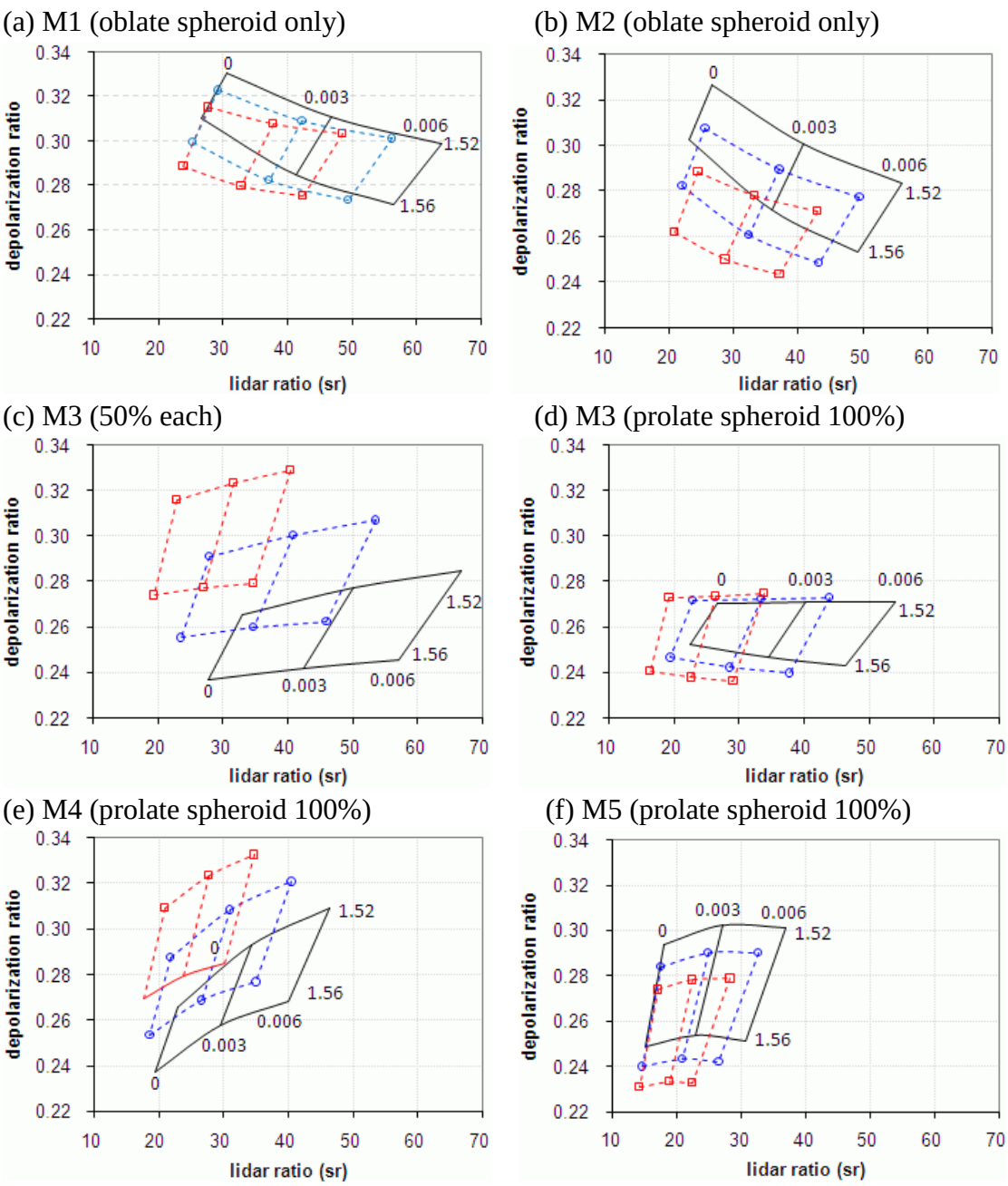

Figure 3.6 Lidar ratio and linear depolarization ratio computed for different refractive indices and five aspect ratio distributions of dust particles for (a) M1 (oblate spheroid only), (b) M2 (oblate spheroid 100%), (c) M3 (50% each), (d) M4 (prolate spheroid 100%), (e) M5 (prolate spheroid 100%), and (f) M5 (prolate spheroid only) with $0.1 \leq r \leq 1$ μm with $r_g = 0.5$ μm for fine mode and $0.1 \leq r \leq 15$ μm with $r_g = 1$ μm for coarse mode ($\ln\sigma^2 = 0.5$ is fixed for each mode) at 532 nm.

(a) M1 (oblate spheroid only)

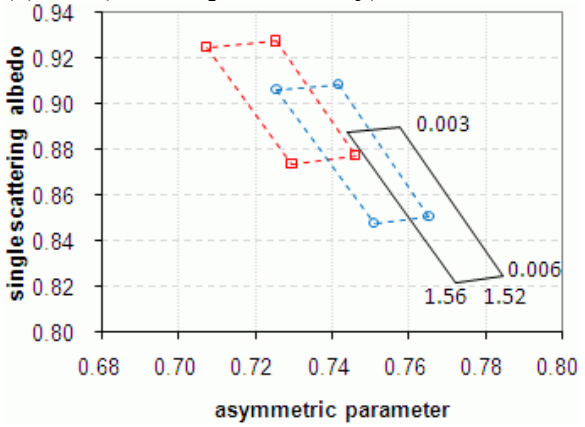

(b) M2 (oblate spheroid only)

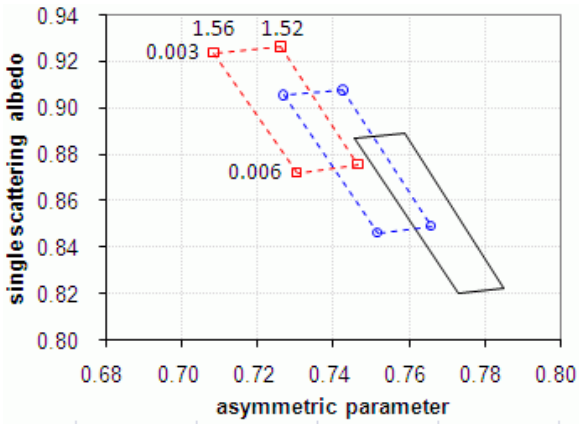

(c) M3 (50% each)

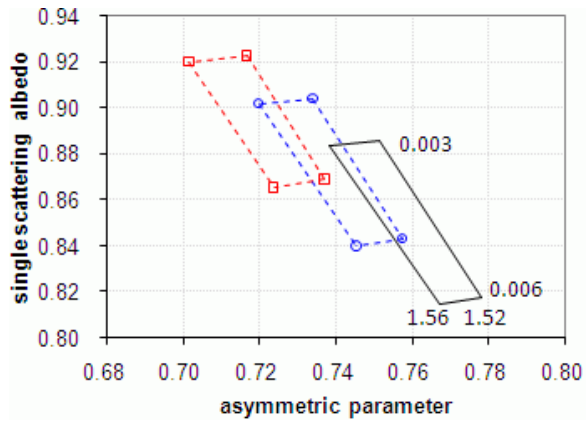

(d) M3 (prolate spheroid 100%)

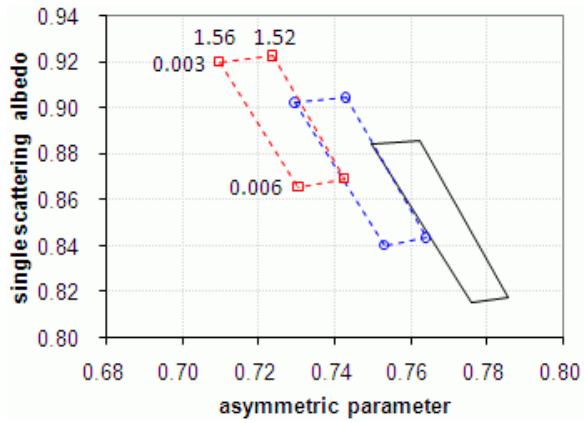

(e) M4 (prolate spheroid 100%)

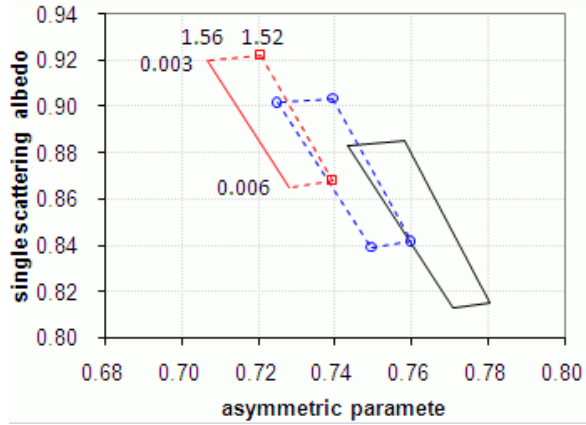

(f) M5 (prolate spheroid 100%)

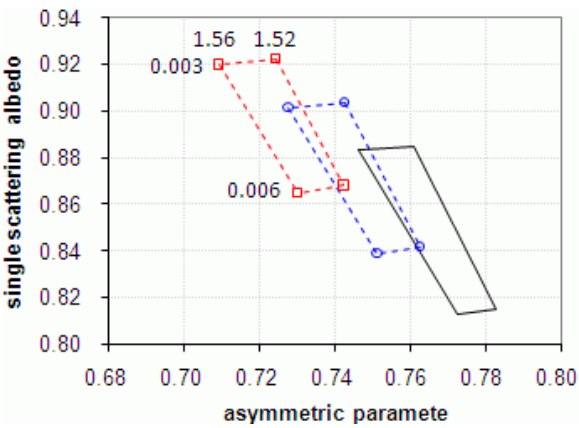

Figure 3.7 Same as Figure 3.6, but for single scattering albedo and asymmetric parameter.

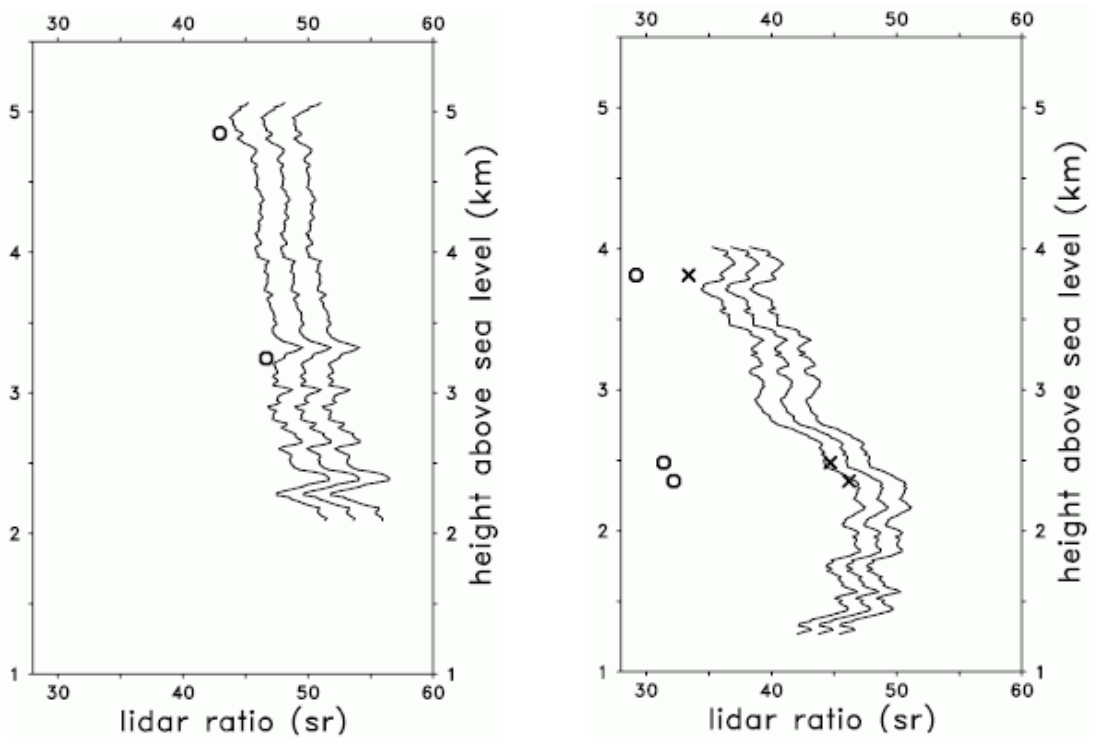

Figure 3.8 HSRL measurement of the lidar ratio and modeled lidar ratio at 532 nm on May 19 2006 (left panel) and on June 3 2006 (right panel) (From Wiegner et al., 2009).

3.5 Summary

This study examined how variations of dust microphysical properties can affect the lidar ratio S_a and particulate depolarization δ_p. The ω_0 and g were also modeled and used in assessments of the dust radiative impact (see Chapters 4 and 5). To perform optical modeling, we developed the TM/IGOM technique, which is a combination of the T-matrix and IGOM methods. TM/IGOM enables optical modeling in the wide size range covering from fine to coarse sizes of dust particles. The upper limit of 15 μm radius was considered in this study.

Examination of the behavior of both lidar optical characteristics S_a and δ_p was performed by considering the representative selection of microphysical properties based on recent measurements. Comparing the results of measurements to modeling, it is noted that only some mixtures can reproduce lidar observations. Dust episodes observed from satellite or ground-based lidar often show the depolarization ratio of above 0.28 and the lidar ratio of between 35 and 60 sr.

The change of size range of the coarse mode from 1-15 μm to 1-6 μm has a small effect on the values of S_a, δ_p, ω_0, and g at 532 nm. These optical characteristics are much more sensitive to the change of r_g from 1.0 μm to 2.0 μm. Increasing r_g causes a noticeable increase in S_a and g and a decrease in ω_0. These results suggest that particles with sizes above 6 μm do not affect the lidar signal at the 532 lidar wavelength.

When the real part of the refractive index was varied from 1.52 to 1.56, δ_p and g decreased down to 0.05 and 0.017, respectively, while S_a and ω_0 increased up to 9.7 and 0.0028, respectively. When the imaginary part increased from 0.003 to 0.006, S_a and g increased while ω_0 decreased and there was no special pattern of δ_p. This result implies that the changes in the imaginary part of refractive index do not have noticeable impact on the particle depolarization ratio, δ_p.

The fact that δ_p remained almost constant with the decreasing fraction of coarse particles implies that this parameter has a relatively low sensitivity to size distribution. Therefore, we believe that the conclusions of Liu et al. (2008), that δ_p remained constant during transport of an African dust episode of 2006 because of little changes in the dust size distribution, are questionable. Moreover, a decrease of S_a during transport implies that varying lidar ratio values should be applied to the retrieval of CALIOP lidar data

instead the currently used fixed value of 40 sr. The variations in the values of ω_0 and g also suggest that different values of ω_0 and g will need to be considered over the dust source and remote areas in satellite retrievals and radiative forcing modeling.

In future work, it would be helpful to model the Angstrom parameter at the wavelength 532 - 1064 nm, which is related to the particulate color ratio in CALIOP data. However, modeling the optics at 1064 nm requires inclusion of even larger size particles for which information on the aspect ratio and composition is still lacking. Establishing relationships between the Angstrom parameter and particulate color ratio and S_a at 532 nm will make it possible to use the particulate color ratio observed by CALIOP in the dust retrieval. It is recommended that different lidar ratios be applied in the CALIOP retrievals based on regional dust sources and the transported distances from sources.

CHAPTER 4

INVESTIGATION OF THE PROPERTIES AND SPATIOTEMPORAL DISTRIBUTION OF ASIAN DUST IN SOURCE REGIONS AND DOWNWIND AND ASSESSMENTS OF DUST RADIATIVE FORCING AND HEATING/COOLING RATES

4.1 Introduction

In Chapter 2, this study demonstrated a procedure for retrieving aerosol properties from the CALIPSO level 1B data and the performance of CALIOP in dust-laden conditions. Distinctive improvements in the latest level 2 version 3.01 data give confidence in using CALIOP data for dust studies, although some biases were identified. Also, version 3.01 data include two new aerosol products (particulate depolarization ratio and particulate color ratio, see Chapter 2) that have not been analyzed by previous studies and analysis of these products will be one of our objectives.

As commented in Chapter2, the characterization of aerosols from CALIPSO is a multi-step process, involving several different algorithms (such as SYBIL, SCA and HERA). In these algorithms, the correct identification of vertical features in CALIOP backscattering signals is a key step in characterizing both aerosols and clouds. Here we use independent observations to examine the accuracy of CALIPSO identification of the presence of dust as well as its vertical distribution (i.e., VFM) in the source regions and downwind. Level 2 data products were retrieved using an improved version of the cloud-aerosol discrimination (CAD) algorithm. However, dense aerosol layers (such as dense

dust in and near the source regions) are hard to discriminate from clouds, and they are likely to be classified as clouds by CALIPSO. We address this issue by utilizing observations of clouds from other ground-based and satellite instruments.

The specific goals of the study presented in this chapter are as follows: 1) examine the vertical distribution and optical properties of Asian dust in the dust sources and during the transport using the new level 2 version 3.01 CALIOP data, in conjunction with independent satellite and ground-based observations; 2) and assess the dust radiative forcing and heating/cooling rates using observed vertical profiles and optical properties of Asian dust along with modeled dust optical properties (e.g., the single scattering albedo and the asymmetry parameter presented in Chapter 3).

Section 4.2 introduces the data and methodology used in this study. Section 4.3 presents the results of our analyses of Asian dust events in the spring (dust) seasons of 2007-2010 in the dust sources and downwind regions affected by mid- and long-range transported Asian dust. Section 4.4 discusses the assessment of the radiative impact of Asian dust, and Section 4.5 summarizes the main findings.

4.2 Data and Methodology

4.2.1 Ground-Based and Satellite data

We analyzed CALIOP data in conjunction with A-Train multi-satellite, multi-sensor products (including MODIS aboard Aqua, some MODIS Terra data, OMI aboard Aura, and CloudSat) as well as with ground-based meteorological, lidar, and AERONET data for the spring seasons of 2007-2010. Figure 4.1 shows the dataset included in the integrative analyses of Asian dust events in our study.

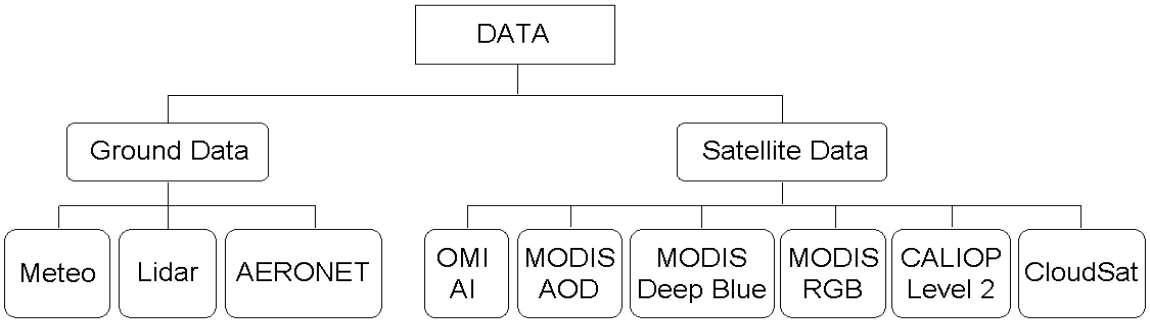

Figure 4.1 Ground-based and satellite data used in the study (see text for details).

Meteorological data are provided by the NOAA National Climatic Data Center (NCDC). According to the World Meteorological Organization (WMO) protocol, SYNOP data report the present weather type. The types of present weather related to dust events are categorized as “dust storm” (corresponding to visibility <1 km), “blowing dust” (1 km<visibility<10 km), and “floating dust” (visibility below 10 km). Figure 4.2 shows the locations of weather stations in Asia used for analysis.

The National Institute for Environmental Studies (NIES) Lidar Network and Asian Dust Network (AD-Net) operate several lidar sites across East Asia (http://www-lidar.nies.go.jp/). We analyzed lidar data from four stations (Seoul and Suwon in Korea, and Toyama and Tsukuba in Japan). Figure 4.2 shows the site locations. The network employs two wavelength lidars operating at 532 and 1064 nm.

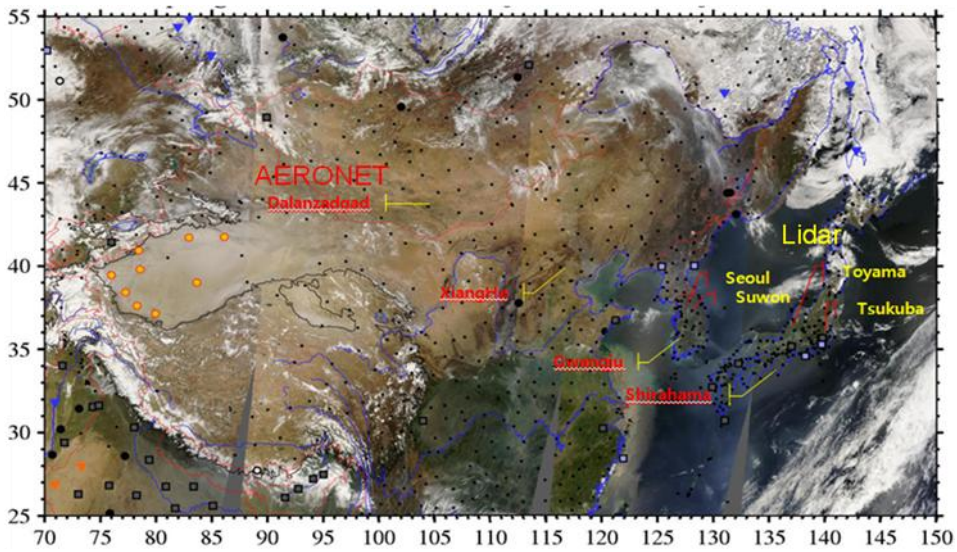

Figure 4.2 Locations of ground weather, Lidar, and AERONET sites in East Asia used in this study.

The AERONET (AErosol RObotic NETwork) is a network of ground-based sun-sky measurement that provides aerosol properties such as spectral AOD, aerosol volume size distribution, and single scattering albedo. The location of four AERONET stations (Dalanzadgad and XiangHe in China, Gwangju in Korea, and Shirahama in Japan) is also shown in Figure 4.2.

The Aerosol Index (AI) retrieved from OMI-Aura is defined as a residual quantity that indicates the departure of the spectral dependence of upwelling radiation relative to molecular (Rayleigh) scattering. The AI data (from TOMS and OMI) have been used for some time to remotely sense UV-absorbing aerosols such as desert dust (e.g., Huang et al., 2007, Moulin and Chiapello, 2004). Figure B.1 in Appendix presents the OMI AI fields in the spring of 2007, clearly showing high values of AI in the dust sources and transported areas.

Similar to the AI from OMI, the AOD and Deep Blue AOD at 550 nm from MODIS-Aqua enable the regional characterization of spatiotemporal distributions of aerosols. This study uses the MODIS Deep Blue AOD over the land and the standard MODIS AOD product over the ocean together because in the latter case, AODs are largely missing over bright surfaces such as desert and semi-desert areas. The MODIS aerosol products are MYD04_L2 data whose spatial resolution is 10 km (at nadir). In addition, RGB images from both MODIS-Terra and MODIS-Aqua (Level-1 data reported as granules of five minutes with the 1 km resolution) were analyzed to confirm the presence of Asian dust and dust-cloud mixed scenes.

The CALIPSO products analyzed in this chapter are mainly level 2 version 3.01 data, including the vertical feature mask (VFM), the aerosol type, the AOD at 532 nm, the volume depolarization ratio (δ_v), the particulate depolarization ratio (δ_p), and the particulate color ratio (χ_p). As described in Chapter 2, CALIPSO aerosol products enable the examination of both the vertical and spatiotemporal distribution of dust, the investigation of dust optical properties over the source and downwind regions, and the assessment of their radiative impact. We also used CloudSat data to validate the discrimination between aerosols and clouds in the CALIPSO vertical feature mask. CloudSat radar is not sensitive to aerosols and detects clouds only.

The NOAA HYSPLIT (Hybrid Single-Particle Lagrangian Integrated Trajectory) model helps to track the mid- and long-range transport of Asian dust plumes. The model has recently been upgraded, including improved advection algorithms, updated stability and dispersion equations, and a new graphical user interface. We perform HYSPLIT modeling using a dedicated website http://www.arl.noaa.gov/ready/.

The NOAA ESRL (Earth System Research System) enables the investigation of daily NCEP/NCAR Reanalysis data from 1948 to the present. These data were used to examine the meteorological conditions of dust events. In this study, the NOAA ESRL analysis was performed at a dedicated website http://www.esrl.noaa.gov/psd/.

4.2.2 Radiative Transfer Code: SBDART

SBDART, a FORTRAN computer code developed by the Earth Space Research Group at the University of California-Santa Barbara, was used to perform radiative transfer calculations. SBDART considers a plane-parallel atmosphere in which the radiative fluxes are computed combining the discrete ordinate radiative transfer module (DISTORT) and low-resolution correlated k-distribution atmospheric transmission model (Ricchiazzi et al., 1998). SBDART requires several input parameters such as the AOD, single scattering albedo, and asymmetry parameter that were computed for representative mixtures of nonspherical (spheroid) dust mixtures (see Chapter 3).

4.2.3 Methodology

We developed a methodology to identify CALIPSO tracks in dust-laden conditions in the regions of interest and perform integrative analysis of selected tracks in conjunction with multi-satellite and ground-based observations on a case-by-case basis. The methodology also includes analysis of synoptic meteorological conditions associated with dust events in source regions and in transported areas. As part of this analysis, selection of representative vertical distributions of Asian dust was done and then used for the assessment of radiative forcing and heating/cooling rates.

For each CALIPSO track, four optical parameters including the layer integrated volume depolarization ratio, the layer integrated particulate depolarization ratio, the layer integrated particulate color ratio, and aerosol-layer optical depth at 532 nm were analyzed to examine their characteristic features in each source region, followed by examination of their changes during the dust transport. In addition, CALIOP AODs at 532 nm were compared to MODIS-Aqua data in each case. For this comparison, we selected the closest footprint of MODIS-Aqua corresponding to each footprint along the CALIPSO track, and then the AOD profiles of CALIPSO for each footprint were integrated to give a total AOD over the entire atmospheric column similarly to MODIS AOD.

In this Chapter, the methodology was applied to the study of Asian dust, while Chapter 5 presents the results for other major dust sources. For Asian dust, our emphasis was on the source regions, mainly the Taklamakan Desert (36°-40°N, 78°-90°W) and Gobi Desert (38°-49°N, 94°-116°W) and downwind regions affected by mid- and long-range dust transport (including Korea (30°-40°N, 124°-132°W), Japan (30°-42°N, 132°-146°W), Western Pacific Ocean (28°-40°N, 150°-180°W), Middle Pacific Ocean (28°-48°N, 180°-140°E), Eastern Pacific Ocean (28°-48°N, 140°-120°E)). Although dust events may occur all year round, the spring season has the highest dust activity.

Figure 4.3 illustrates how this methodology is being used in Chapter 4.

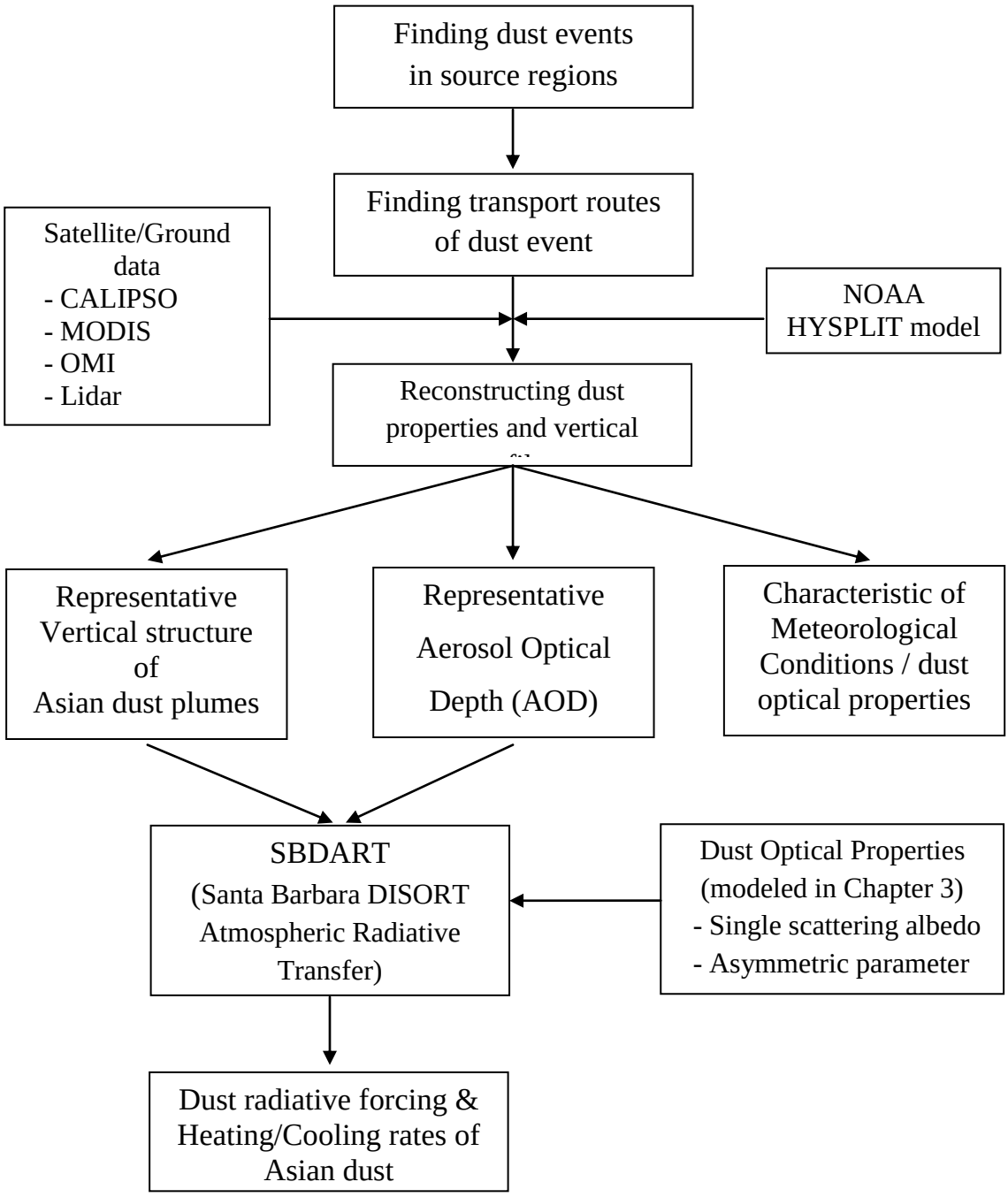

Figure 4.3 Schematic diagram of the methodology used in Chapter 4.

4.3 Results

To demonstrate how the developed methodology was applied to analyze Asian dust events on a case-by-case basis, here we present in detail the results for selected events in the source regions and transported areas. The section begins by discussing a dusty day (March 30, 2007) when CALIPSO passed over both the Taklamakan Desert and the Gobi Desert, as shown in Figure 4.4. Then it presents the results for mid-range transport cases (March 30, 31, and April 1, 2007) over South Korea and Japan and finally, it examines the cases of long-range transport dust (May 9, 10, 12, 13, and 15, 2007).

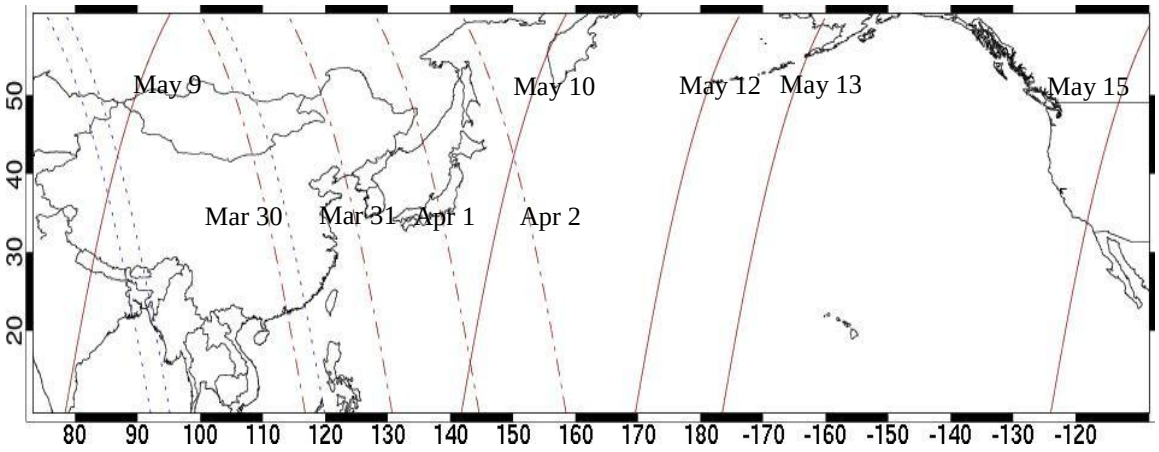

Figure 4.4 CALIPSO orbits for selected days discussed in section 4.3. Dotted lines are for the dust cases in the source area, double-dotted lines for the mid-range transport cases, and solid lines for long-range transport.

4.3.1 Characterization of Asian Dust in the Taklamakan and Gobi Deserts

4.3.1.1 The March 30 Case (daytime)

Figure 4.5 shows the true color MODIS image augmented by the meteorological observations of present weather types (dust storm, blowing dust, and floating dust) (Figure 4.5a) and coincident retrievals of Aerosol Index from OMI-Aura (Figure 4.5b).

(a)

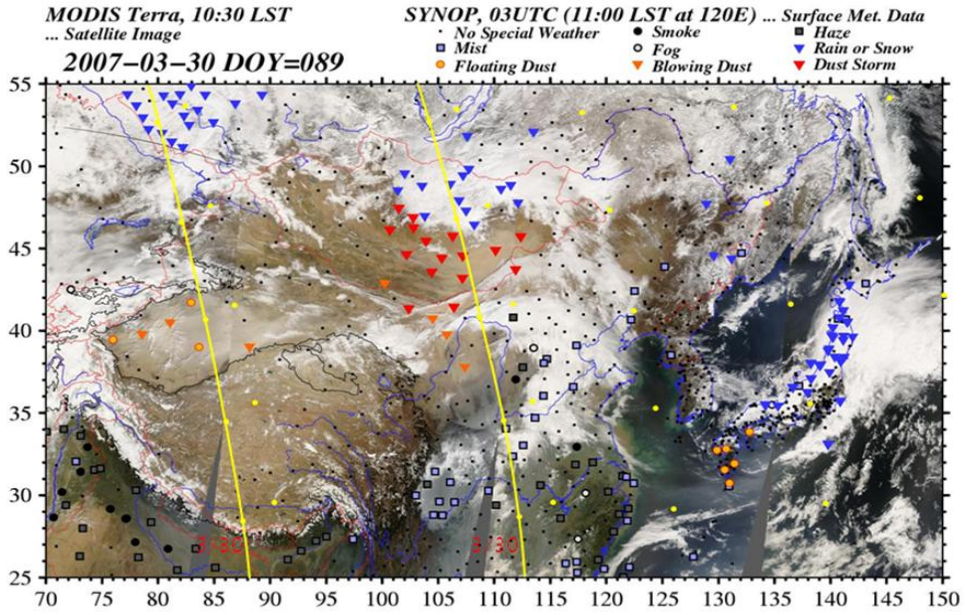

(b)

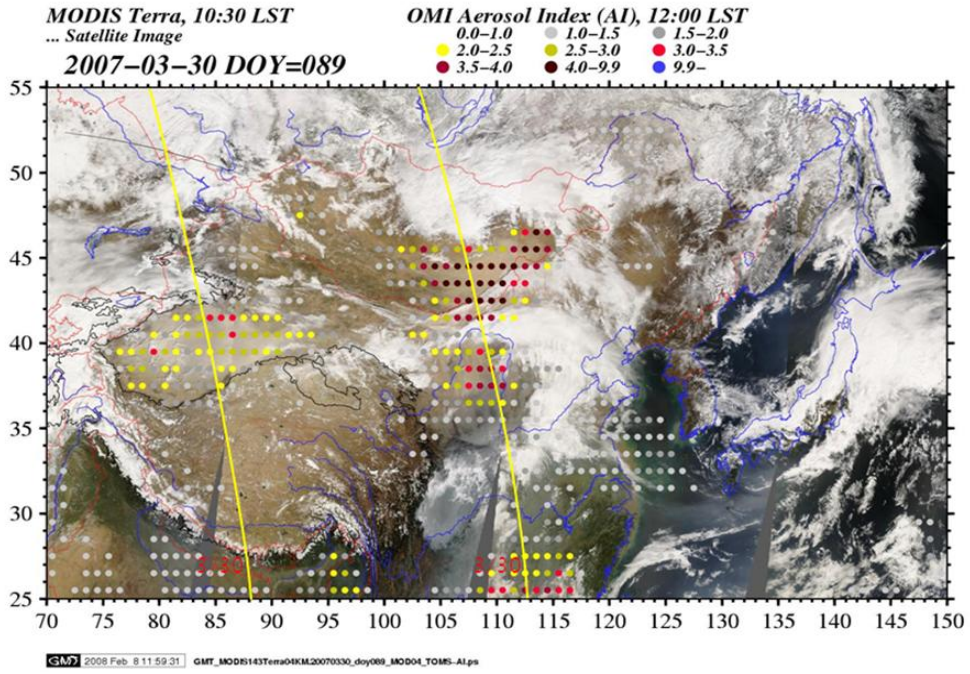

Figure 4.5 Integrated analyses of Asian dust events on March 30, 2007: (a) MODIS-Terra and ground observations of present weather, and (b) MODIS-Terra and OMI-AI. CALIPSO tracks are shown by yellow lines.

Meteorological observations on this day clearly show the presence of dust events in both the Taklamakan and the Gobi regions, especially strong dust storms in the Gobi. High values of Aerosol Index (AI) confirm that there was a heavy loading of dust in the atmosphere on that particular day. It was suggested that AI >0.7 serves as a good indicator of the presence of dust (Prospero et al., 2002). Clearly, AI is much higher than 0.7 in the region of interest.

Figure 4.6 presents the spatial distribution and some properties of dust determined from CALIPSO over the Taklamakan on March 30. The profile of the attenuated backscatter coefficient at 532 nm is shown in Figure 4.6(a). An enhanced backscattering signal is clearly detected. Figure 4.6(b) shows CALIPSO vertical feature mask (VFM) of version 2 (right) and 3.01 (left), and Figure 4.6(c) demonstrates the aerosol types of version 3.01. Examining the VFM and aerosol subtype in Figure 4.6(c), one can notice that CALIPSO does identify dust but in some instances aerosol (dust) is misclassified as clouds. The deep blue AOD (Figure 4.6(d)) and true color image from MODIS-Aqua (Figure 4.6(f)), and Aerosol Index (AI) (Figure 4.6(e)) confirm that there was a heavy dust loading. The case of the daytime orbit on March 30, 2007 over the Taklamakan Desert shows a good example of the misclassification of dust aerosols as clouds due to the similarity of scattering properties between the dense dust layers and the optically thin clouds.

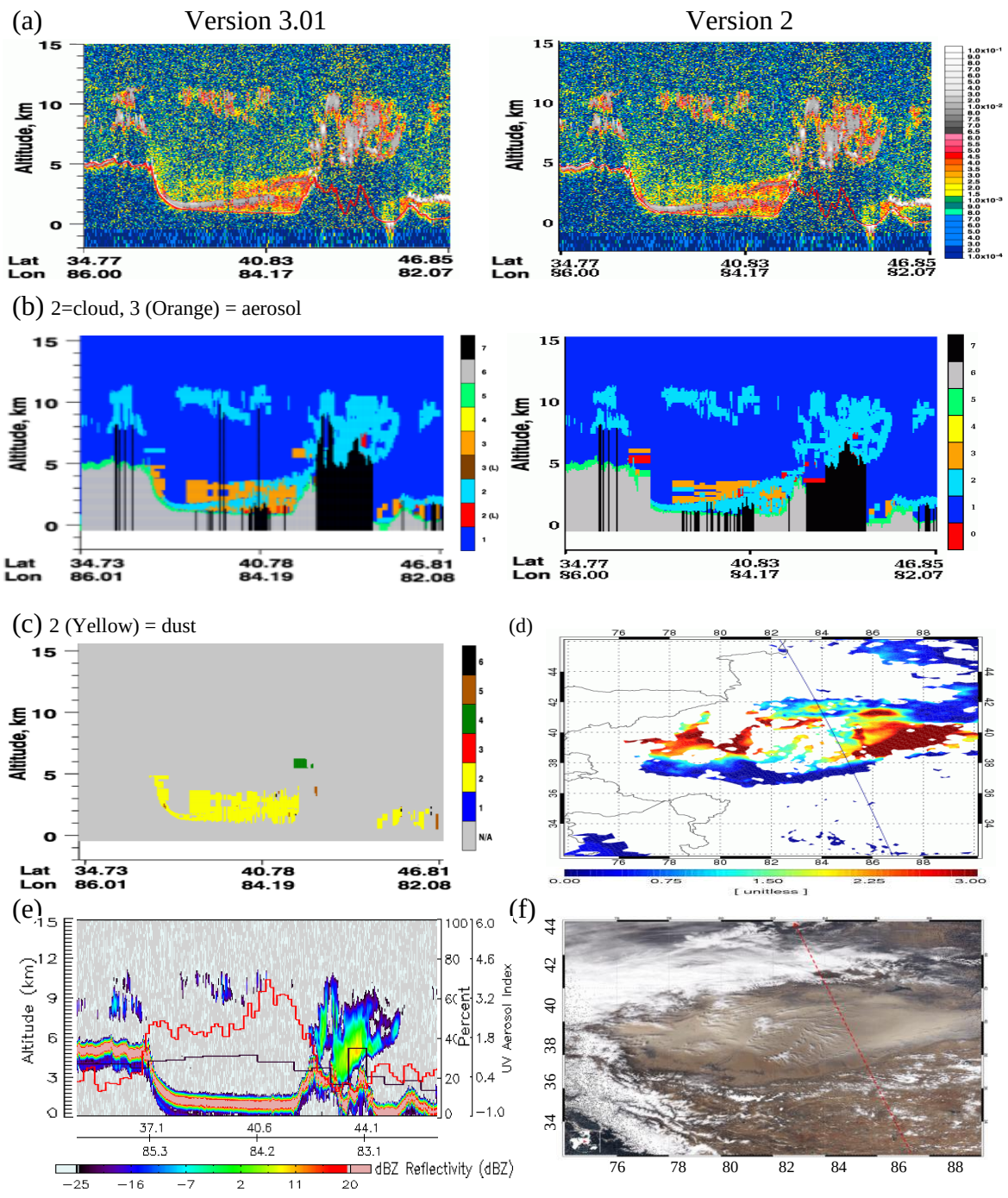

Figure 4.6 (a) Attenuated backscatter coefficient at 532 nm from CALIPSO, (b) vertical feature mask from versions 2 (right) and 3.01 (left) in CALIPSO, (c) aerosol subtype from version 3.01 in CALIPSO, (d) deep blue AOD from MODIS-Aqua, (e) Reflectivity (dBz) from CloudSat with surface albedo (black line) from MERRA Model and Aerosol Index (red line) from OMI-Aura, and (f) True color image from MODIS-Aqua with the orbit of CALIPSO (red dotted line) over the Taklamakan Desert on March 30, 2007.

The dust properties over the Taklamakan were further analyzed using the layer-integrated volume linear depolarization ratio $\delta_{v,layer}$, the layer integrated particulate linear depolarization ratio $\delta_{p,layer}$, aerosol-layer optical depth, and the layer integrated particulate color ratio retrieved from CALIPSO. The results of this analysis are shown in Figure 4.7. The vertical structure of aerosol layers is shown as a function of the latitude (about sea-surface level) along the CALIPSO orbit segment. The color of each identified layer shows the range of values of (a) $\delta_{v,layer}$ and (b) $\delta_{p,layer}$, shown at the right side of figure. Numbers in different colors give values of $\delta_{v,layer}$ (in red), $\delta_{p,layer}$ (in blue), the AOD (in black) and the layer integrated particulate color ratio (in violet) for each dust layer. The high values of $\delta_{v,layer}$ in Figure 4.7(a) are indicative of dust. Examining Figure 4.7(a) and (b), one can notice that $\delta_{v,layer}$ and $\delta_{p,layer}$ change with height as well as horizontally along the CALIPSO track. The $\delta_{p,layer}$ values vary from 0.231 to 0.853, with an average value of 0.443. This confirms that dust in the Taklamakan is composed of nonspherical particles. However, high values of $\delta_{p,\,layer}$ in high altitudes up to around 4 km (surface is 1 km) as well as in low altitudes are found. The difference in the values between $\delta_{v,\,layer}$ and $\delta_{p,\,layer}$ might be due to the mass concentration of dust particles because the value of $\delta_{v,\,layer}$ depends on both the nonsphericity of dust and the amount of dust. The gray shaded bars in Figure 4.7(b) denote the negative values of $\delta_{p,layer.}$ The large number of gray shaded bars indicates that problems still remain in $\delta_{p,layer}$ in the level 2 version 3.01 CALIOP data under heavy dust conditions. The $\delta_{v,layer}$ ranges from 0.172 to 0.582, with an average value of 0.285. In Figure 4.7(a), $\delta_{v,\,layer}$ has very high values near the surface (higher than 0.35) and lower values above 2 km. This fact suggests that it is likely that coarse dust particles are not well mixed vertically.

(a) Blue: δ_p, Red: δ_v, Black: AOD, Violet: χ_p

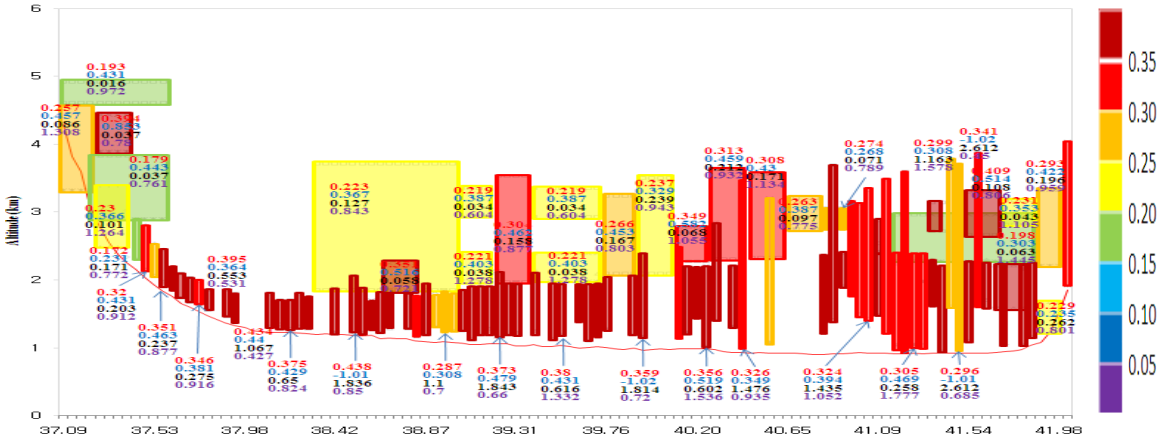

(b) Blue: δ_p, Red: δ_v, Black: AOD, Violet: χ_p

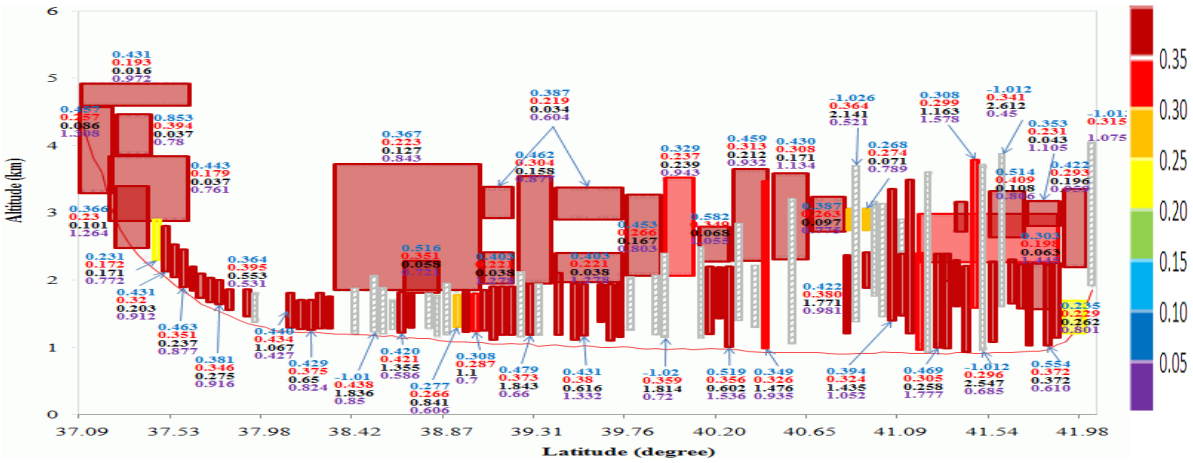

(c) Black solid line: CALIPSO version 3.01, blue dotted line: MODIS-Aqua

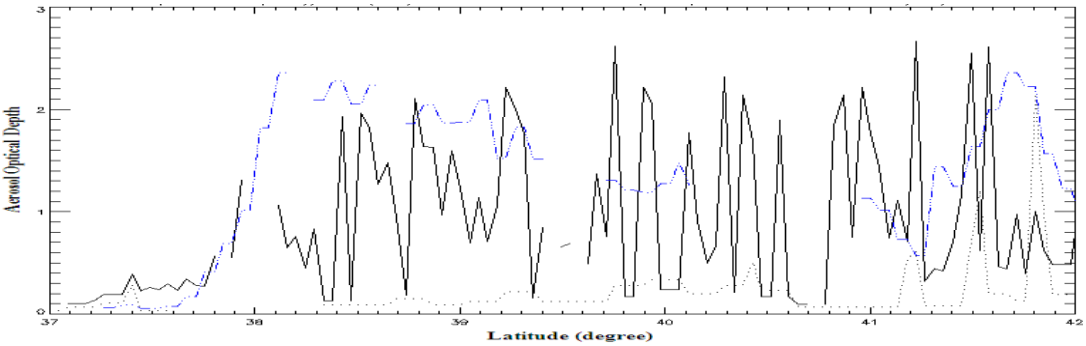

Figure 4.7 (a) Distribution of layer-integrated volume depolarization ratio, and (b) distribution of layer-integrated particulate depolarization ratio from CALIPSO over the Taklamakan Desert on March 30, 2007.

The $\chi_{p,layer}$ varies from 0.427 to 2.361, with a relatively high average value of 0.917, indicating that coarse dust particles are dominant in the Taklamakan Desert. As seen in Figure 4.7(b), $\chi_{p,layer}$ also shows high vertical variation, having high values near the surface (1.278) and lower values above 3 km. These vertical variations in $\delta_{v,\,layer}$ and $\chi_{p,\,layer}$ indicate that the lidar ratio S_a must also vary, and the CALIPSO retrievals, which assume that S_a is constant for desert dust, may be biased. The AOD ranges from 0.006 to 2.666, with an average value of 0.869 (Figure 4.7(b)). Figure 4.7(c) shows the CALIPSO total aerosol optical depth from version 2 and version 3.01, i.e., the sum of aerosol optical depth of individual vertical layers over a given CALPSO footprint and the MODIS deep blue from MODIS-Aqua. The aerosol optical depth from CALIPSO version 3.01 is in the range from 0.427 to 2.361, while those values of CALIPSO version 2 are unrealistically low. The MODIS deep blue AOD from MODIS-Aqua is up to around 2.4. The AOD values in version 3.01 seem to be improved from the unrealistically low AOD in version 2. However, the large difference in AOD values (up to2) between CALIPSO version 3.01 and MODIS-Aqua indicates that the aerosol lidar ratio S_a selected for the CALIPSO algorithm could be inadequate.

The results of analyses of dust over the Gobi are presented in Figure 4.8, which is organized similarly to Figure 4.6 to facilitate comparison. There were strong dust storms on March 30, 2007 in this region demonstrated by meteorological data and high AI values (see Figures 4.8(e)). The CALIPSO lidar measures strong backscattering signal (see the image in Figure 4.8(a)). However, again the vertical feature mask wrongly classifies dust as a cloud (see blue area between 41^0 and 47^0). This feature is confirmed by the image of CloudSat shown in Figure 4.8(e).

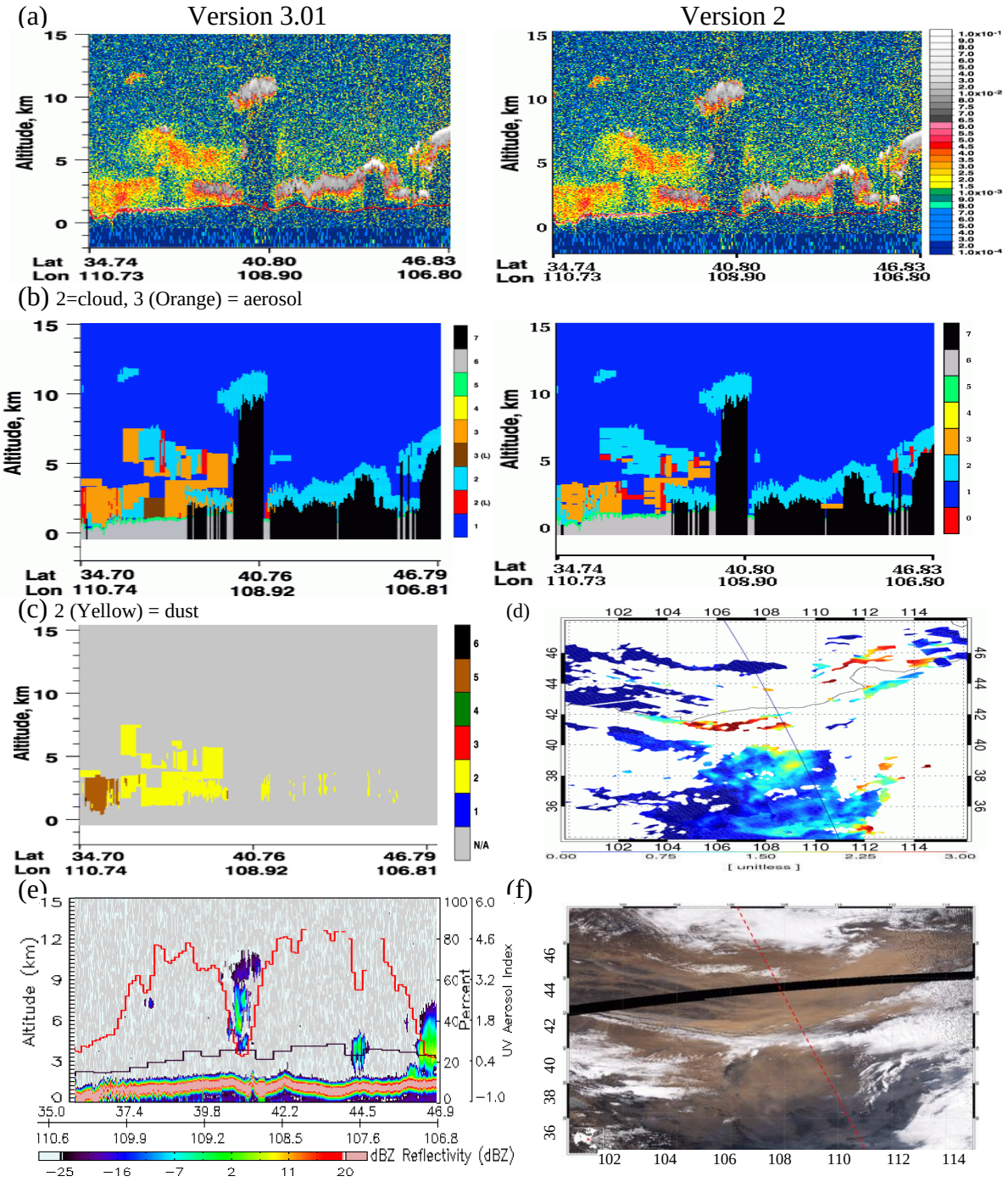

Figure 4.8 Same as Figure 4.6, except for the Gobi Desert on March 30, 2007.

Thus, our analyses reveal a consistent problem in the CALIPSO algorithms in discriminating dust from clouds which will need to be addressed to improve characterization of dust in the source regions.

Figure 4.9 shows that $\delta_{v,\ layer}$ has very high values near the surface (higher than 0.35) and lower values at 3-4 km. However, $\delta_{p,\ layer}$ shows an even distribution of high values at 3-4 km in Figure 4.9(b). This is similar to the $\delta_{v,\ layer}$ and $\delta_{p,\ layer}$ behavior discussed above in the Taklamakan case. This fact might suggest that the coarse dust particles are well mixed vertically and the nonsphericity effect is similar between Taklamakan dust and Gobi dust. The vertical distribution of the layer integrated particulate color ratio, varying from 0.454 to 4.802, supports that the coarse particles are in high altitude. The distribution of AOD over the Gobi Desert shows a similar pattern with the AOD over the Taklamakan Desert, varying from 0.032 to 2.496. Figure 4.9(c) shows good agreement between CALIPSO version 3 AOD the MODIS Deep Blue AOD, although the high variation of CALIPSO AOD retrieved with the version 3 algorithm seems unrealistic.

(a) Blue: δ_p, Red: δ_v, Black: AOD, Violet: χ_p

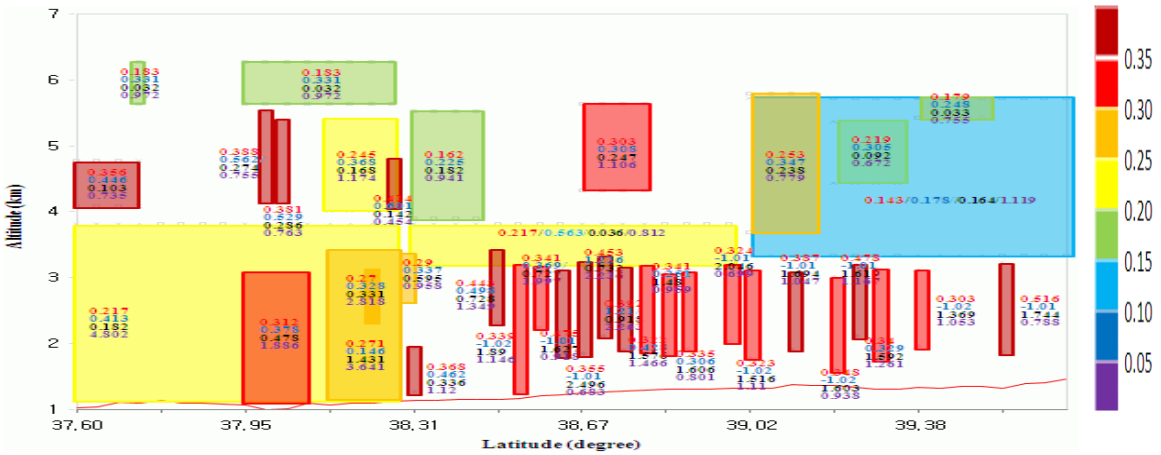

(b) Blue: δ_p, Red: δ_v, Black: AOD, Violet: χ_p

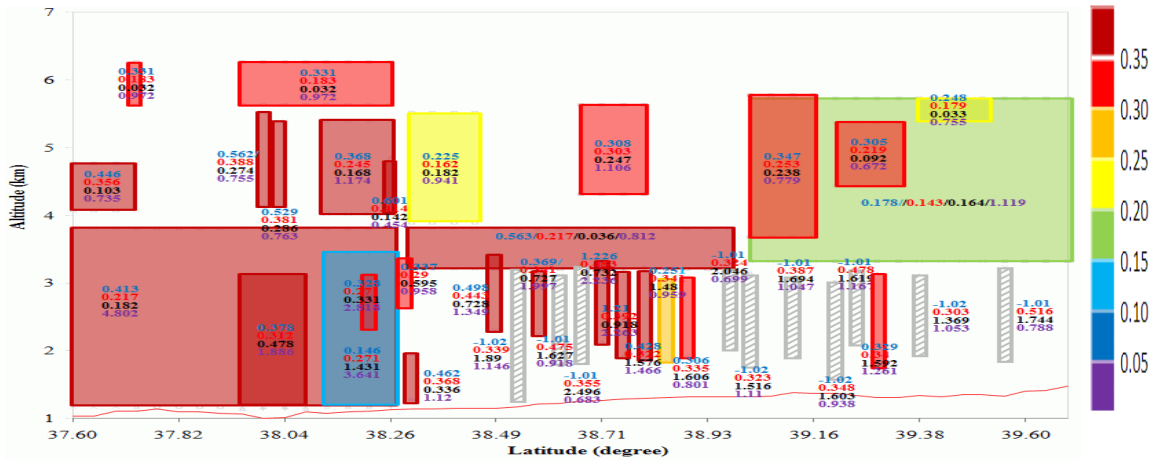

(c) Black solid line: CALIPSO version 3.01, blue dotted line: MODIS-Aqua

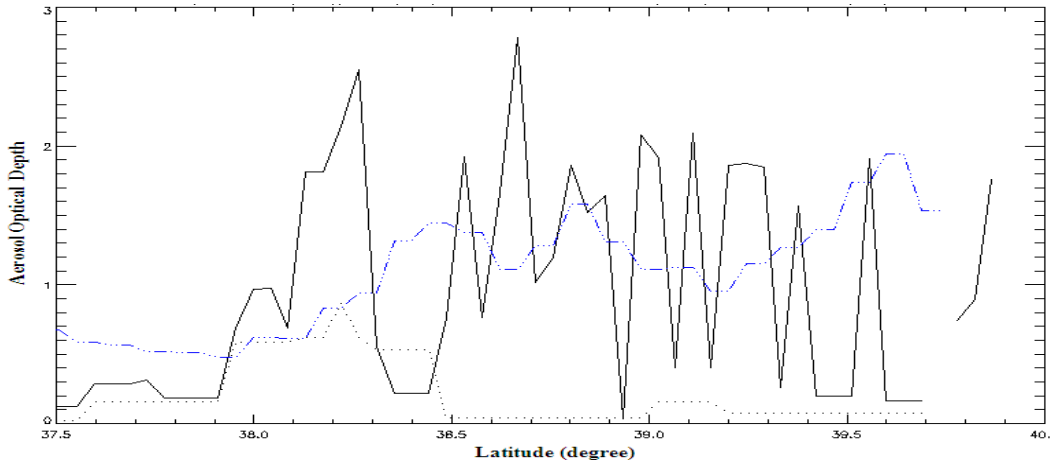

Figure 4.9 Same as Figure 4.7, except for the Gobi Desert on March 30, 2007.

4.3.1.2 The May 7 Case (nighttime)

Figures 4.10 show the results of analysis for the dust case in the Taklamakan Desert on May 7, 2007. There are no true color images from MODIS and OMI AI because two figures are the results from nighttime CALIPSO data. Figure 4.10 shows that there was a dust event over the Taklamakan Desert on that night. The total backscattering coefficient in Figure 4.10(a) shows high values over the desert, and the VFM in Figure 4.10(b) indentifies that both dust and clouds were present over the Taklamakan. The cloud detected at a higher altitude of about 4.5-6 km between 40.5°-41° is likely a misclassified dust. Figure 4.10(d) supports this fact that there were no cloud signals between 41°-41.5° from the CloudSat data.

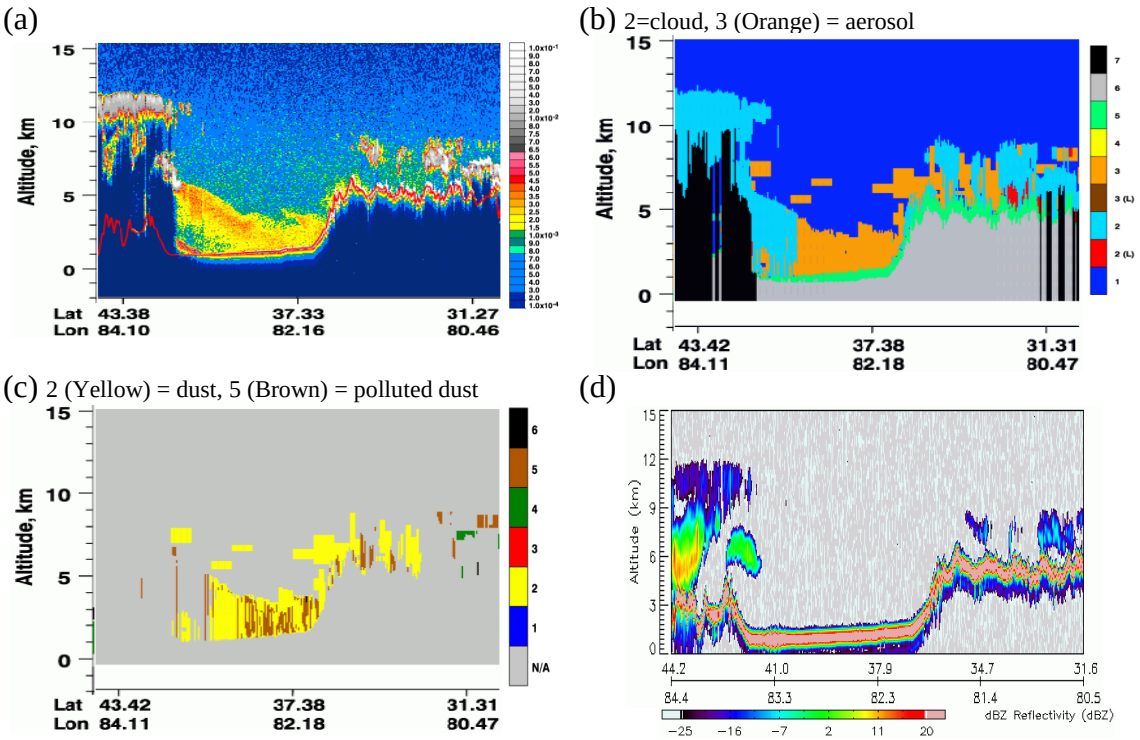

Figure 4.10 (a) Attenuated backscatter coefficient at 532 nm, (b) vertical feature mask from version 3.01, (c) aerosol subtype from version 3.01 from CALIPSO, and (d) Reflectivity (dBz) from CloudSat over the Taklamakan Desert on May 7, 2007.

Figure 4.11 shows that the dust layer spreads from the surface to ~5 km. Unlike the case of March 30, values of $\delta_{v,\,layer}$ are relatively low. This might be explained by the lower concentrations of dust during floating dust events compared to dust storms. Another possible explanation is that dust particle nonsphericity differs depending on the intensity of dust emissions. However, high values $\delta_{p,\,layer}$ in Figure 4.11(b) indicate that dust in the Taklamakan Desert is composed of nonspherical particles.

Interestingly, the results of the dust particulate depolarization ratio over the sources might be explained by dust particle nonsphericity that remains during vertical mixing within the boundary layer, but values of $\delta_{v,layer}$ depend on the dust concentration. CALIPSO observations do not show clear relations between AOD and $\delta_{v,\,layer}$.

To summarize CALIPSO observations over the dust sources, Table 4.1 compares the dust optical properties over the Taklamakan and the Gobi. Examining Table 4.1, $\delta_{v,layer}$ varies from 0.042 to 0.582, and $\delta_{p,layer}$ distributes from 0.088 to 2.957, with a high average value above 0.364 in the Taklamakan Desert. The $\chi_{p,layer}$ varies from 0.098 to 2.361, with a relatively high average value above 0.9. The Gobi Desert also has a high value of $\chi_{p,layer}$ up to 3.75 and $\delta_{p,layer}$, with a high average value above 0.3. The high values of $\delta_{p,layer}$, might suggest that the nonsphericity effect is similar between Taklamakan dust and Gobi dust. Dust layers are detected at high altitudes of 9-10 km in the Gobi and Taklamakan Deserts. This fact might provide some insight that these layers lofted to the upper troposphere around 8-10 km can travel around the globe (Uno et al. (2009)). In order to investigate the relationship between vertical distribution and synoptic meteorological conditions, we will investigate the synoptic meteorological conditions in the next section.

(a) Blue: δ_p, Red: δ_v, Black: AOD, Violet: χ_p

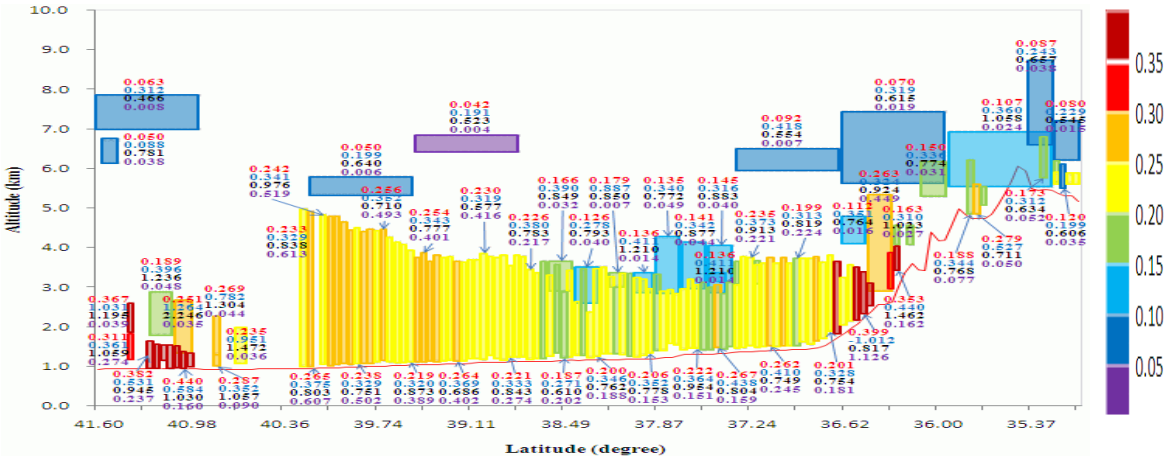

(b) Blue: δ_p, Red: δ_v, Black: AOD, Violet: χ_p

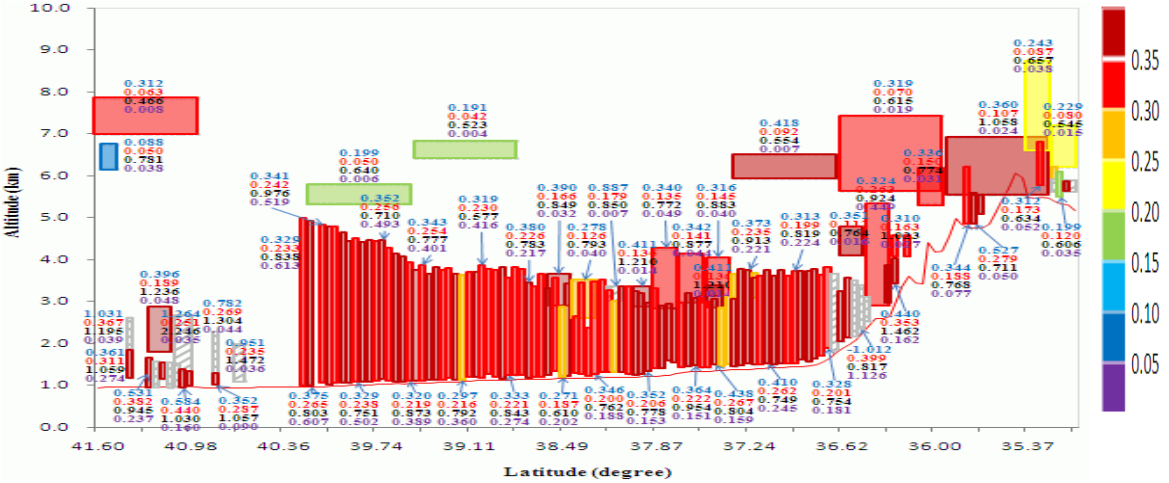

(c) Black solid line: CALIPSO version 3.01

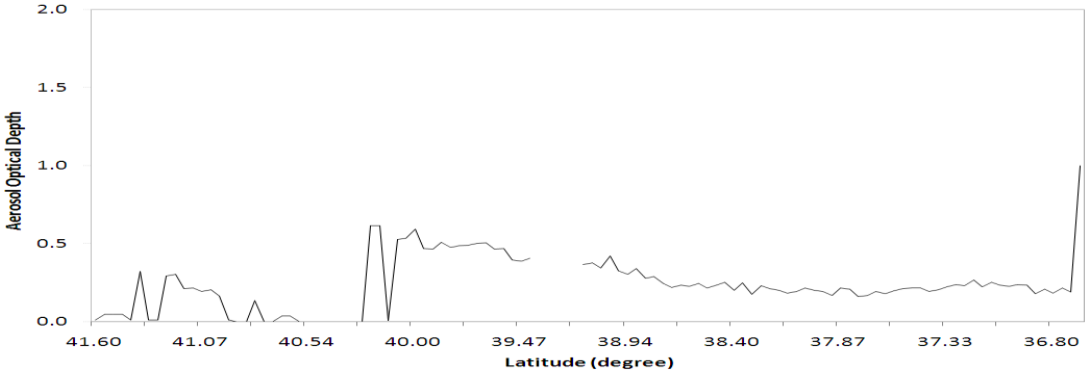

Figure 4.11 Same as Figure 4.7, except for the Taklamakan Desert on May 7, 2007.

Table 4.1 Comparative summary of dust properties retrieved from CALIPSO over dust source regions for the spring season.

Date	Taklamakan Desert				
	3/29/2007 (nighttime)	3/30/2007 (daytime)	4/1/2007 (daytime)	5/7/2007 (nighttime)	5/9/2007 (nighttime)
Location (degree)	35.45N, 83.14E-40.03N, 84.52E	37.09N, 85.33E-42.03N, 83.78E	38.13N,88.11E-42.62N,86.67E	37.0N,82.06E-41.6N,83.5E	37.5N,85.3E-42.44N,86.87E
Synoptic Condition	Blowing Dust	Dust Storm	Blowing Dust	Floating Dust	Dust Storm
Vertical extent (km)	1.197-9.097	0.958-4.915	0.928-6.474	1.018-7.853	0.898-9.696
$\delta_{v,layer}$ (average)	0.069-0.299 (0.151)	0.172-0.582 (0.285)	0.184-0.621 (0.299)	0.042-0.440 (0.167)	0.05-0.448 (0.184)
$\delta_{p,layer}$ (average)	0.111-2.957 (0.472)	0.231-0.853 (0.443)	0.309-1.502 (0.524)	0.088-1.264 (0.364)	0.194-1.557 (0.461)
$\chi_{p,layer}$ (average)	0.098-1.662 (0.996)	0.427-2.361 (0.917)	0.420-2.071 (1.097)	0.466-2.246 (0.786)	0.352-2.097 (0.920)
Aerosol optical depth	0.020-0.772 (0.193)	0.068-1.597 (0.470)	0.033-1.654 (0.354)	0.006-0.613 (0.267)	0.011-1.547 (0.157)

Date	Gobi Desert			
	3/29/2007 (nighttime)	3/30/2007 (daytime)	4/1/2007 (daytime)	3/19/2010 (nighttime)
Location (degree)	36.77N,108.2E-41.08N, 109.6E	37.6N,109.9E-39.69N, 109.26E	36.14N,113.42E-40.19N,112.19E	27.6N, 102.7E-44.5N, 107.7E
Synoptic Condition	Floating Dust	Dust Storm	Floating Dust	Dust Storm
Vertical extent (km)	1.287-8.497	1.137-6.264	0.898-5.934	0.532-11.414
$\delta_{v,layer}$ (average)	0.070-0.280 (0.144)	0.143-0.478 (0.238)	0.111-0.471 (0.205)	0.025-0.490 (0.128)
$\delta_{p,layer}$ (average)	0.146-0.650 (0.311)	0.178-1.226 (0.385)	0.106-0.709 (0.339)	0.038-4.734 (0.390)
$\chi_{p,layer}$ (average)	0.415-2.359 (0.888)	0.454-2.818 (1.036)	0.425-2.975 (1.157)	0.167-3.750 (0.982)
Aerosol optical depth	0.007-0.720 (0.262)	0.036-2.779 (0.569)	0.053-2.665 (0.511)	0.006-4.574 (0.586)

- $\delta_{v,layer}$: The layer integrated volume depolarization ratio
- $\delta_{p,layer}$: The layer integrated particulate depolarization ratio
- $\chi_{p,layer}$: The layer integrated particulate color ratio

4.3.1.3 Synoptic Meteorological Conditions of Asian Dust Events

Understanding the meteorological conditions associated with dust in the sources and during the transport aids in the interpretation of vertical profiles measured by CALIOP. Emission of dust aerosol in the arid and semi-arid regions (e.g., the Taklamakan and Gobi Deserts) occur in the condition of wind speed above 10 m/s. Transport of dust is associated with the westerly jet streams that carry dust over China, Korea, and Japan, and sometimes across the Pacific Ocean reaching North America (Huang et al., 2008, Uno et al., 2010). Huang et al. (2008) suggested that floating dust events are more common in the Taklamakan Desert, while strong dust storms prevail in the Gobi Desert due to the different weather conditions influencing these two desert regions.

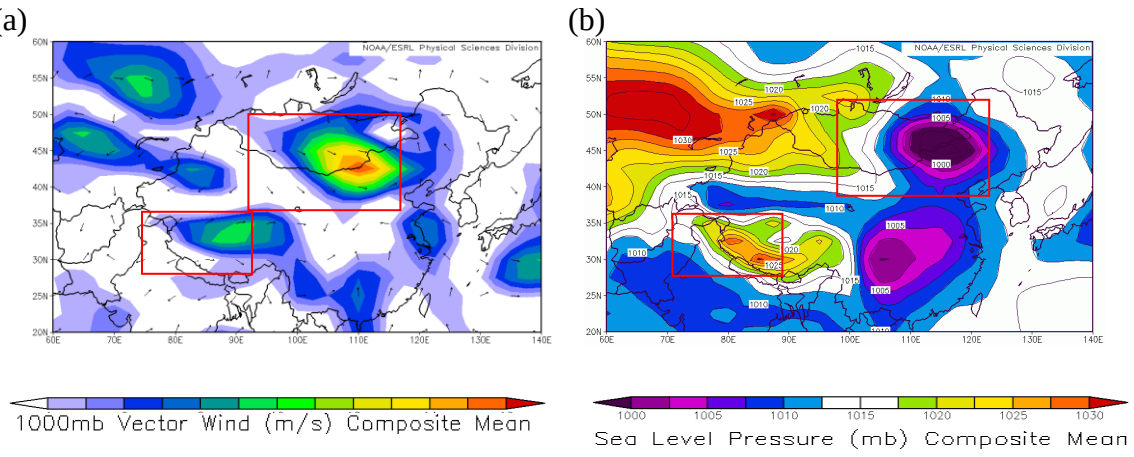

Figure 4.12 (a) 100 mb Vector wind (m/s) composite mean and (b) Sea level pressure (mb) composite mean over Asia on March 30, 2007, produced with the NOAA ESRL (Earth System Research System).

The dust events in the Taklamakan Desert are thought to be generated by mesoscale cold winds induced by synoptic-scale cold high-pressure systems. The cold air

moves into the Taklamakan basin causing the instability of hot desert air. This leads to the formation of strong surface winds, often exceeding 10 m/s, and dust emission. Figure 4.12(a) shows the wind vector composite mean at 1000 hPa on March 30, 2007. These strong winds caused both blowing and floating dust episodes in the Taklamakan Desert. Similar wind pattern occurred in the Taklamakan Desert on May 7, 2007 as shown in Figure 4.13. In this case, floating dust present weather was reported. D. Liu et al. (2008) reported that the mean top height of dust layer in spring is the highest over the Taklimakan and Gobi deserts and suggested that these two major dust sources are related to long-range transport in the spring season.

(a) (b)

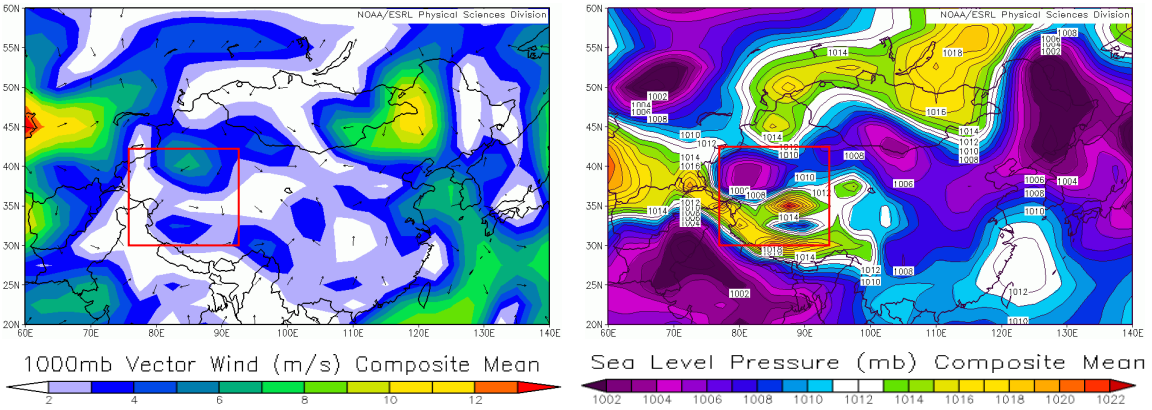

Figure 4.13 Same as Figure 4.12, but for May 7, 2007.

The emission of dust in the Gobi is associated with the development of the synoptic-scale cyclones. As shown in Figure 4.12(b), on March 30, 2007, the synoptic-scale cyclone was positioned over the Gobi Desert, causing dust storms in the region. Dust events originating in the Gobi can be transported at various distances, including mid- and long-range transport. The transport route depends on specific meteorological conditions and lifting height. For instance, the Gobi dust can be uplifted to the upper

troposphere when the Gobi desert is located below downstream of a trough (Tsai et al., 2008). The lift height can be as large as 8–9 km. The CALIPSO data show that in this case dust can be transported over the Pacific Ocean in the lower and upper troposphere by the westerly jet stream. In the case of the Taklamakan, high initial uplifting is required because the desert is surrounded by mountains of about 5 km high to the north, west, and south (Huang et al., 2009).

4.3.2 Analyses of Transported Asian Dust

4.3.2.1 Case of a Mid-range Transport

Figure 4.1 shows CALIPSO orbits for a mid-range transport case that will be presented here. The dust event started on March 30 and then passed over northeast China, South Korea, and Japan. Figure 4.14 shows the backward and forward trajectories for this event reconstructed with the NOAA HYSPLIT model.

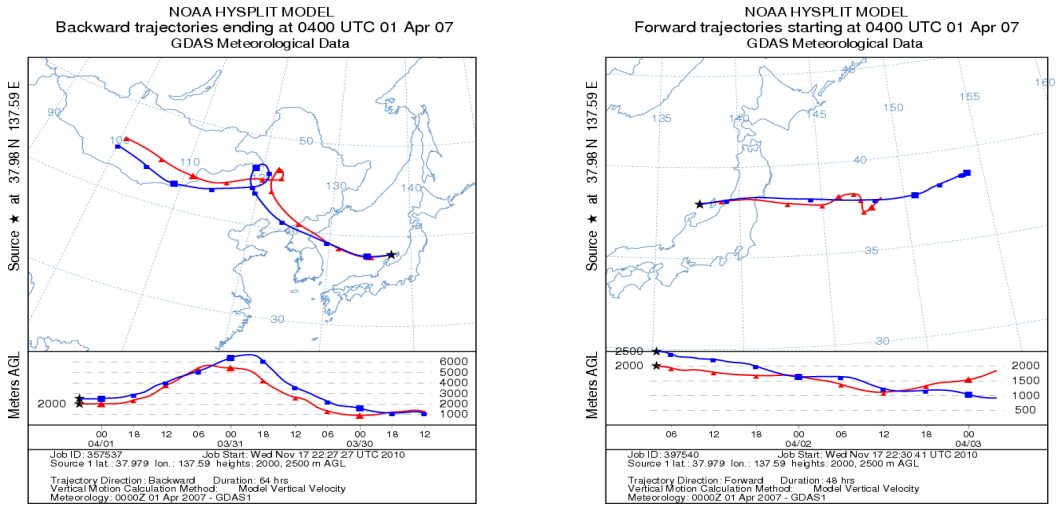

Figure 4.14 Backward and forward trajectories started at UTC 04:00 on April 1, 2007, at a location 37.979˚N and 137.59˚E and for an altitude of 2000 and 2500 meters, produced with the NOAA HYSPLIT model.

Combining trajectories and CALIPSO VFM, we reconstructed the mid-range transport of this dust event. Figure 4.15 presents the reconstructed mid-range transported plume, showing the presence of dust layer (in brown) in each CALIPSO pass. Here we will use the term 'mid-range transport of Asian dust' to refer to transport cases to Japan or the eastern Japan.

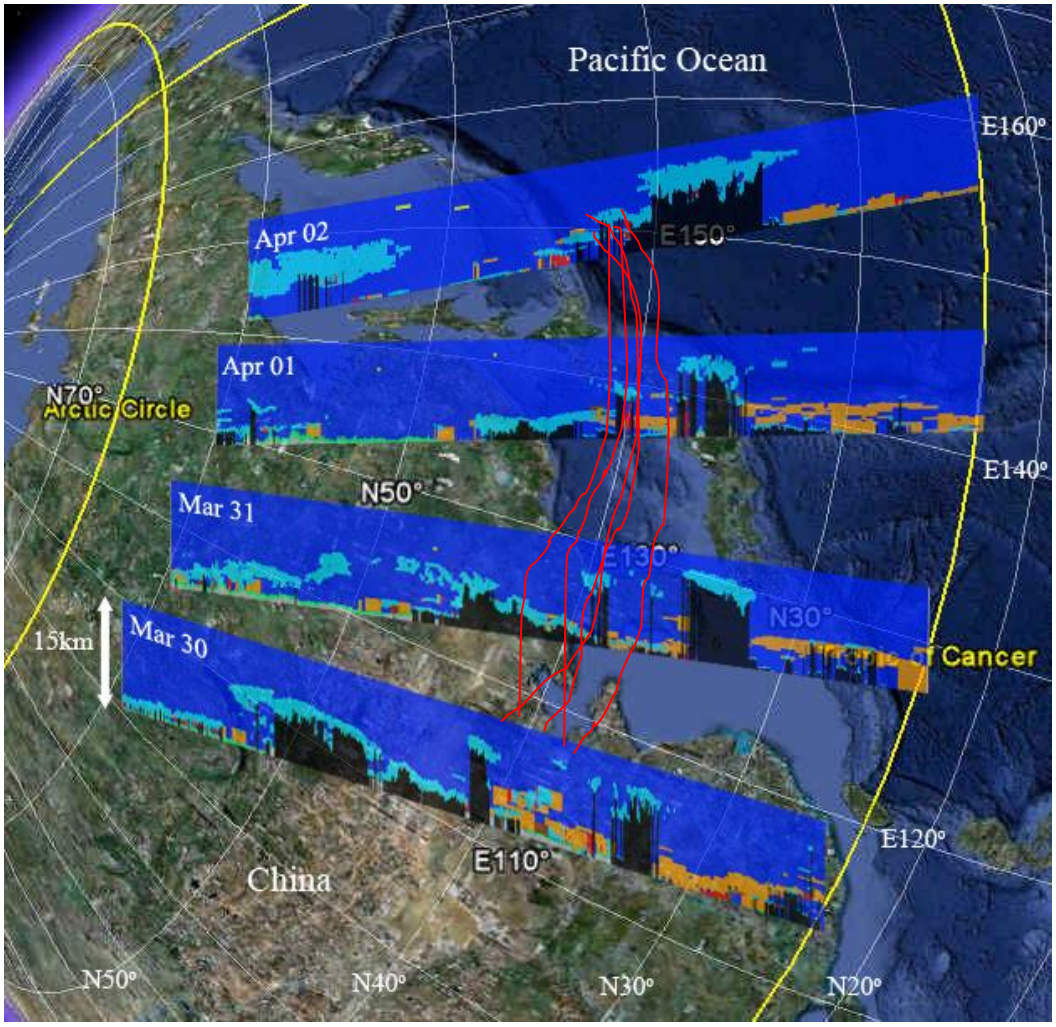

Figure 4.15 Reconstructed mid-range transport of an Asian dust event originating in the Gobi Desert on March 30, 2007 and transported to the Pacific Oceans. The brown color denotes dust plumes and light blue denotes clouds.

Examination of the aerosol profiles shown in Figure 4.15 reveals that the vertical structure of Asian dust plumes changes during transport. These changes are important to the dust radiative heating rates and thus to dust impact on clouds and atmospheric dynamics. It is also apparent that dust layers are mixed with clouds. CALIPSO can detect dust under the optically thin clouds, but no detection will be possible under the heavy clouds.

Figures 4.16, 4.19, and 4.22 show meteorological conditions and AI over the study regions on March 31, April 1, and April 2, respectively. Unfortunately, there were no AIs retrieved from OMI on April 1 (Figure 4.19(b)). The results of CALIPSO data analyses for these days are shown in Figures 4.17, 4.18, 4.20, 4.21, 4.23 and 4.24. Again these figures are organized similar to Figures 4.5-4.9 and 4.16-4.24 to facilitate intercomparison. The gray shaded bars in Figure 4.18(b), 4.21(b), and 4.24(b) denote the negative values of $\delta_{p,layer.}$ The large number of gray shaded bars indicates that problems still remain in $\delta_{p,layer}$ in the level 2 version 3.01 CALIOP under mixed conditions of dust and clouds. CALIPSO data were also compared against both ground-based lidars and AERONET sites located in China, South Korea, and Japan (shown in Figure 4.2). Figure 4.25 shows the aerosol optical depth from AERONET. Figure 4.26 shows ground-based lidar backscatter and depolarization ratio at selected locations as a function of time. Time corresponding to the CALIPSO overpasses is shown with black vertical lines.

The summary of representative properties of transported Asian dust is given in Table 4.2, which may be compared to results in Table 4.1. Various differences as well as some similarities in properties of Asian dust in the source regions and downwind are clearly seen.

(a)

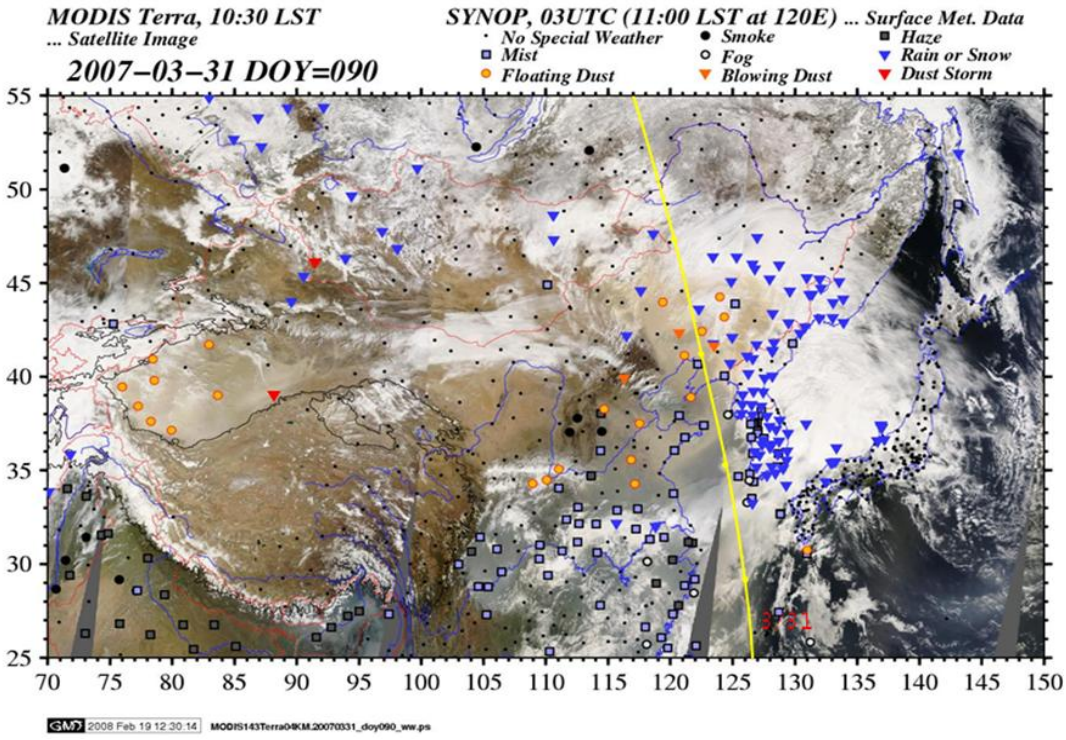

(b)

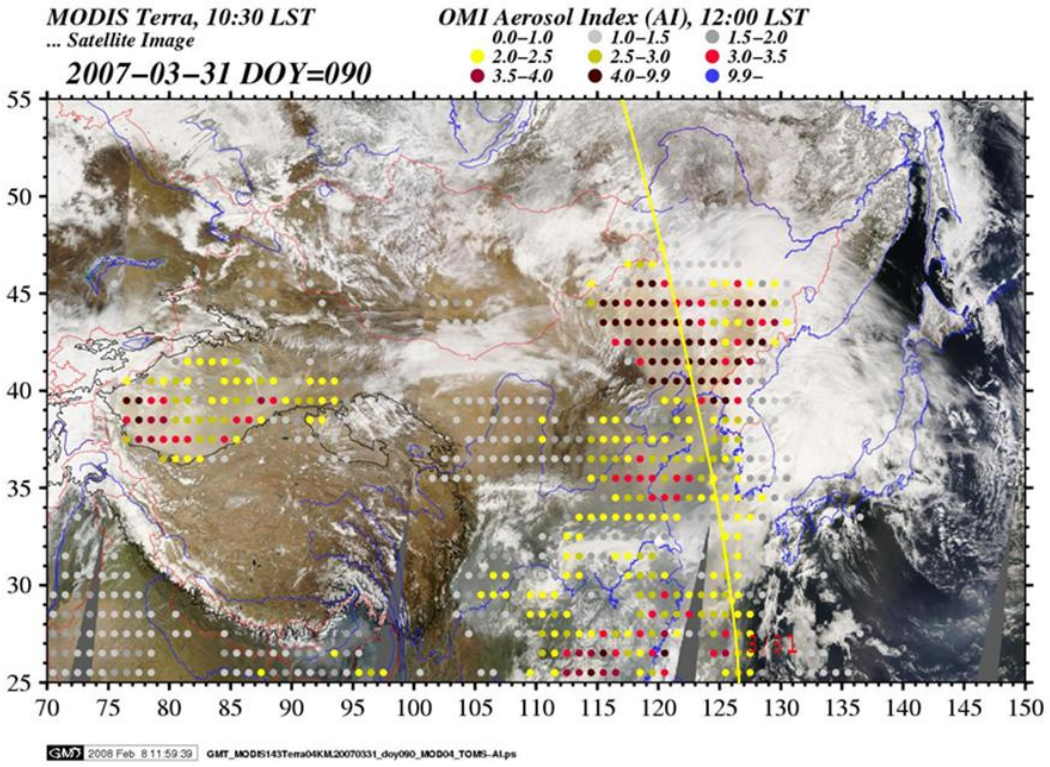

Figure 4.16 Same as Figure 4.5, except for March 31, 2007.

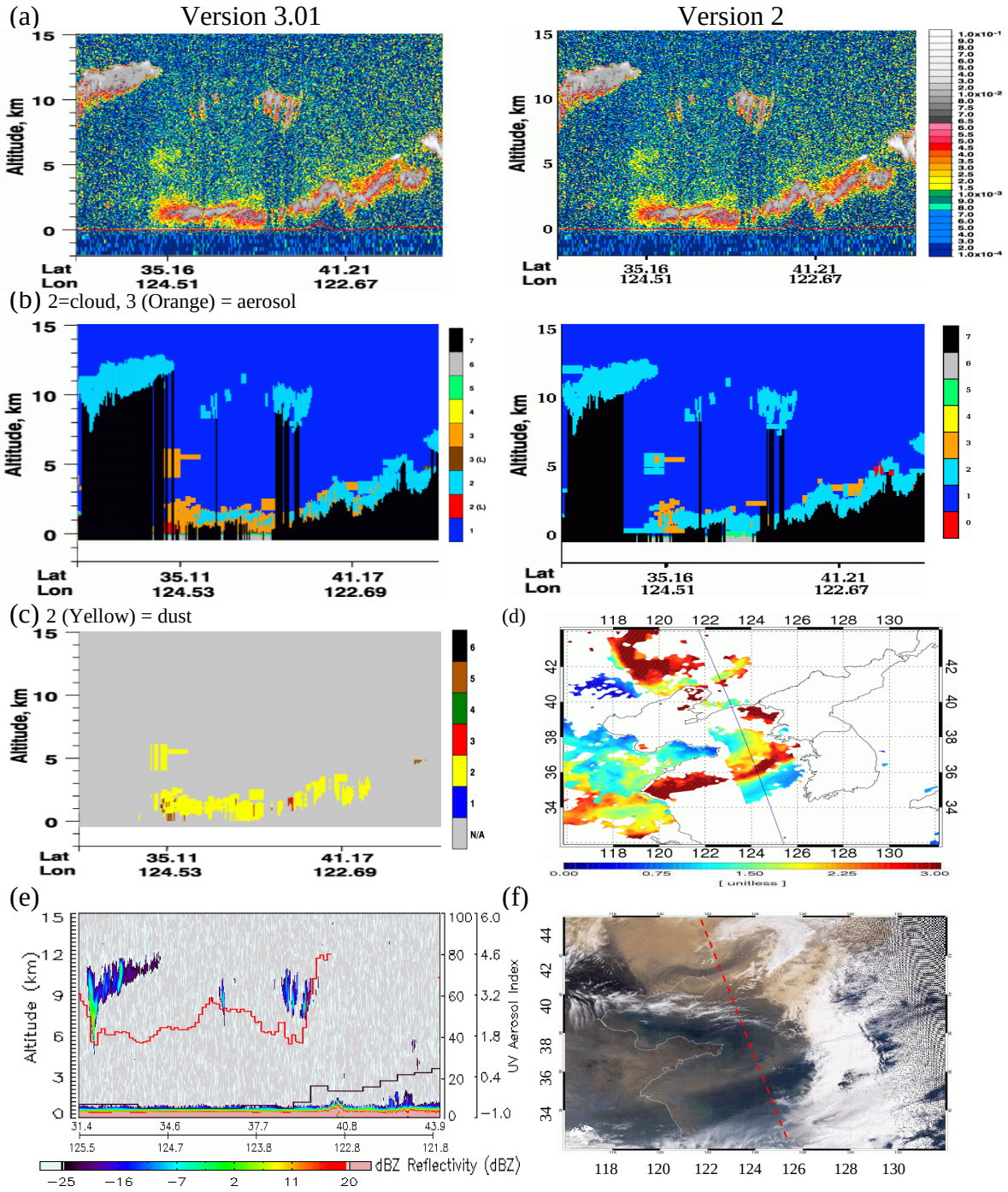

Figure 4.17 Same as Figure 4.6, except for the East China on March 31, 2007.

. (a) Blue: δ_p, Red: δ_v, Black: AOD, Violet: χ_p

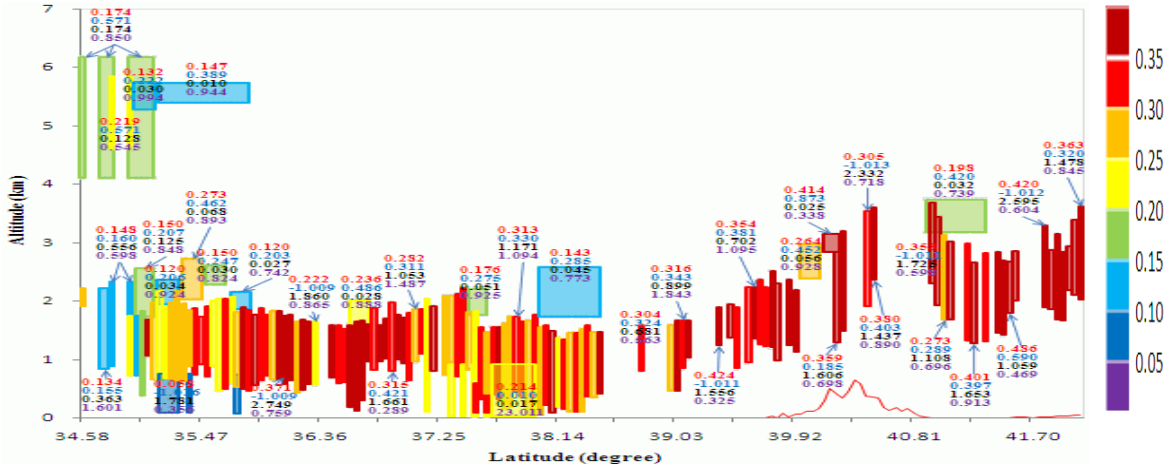

(b) Blue: δ_p, Red: δ_v, Black: AOD, Violet: χ_p

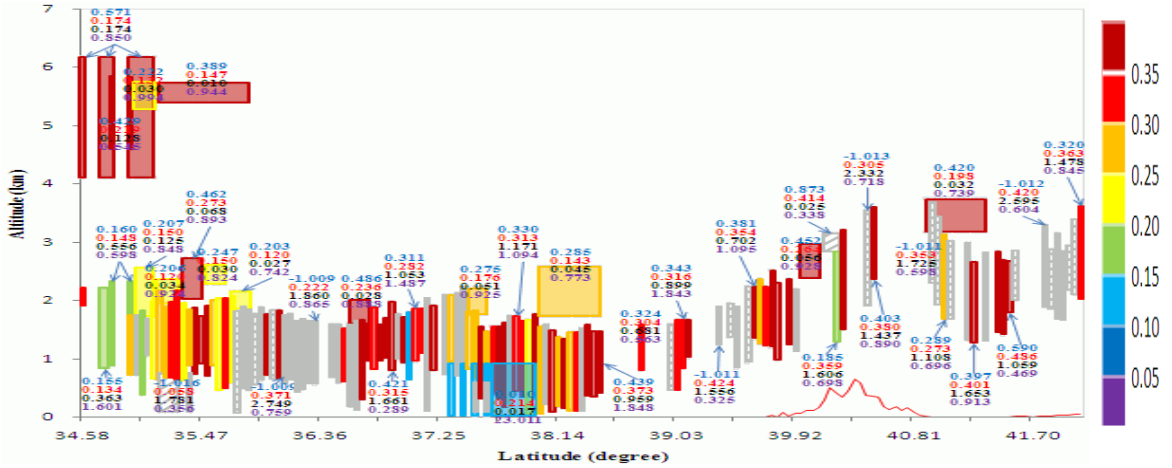

(c) Black: AOD CALIPSO, blue: Deep Blue AOD, Red: AOD MODIS-Aqua

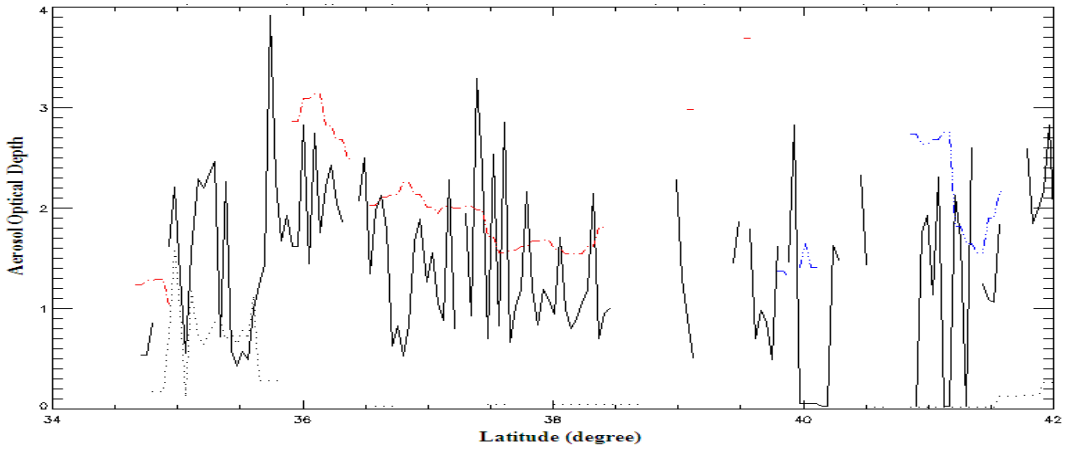

Figure 4.18 Same as Figure 4.7, except for the East China on March 31, 2007.

(a)

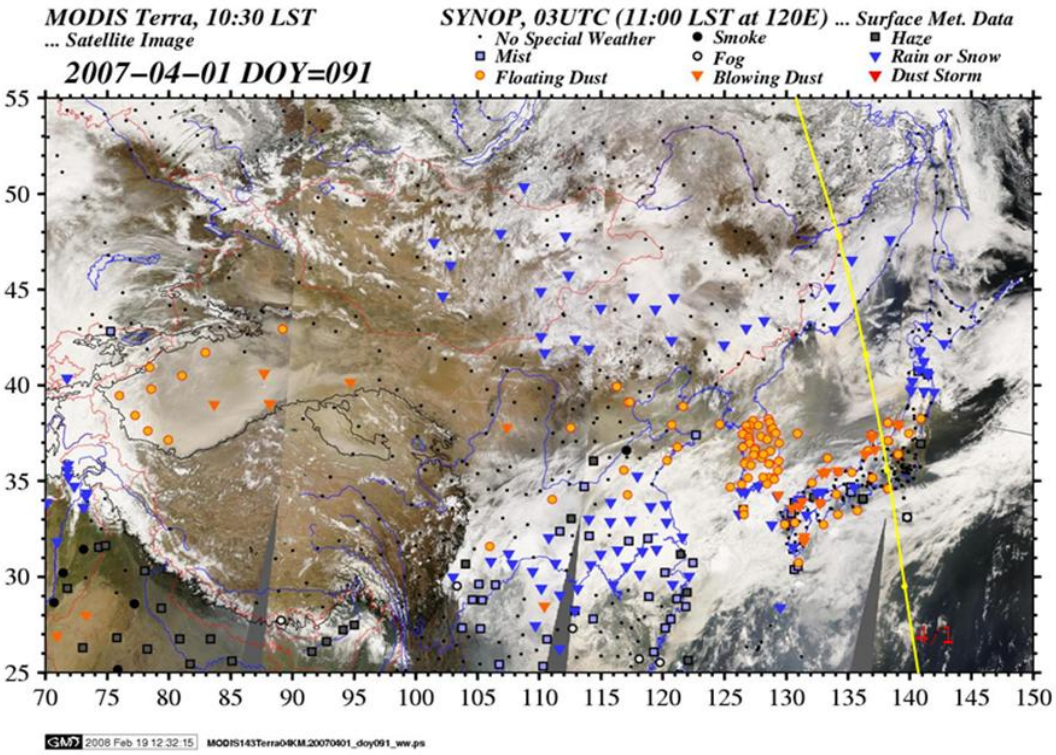

(b)

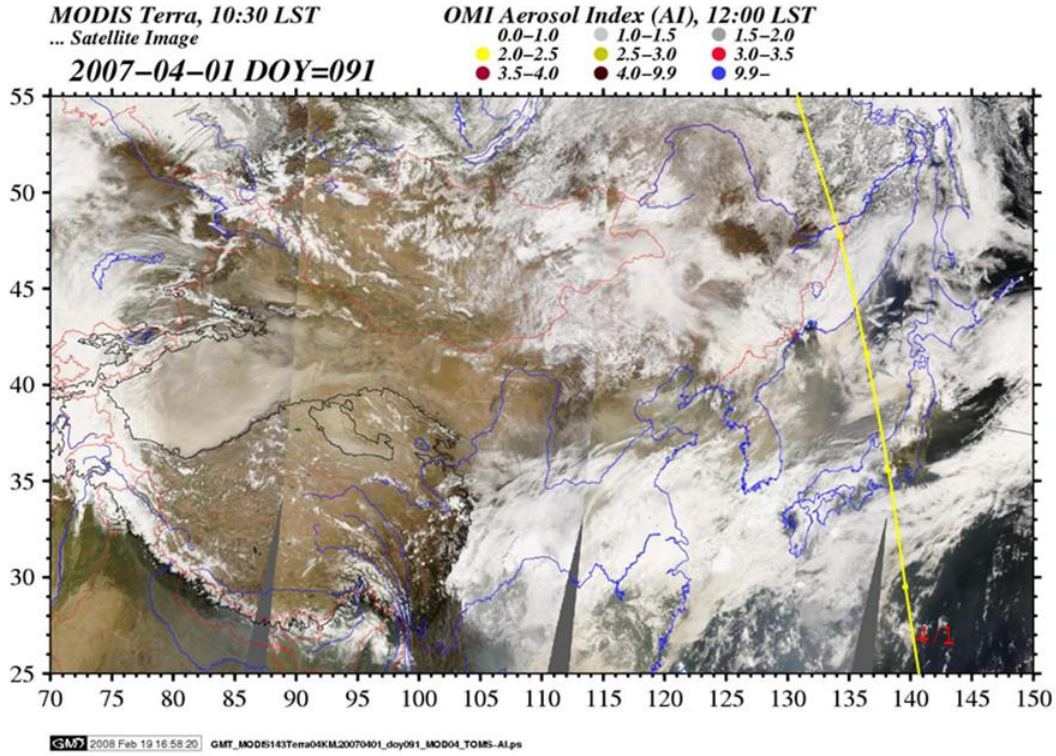

Figure 4.19 Same as Figure 4.5, except for April 1, 2007.

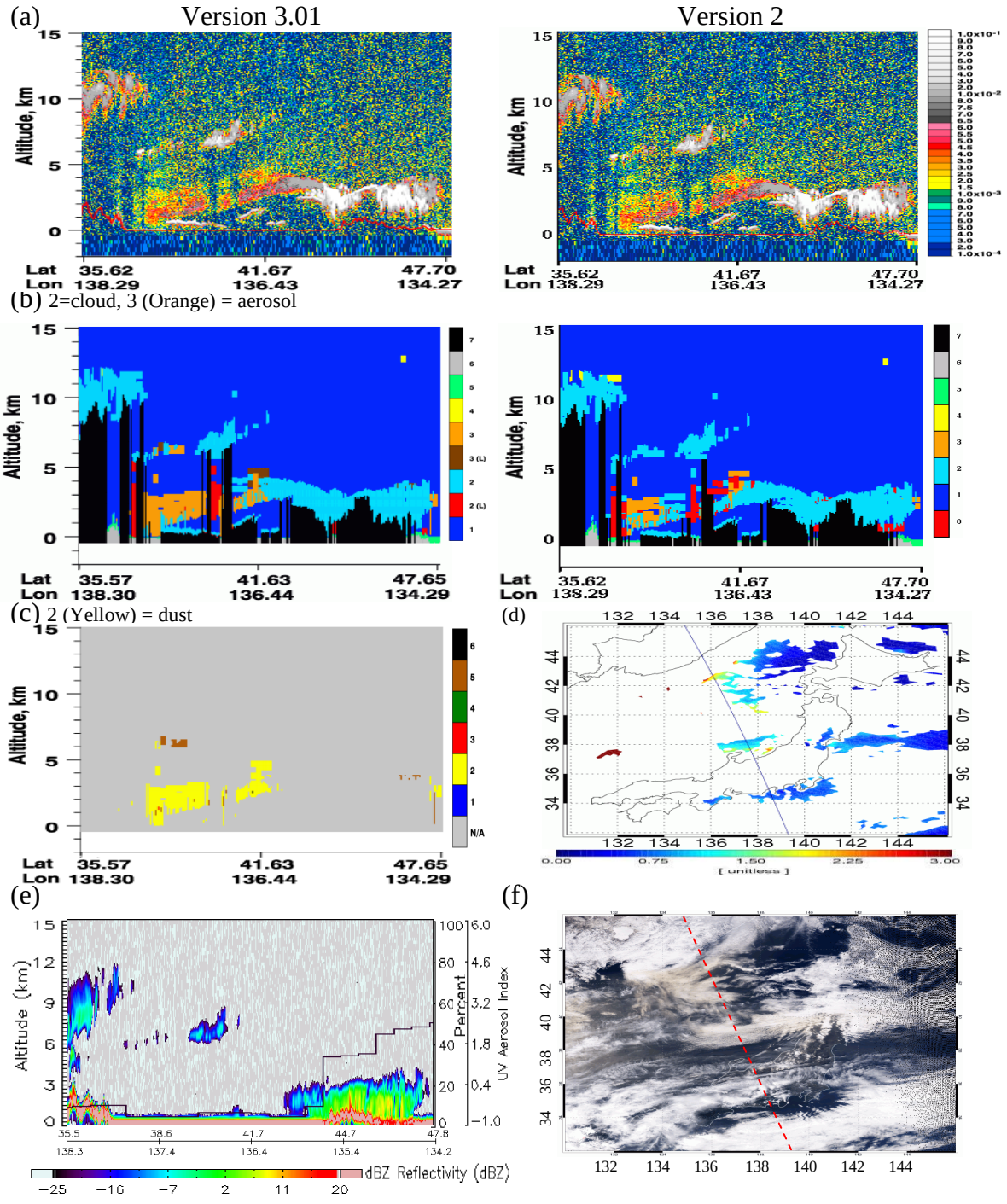

Figure 4.20 Same as Figure 4.6, except for Japan on April 1, 2007.

(a) Blue: δ_p, Red: δ_v, Black: AOD, Violet: χ_p

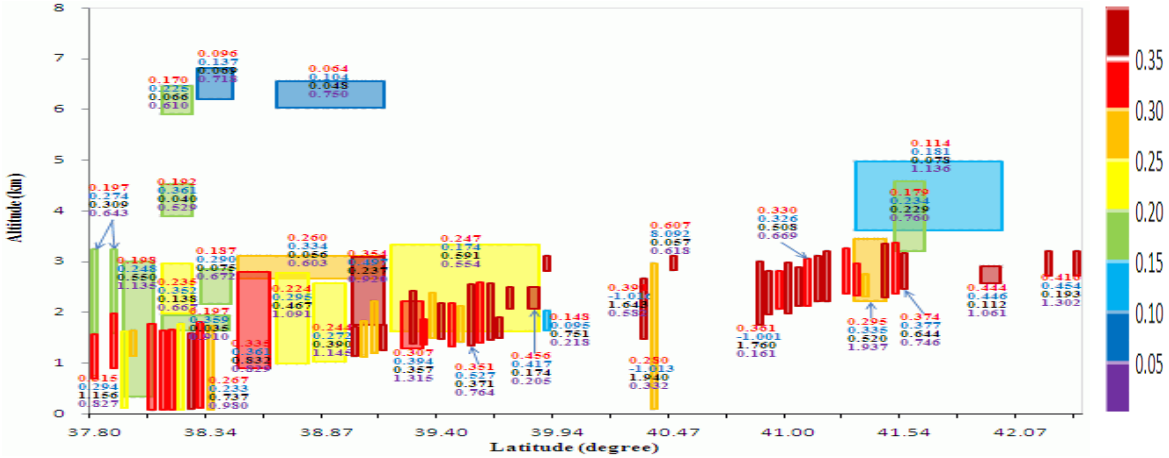

(b) Blue: δ_p, Red: δ_v, Black: AOD, Violet: χ_p

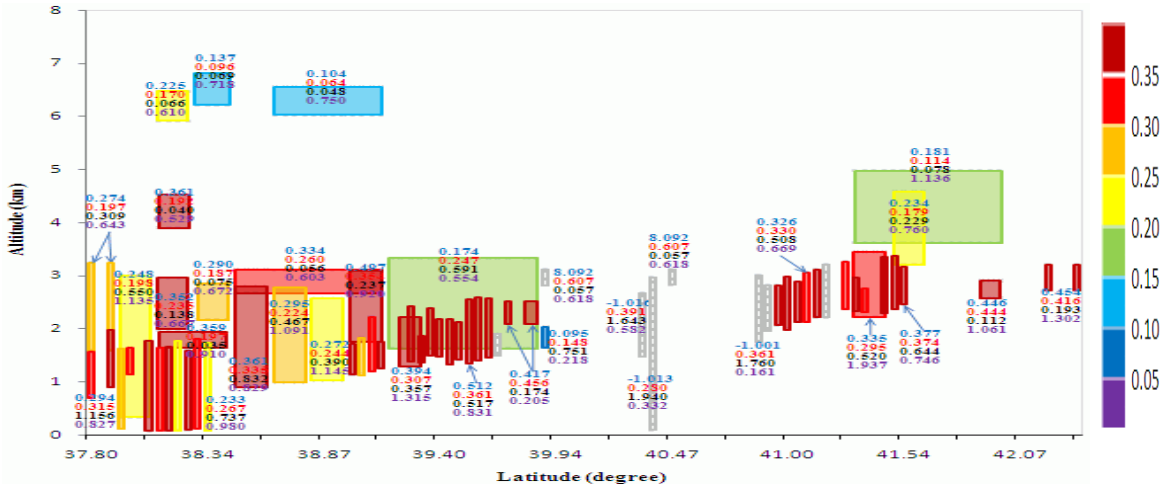

(c) Black: AOD CALIPSO, blue: Deep Blue AOD, Red: AOD MODIS-Aqua

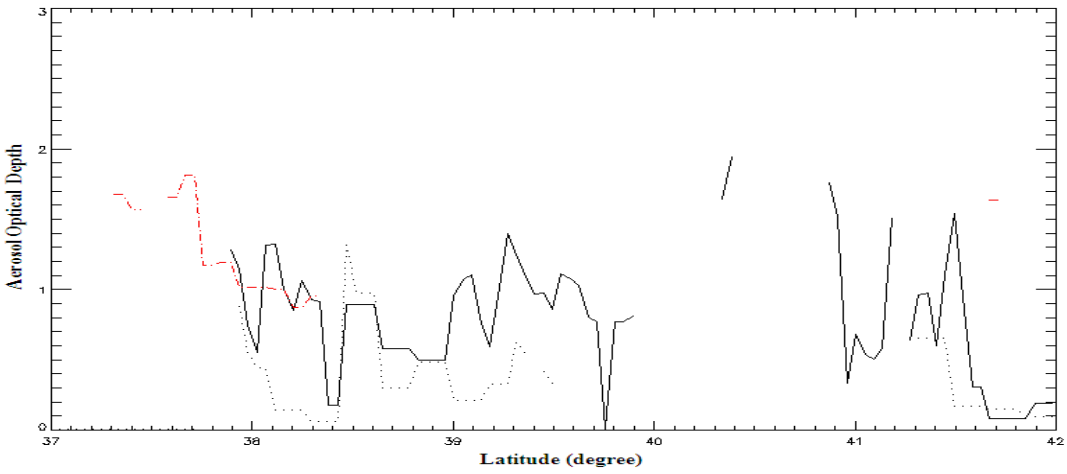

Figure 4.21 Same as Figure 4.7, except for Japan on April 1, 2007.

(a)

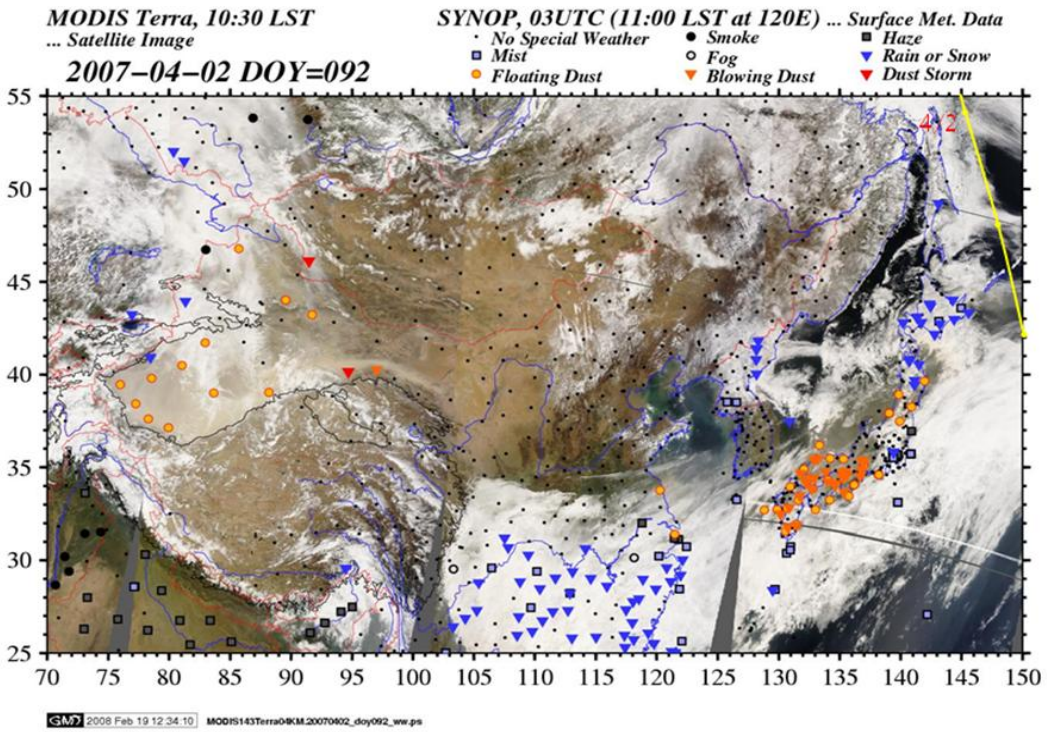

(b)

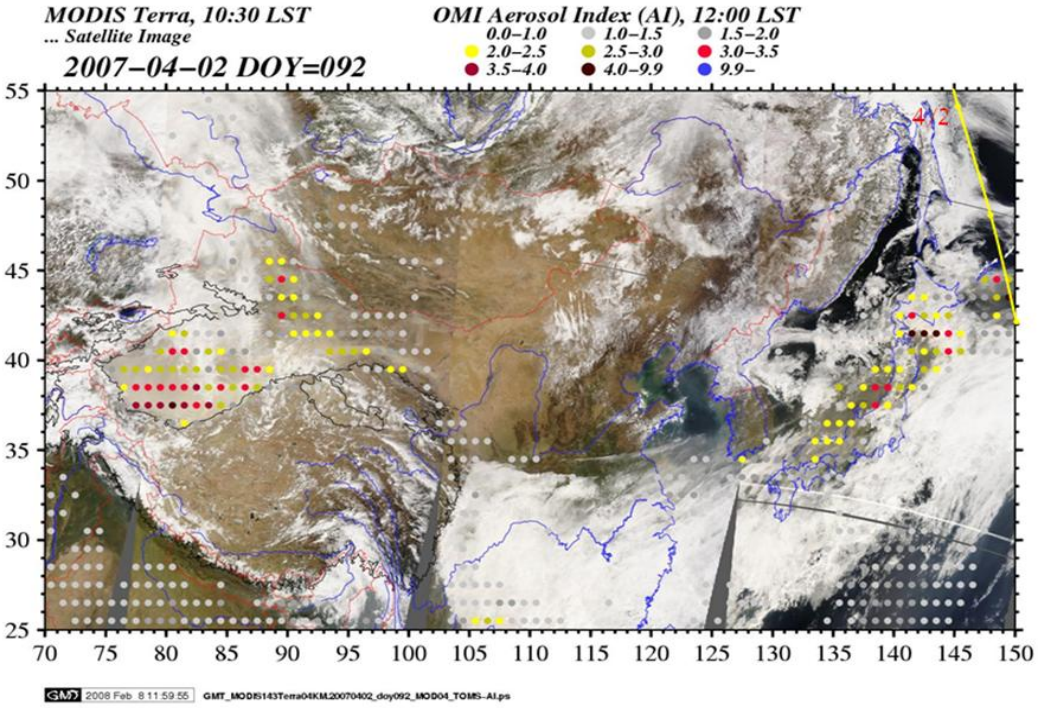

Figure 4.22 Same as Figure 4.5, except for April 2, 2007.

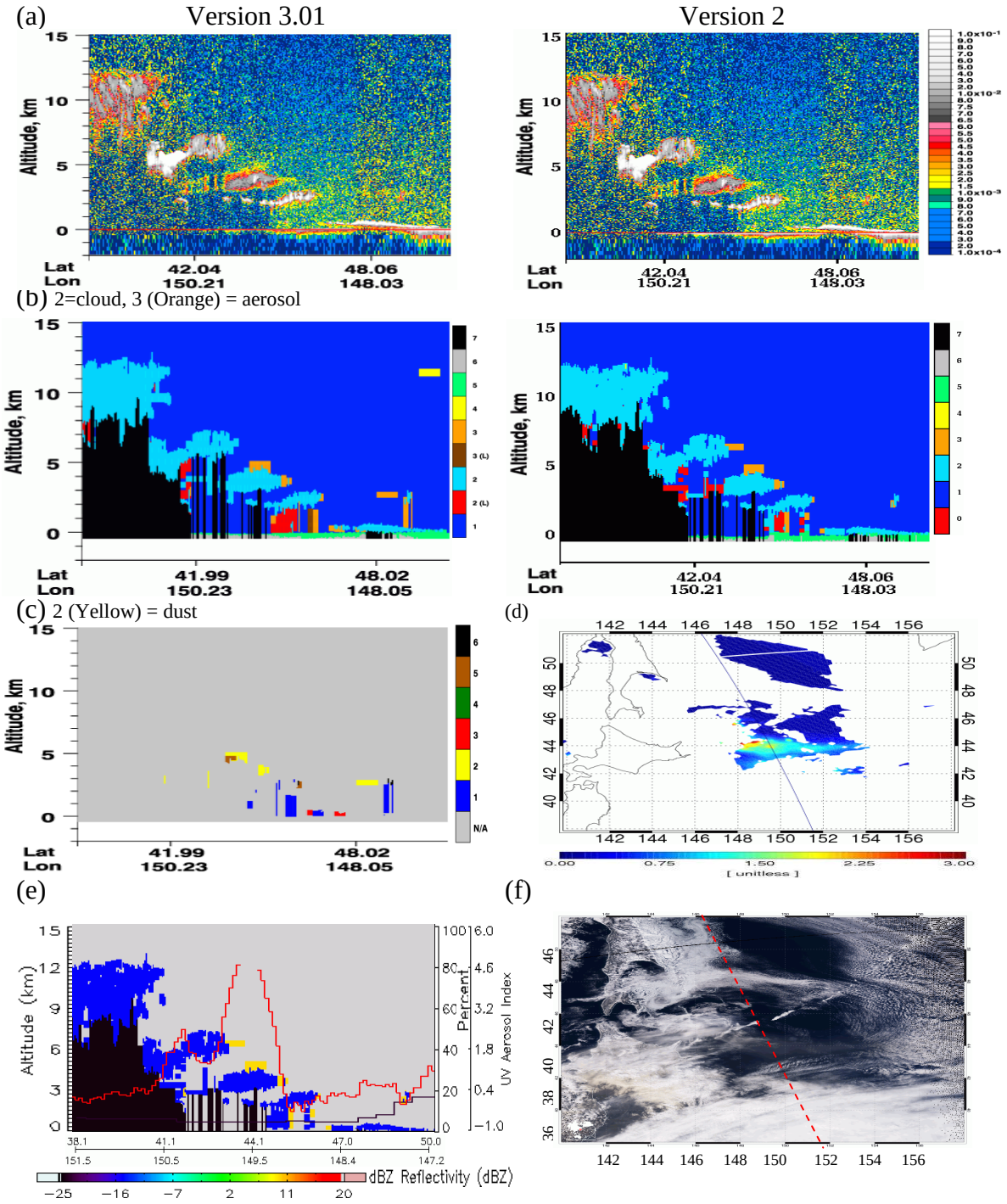

Figure 4.23 Same as Figure 4.6, except for the western Pacific Ocean on April 2, 2007.

. (a) Blue: δ_p, Red: δ_v, Black: AOD, Violet: χ_p

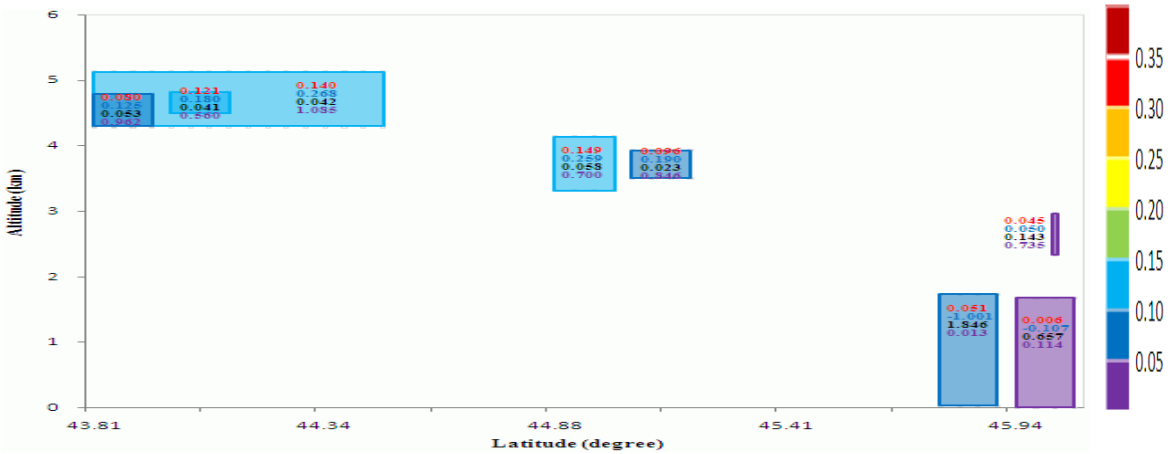

(b) Blue: δ_p, Red: δ_v, Black: AOD, Violet: χ_p

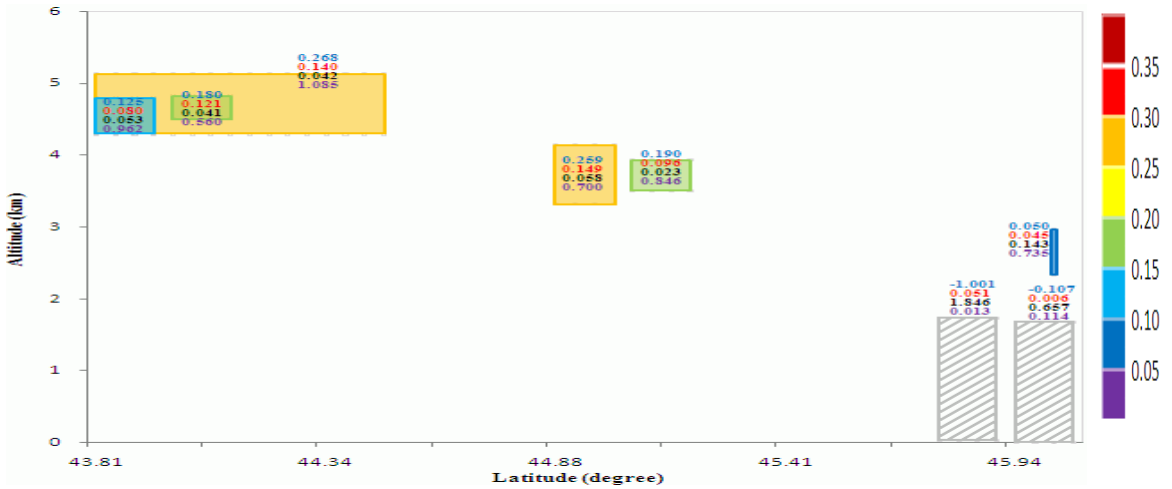

(c) Black: AOD CALIPSO, blue: Deep Blue AOD, Red: AOD MODIS-Aqua

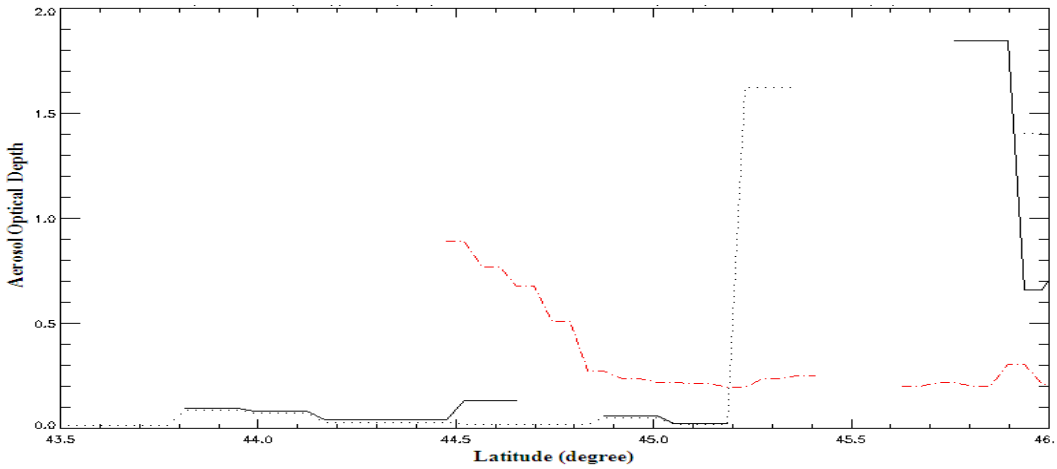

Figure 4.24 Same as Figure 4.7, except for the western Pacific Ocean on April 2, 2007.

(a) Dalanzadgad (longitude:104.42°, latitude: 43.58°)

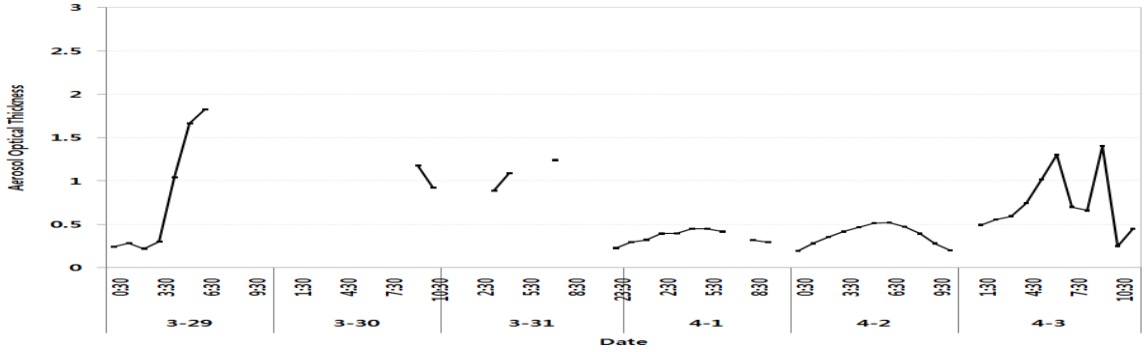

(b) XiangHe (longitude: 116.96°, latitude: 39.75°)

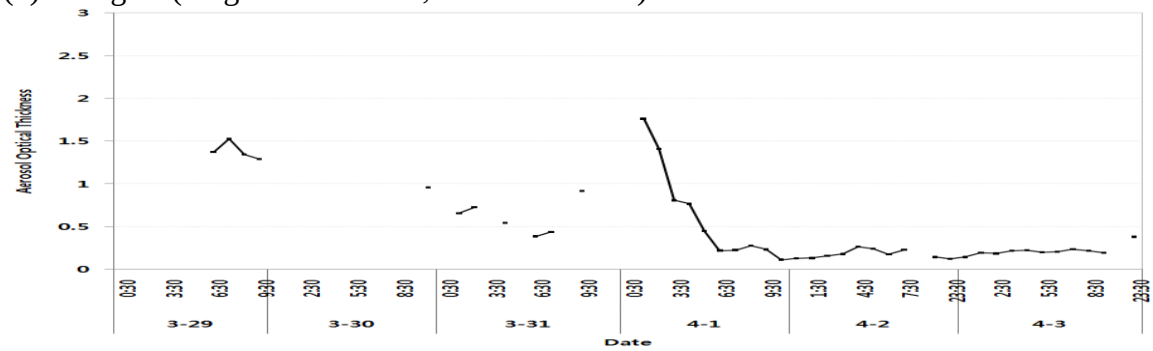

(c) Gwangju (longitude: 126.84°, latitude: 35.23°)

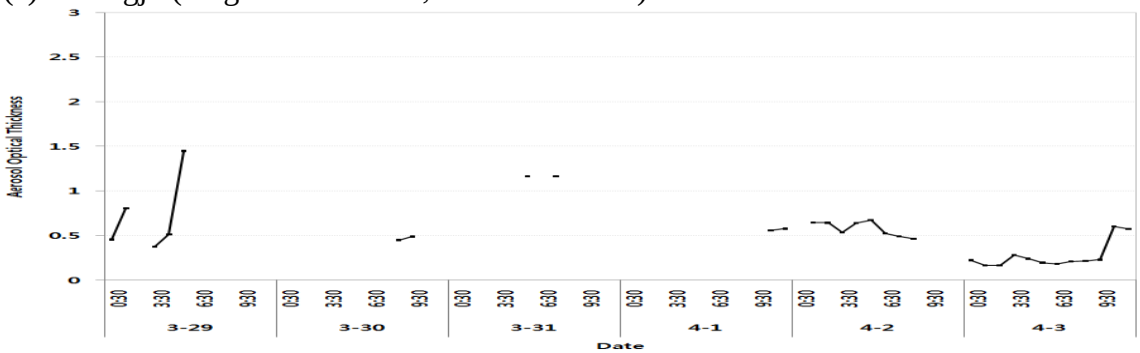

(d) Shirahama (longitude: 135.36°, latitude: 33.69°)

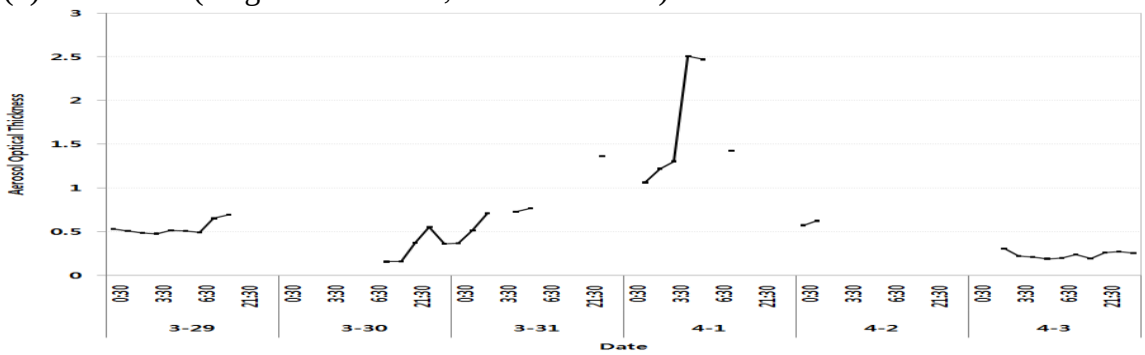

Figure 4.25 Aerosol optical depth from AERONET over (a) Dalanzadgad and (b) XiangHe in China, (c) Gwangju in Korea, and (d) Shirahama in Japan for spring 2007.

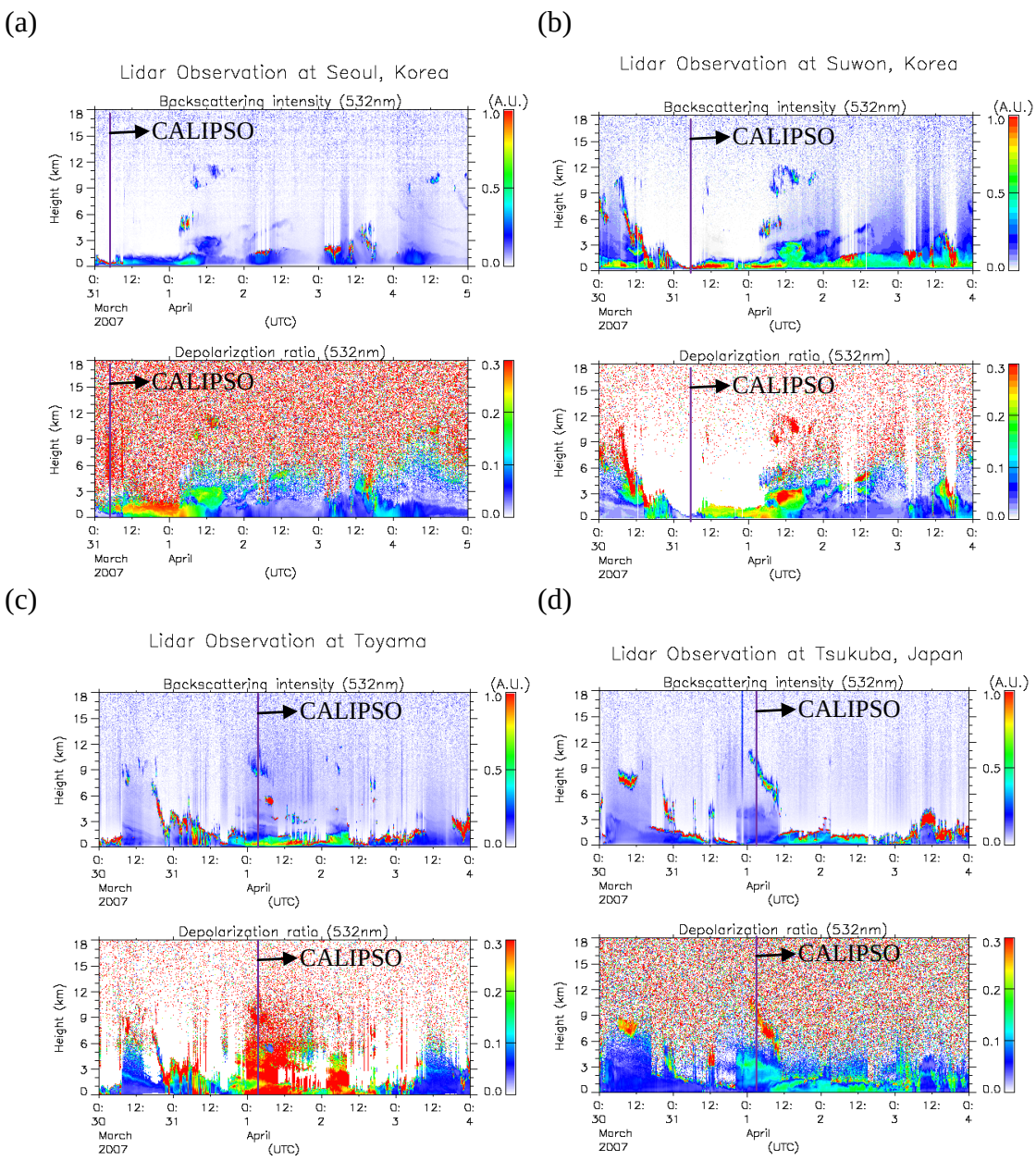

Figure 4.26 Backscattered signal and depolarization ratio at 532 nm over (a) Seoul and (b) Suwon in Korea, over Toyama (c) and Tsukuba (d) in Japan distributed by National Institute for Environmental Studies (NIES) Lidar network (http://www-lidar.nies.go.jp/).

Table 4.2 Comparative Summary of Dust Properties Retrieved from CALIPSO and the ground-based lidars for mid-range transported dust events during March 30-April 2, 2007.

Date	03/30	03/31		04/01		04/02
	CALIOP	CALIOP	Ground	CALIOP	Ground	CALIOP
Location (degree)	Gobi desert (38N, 110E-40N, 109E)	East China (35N, 125E-42N, 123E)	Seoul (Korea) 37.3N,126.6E	Japan (38N,138E-42N, 136E)	Toyama (Japan) 36.7N,137.1E	East Japan (44N,150E-45N,149E)
Vertical extent (km)	1.14-6.26	0.06~6.17	0~2	0.06~6.8	0~1.5	3.33~5.13
$\delta_{v,layer}$ (average)	0.143-0.478 (0.238)	0.12~0.486 (0.237)		0.114~0.501 (0.261)		0.096~0.149 (0.135)
$\delta_{p,layer}$ (average)	0.178-1.226 (0.385)	0.155-0.873 (0.364)	Max 0.3	0.174-0.89 (0.321)	Max 0.3	0.19-0.268 (0.253)
$\chi_{p,layer}$ (average)	0.454-4.802 (1.615)	0.338-2.508 (1.026)		0.205-1.937 (0.866)		0.7-1.085 (0.981)
Aerosol optical depth	0.032-2.496 (0.263)	0.01-2.098 (0.44)		0.035-1.236 (0.335)		0.023-0.058 (0.042)

- $\delta_{v,layer}$: The layer integrated volume depolarization ratio
- $\delta_{p,layer}$: The layer integrated particulate depolarization ratio
- $\chi_{p,layer}$: The layer integrated particulate color ratio

We found that during mid-range transport, there were many instances of dust layers with high values of the volume and particulate depolarization ratios observed by CALIPSO as well as ground-based lidars. For instance, Figure 4.18(a) and (b) show that the values of volume depolarization ratio in the 1-3 km dust layer are in the range of 0.12 to 0.486, with an average value of 0.237, and $\delta_{p,\,layer}$ has high average values (~ 0.364). The AOD of this layer retrieved by CALIPSO was also large (maximum 2.508). These values are similar to those observed over the Taklamakan and Gobi Deserts. At the same time, we found transported dust layers with much lower $\delta_{v,layer}$ values (~0.1-0.15), e.g., the case shown in Figure 4.24(a). Thus, aged dust can cause either low or high depolarization. Examining the factors controlling these changes in volume and particulate depolarization ratios has the potential to provide new insights on how dust microphysical

properties evolve during transport, providing important information for improved treatments of dust in regional and global models.

4.3.2.2 Case of a Long-range Transport

In addition to the mid-range transport March 30 case, CALIPSO detected another mid-range transport event of Asian dust on May 10, 2007, which then was transported across the Pacific. At the location 34.067˚N, 147.659˚W with the altitudes 5000–7000 m, the backward and forward trajectories simulated for this case are shown in Figure 4.27.

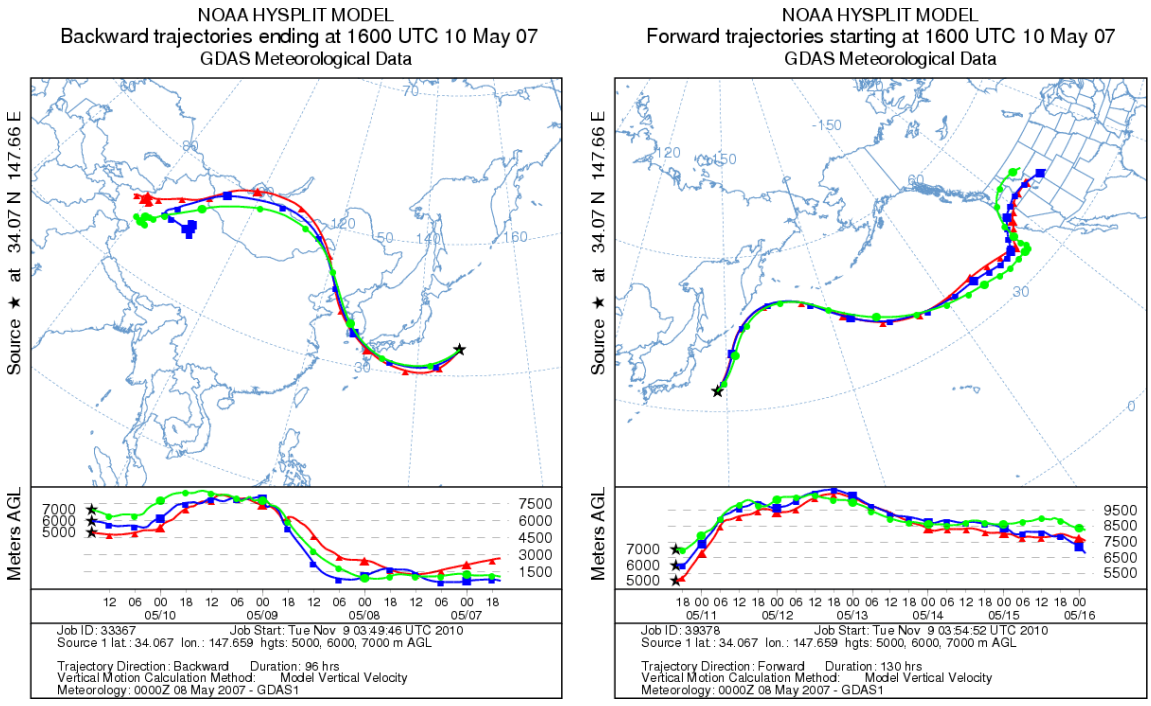

Figure 4.27 Backward and forward trajectories started at UTC 16:00 on May 10, 2007, at a location 34.067˚N and 147.659˚W and at altitude of 5000, 6000, and 7000 meters, produced with the NOAA HYSPLIT model.

The trajectories indicate that the dust event started in the Taklamakan Desert on May 7, 2007 and passed over the eastern Japan on May 10, 2007 and then moved to the western United States on May 15, 2007. The trajectories suggest the likely route of the long-range transport of this Asian dust episode.

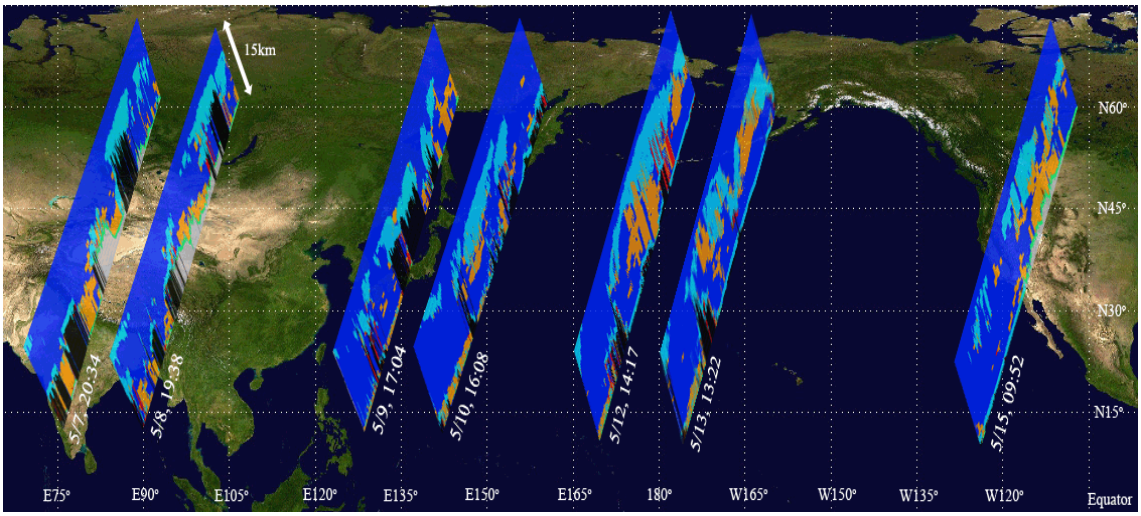

Figure 4.28 A reconstructed long-range transport dust event originating in the Taklamakan Desert on May 7, 2007 and then transported to the western United States. Brown color denotes dust plumes.

Figure 4.28 shows the reconstructed long-range transported dust event with the nighttime VFM CALIPSO images. In this case, daytime CALIPSO data have too low dust signals and cannot be used for dust transport analyses. Examination of Figure 4.28 shows dust layers at about 5–6 km, and the altitudes of the layers did not change significantly during the long-range transport.

The results of CALIPSO data analyses for the long-range transported dust are shown in Figures 4.29-4.34. Again these figures are organized similar to Figures 4.10-4.11 and 4.29-34 to facilitate intercomparison.

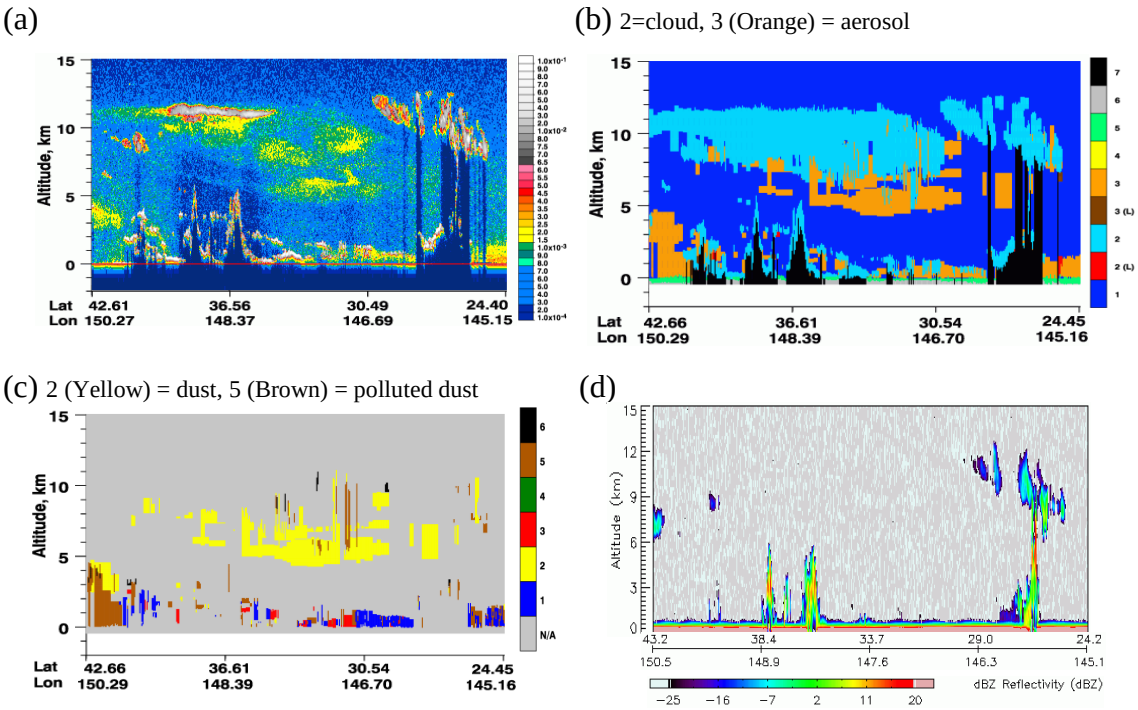

Figure 4.29 Same as Figure 4.10, except for the western Pacific Ocean on May 10, 2007.

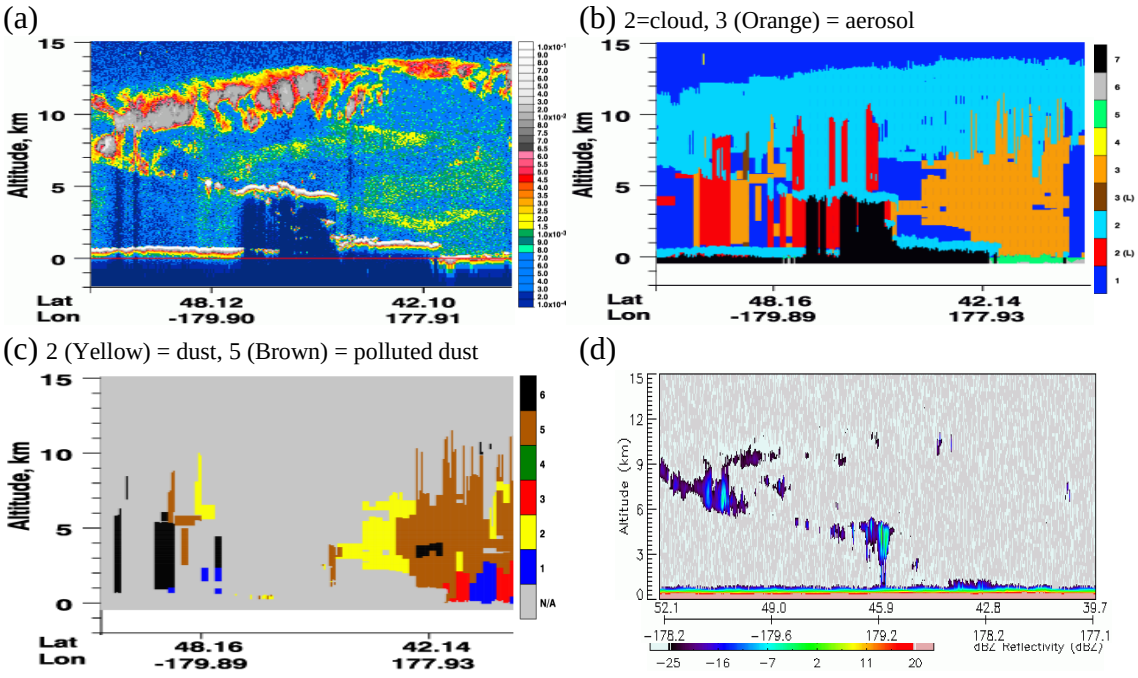

Figure 4.30 Same as Figure 4.10, except for the mid-Pacific Ocean on May 12, 2007.

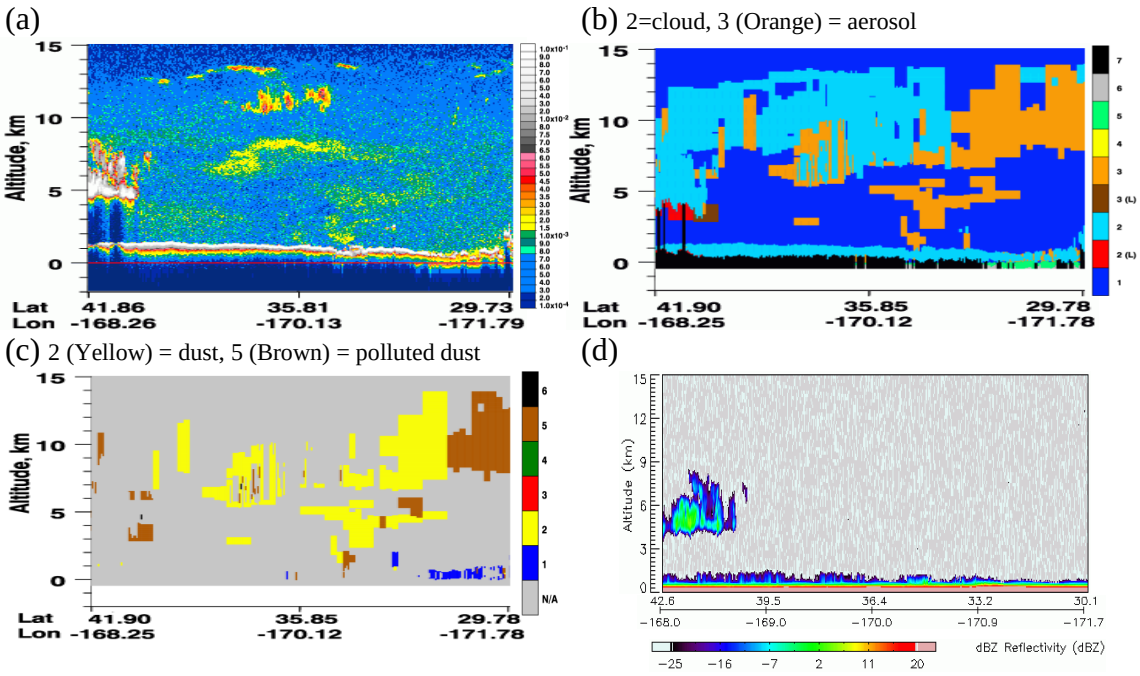

Figure 4.31 Same as Figure 4.10, except for the mid-Pacific Ocean on May 13, 2007.

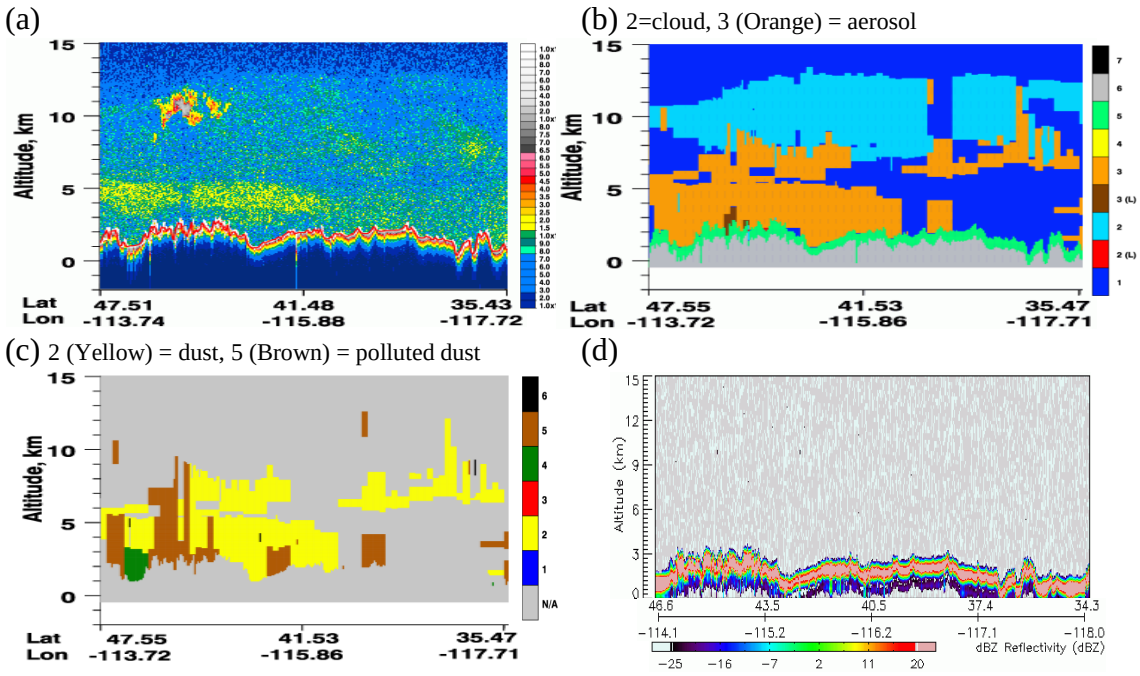

Figure 4.32 Same as Figure 4.10, except for the United States on May 15, 2007.

Figures 4.33 (left side panels) display the horizontal and vertical distribution of $\delta_{p,layer}$ for the long-range transport cases. Interestingly, the high $\delta_{p,\ layer}$ above 0.3 are observed not only in the Taklamakan Desert but also in Japan. This is very similar to the distribution of $\delta_{p,\ layer}$ in the mid-range transport case. The gray shaded bars in Figure 4.33(2) denote the negative values of $\delta_{p,layer.}$ The large number of gray shaded bars indicates that problems still remain in $\delta_{p,layer}$ in the level 2 version 3.01 CALIOP under mixed conditions of dust and clouds. Figures 4.33 (right side panels) show that the values of $\delta_{v,layer}$ were smaller far from the source areas during long-range transport, while the particulate depolarization ratio still remained high even when the dust reached the United States.

Figure 4.34 displays the distribution of AODs for the long-range transported dust (May 7-15, 2007). Solid black lines and dotted blue lines represent AODs from CALIPSO version 3.01 and version 2 data, respectively, and blue and red dotted lines show Deep Blue AOD and standard AOD from MOIDS-Aqua, respectively. The AODs are very low compared to those of mid-range transport.

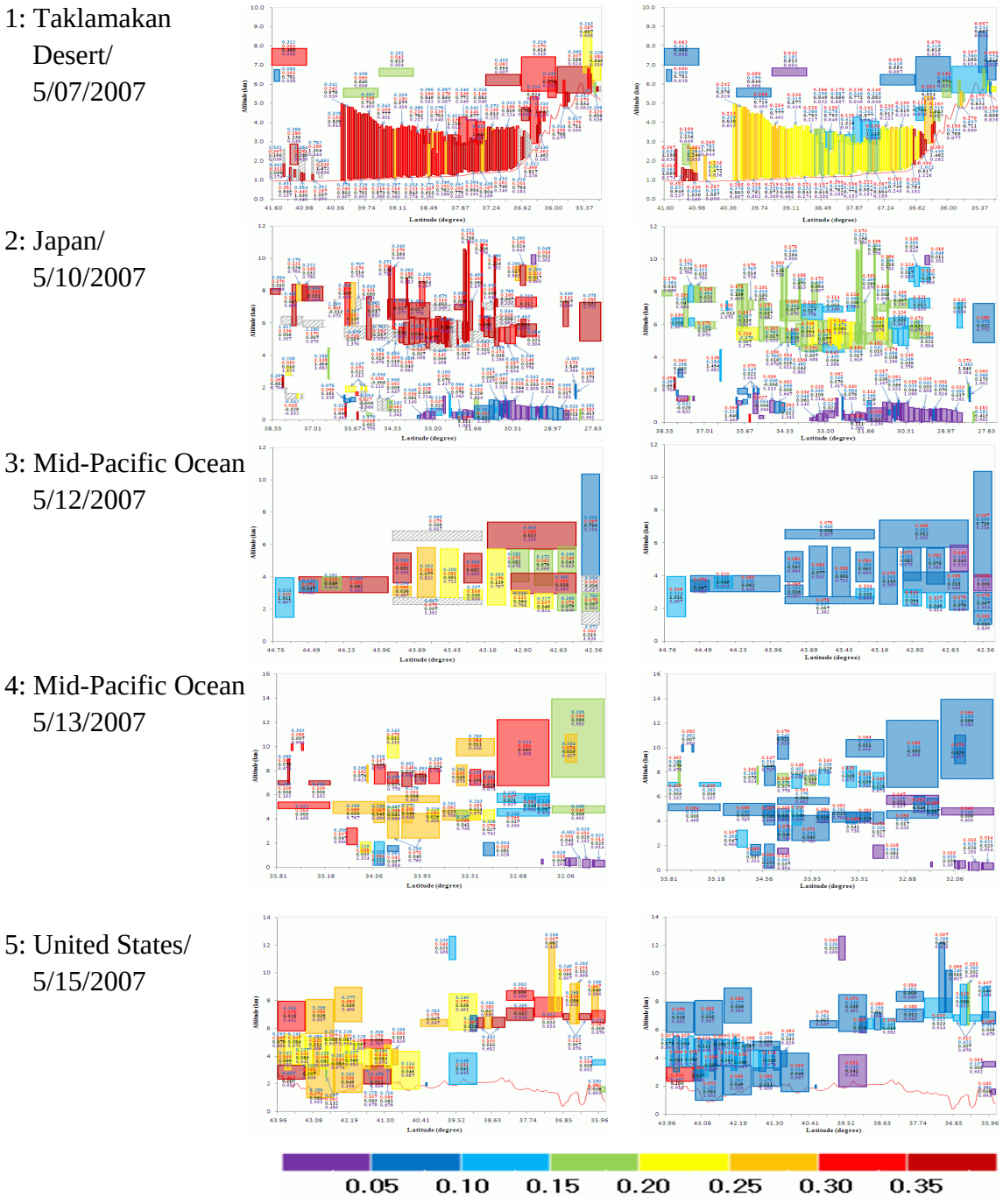

Figure 4.33 Distributions of layer-integrated particulate depolarization ratio (left side panels) and layer-integrated volume depolarization ratio (right side panels) for the long-range transport from May 7, 2007 to May 15, 2007.

(a) May 7, 2007

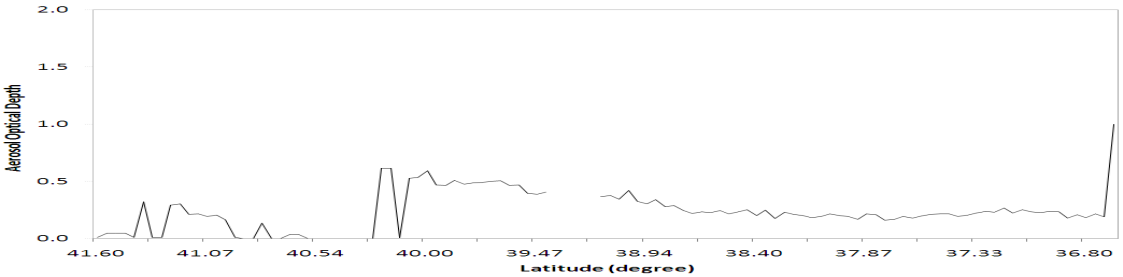

(b) May 10, 2007

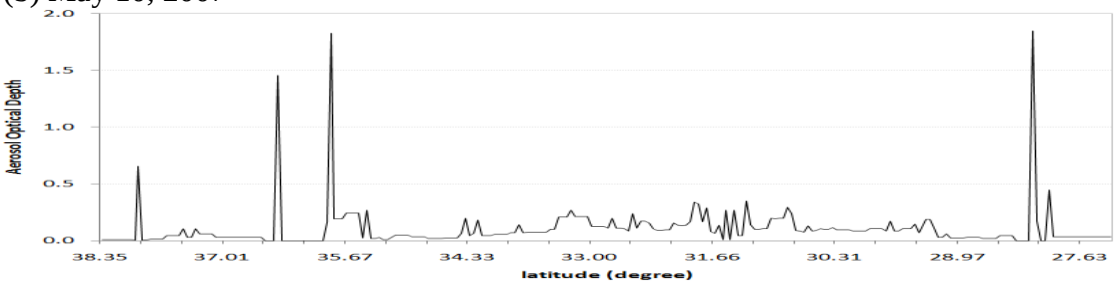

(c) May 12, 2007

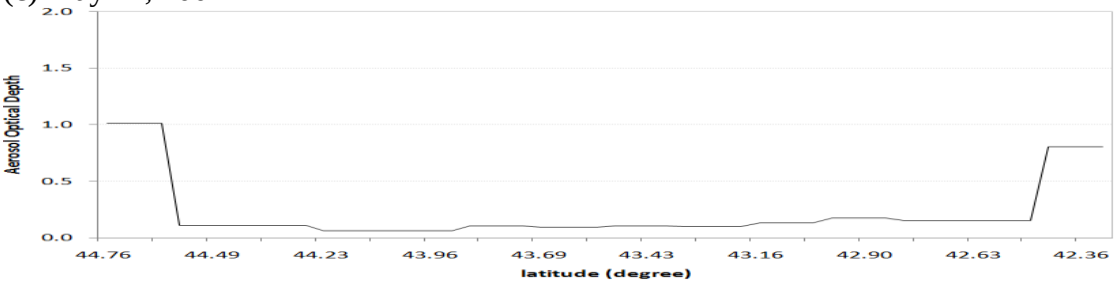

(d) May 13, 2007

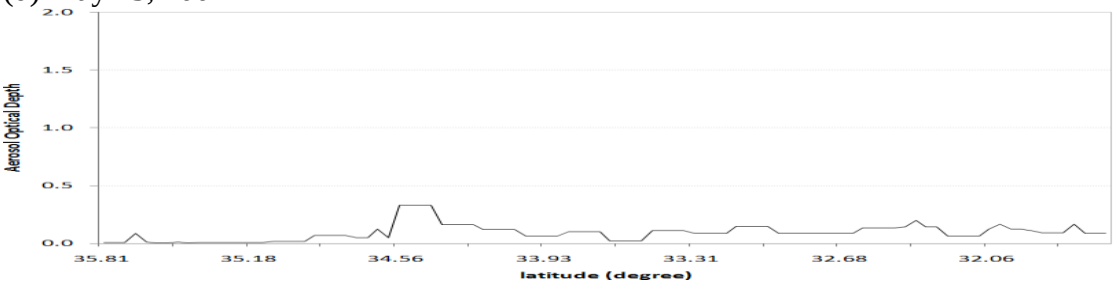

(e) May 15, 2007

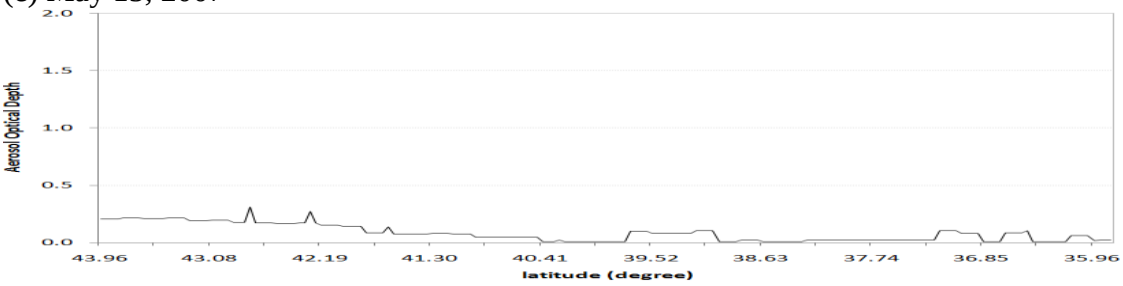

Figure 4.34 CALIPSO AOD for the cases of long-range transported dust from 7 to 15 May 2007.

The summary of optical properties of long-range transported Asian dust is given in Table 4.3 which may be compared to results in Table 4.1 and Table 4.2. In the table, the vertical extent of dust varies from 1.018 km to 13.95 km. The high height is related to the transportation of Asian dust over the Pacific Ocean by the westerly jet stream. The low values of $\delta_{v,layer}$ indicate the low concentration of dust particles.

Table 4.3 Comparative Summary of Dust Properties Retrieved from CALIPSO for long-range transported dust events during May 7-May 15, 2007 (Dust properties means that data retrieved with the lidar ratio of 40 sr).

Date	5/7	5/10	5/12	5/13	5/15
Location (degree)	Taklamakan Desert (37.0N,82.06E-41.6N,83.5E)	Eastern Japan (29N, 146E-36N, 148E)	Mid-Pacific Ocean (43N,178E-45N, 179E)	Mid-Pacific Ocean (32N, 171W-36N, 170W)	United States (36N,118W-40N,116W)
Vertical extent (km)	1.018-7.853	4.32-11.14	2.04-7.4	1.26-13.95	1.44-12.16
$\delta_{v,layer}$ (mean)	0.042-0.440 (0.167)	0.114-0.319 (0.166)	0.069-0.12 (0.083)	0.046-0.192 (0.081)	0.04-0.151 (0.088)
$\delta_{p,layer}$ (mean)	0.088-1.264 (0.364)	0.287-1.439 (0.605)	0.181-0.957 (0.487)	0.145-0.423 (0.267)	0.18-0.442 (0.311)
$\chi_{p,layer}$ (mean)	0.466-2.246 (0.786)	0.62-1.948 (1.071)	0.448-1.392 (0.898)	0.31-1.458 (0.731)	0.356-0.987 (0.555)
Aerosol optical depth	0.006-0.613 (0.267)	0.003-0.306 (0.031)	0.007-0.119 (0.038)	0.005-0.079 (0.026)	0.006-0.102 (0.023)

- $\delta_{v,layer}$: The layer integrated volume depolarization ratio
- $\delta_{p,layer}$: The layer integrated particulate depolarization ratio
- $\chi_{p,layer}$: The layer integrated particulate color ratio

The developed methodology was applied to the entire CALIPSO data set from 2007-2010. Examples of Asian dust events reconstructed in different years are shown in Figure 4.35, 4.36, and 4.37. Figure 4.35 shows a dust event originating in the Gobi Desert on May 28, 2008 and its transport to Japan. Figure 4.36 presents an example of a Gobi dust event that was transported across the Pacific Ocean in 2009. Figure 4.37 shows

another example of inter-continental transport of Asian dust: dust event originating in the Gobi Desert on 19 March 2010. This dust event reached the western United States.

Overall, this type of analyses of the CALIPSO multi-year record provided statistically representative information of vertical profiles of Asian dust and its properties as discussed below. The summary of optical properties of transported Asian dust is given in Table A.1, A.2, and A.3, respectively.

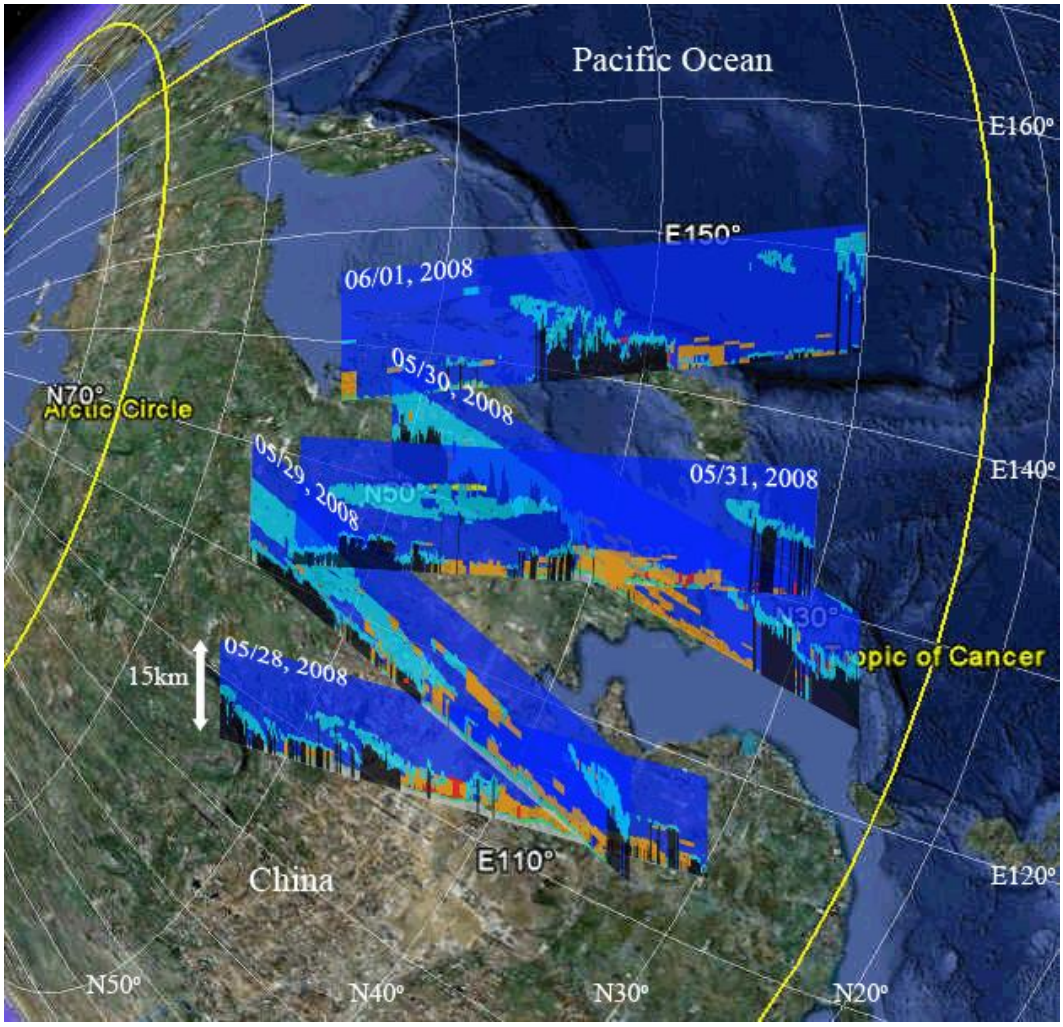

Figure 4.35 Reconstructed transport of a dust event originating in the Gobi Desert on May 28, 2008 and transported to Japan. Brown color denotes dust plumes.

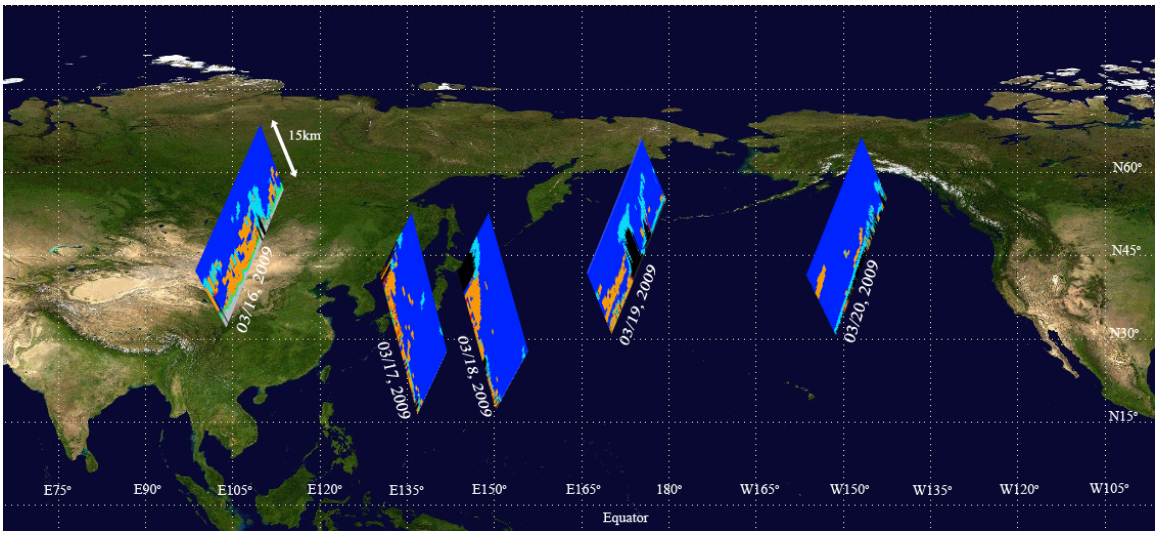

Figure 4.36 Reconstructed transport of a dust event originating in the Gobi Desert on March 16, 2009 and transported over the Pacific Ocean. Brown color denotes dust plumes.

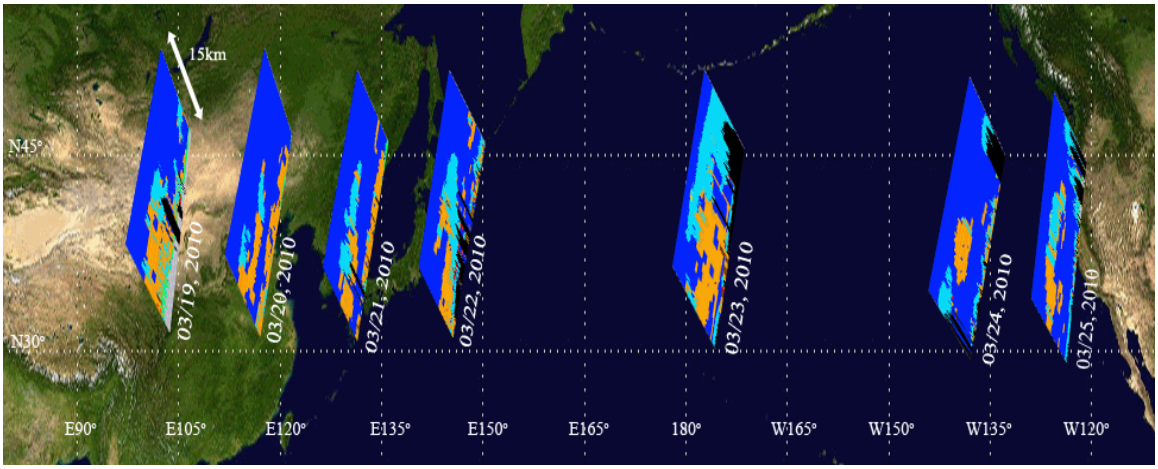

Figure 4.37 Reconstructed transport of a dust event originating in the Gobi Desert on March 19, 2010 and transported to the western United States. Brown color denotes dust plumes.

4.3.3 Analysis of the Spring Season of 2007

4.3.3.1 Vertical Structure of Asian Dust Plumes

Existence of two different synoptic meteorological conditions controlling dust events in two major sources in East Asia suggests that vertical structures of dust plumes will most likely differ between the Taklamakan and the Gobi. This also may lead to different vertical profiles of mid- and long-range transported Asian dust. Since the vertical distribution of dust plays a major role in the radiative forcing and heating/cooling rates (Sokolik et al., 2002, Guan et al., 2010), we performed a detailed analysis of vertical dust profiles observed by CALIOP, comparing different source regions (i.e., Taklamakan vs. Gobi) and transport routes. One goal was to determine characteristic vertical profiles of Asian dust plumes for the modeling of dust radiative forcing.

Figure 4.38 presents the mean top altitude of dust layers of selected Asian dust events, including dust episodes in sources and in mid-range and long-range transported dust cases. Examination of these data shows that there are some specific differences in mean top altitudes between the mid- and long-range transported events, i.e., below and above the 6 km altitude.

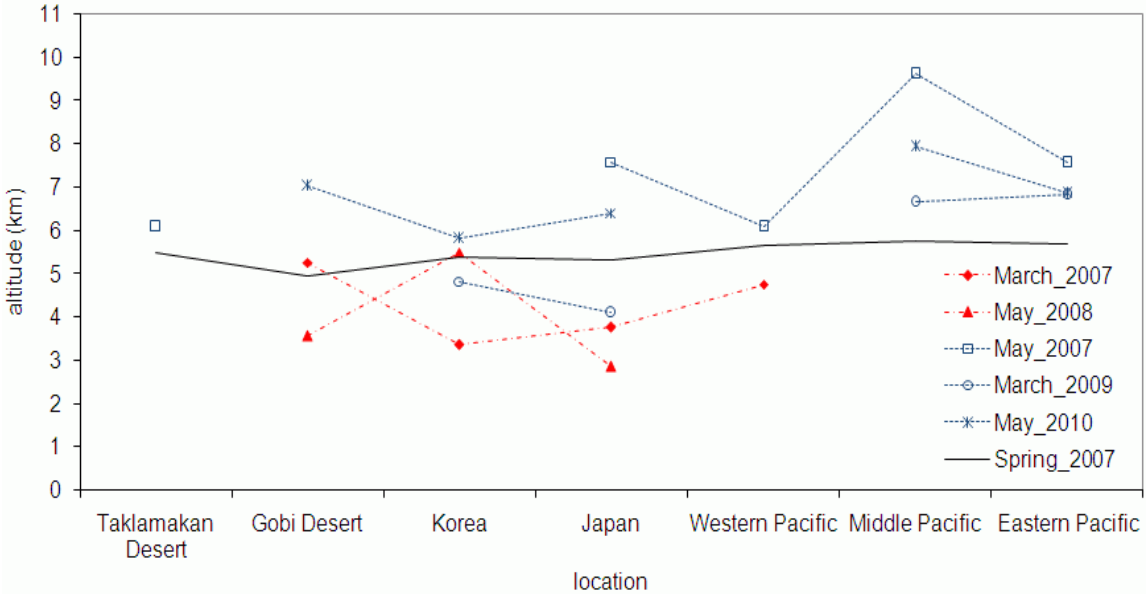

Figure 4.38 Mean top altitudes of Asian dust plumes for two mid-range transport events (March 30-April 2, 2007, and May 28-June 1, 2008), three long-range transport events (May 7-15, 2007, March 17-20, 2009, and March 19-25, 2010), and dust layers observed in 2007 spring in seven areas: Taklamakan Desert (36°-40°N, 78°-90°W), Gobi Desert (38°-49°N, 94°-116°W), Korea (30°-40°N, 124°-132°W), Japan (30°-42°N, 132°-146°W), Western Pacific Ocean (28°-40°N, 150°-180°W), Mid-Pacific Ocean (28°-48°N, 180°-140°E), and Eastern Pacific Ocean (28°-48°N, 140°-120°E)).

In order to select profiles for radiative transfer modeling, we examined in more detail three regions: the source region, including the Taklamakan and Gobi Desert; mid-range transport region, including Korea and Japan; and long-range transport region (the Pacific Ocean). Figure 4.39 displays the vertical distributions of the representative dust cases in these regions. In the source regions, the dust layer with the altitude of 9 km was selected as representative. For transported events, we selected two dust layers with the altitude of 0-3 km and 6-10 km, which represent the mid-range transport (0-3 km) and long-range transport (6-10 km) over Korea, respectively. For the inter-continental transport across the Pacific Ocean, a dust layer with the altitude of 6-10 km was selected.

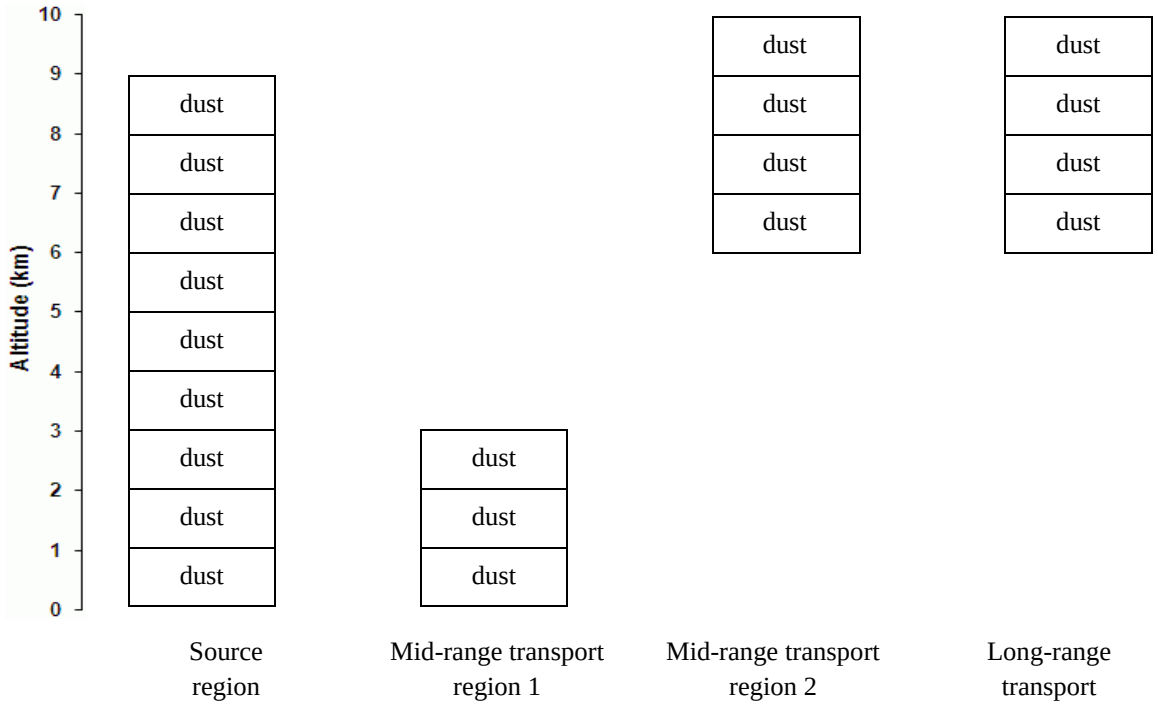

Figure 4.39 Schematic representation of vertical profiles of Asian dust selected for radiative forcing modeling.

4.3.3.2 Characterization of Aerosol Optical Depth

The value of AOD is an important parameter for the calculation of the dust radiative forcing. In addition, the vertical distribution of AOD enables more exact computation of heating/cooling rates of dust. Accordingly, this section investigates both the vertical distribution of CALIPSO AODs and the mean AODs for the mid- and long-range transported Asian dust, focusing on the seven areas introduced above. Figure 4.40 presents AOD from CALIPSO version 3.01 data. The mean AODs of long-range transported Asian dust (May 7-15, 2007) for each orbit are very similar to those observed over the seven areas in the Spring of 2007.

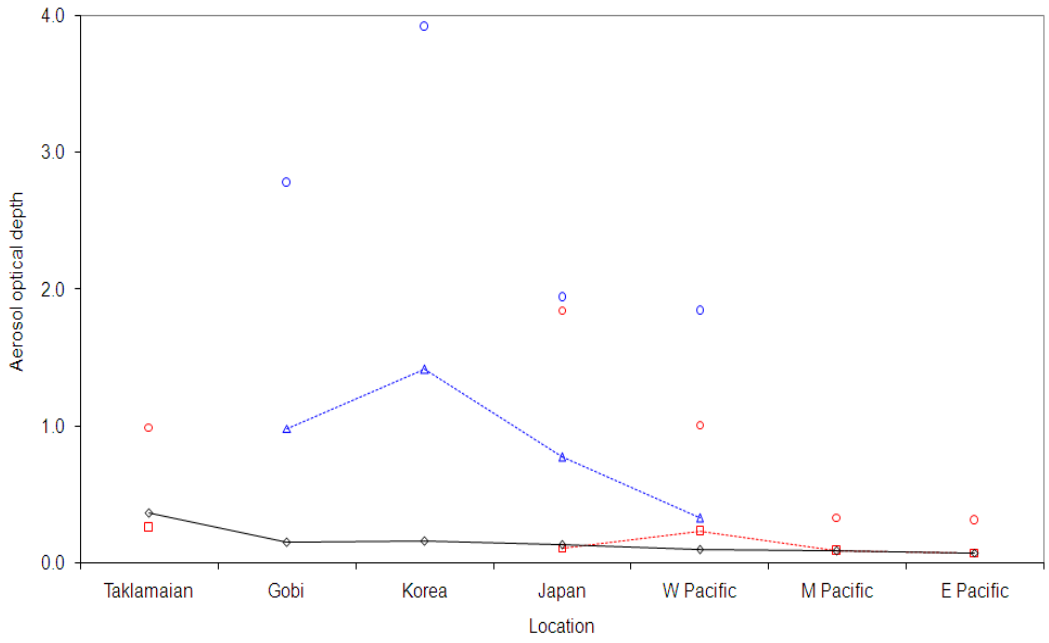

Figure 4.40 Mean aerosol optical depths (blue and red lines) and maximum AODs (blue and red circles) of each orbit for the mid- (blue), long-range (red) transported dust and mean AODs (black diamond) in seven areas in the Spring of 2007 (March-May).

The AODs of the mid-range transported dust events are higher than the long-range transported dust. For each dust event observed by CALIPSO, AODs from CALIPSO were compared against MODIS-Aqua AOD. As discussed in Chapter 2, version 3.01 CALIPSO AOD data were significantly improved. Better agreement of version 3.01 data with the Deep Blue AOD and AOD from MODIS-Aqua is apparent, although the variation of AOD in version 3.01 is considerably high compared to AODs from MODIS-Aqua. The AODs between the latitude 38.4° and 39.7° on March 30, 2007 show values above 1 in CALIPSO and MODIS-Aqua, and on March 31 the AODs along the CALIPSO orbit are above 1 with a maximum value of about 4. After the dust passed the Korean region, AODs were decreasing continuously, which is similar to the pattern of the mean AOD shown in Figure 4.40.

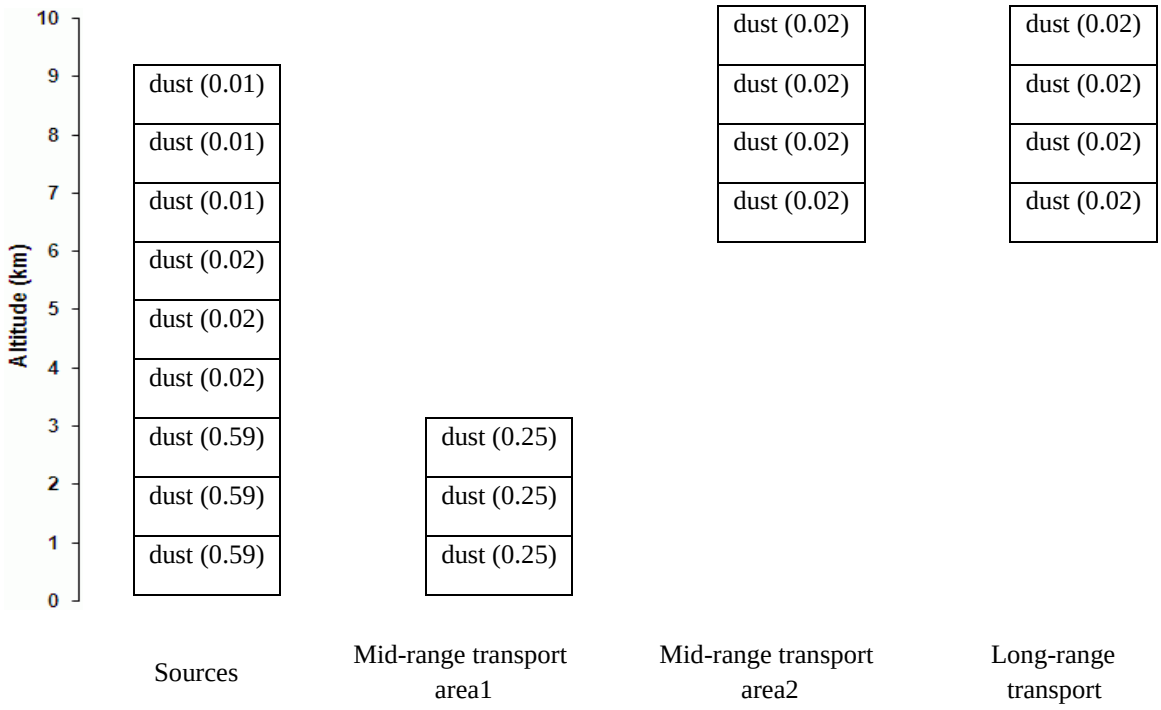

Figure 4.41 Aerosol optical depth selected for vertical profiles of dust events shown in Figure 4.39.

The AOD values, corresponding to the representative vertical distribution of transported dust shown in Figure 4.39, are presented in Figure 4.41, and these values will be used in the calculation of dust radiative forcing and heating/cooling rates presented in Section 4.3.6.

4.3.3.3 Characterization of Optical Properties of Asian Dust

In this study, the optical properties of dust particles that are classified as dust by the CALIPSO algorithm are averaged over the considered seven regions for the Spring of 2007. The CALIPSO lidar ratio used in the retrievals was 40 sr. The values above 3 or below 0 were not considered in the calculation of average color ratio, particulate and

volume depolarization ratios because those values are unrealistic. In Figure 4.42, the mean particular color ratio (black cross line) varies from around 0.9 in the source regions to around 0.7 in the remote areas, and the mean particulate depolarization ratio (blue triangle line varies from 0.392 in the Taklamakan to 0.3 in the eastern Pacific. The values of mean color ratio decreases during the transport from the source to remote regions, and this decline indicates the likely decrease of coarse size particles. However, despite the decrease of large-size particles, the change in mean particulate depolarization ratio is very small, and this suggests that dust particles remain nonspherical during transport. The mean volume depolarization ratio (red diamond line) also shows small variation with values between 0.1 and 0.135, with the exception of the Taklamakan Desert, where the volume depolarization ratio is about 0.204. The mean dust optical depth (brown circle line) reaches the maximum value of 0.227 in the Taklamakan and gradually decreases as the particles move across the other six regions, which were divided into two different groups according to their dust optical depth values. One group included the Gobi Desert (AOD = 0.098), Korea (0.076), and Japan (0.072) and another group included the western Pacific Ocean (0.043), the Mid-Pacific Ocean (0.036), and the eastern Pacific Ocean (0.034). This classification rule can also be applied to the mean AODs, and thus the seven regions, including the Taklamakan Desert, can be divided into three groups according to the AOD values: the first is the Taklamakan Desert (AOD=0.363); second group includes the Gobi Desert (0.149), Korea (0.157), and Japan (0.132); and the last includes the Pacific Ocean. These groups are then considered as region-representative AOD values in radiative transfer calculations.

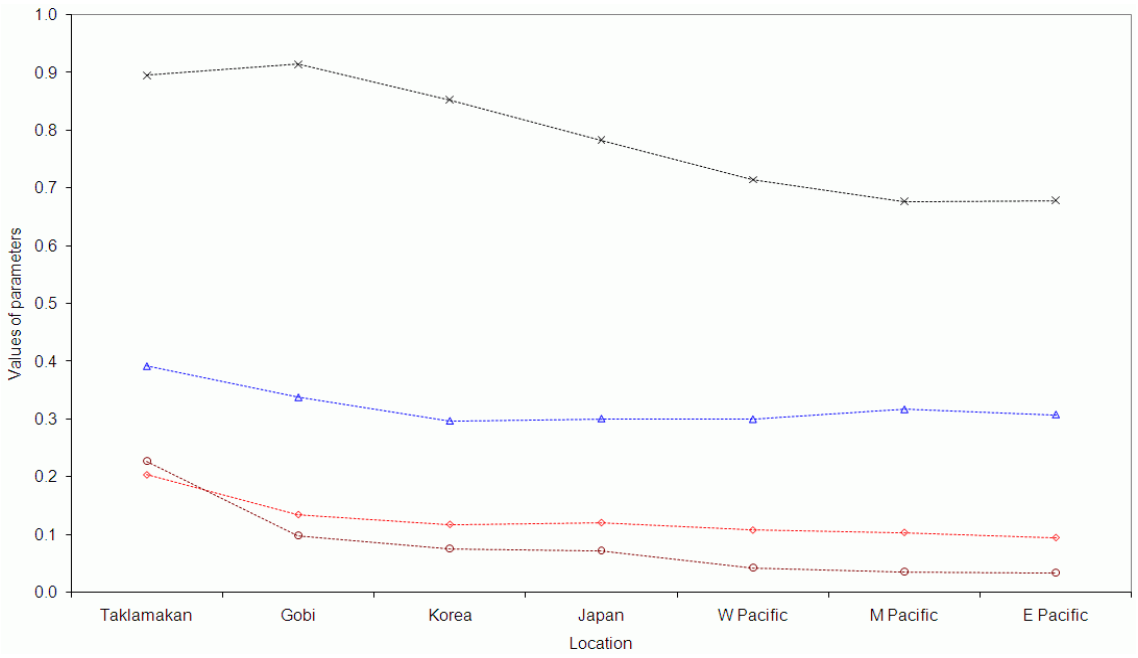

Figure 4.42 Mean particulate color ratio (black cross line), mean particulate depolarization ratio (blue triangle line), mean volume depolarization ratio (red diamond line), and mean AOD (brown circle line) over seven regions.

Based on the investigation of meteorological condition in the Taklamakan Desert, we also examine the characteristics of dust above the altitude of 6 km. Figure 4.43 shows the mean dust optical properties above the regional plume's mean top height for the seven regions. The figure displays that the dust optical properties above the altitude of 6 km in the source areas are almost same as those in the remote areas. This suggests that dust particles lifted high in the source regions preserve their characteristics (e.g., dust optical properties) during the transport, although large size particles, or the particulate color ratios, decrease continuously as shown in Figure 4.42.

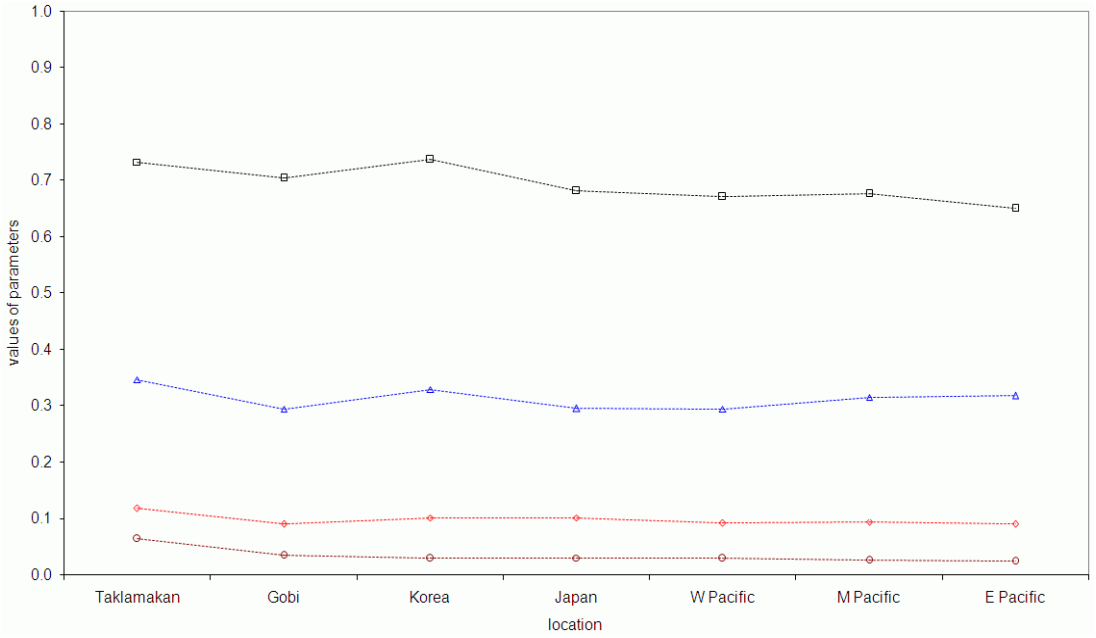

Figure 4.43 Same as Figure 4.42, but above the altitude of the regional plume's mean top height.

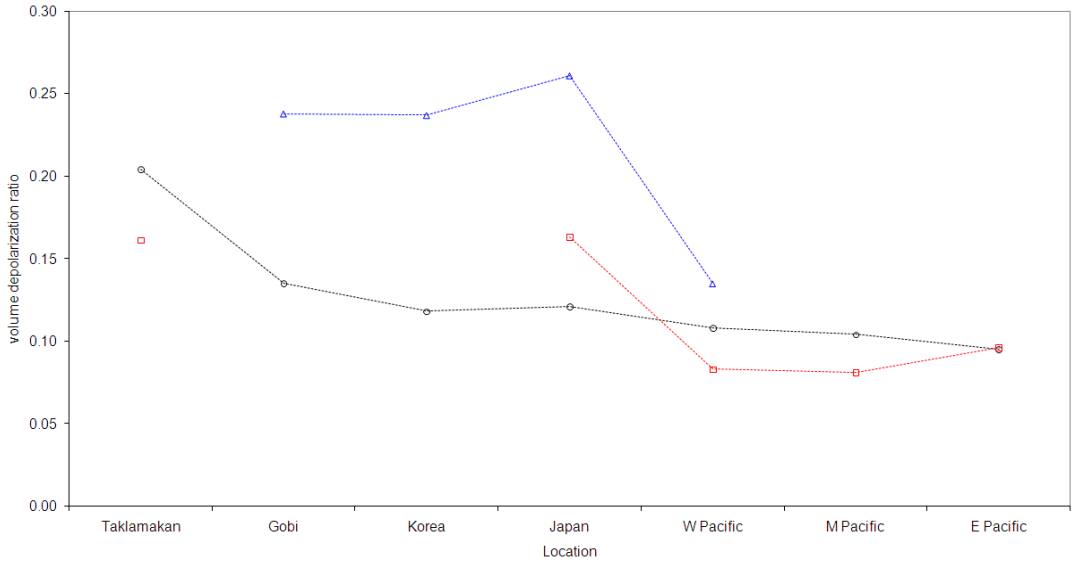

Figure 4.44 Mean integrated volume depolarization ratios of mid- (blue triangle line) and long- (red square line) range transported dust events for each orbit of CALIPSO and mean integrated volume depolarization ratio (black circle line) for the spring (March-May) of 2007 over seven regions.

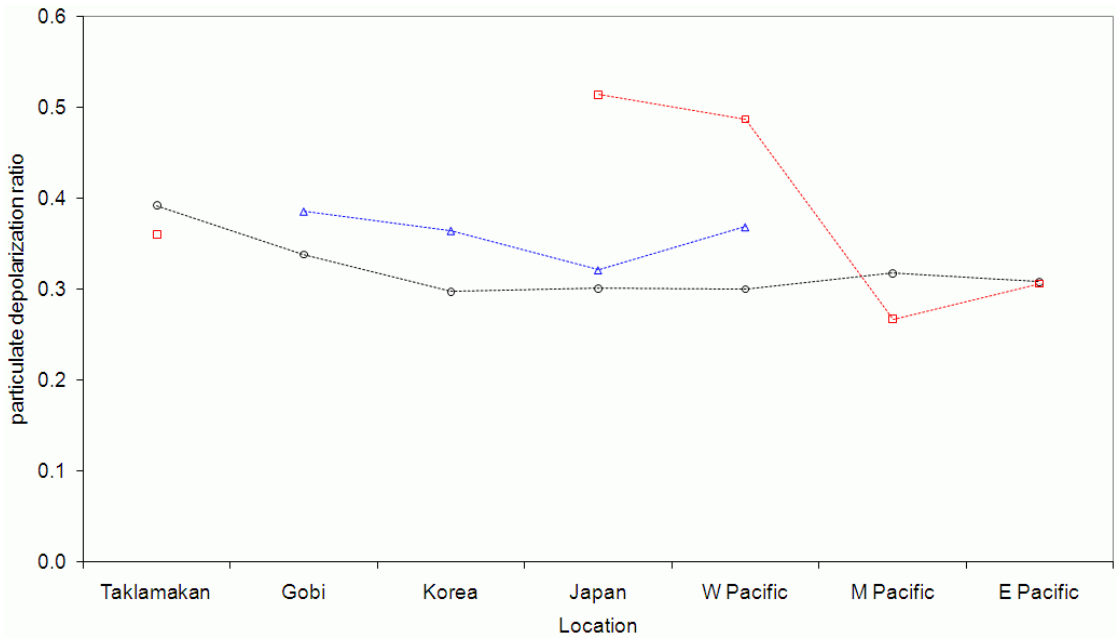

Figure 4.45 Same as Figure 4.44, but for mean integrated particulate depolarization ratios.

Figure 4.45 shows the mean particulate depolarization ratio. As expected, it shows high values ranging from 0.3 to 0.4, in general, except for the long-range transported dust event (red square line) over Japan on May 10 and the Western Pacific on May 12, 2007, where the values exceed 0.4. Further analyses are necessary to find the reason why the mean particulate depolarization ratios are high over those two locations, i.e., Japan and the Western Pacific.

The mean particulate color ratios are shown in Figure 4.46. Overall, the mean particulate color ratios decrease during transport. The mid- (blue dotted line) and long-range (red dotted line) transported dust events have some high values when compared to the mean values of Spring 2007 (black solid line). For the mid-range transported dust events, high mean particulate depolarization ratios of above 0.9 are observed in the Gobi Desert, Korea, and Japan. This indicates the dominance of coarse-mode dust. The fine

mode fraction from MODIS-Aqua (blue solid line) supports the dominance of coarse-mode dust over Korea and Japan.

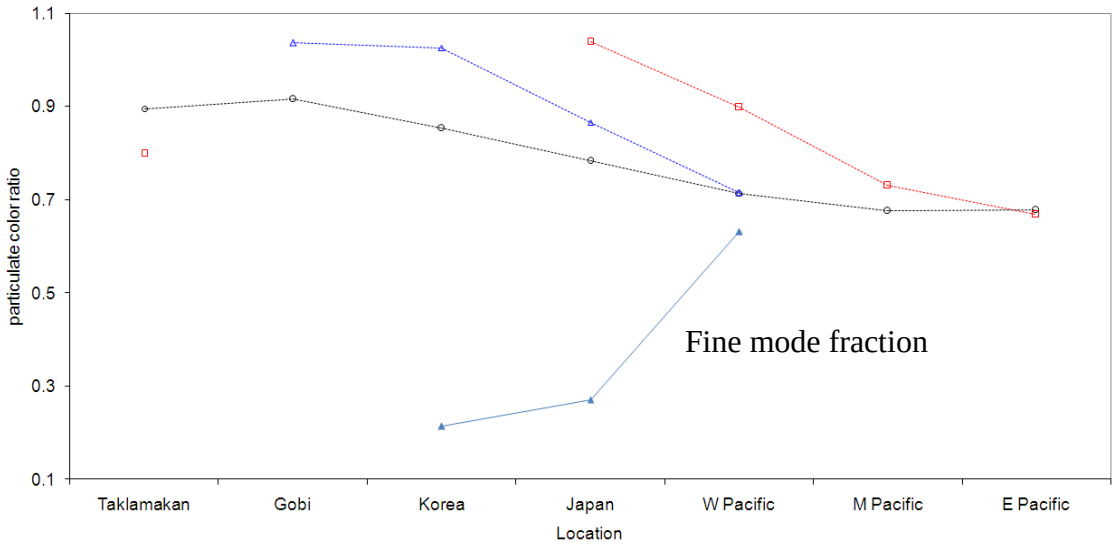

Figure 4.46 Mean integrated particulate color ratios of mid- (blue triangle line) and long- (red square line) range transported dust events for each orbit of CALIPSO, mean integrated particulate color ratio (black circle line) for the spring (March-May) of 2007 over seven regions, and fine mode fraction from MODIS-Aqua (Blue solid line).

4.4 Radiative Forcing and Heating/Cooling Rates of Asian Dust

Given existing problems in AOD retrievals from CALIPSO, it seems to be meaningless at the moment to perform calculations of the dust radiative forcing for each CALIPSO foorprint. Instead, we consider here only several representative vertical profiles of Asian dust observed by CALPSO in the deserts and downwind over the water to investigate the distribution of radiative heating/cooling rates and top-of-the atmosphere (TOA) radiative forcing. Description of modeling experiments is given in Table 4.4. The

1D radiative transfer model used in this study is the Santa Barbara DISORT Atmospheric Radiative Transfer (SBDART) discussed in Chapter 2. The SBDART model requires input data such as aerosol type, AOD, altitude and thickness of the aerosol layer, atmospheric profile (i.e., single scattering albedo and asymmetric parameter), solar zenith angle, and surface type. The summary of the input data for four representative dust loading cases is also provided in the table.

Table 4.4 Description of radiative modeling experiments.

		Source	Mid-range transport area		Long-range transport area
			Mid 1	Mid 2	
Solar zenith angle		0° (high Sun angle), 31° (local noon), 75° (low Sun angle)			
Atmospheric profile		Mid-latitude summer			
Albedo (Surface type)		0.22 (Desert)	0.05(Sea water)		
Type of aerosol (Desert dust)	ω_0	0.8897	0.9085		0.9273
	g	0.7578	0.7416		0.7253
Vertical distribution of dust layers (AODs for each 1 km layer)		0-9 km (0-3 km: 0.59, 3-6 km: 0.02, 6-9 km: 0.01)	0-3 km (0.25)	6-10 km (0.02)	6-10 km (0.02)

We considered three solar zenith angles as shown in the table to capture the diurnal variability of the dust radiative impact; 0° (the cosine of solar zenith angle: 1) for the case of a high Sun angle, 31° (the cosine of solar zenith angle: 0.85) for local noon, and 75° (the cosine of solar zenith angle: 0.25) for the case of a low Sun angle in mid-latitudes. Since SBDART does not provide the 'mid-latitude spring' as an option, a mid-latitude summer, the atmospheric condition of which is similar to that of a mid-latitude spring, was chosen for the atmospheric profile. The surface albedo of 0.22 from MODIS is used for the dust source regions in East Asia, and the albedo of 0.05 is selected for ocean. For ω_0 and g, the calculated optical properties of representative dust mixtures of local or transported dust (see Chapter 3) are used. Lastly, the vertical distribution and corresponding AODs of dust layers, as discussed in the previous section, are selected as inputs for the dust radiative modeling.

Based on the input parameters in Table 4.4, we computed the heating/cooling rates of dust layers. Figure 4.47 shows the results of four cases: source, mid-range transport 1, 2, and long-range transport. As shown in Figure 4.47, the profile and values of heating/cooling rates are strongly affected by the optical depth and layer height. In addition, the maximum rates are always at the top of the layer. The largest heating rate is shown in the case of the source with the solar zenith angle of 0° in Figure 4.47(a), which indicates that the increasing dust loadings result in increasing radiative heating rate. For the effect of the solar zenith angle, dust radiative heating rates with high Sun angles is larger than those with low Sun angles. Between the solar zenith angle 0° and 31°, however, the corresponding radiative heating rate values remain almost constant for all cases, except in the case of the source where the rate difference between the two solar

zenith angle (i.e., 0° and 31°) is getting larger as the altitude gets lower.

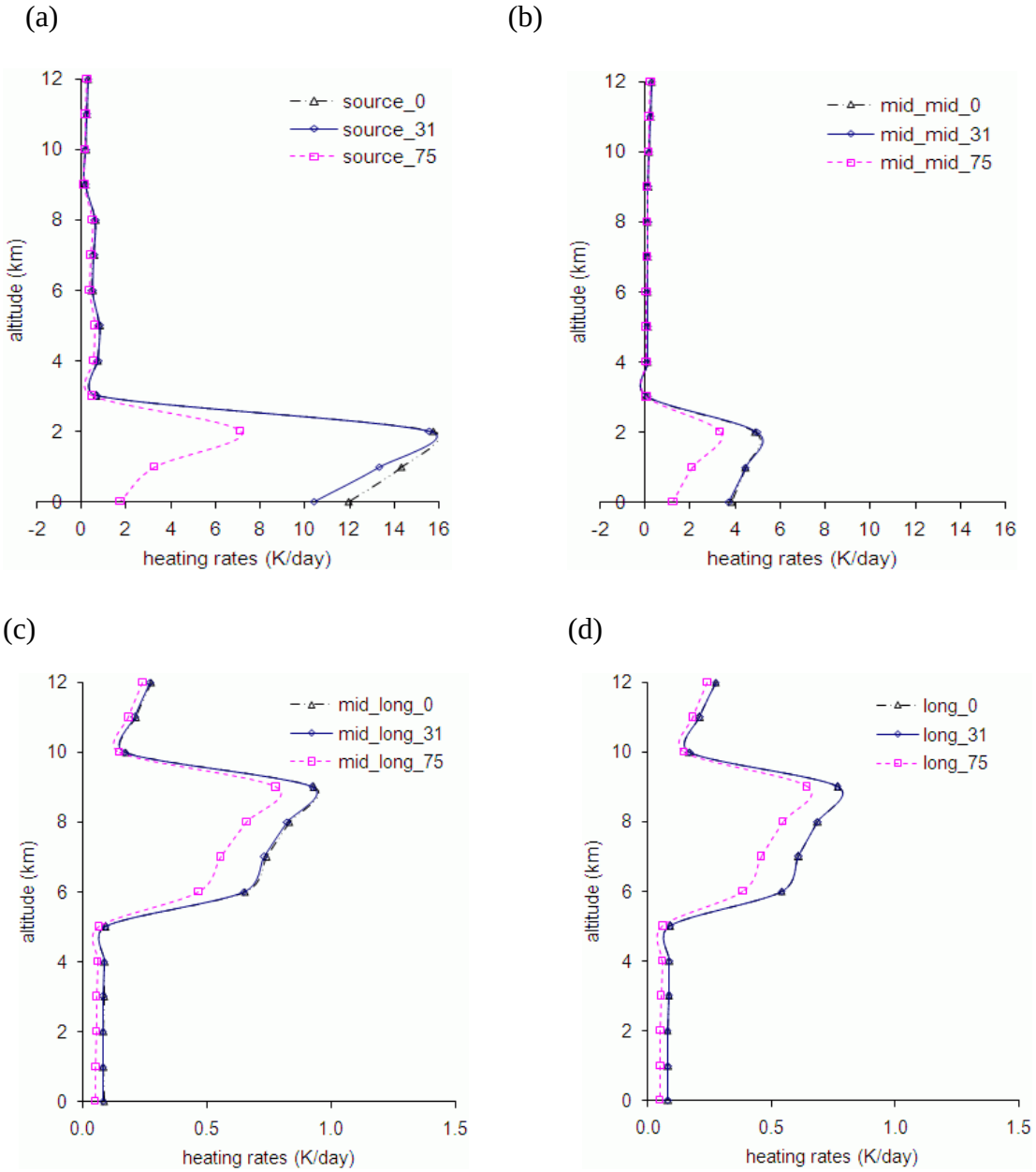

Figure 4.47 Heating rates of dust layers for four cases: (a) source, (b) mid-range transported dust, (c mid-range transport area, and (d) long-range transport area. Calculations are shown for three solar zenith angles: 0° (high Sun angle), 31° (local noon), and 75° (low Sun angle).

This large difference in radiative heating values near the surface in the source is related to the value of the surface albedo. For the effect of ω_0 and g, Figures 4.47(c) and (d) display little difference of dust heating rates, which implies that the dust heating rates are not too sensitive to changes in ω_0 and g in the case of dust layers with low dust optical depth at high altitudes.

Figure 4.48 shows the comparison of dust heating rates with the solar zenith angles of 31° (local noon) and 75° (low Sun angle) for four cases: source (blue line), mid-range transported dust (red line) and long-range transported dust (black line) in the mid-range transport area, and long-range transport area (green line). The figure displays that the dust heating rates decrease with the decrease of AODs.

This study also assesses the radiative forcing of dust. The dust radiative forcing at the top of the atmosphere (TOA), ΔF_{TOA},(in units of Wm^{-2}) is defined as the difference of upwelling flux between dust and clear condition as follow:

$$\Delta F_{TOA} = -(F_{up,dust} - F_{up,clear})_{TOA,} \quad (4.1)$$

At the surface, $\Delta F_{surface}$ is defined as the difference of downwelling flux under the same condition as that of Equation (4.1) as follows;

$$\Delta F_{surface} = (F_{down,dust} - F_{down,clear})_{surface.} \quad (4.2)$$

Negative values for ΔF_{TOA} and $\Delta F_{surface}$ indicate that a cooling effect is produced by dust at either TOA or the surface.

(a) (b)

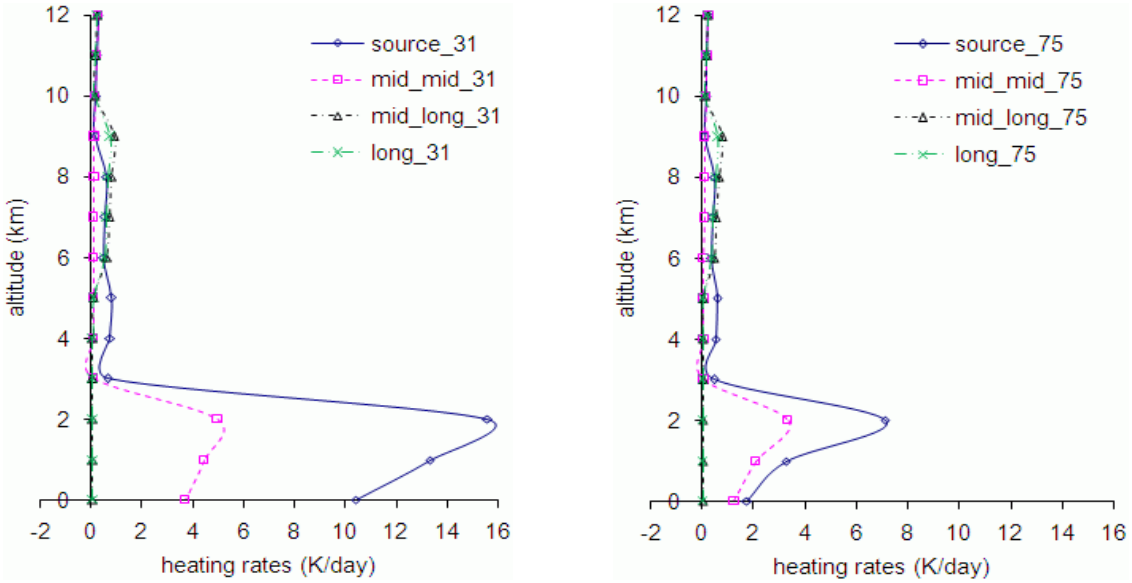

Figure 4.48 Comparison of dust heating rates for four cases with the solar zenith angle of 31° (local noon) and 75° (low Sun angle), respectively.

Figure 4.49 displays the values of dust radiative forcing at TOA (a) and surface (b). For the net dust forcing at TOA (a), there is a positive forcing (49.4 W/m^2) of dust over source (albedo=0.22) at high Sun angle (solar zenith angle=31°) due to the difference between the albedo on dust layers and on desert surface. A negative forcing occurs over the bright surface of source when the Sun angle increases from 31° to 75°, due to the increase of dust scattering, whereas it occurs over dark surfaces (albedo=0.5) in the mid- and long-range transport areas at both low and high Sun angles. This means that dust contributes to the cooling of atmosphere at the TOA during transport. For the net dust forcing at the surface (b), dust causes a negative forcing at two angles over the surface of all areas. The maximum magnitude (-557.97) of the dust negative forcing is at high Sun angle over the bright surface because of the reflection and absorption of

sunlight by dust layers. The negative forcing of dust decreases as dust transports to the remote areas, at which the surface is dark and the dust optical depth decreases. In addition, the magnitude of the negative radiation is slightly changed when the dust optical properties (ω_0 and g) are changed during transport. All these results support that dust radiative forcing depends on the dust optical depth, solar zenith angle, surface albedo, and dust optical properties.

(a)

(b)

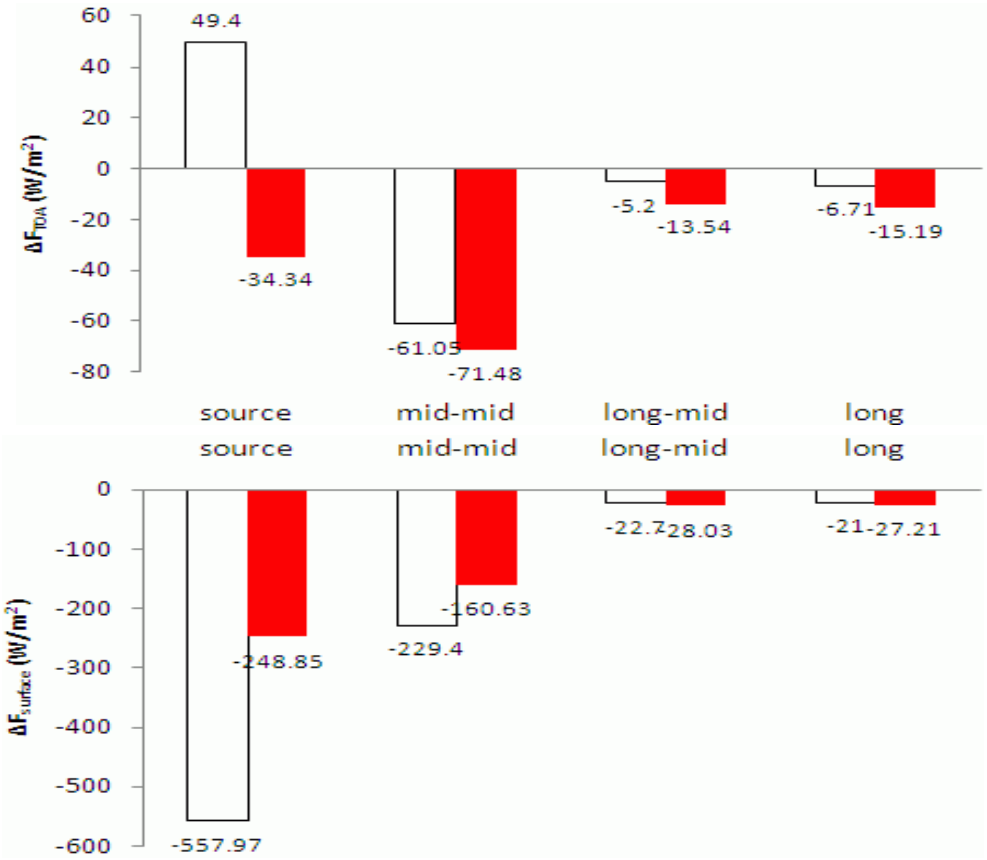

Figure 4.49 (a) Net dust radiative forcing at TOA and (b) at the surface for the solar zenith angle of 31° (white bar) and 75° (red bar) over source, mid- and long-range transport areas.

4.5 Summary

In this chapter, we used the new version 3.01 data from the CALIPSO lidar to characterize the spatial and optical properties of Asian dust over the source and downwind regions in the springs of 2007-2010. Our analysis of CALIPSO data was augmented by data from the A-train constellation (MODIS, OMI and CloudSat satellite sensors) and meteorological, AERONET, and ground-based lidar observations. This is the first study that presents a comprehensive analysis of multi-year CALIPSO version 3.01 data. The new methodology was developed for merging multi-satellite/multi-sensor active (lidar) and passive remote sensing data, various ground-based measurements, and modeling data to improve understanding of properties of dust aerosols. In this Chapter, the methodology was applied for Asian dust.

Some major findings are as follows:

1) Our analysis demonstrated that the new version 3.01 CALIPSO data, including particulate depolarization and color ratios, provides a unique dataset to investigate the optical characteristics of Asian dust and their vertical profiles over the dust sources as well as downwind areas.

2) CALIPSO observations in the Taklamakan and Gobi Deserts showed that the high values of $\delta_{p,layer}$ suggest that the nonsphericity effect is similar between Taklamakan dust and Gobi dust. Observed high values of $\chi_{p,layer}$ (above 0.9) indicate the significant presence of coarse dust particles in the Taklamakan and Gobi Deserts.

3) We found that during mid- and long-range transport, the particulate depolarization ratio values of Asian dust remain as high (above 0.3) in the remote areas as in the sources, but the volume depolarization and color ratios continuously decrease

from the deserts to the Pacific Ocean. This finding suggests that dust particles remain nonspherical, although the number of coarse dust particles decreases during transport. Constant $\delta_{p,layer}$ values indicate the importance of representing dust nonsphericity in climate models and remote sensing applications during the entire dust lifecycle.

4) Assessments of the radiative forcing and heating rate of Asian dust was performed for selected representative vertical profiles at different distances from the dust sources using the dust optical properties simulated in Chapter 3. There was a positive forcing (49.4 W/m^2) of dust at TOA over source (albedo=0.22) at the high Sun angle (solar zenith angle=31°). However, a negative forcing occurred over the bright source surface when the Sun angle increased from 31° to 75° while it occurred over dark surfaces (albedo=0.05) in the mid- and long-range transport areas at both low and high Sun angles. In addition, the maximum magnitude (-557.97) of the dust negative forcing is at high Sun angle over the bright surface, which explains the drastic change in daily temperature in desert areas.

CHAPTER 5

INVESTIGATION OF DUST CHARACTERISTICS IN WORLD'S DUST SOURCE REGIONS AND ASSESSMENTS OF DUST RADIATIVE FORCING AND HEATING/COOLING RATES

5.1 Introduction

In Chapter 4, we examined the vertical distribution and optical properties of Asian dust and computed the Asian dust radiative forcing and heating/cooling rates. Here we focus our analyses on the major world's dust sources introduced in Chapter 1, contrasting the regional features and identifying major similarities.

Understanding of the regional dust properties is important to assess the radiative forcing and heating/cooling rates because the characteristics of the regional dust aerosols are different. The vertical distribution of dust aerosols as well as the microphysical properties is critical issue in the assessment of dust impact on climate (Darmenov and Sokolik, 2005). The vertical distribution of dust also determines the indirect effect of dust on the microphysics of cloud. However, the limitation of global observation for the vertical distribution of dust aerosols is one of remained problem. Therefore, investigation of the global and vertical distribution of dust aerosols is necessary to better assess the radiative forcing and heating/cooling rates of dust (D. Liu et al., 2007).

As discussed in Chapter 1, passive satellite remote sensors have been providing the information about the global distribution of dust aerosol, but their measurements are limited. For example, MODIS cannot observe the scattered radiance over bright land

surfaces. In contrast, total ozone mapping spectrometer (TOMS), which use the wavelength of UV to detect the reflectivity, can observe the scattered radiance over bright land surface as well as over the sea, although it cannot distinguish between dust aerosols and pollutants or biomass burning aerosol (Prospero et al., 2002). Most importantly, passive remote sensing gives column-integrated (2D) view only and thus cannot detect the vertical distribution of aerosols.

The CALIPSO has been providing the multiyear global aerosol profiling for the first time, which adds value to the research of cloud and aerosol by complementing the growingly sophisticated passive remote sensing of columnar aerosol such as AOD. In addition, this unique capability of CALIPSO provides an opportunity for assessing model simulations of aerosol vertical distributions on regional and global scales. However, only two previous studies (Yu et al., 2010, D. Liu et al., 2008) presented the global analysis of mineral dust from CALIPSO. Yu et al. (2010) analyzed the seasonal variations of the vertical distribution of aerosols by using the cloud-free nighttime of CALIPSO data from June 2006 to November 2007. D. Liu et al. (2008) showed both the occurring frequency and the vertical distribution of aerosol extinction for both dust and non-dust aerosol. In addition, only a few studies investigated the vertical distribution of dust in dust sources regions, mainly focusing on North Africa (Saharan dust) and to some extent on Asian dust. The scarcity of research about dust in the major world's desert areas has prevented the accurate understanding of the dust radiative forcing and heating/cooling rates not only on the regional scale but also on the global scale.

The specific goals of the study presented in this Chapter are as follows: 1) examine and compare the dust characteristics in the major dust sources for the spring

season using the new level 2 version 3.01 CALIOP data, 2) intercompare regional dust properties in terms of observed CALIPSO aerosol products, and 3) assess the dust radiative forcing and heating/cooling rates representative of each region.

Section 5.2 introduces the data and methodology used in analysis. Section 5.3 presents the results of satellite data analyses and Section 5.4 discusses the radiative impact of dust based on optical and radiative transfer calculations. Finally, Section 5.5 summarizes the main findings.

5.2 Data and Methodology

5.2.1 Data

Satellite data used for analysis (e.g., CALIOP, MODIS and OMI from Aqua, and CloudSat) were introduced in Chapter 4. The considered dust source regions are shown in Figure 5.1. For each region, we analyzed CALIPSO and multiple-satellite data during the spring seasons (March-May) of 2007-2008 with an exception of Australia, where the spring season lasts from September to November. Table 5.1 summarizes representative regional dust events that were selected for analysis.

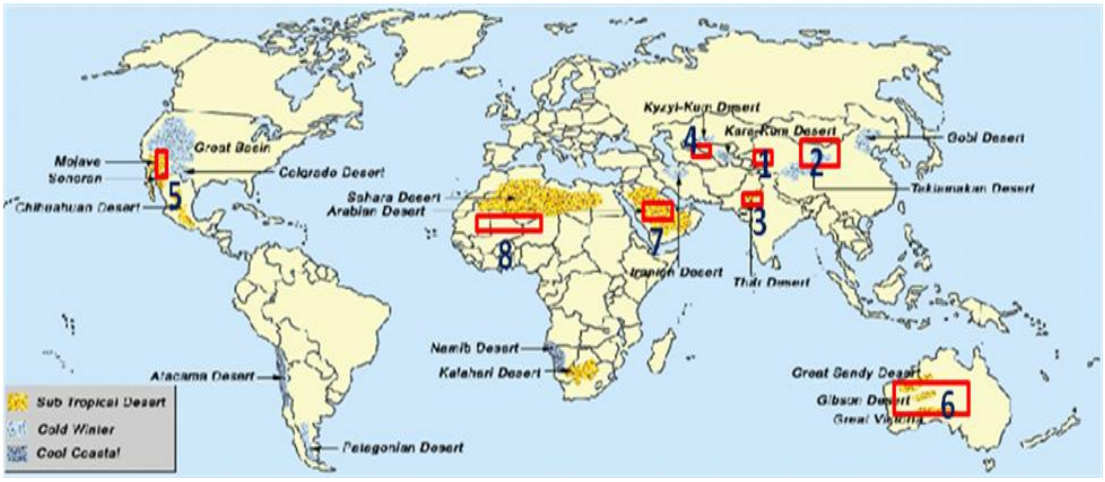

Figure 5.1 Eight source regions of interest (1: Taklamakan Desert (36°-40°N, 78°-90°E), 2: Gobi Desert (38° -49°N, 94° -116°E), 3: Thar Desert (23°-30°N, 70°-75°E), 4: Central Asia (39°-48°N, 55°-65°E), 5: Mojave Desert (32°–36°N, 115°–110°W), 6: Australia Desert (20°–30°S, 125°–140°E), 7: Arabian Peninsula (20°-25°N, 45°-50°E), and 8: Northern Africa (15°-20°N, 10°W-15°E)).

Table 5.1 Selected dust cases in the world's dust source regions.

Region	1*	2*	3*	4*	5*	6*	7*	8*
Date	03/30/07	03/30/07	05/07/07	04/22/07	04/29/07	05/18/07	09/23/09	05/25/07
	04/01/07	04/01/07	06/10/07	04/23/07	05/03/07	05/07/08		

* The numbers denotes the selected regions as follows: 1 (Taklamakan Desert), 2 (Gobi Desert), 3 (Thar Desert), 4 (Central Asia), 5 (Mojave Desert), 6 (Arabian Peninsula), 7 (Australia Desert), 8 (North Africa).

5.2.2 Methodology

The methodology developed in Chapter 4 was applied to study the regional dust sources. This study begins with the investigation of the dust events during the spring season based on the information of the dust spatiotemporal distribution from OMI AI (Figure B.1) and MODIS RGB images. For the selected dust events, we examined the dust characteristics by using the CALIOP data (i.e., the layer integrated volume

depolarization ratio, the layer integrated particulate depolarization ratio, the layer integrated particulate color ratio, and aerosol-layer optical depth at 532 nm). In addition, monthly means of dust characteristics were estimated and used to perform intercomparison between the regions. Finally, we computed the regional radiative forcing and heating/cooling rates. Figure 5.2 presents the schematic diagram of the performed analysis.

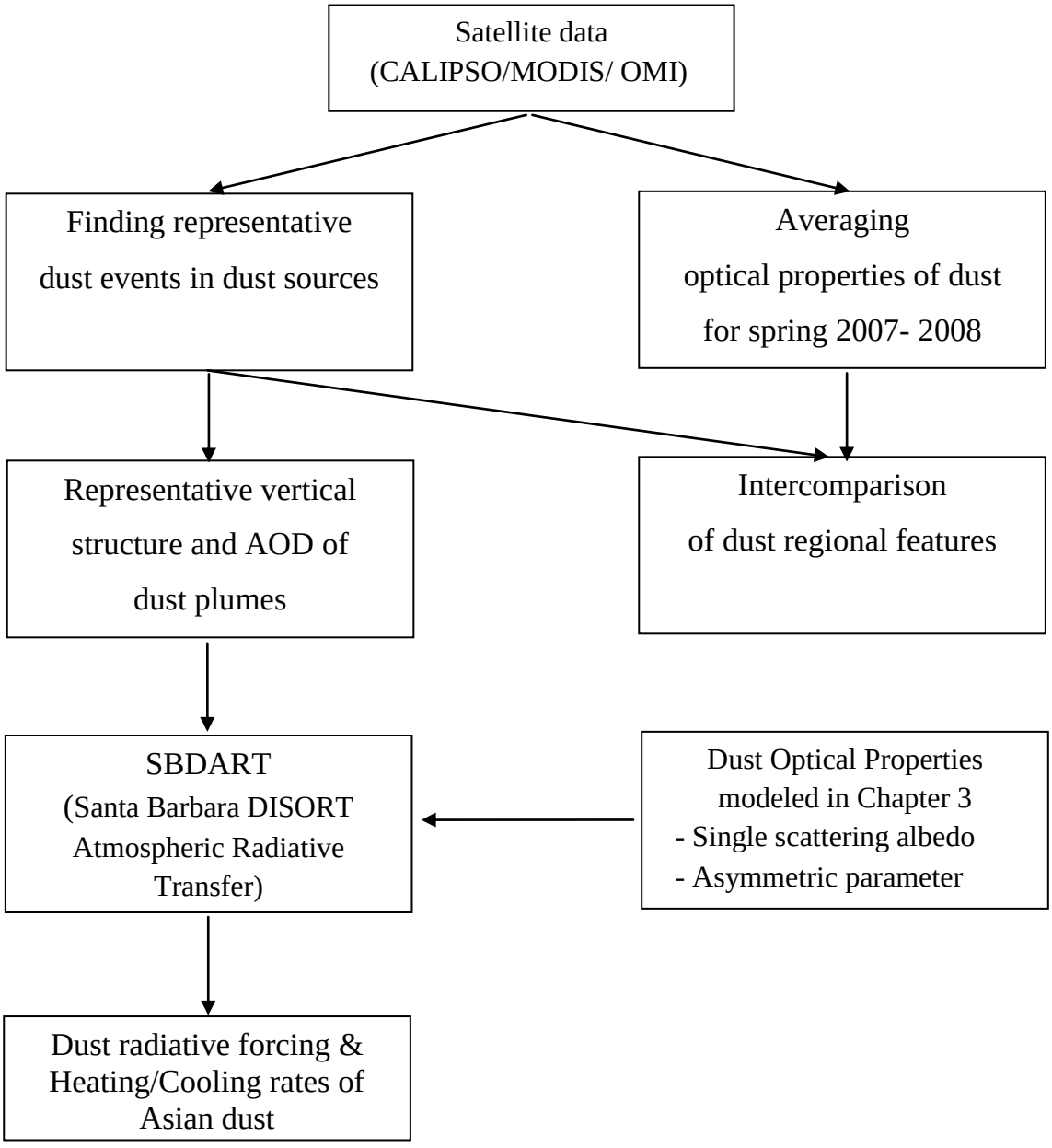

Figure 5.2 Schematic diagram of the research presented in Chapter 5.

5.3 Results

5.3.1 Analyses of Regional Dust Events

We first present a detailed analysis of the May 7, 2007 episode when the CALIPSO passed over the Thar Desert. Then the results for other dust events (Central Asia on April 22, 2007, the Mojave Desert on April 29, 2007, Arabian Peninsula on May 18, 2007, the Australia Desert on September 23, 2009, and Northern Africa on May 25, 2007) will be presented.

5.3.1.1 Thar Desert in India: dust event of May 7, 2007

Figure 5.3 presents a multi-satellite perspective of the spatial distribution of the May 7 dust event and vertical profiles of aerosol properties from the CALIPSO pass over the Thar Desert. Figure 5.3(a) shows the true color MODIS image with the orbit of CALIPSO. The true color MODIS image shows the presence of dust in the Thar Desert. Figure 5.3(b) displays the reflectivity (dBz) from CloudSat with surface albedo (black line) from the MERRA model, and Aerosol Index (red line) from OMI-Aura. CloudSat and Aerosol Index (AI) confirm that there was a heavy loading of dust in the atmosphere on this day and no low level clouds. It was suggested that AI >0.7 serves as a good indicator for dust (Prospero et al., 2002). Clearly, AI is much higher than 0.7 in this particular case. Examining the vertical feature mask (VFM) in Figure 5.3(c), one can notice that CALIPSO does identify dust spreading from the surface to 5 km.

The dust properties over the Thar Desert were further analyzed using the layer-integrated particulate linear depolarization ratio $\delta_{p,layer}$, the layer-integrated volume linear depolarization ratio $\delta_{v,layer}$, aerosol-layer optical depth AOD, and the layer-integrated

particulate linear color ratio $\chi_{p,layer}$, retrieved from CALIPSO. The results of this analysis are shown in Figure 5.3(e). The vertical structure of aerosol layers is shown as a function of latitude (about sea-surface level) along the CALIPSO pass. Color of each identified layer shows the range of values of $\delta_{p,layer}$, shown at the right side of Figure. Numbers in different colors give values of $\delta_{v,layer}$ (red), $\delta_{p,layer}$ (blue), AOD (black), and $\chi_{p,layer}$ (violet) for each dust layer. The independent observations along with very high values of $\delta_{p,layer}$ are indicative of the presence of dust. Finally, Figure 5.3(d) shows the column aerosol optical depth at 532 nm over each CALPSO footprint.

Examining Figure 5.3(e), one can notice that $\delta_{p,layer}$ ranges from 0.146 to 0.646, with the average values of 0.262. The mean value (0.262) is high but when compared with the two mean values for the Taklamakan and Gobi Deserts in Chapter 4, it is relatively low. Unlike the cases of March 30 in the Taklamakan and Gobi, values of $\delta_{v,layer}$ are relatively low. This might be explained by the lower concentrations of dust. The $\chi_{p,layer}$ varies from 0.317 to 2.245, with an average value of 0.909, which is similar to the value of $\chi_{p,layer}$ discussed above in the Taklamakan case. This indicates that the size of dust particles between the Thar and Taklamakan Deserts might be similar. Interestingly, AOD retrieved in this case was unrealistically low (mean value below 0.428 and maximum value around 0.8). One of the explanations that the lidar ratio used by CALIPSO poorly represents the optical properties of dust in this region.

(a) True color image from MODIS-Aqua

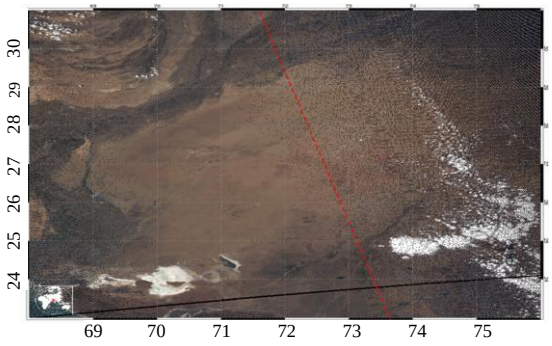

(b) Reflectivity dBZ from CloudSat

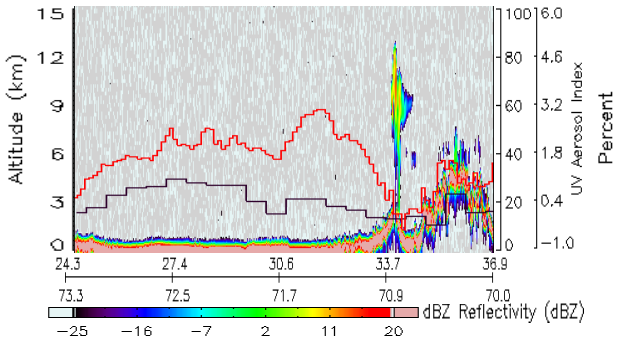

(c) Vertical feature mask (Aerosol: Orange)

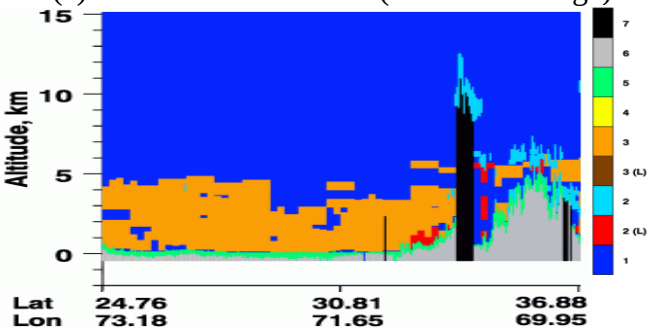

(d) Column Aerosol optical depth from

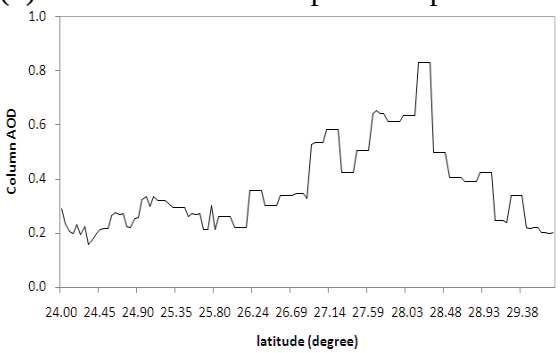

(e) Blue: δ_p, Red: δ_v, Black: AOD, Violet: χ_p

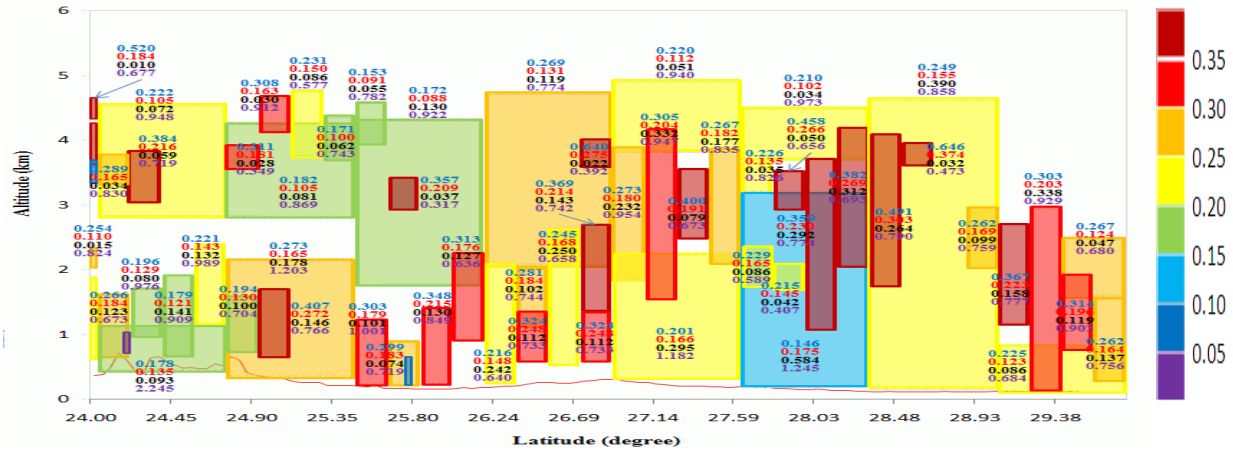

Figure 5.3 (a) True color image from MODIS-Aqua with the orbit of CALIPSO (red dotted line), (b) Reflectivity (dBz) from CloudSat with surface albedo (black line) from MERRA Model and Aerosol Index (red line) from OMI-Aura, (c) Vertical feature mask, (d) Column Aerosol optical depth, (e) and Distribution of layer-integrated particulate depolarization ratio from CALIPSO over the Thar Desert on May 7, 2007.

5.3.1.2 Central Asia: dust event of April 22, 2007

The results of analyses of dust in Central Asia are presented in Figure 5.4, which is organized as Figure 5.3. There were floating dust events on April 22, 2007, in this region seen in the MODIS true color image (see Figure 5.4(a) and AI (see red line in Figures 5.4(b)). The values of AI were somewhat low, around 0.4 that is a common feature for dust in this region. Examination of the CloudSat reflectivity image (Figure 5.4(b)) and CALIPSO VFM image (Figure 5.4(c)) also shows the presence of dust and no clouds over Central Asia. The dust layer spreads from the surface to 3 km. Unlike dust particles in the Taklamakan, Gobi, and Thar Deserts, the values of $\delta_{p,layer}$ and $\delta_{v,layer}$ are relatively low with mean values 0.224 and 0.112, respectively, for dust in Central Asia. This might be explained by the differences in particle shapes or by the lower concentrations of dust during floating dust events compared to dust storms in the Taklamakan and Gobi Deserts. The $\chi_{p,layer}$ varies from 0.44 to 5.072, with an average value of 1.427, which is the highest value among all three desert regions discussed above. This indicates that the size of dust particles in Central Asia is large. Compare with other regions, AODs in this case are the lowest (mean value below 0.164 and maximum value around 0.576). Overall, this analysis supports the existence of distinct differences of optical properties of dust in Central Asia compared to other regions.

(a) True color image from MODIS-Aqua

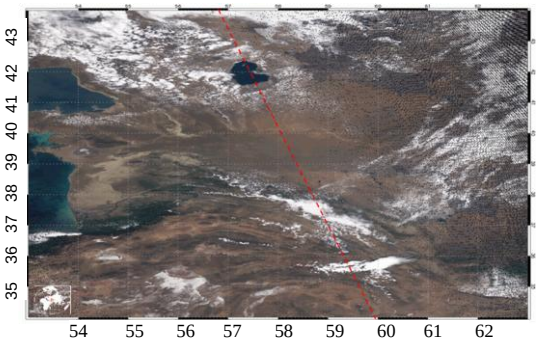

(b) Reflectivity dBZ from CloudSat

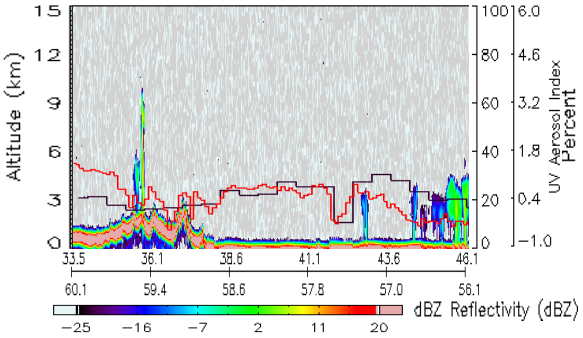

(c) Vertical feature mask (Aerosol: Orange)

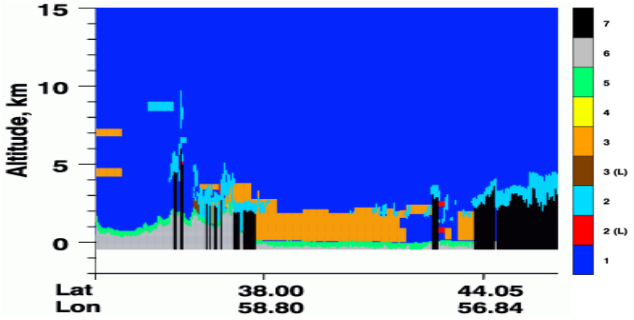

(d) Column Aerosol optical depth from

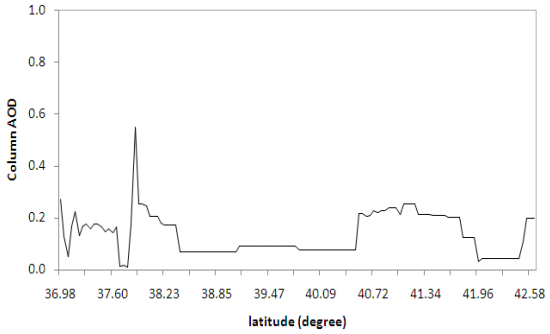

(e) Blue: δ_p, Red: δ_v, Black: AOD, Violet: χ_p

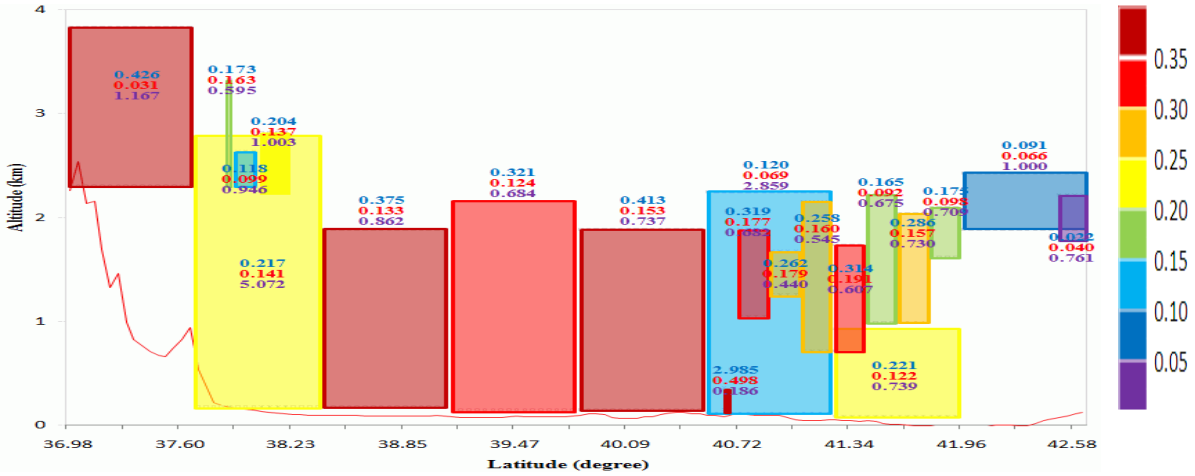

Figure 5.4 Same as Figure 5.3, except for Central Asia on April 22, 2007.

5.3.1.3 Mojave Desert, U.S.A.: dust event of April 29, 2007

Figure 5.5 summarizes the results for the dust event occurred over the Mojave Desert in the United States on April 29, 2007. The image from CloudSat and Aerosol Index (AI) in Figure 5.5 confirm that there was a floating dust event and cloud-free conditions over the Mojave Desert. Examination of the true color MODIS image (Figure 5.5(a)) and CALIPSO VFM image (Figure 5.5(c)) also shows the presence of dust and no clouds. The dust layer in this case spreads from the surface to 5 km, but there were only a few dust layers detected aloft as can be seen in the Figure 5.5(e). The $\delta_{p,layer}$ ranges from 0.173 to 0.828, with an average value of 0.465, which is very high compared to the mean values in the other deserts. The $\delta_{v,layer}$ varies from 0.058 to 0.217, with an average value of 0.117. This is similar to the value of $\delta_{v,\ layer}$ in the case of Central Asia. The $\chi_{p,layer}$ varies from 0.216 to 2.531, with an average value of 1.128. The high mean $\chi_{p,layer}$ indicates the size of dust in Central Asia is large. The AODs in this case are very low (mean value below 0.026 and maximum value around 0.059).

(a) True color image from MODIS-Aqua

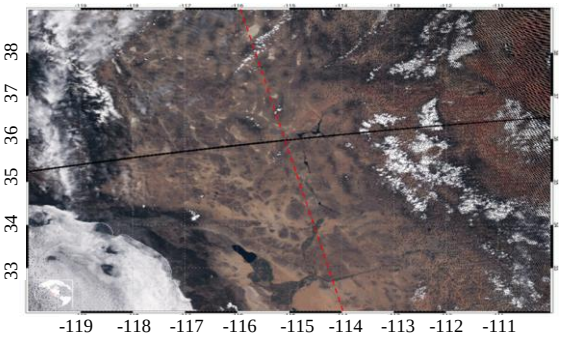

(b) Reflectivity dBZ from CloudSat

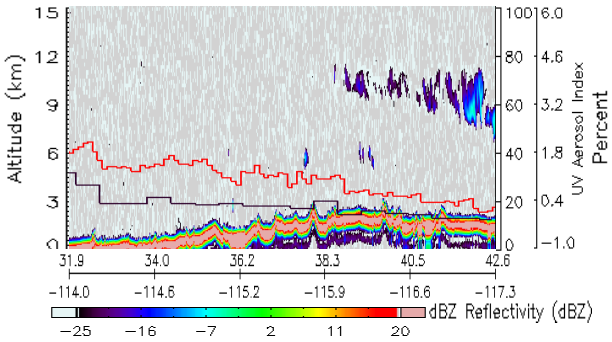

(c) Vertical feature mask (Aerosol: Orange)

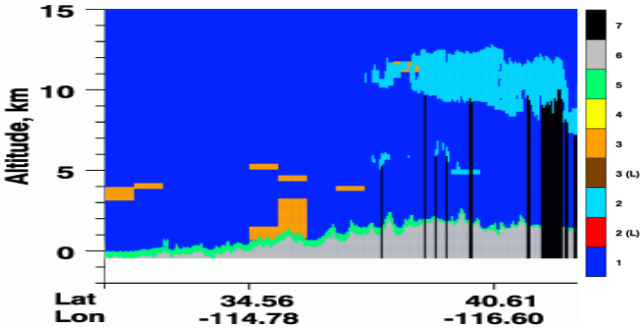

(d) Column Aerosol optical depth from

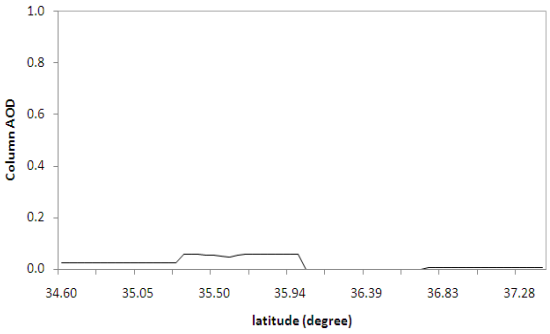

(e) Blue: δ_p, Red: δ_v, Black: AOD, Violet: χ_p

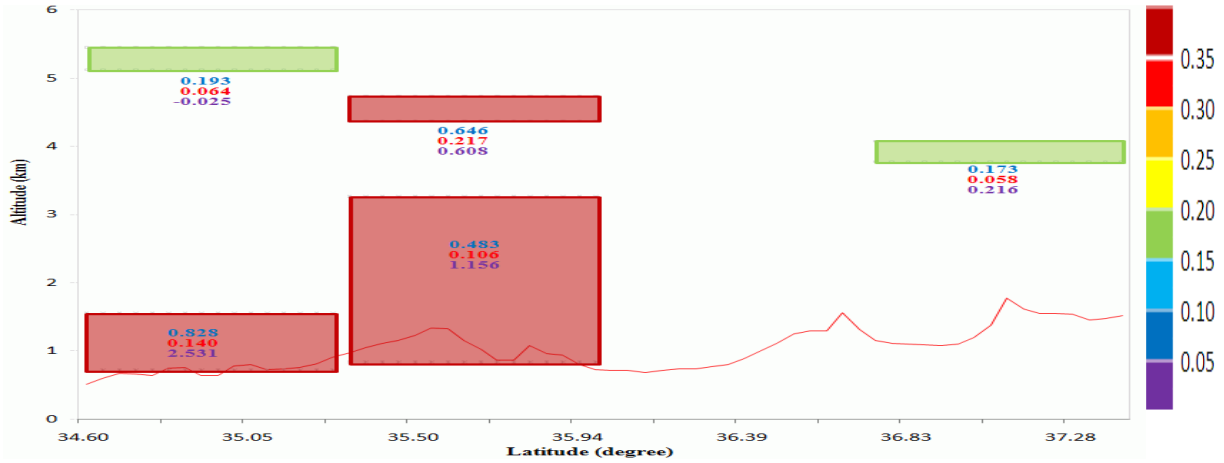

Figure 5.5 Same as Figure 5.3, except for the Mojave Desert on April 29, 2007.

5.3.1.4 Australia Desert: dust event of September 23, 2009

The results of analyses of dust over the Australia Desert are presented in Figure 5.6. There was a dust event on September 23, 2009 in this region seen in the true color image (see Figure 5.6(a)). Unfortunately, there was no AI retrieved from OMI on this day (Figure 5.6(b)). Examination of the CloudSat reflectivity image (Figure 5.6(b)) and CALIPSO VFM image (Figure 5.6(c)) also shows the presence of a dust event over the Australia Desert. No clouds were observed in this day. The dust layer spreads from the surface to 3 km. The $\delta_{p,layer}$ ranges from 0.146 to 0.969, with a mean value of 0.321. The $\delta_{v,layer}$ varies from 0.074 to 0.484, with an average value of 0.192. Unlike $\delta_{v,\ layer}$ in the case of Taklamakan and Gobi Deserts, the $\delta_{v,\ layer}$ is homogeneous from the surface to the top layer of the dust plume observed in the Australia Desert. The $\chi_{p,layer}$ varies from 0.246 to 2.773, with a high average value of 1.185, indicating that the size of dust particles in the Australia Desert is also large. The AODs in this case are very low (mean value of 0.279 and maximum value around 2.254).

.

(a) True color image from MODIS-Aqua

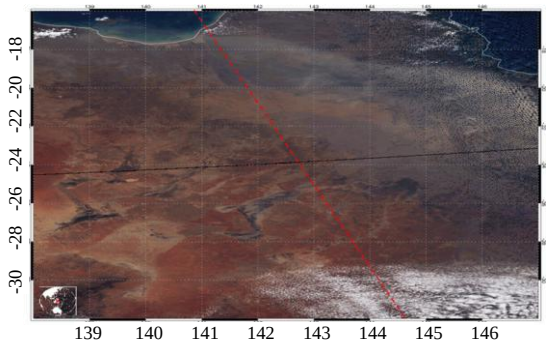

(b) Reflectivity dBZ from CloudSat

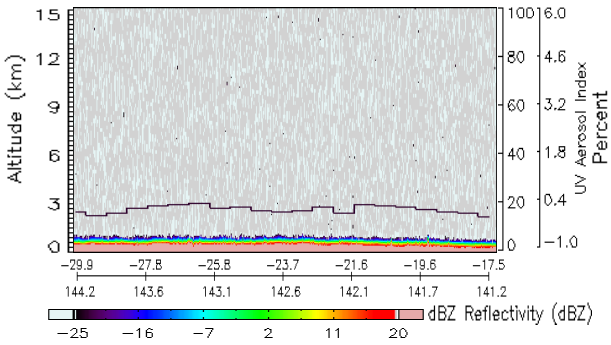

(c) Vertical feature mask (Aerosol: Orange)

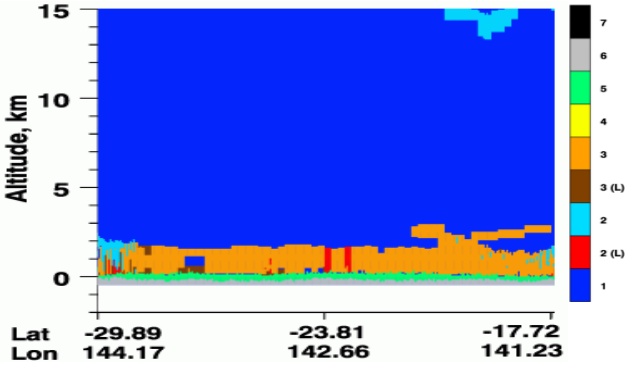

(d) Column Aerosol optical depth from

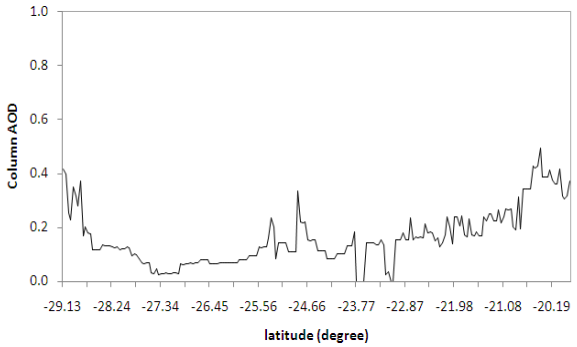

(e) Blue: δ_p, Red: δ_v, Black: AOD, Violet: χ_p

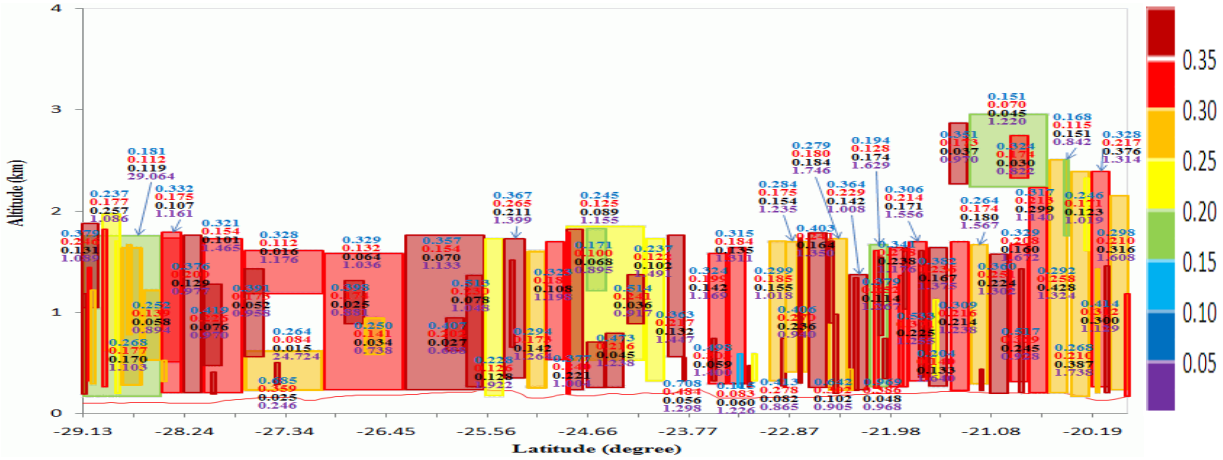

Figure 5.6 Same as Figure 5.3, except for Australia on September 23, 2009.

5.3.1.5 Arabian Peninsula: dust event of May 18, 2007

Figure 5.7 summarizes the results for the dust over Arabian Peninsula on May 18, 2007. There were strong dust storms on May 18, 2007 in this region. MODIS true color image (see Figure 5.7(a)) clearly show the extensive dust outbreak across the region. OMI AI values were also high (see red line in Figures 5.7(b)). No clouds were observed in CloudSat image (Figure 5.7(b)), the CALIPSO VFM image (Figure 5.7(c)) correctly detects dust over the Arabian Peninsula. Figure 5.7(e) shows that the dust layer spreads from the surface to 5 km. However, there are two layers with the high values of $\delta_{p,\ layer}$ (higher than 0.35) near the surface and relatively lower values (0.25-0.35) above between latitude 20° - 26.5°. This is similar to the $\delta_{p,\ layer}$ behavior discussed in the Taklamakan and Gobi cases. This fact might suggest that the nonsphericity effect is similar for dust aerosol originating in these sources. The value of $\delta_{v,\ layer}$ is also similar to $\delta_{p,\ layer}$ discussed above for East Asia. The $\delta_{v,\ layer}$ ranges from 0.098 to 0.540, with an average value of 0.2. The $\chi_{p,layer}$ varies from 0.382 to 2.083, with an average value of 0.947. This indicates that the size of dust particles in Arabian Peninsula is likely larger than in the Taklamakan Desert. The AODs range from 0.141 to 2.408, with an average value of 0.730. The maximum AOD is 2.408 and comparable to that in the Taklamakan and Gobi deserts.

.

(a) True color image from MODIS-Aqua

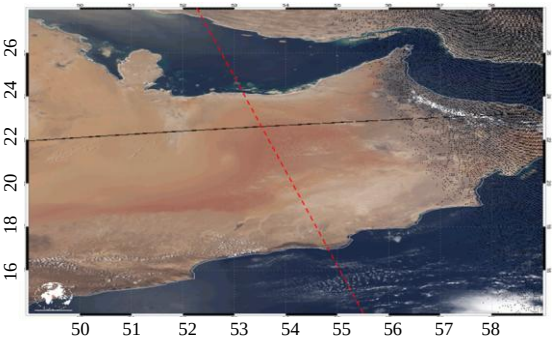

(b) Reflectivity dBZ from CloudSat

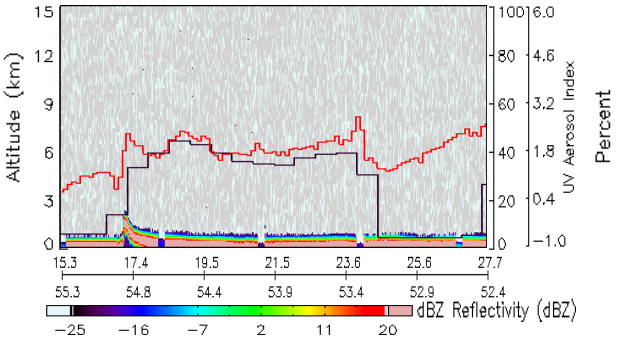

(c) Vertical feature mask (Aerosol: Orange)

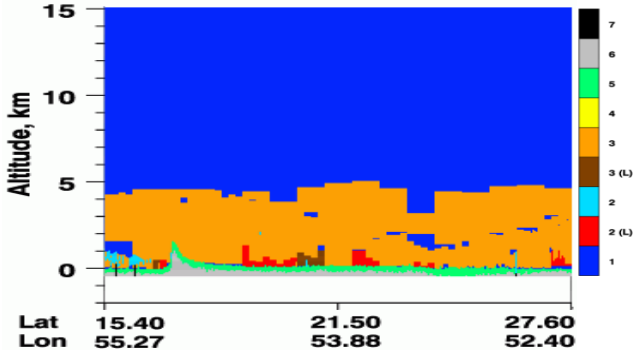

(d) Column Aerosol optical depth from

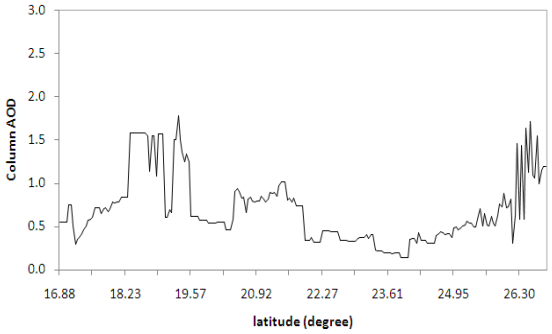

(e) Blue: δ_p, Red: δ_v, Black: AOD, Violet: χ_p

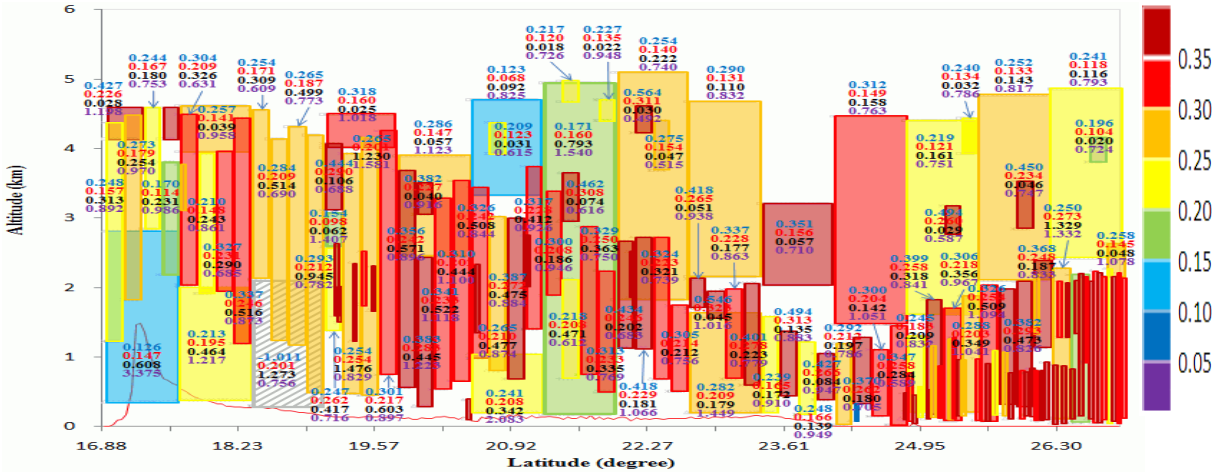

Figure 5.7 Same as Figure 5.3, except for Arabian Peninsula on May 18, 2007.

5.3.1.6 Northern Africa: dust event of May 25, 2007

There are numerous dust events observed by CALIPSO in the northern Africa. Here we show one case of a strong dust storm observed on 25 May. Figure 5.8 shows the analyses of this event similarly to Figures 5.3-5.7. Figure 5.8(a)) shows a MODIS Aqua true color image and Figure 5.8(b) presents AI retrieved from OMI and CloudSat reflectivity image (Figure 5.8(b)). All supporting the presence of dense dust plumes in cloud-free conditions. The CALIPSO VFM image (Figure 5.8(c)) also detects an extensive dust plume. Figure 5.8(e) shows that the dust layer spreads from the surface to 5.5 km and there are two layers with the low values of $\delta_{p,\ layer}$ (below 0.25) near the surface and high values (above 0.3) above 2 km between latitude 9.56° - 16.3°. This is different from the $\delta_{p,\ layer}$ behavior discussed above in the Taklamakan, Gobi, and Arabian Peninsula cases. This fact might suggest that the area between latitude 9.56° and 16.3° is not a dust source, and the dust plume with high $\delta_{p,\ layer}$ was transported from other desert areas. The AODs range from 0.113 to 0.659, with the average value of 0.371. The $\delta_{v,\ layer}$ ranges from 0.108 to 0.372, with an average value of 0.183. The horizontal and vertical distributions of $\delta_{v,\ layer}$ in this area are similar to those in the Thar and Australia Deserts. The $\chi_{p,layer}$ varies from 0.276 to 4.648, with an average value of 1.036, indicating that the dust particle size in Northern Africa is large. Overall, all dust sources show the strong signal from coarse mode particles, supporting the need for including this mode in optical modeling (see Chapter 3).

.

(a) True color image from MODIS-Aqua

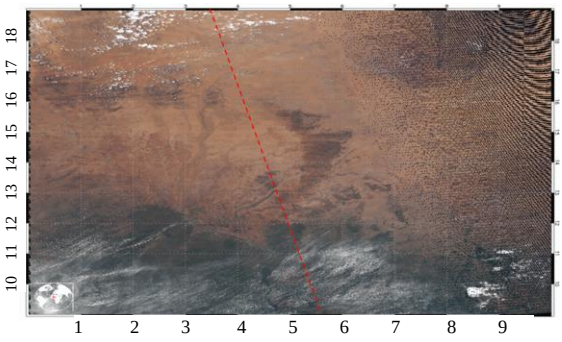

(b) Reflectivity dBZ from CloudSat

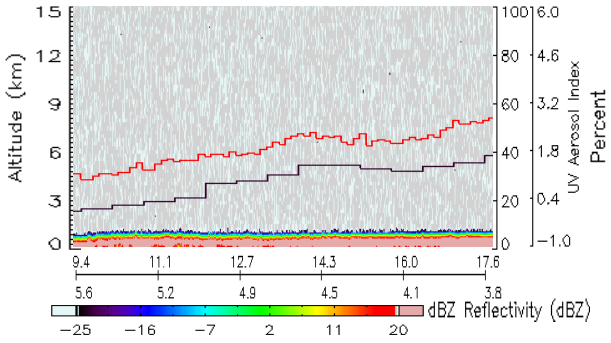

(c) Vertical feature mask (Aerosol: Orange)

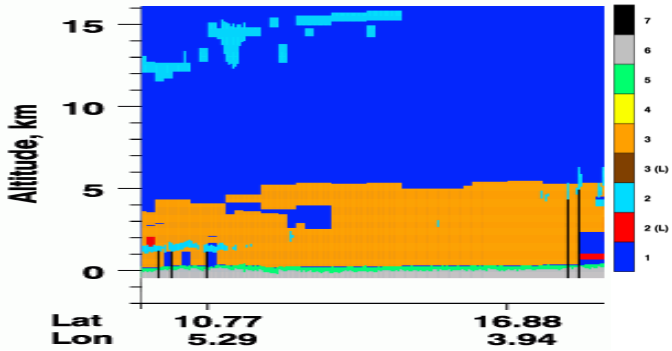

(d) Column Aerosol optical depth from

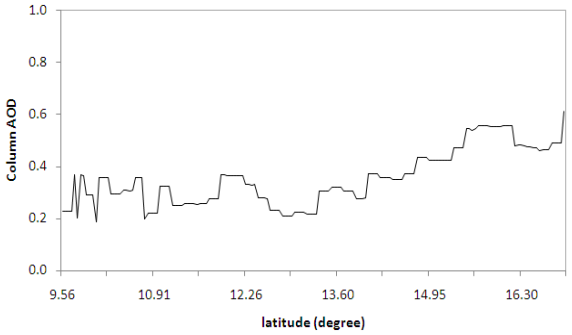

(e) Blue: δ_p, Red: δ_v, Black: AOD, Violet: χ_p

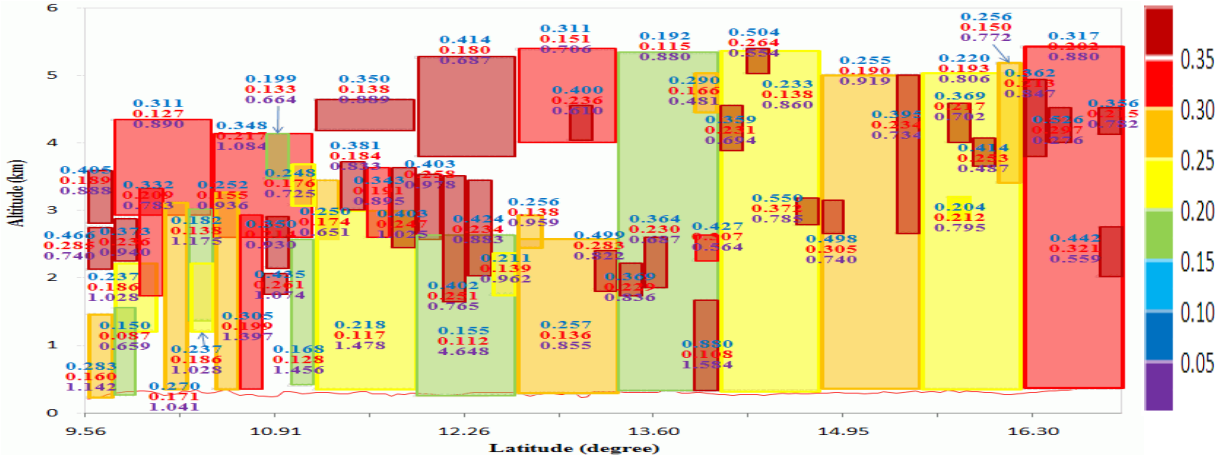

Figure 5.8 Same as Figure 5.3, except for Northern Africa on May 25, 2007.

5.3.2 Comparison of Dust Region-Specific Characteristics

5.3.2.1 Selected representative dust cases

To find the similarities and differences in dust characteristics among the selected dust events over the source regions, Table 5.2 compares the characteristics of dust over the eight sources. In the table, the vertical extent of dust varies from 2.52 km to 10.36 km, but the variation is not significant. The mean $\delta_{p,\,layer}$ is, for the most cases, above 0.3 except for two cases; the Thar Desert (0.262) on May 7, 2007 and Central Asia (0.224) on April 22, 2007. Figures 5.9(left panel) display observed $\delta_{p,\,layer}$ values for the eight source areas, and one can notice that the mean $\delta_{p,\,layer}$ values are high (above 0.3) throughout the eight sources, horizontally and vertically. Interestingly, the mean $\delta_{p,\,layer}$ above 0.4 are observed not only in the Taklamakan Desert but also in the Mojave Desert. The reason that the dust in the Mojave Desert has high mean $\delta_{p,\,layer}$ can be explained by the small number of dust layers detected and needs to be further investigated. The mean $\delta_{v,\,layer}$, is the highest in the Taklamakan Desert (0.299) and similar between the Gobi Desert (0.238 and 0.205 on March 30 and April 1, respectively) and Arabian Peninsula (0.232 and 0.2 on May 18, 2007 and May 7, 2008, respectively). The lowest values are observed in Central Asia (0.065) and the Mojave Deserts (0.097). Figures 5.9 (right panel) shows the horizontal and vertical distribution of layer-integrated volume depolarization ratio for all considered dust sources. The $\chi_{p,layer}$ are generally above 0.9 for all but two cases; the Thar Desert on June 10, 2007 and the Mojave Desert on May 3, 2007. The AODs with high mean value (above 0.6) and high maximum value (above 2.0) are observed in five cases; the Taklamakan and Gobi Deserts on March 30 and April 1, 2007, and the Thar Desert on June 10, 2007. Dust events in Central Asia and the Mojave

Desert had very low AODs (maximum value of below 0.6). To summarize, heavy dust cases were shown in the Taklamakan Desert, the Gobi Deserts, and Arabian Peninsula, and light dust cases occurred in Central Asia and the Mojave Desert. However, the values of $\delta_{p,\ layer,}$ $\delta_{v,\ layer,}$ $\chi_{p,layer,}$ and AOD varied depending on the event and not on the area the event occurred. Accordingly, we investigated the mean values of $\delta_{p,\ layer,}$ $\delta_{v,\ layer,}$ $\chi_{p,layer,}$ and AOD for each spring season in next section.

Table 5.2 Comparison of dust characteristics for selected representative cases.

Location (Albedo)	Date (d:day/ n:night)	Mean Vertical Extent	Mean $\delta_{p,\ layer}$	Mean $\delta_{v,\ layer}$	Mean $\chi_{p,layer}$	Mean AOD(max)
Taklamakan Desert (0.22)	3/30/07(d)	4.92 km	0.443	0.285	0.917	0.869(2.67)
	4/01/07(d)	6.47 km	0.524	0.299	1.097	0.749(2.86)
Gobi Desert (0.22)	3/30/07(d)	6.26 km	0.385	0.238	1.036	0.918(2.62)
	4/01/07(d)	5.93 km	0.339	0.205	1.157	0.609(2.47)
Thar Desert in India (0.22)	5/07/07(d)	4.92 km	0.262	0.160	0.909	0.370(0.83)
	6/10/07(d)	5.13 km	0.333	0.187	0.741	0.879(2.66)
Central Asia (0.22)	4/22/07(d)	3.84 km	0.224	0.112	1.427	0.135(0.55)
	4/23/07(n)	10.36 km	0.326	0.065	1.237	0.062(0.14)
Mojave Desert (0.18)	4/29/07(d)	5.45 km	0.465	0.117	1.128	0.059(0.02)
	5/03/07(n)	2.52 km	0.460	0.097	0.879	0.040(0.33)
Arabian Peninsula(0.35)	5/18/07(d)	5.1 km	0.307	0.200	0.947	0.730(2.41)
	5/07/08(d)	4.6 km	0.361	0.232	1.031	0.407(1.35)
Australia Desert (0.18)	9/23/09(d)	2.96 km	0.321	0.192	1.185	0.279(2.25)
Northern Africa (0.35)	5/25/07(d)	5.42 km	0.315	0.183	1.036	0.371(0.66)

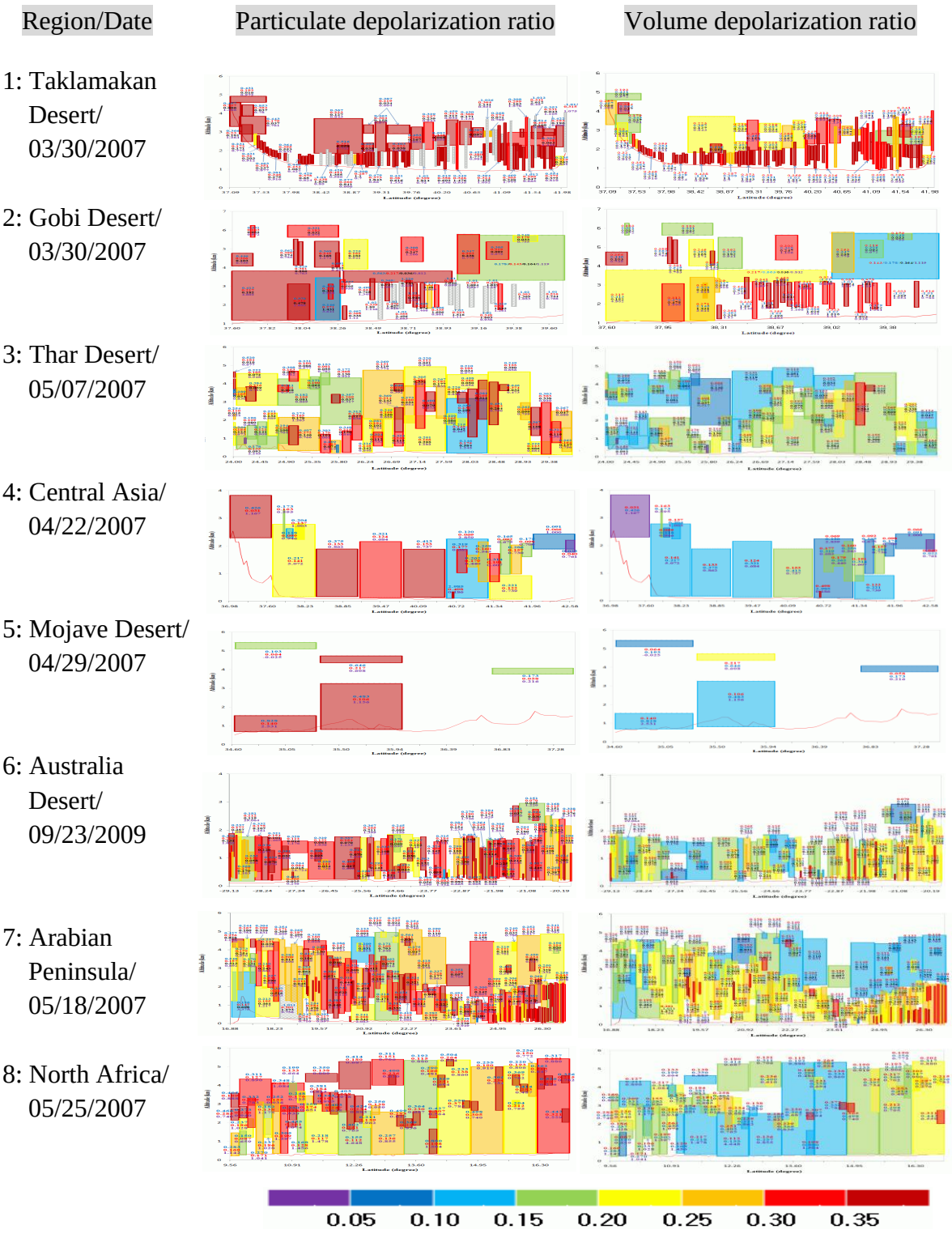

Figure 5.9 Distributions of layer-integrated particulate depolarization ratio (left panel) and layer-integrated volume depolarization ratio (right panel) over eight sources.

5.3.2.2 Intercomparison of Regional Spring Dust Events

To enable intercomparison of regional dust properties, we computed spring season-mean values of of $\delta_{p,\ layer,}$ $\delta_{v,\ layer,}$ $\chi_{p,layer,}$ and AOD in each considered dust source region. The mean properties were computed for all aerosol layers identified by the CALIPSO retrievals as dust. Values of $\delta_{p,\ layer,}$ $\delta_{v,\ layer,}$ $\chi_{p,layer}$ above 3 and below 0, which were deemed unrealistic, were not included in averaging and counting the particulate depolarization and color ratios. Note that the same lidar ratio of 40 sr was used by the CALIPSO algorithms in all cases (see Chapter 2).

Figure 5.10 shows the comparison of the normalized frequency distribution of mean $\delta_{p,layer}$ in all sources for the spring of 2007. Figures are arranged in the order of decreasing values of $\delta_{p,layer}$. The mean value of $\delta_{p,layer}$ is above 0.3 in most regions, except the Australia Desert. The largest mean value (0.385) of $\delta_{p,\ layer}$ was observed in the Taklamakan Desert. Northern Africa, the Gobi Desert, and Arabian Peninsula have high mean $\delta_{p,\ layer}$ (0.335-0.35), and the Australia Desert has the smallest mean $\delta_{p,\ layer}$ (0.274).

The results of our analyses of the normalized frequency distribution of mean $\chi_{p,layer}$ are presented in Figure 5.11, which is organized similarly to Figure 5.10 to facilitate comparison. Central Asia has the smallest mean value (0.814) of $\chi_{p,layer}$, and the Australia Desert has the largest value (1.058) of $\chi_{p,layer}$. Sorting the mean values of $\chi_{p,layer}$ and $\delta_{p,\ layer}$ in the descending order (maximum to minimum), one can notice that the order of mean $\chi_{p,layer}$ is approximately the opposite of $\delta_{p,layer}$. This finding suggest that dust particles in the Taklamakan Desert are likely smaller and more nonspherical than in the other deserts, and the dust particles in the Australia Desert are coarser and less nonspherical compared to other deserts as shown in Figure 5.12(a). Figure 5.12(b) shows that the mean values of $\delta_{p,layer}$ and $\chi_{p,layer}$ are the regional plume's mean top height (i.e.,

the Taklamakan Desert (5.5 km), Northern Africa (4.165 km), Gobi Desert (4.94 km), Arabian Peninsula (4.471 km), Central Asia (3.627 km), Mojave Desert (4.742 km), Thar Desert (3.515 km), and Australia Desert(2.089 km)). The figure also displays that the source regions in the mid-latitude (i.e., the Taklamakan Desert, the Gobi Desert, Central Asia, and Mojave Desert) have relatively low (0.718-0.774) values of $\chi_{p,layer}$, which are related to the jet stream in the mid-latitude.

(a) Taklamakan Desert

(b) Northern Africa

(c) Gobi Desert

(d) Arabian Peninsula

(e) Central Asia

(f) Mojave Desert

(g) Thar Desert

(h) Australia

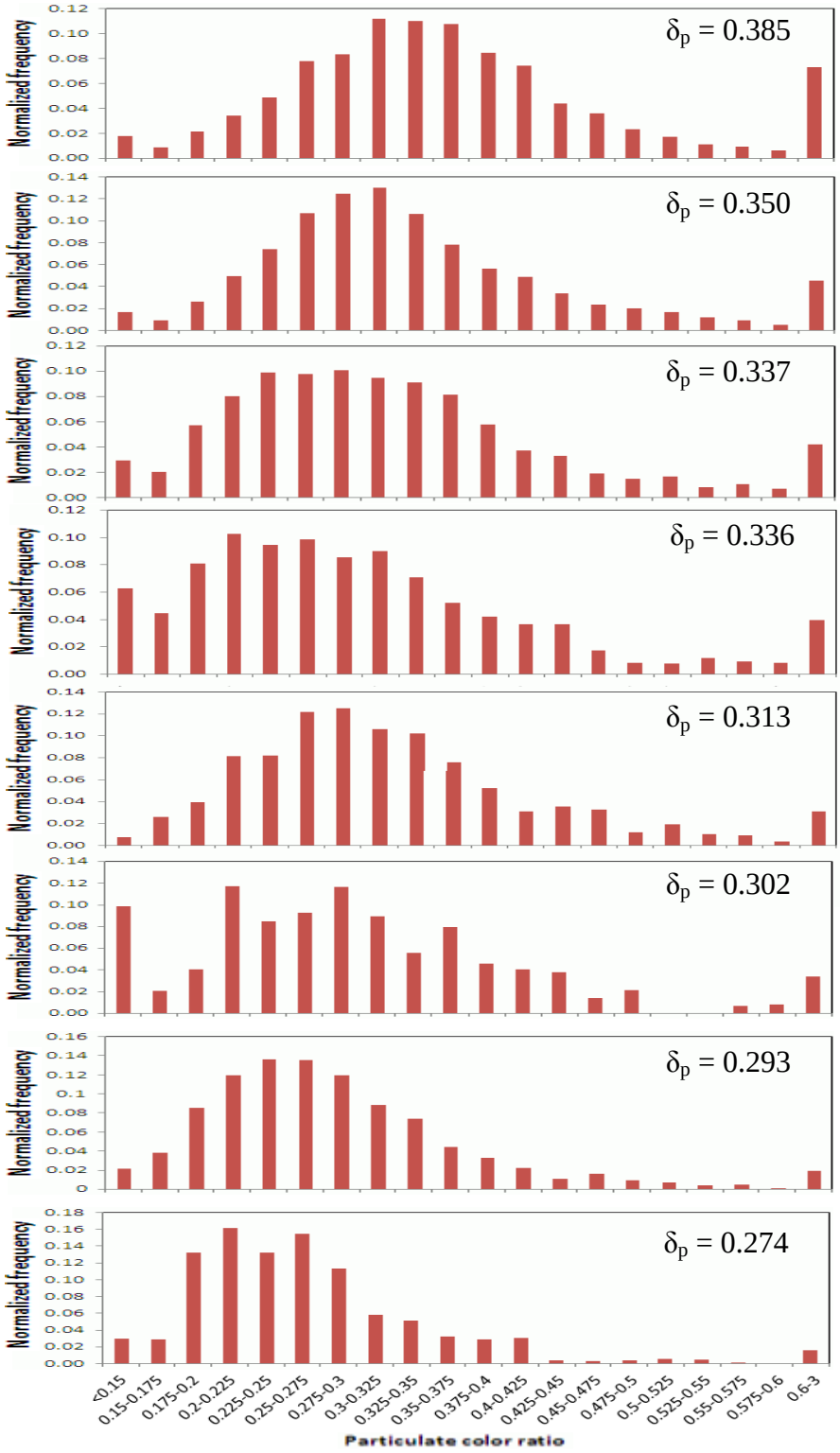

Figure 5.10 Comparison of spring mean δ_p in dust sources (unit is normalized frequency).

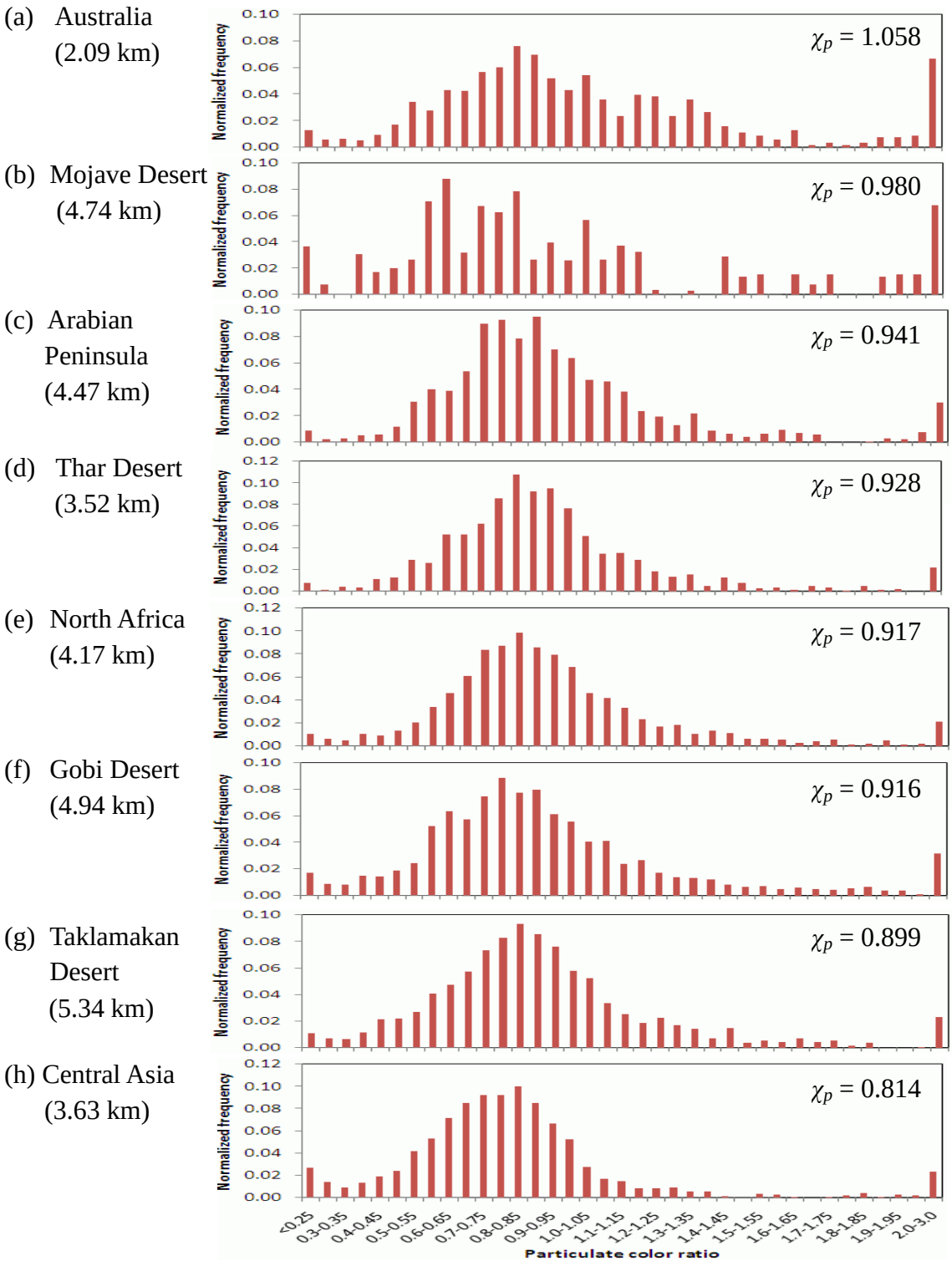

Figure 5.11 Comparison of spring mean χ_p in dust sources (unit is normalized frequency).

(a)

(b)

(c)

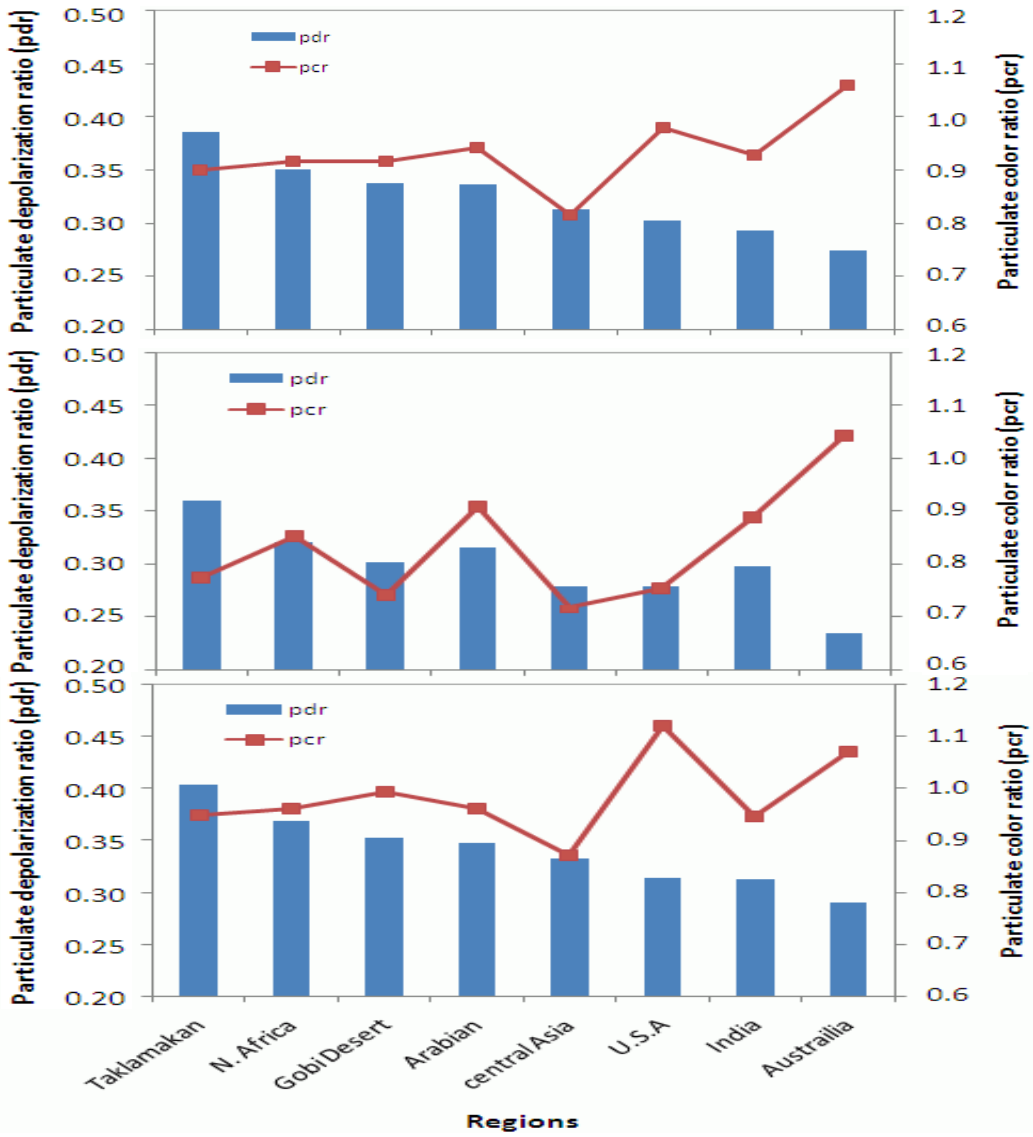

Figure 5.12 Comparison of spring mean values (a) with the values above mean top height (km) (b), and below mean top height (c) of δ_p and χ_p in dust sources.

5.4 Assessments of Radiative Forcing and Heating/Cooling Rates

The radiative transfer modeling was performed with SBDART introduced in Chapter 4. Description of the modeling experiments is given in Table 5.3. They were broadly divided into six cases by the distribution of AODs and re-grouped into three categories according to the surface albedo. The representative values of regional surface albedos were taken from MODIS albedo products.

Table 5.3 Description of dust radiative modeling experiments

		Case 1-1	Case 1-2	Case 2-1	Case 2-2	Case 3-1	Case 3-2
Land Surface Albedo		0.35		0.22		0.18	
Vertical distribution of dust layers (AODs for each 1 km layer)		0-5 km (0.4)	0-6 km (0-3km:0.3, 3-6km:0.03)	0-5 km (0.4)	0-6 km (0-3 km:0.3, 3-6km:0.03)	0-4 km (0.25)	0-2 km (0.25)
Solar zenith angle		31° (local noon), 75° (low Sun angle)					
Atmospheric profile		Mid-latitude summer					
Type of aerosol	ω_0	0.8897					
	g	0.7578					

Two Solar zenith angles are selected for all six cases as shown in Table 5.3; 31° (the cosine of solar zenith angle: 0.85) for local noon, and 75° (the cosine of solar zenith angle: 0.25) for the case of a low Sun angle over mid-latitude area. As mentioned in Chapter 4, the mid-latitude summer, the atmospheric condition of which is similar to that of a mid-latitude spring, was chosen for the atmospheric profile in the study. The albedo of 0.18, 0.22, and 0.35 observed from MODIS is used for desert surface of source. The calculated optical properties of representative dust mixture in Chapter 3 are used to provide SBDART inputs for ω_0 and g. Lastly, the vertical distribution and corresponding AODs of dust layers were constructed for all analyzed cases from CALIPSO

observations.

Figure 5.13 present the results of heating/cooling rates. It is noted that the profile and values of heating/cooling rates are strongly affected by the optical depth, layer height, and surface albedo.

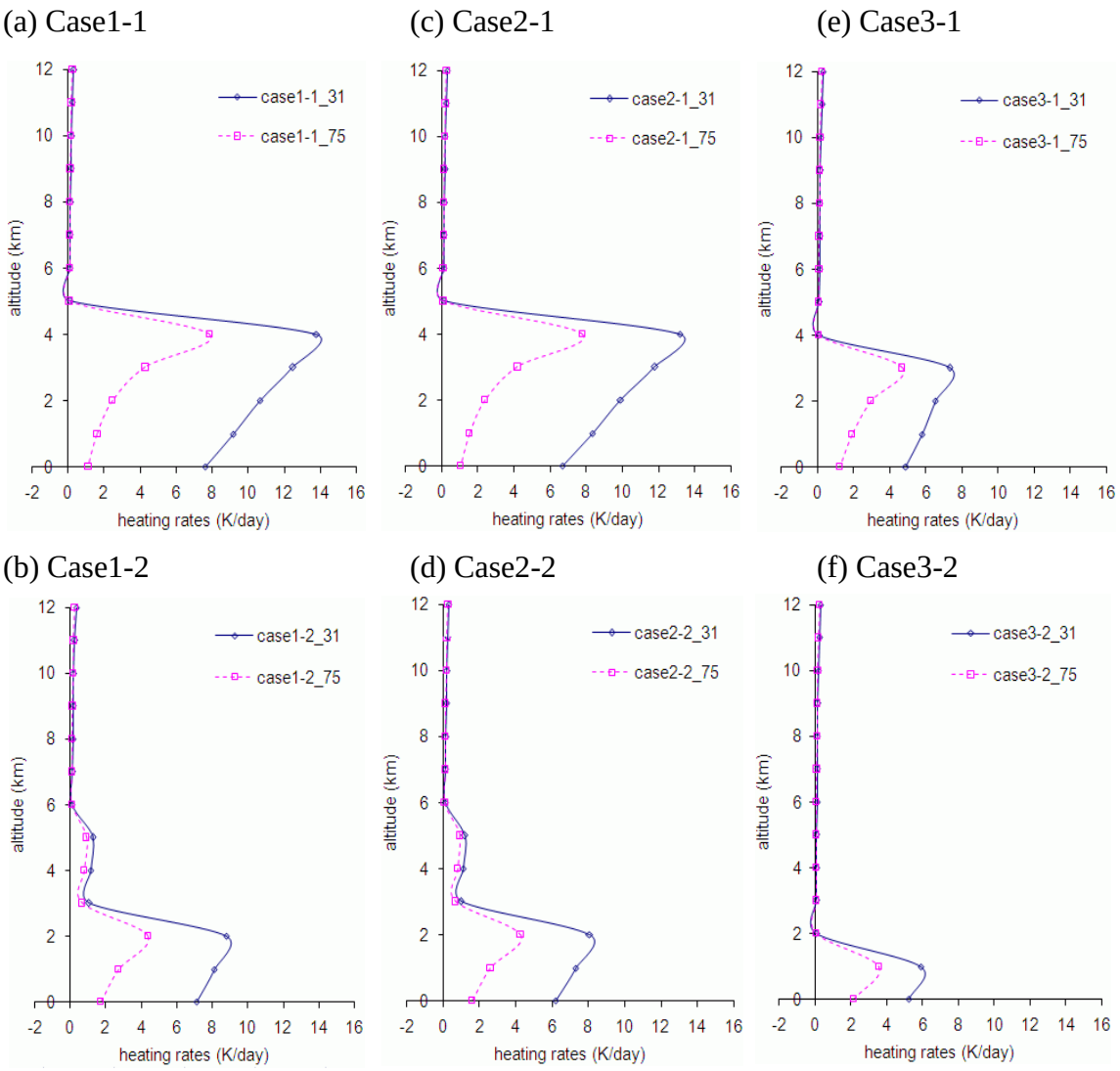

Figure 5.13 Heating rates of dust layers for six cases ((a) case1-1, (b) case1-2, (c) case2-1, (d) case2-2, (e) case3-1, and (f) case3-2) for two solar zenith angles; 31° (local noon) and 75° (low Sun angle).

Figures 5.13(a), (b) (c), and (e) show that the increasing dust loading cause an increase of radiative heating rates. Examining the effect of solar zenith angle reveals that differences in dust radiative heating rates between high and low Sun angle are larger in the case of high surface albedo (0.35) than low albedo (0.22). The higher albedo leads to higher radiative heating rates (see Figures 5.13(a) and (b)).

Figure 5.14 shows the comparison of dust heating rates for the solar zenith angles of 31° (local noon) (Figure 5.14(a)) and 75° (low Sun angle) (Figure 5.14(b)), and for the case 1-2 and case 2-2 (Figure 5.14(c)). The figures display that the dust heating rates depends on the value of AODs (and the surface albedo as discussed above). The difference of albedo near the surface between the case 1-1 and 2-1 in Figure 5.14(a) causes the change in dust heating/cooling rate of those two cases, while AOD differences do not affect dust heating/cooling rate near the surface in the case3-1 and 3-2.

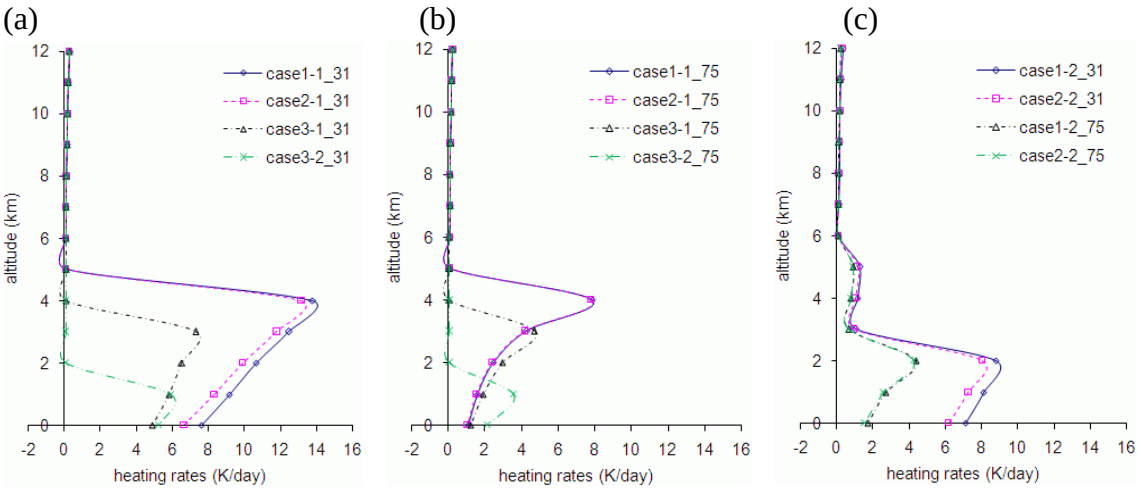

Figure 5.14 Comparison of dust heating rates for (a) the solar zenith angle of 31° (local noon), (b) 75° (low Sun angle), and (c) case1-2 vs. case2-2, respectively.

When the Solar angle is low (75°), the dust heating/cooling rates near the surface are very similar in three cases (i.e., case1-1, 2-1, and 3-1) as shown in Figure 5.14(b). The albedo difference affects the heating/cooling rate in high Sun angle (31°) but not in low Sun angle (75°) as in Figure 5.14(c).

Similar to Chapter 4, here we also computed the radiative forcing of dust in the regional dust sources. The definition of the ΔF_{TOA} and ΔF_{sur} (in W m^{-2}) is given by Eqs (4.1) and (4.2) in Chapter 4. Figure 5.15 displays the values of dust radiative forcing at TOA (a) and at the surface (b). At the top of the atmosphere, dust causes a positive forcing at high Sun angle (solar zenith angle=31°) due to the difference between the albedo of dust layers and desert surface; however, the positive forcing decreases with decreasing AODs and surface albedo. A negative forcing occurs over the bright surface when the Sun angle changes from 31° to 75° due to the increase in dust scattering as mentioned in Chapter 4, except for the case1-1 (ΔF_{TOA} =3.61) with the solar zenith angle of 75°. This means that dust contributes to the heating (at high Sun angle) and cooling (at low Sun angle) of the atmosphere-underlying surface system.

At the surface, dust causes a negative forcing at all Sun angles and over all surface types. Interestingly, the magnitude of the dust negative forcing at high Sun angle (31°) is very similar to that in case1-1 (ΔF_{sur}=-586.3) and case1-2 (ΔF_{sur}=-593.16). The negative forcing of dust at two Sun angles in cases 1-2, 2-2, and 3-1 are also very similar. Based on this modeling we conclude that the AODs are more important than the surface albedo in dust radiative forcing in desert and semi-desert regions.

(a)

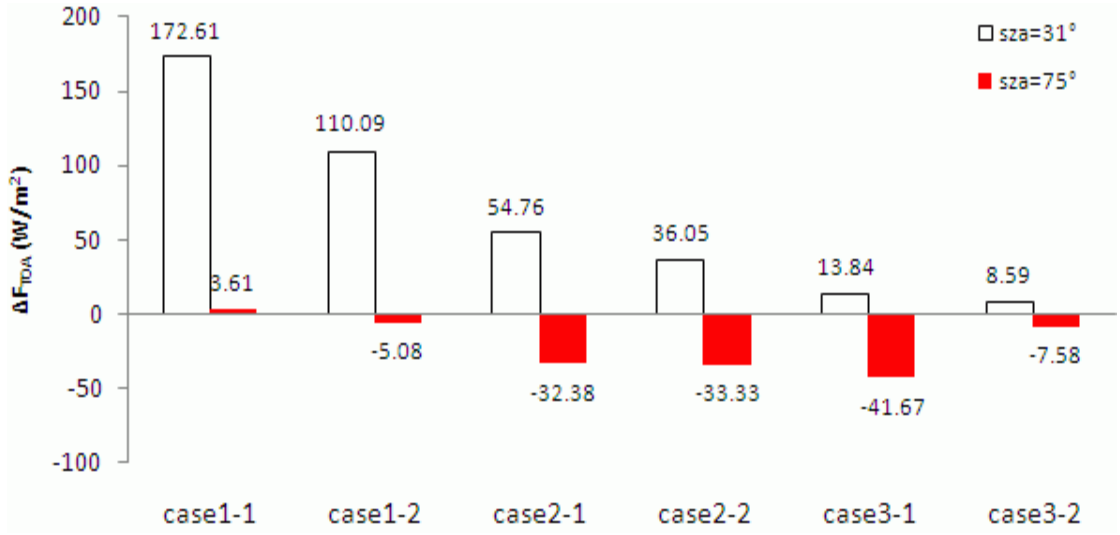

(b)

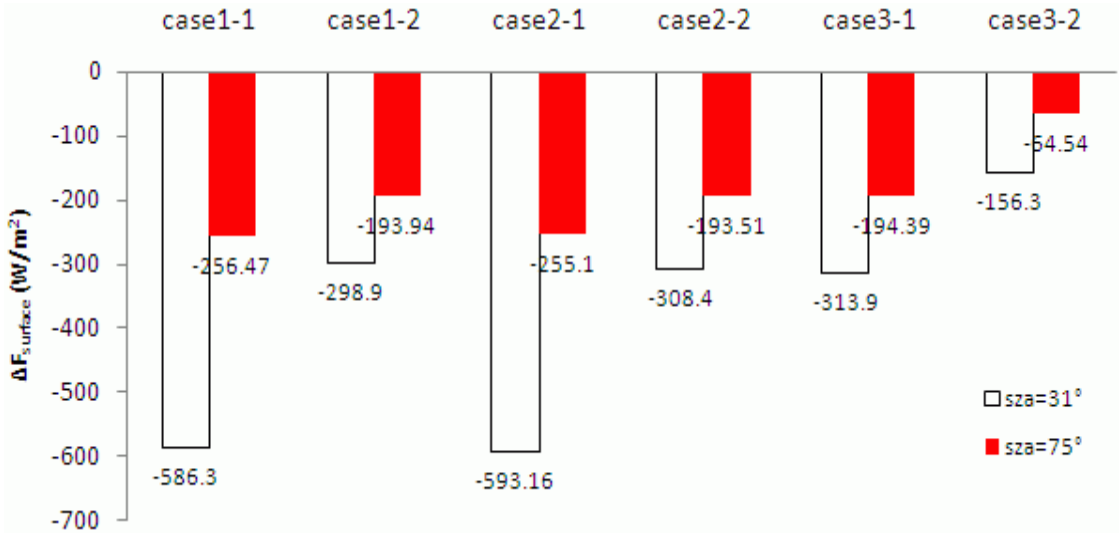

Figure 5.15 Net dust radiative forcing at TOA (a) and at the surface (b) for the solar zenith angle of 31° (white bar) and 75° (red bar) for six cases (see Table 5.3).

5.5 Summary

In this chapter, we examined and compared the spatial and optical properties of dust in the world's source regions, focusing on the active dust season (spring). Similar to Chapter 4, our analysis of CALIPSO data was augmented by data from the A-Train constellation (MODIS, OMI, and CloudSat satellite sensors). This is a first study that examined multi-year CALIPSO data records in the major dust sources. The results provide important insights into the regional nature of mineral aerosols and contribute to improve understanding of properties of dust originating from various deserts and its impacts on the Earth's climate system.

Some major findings are as follows:

1) Our analysis demonstrated that the new version 3.01 of CALIPSO data which includes particulate depolarization and color ratios provides a good opportunity to examine the characteristics of dust originating from dust sources over the world.

2) This study found that the values of mean $\delta_{p,\,layer,}$ of dust originating from eight dust sources vary from 0.274 in the Australia Desert to 0.385 in the Taklamakan Desert. Examining the mean $\chi_{p,layer}$ revealed that, with the exception of Central Asia, the size of dust particles is large in all source areas with the mean $\chi_{p,layer}$ above 0.9. In addition, the mean $\chi_{p,layer}$ in six dust sources (i.e., Taklamakan Desert, Gobi Desert, Thar Desert, Australia Desert (20°–30°S, 125°–140°E), Arabian Peninsula, Northern Africa) show an opposite trend to the mean $\delta_{p,\,layer}$, increasing in values when the mean $\delta_{p,\,layer}$, decreases decreasing. This indicates that dust particles although nonspherical in all sources, still exhibit the regional specific nonspherical features, most likely due to differences in shapes. .

3) This study found that the particulate depolarization ratio remain high (above 0.3) across dust plumes in dust source regions, but the volume depolarization and color ratios continuously decrease from the surface to the elevated altitude. This suggests that dust particles keep their shapes although the number of larger dust particles decreases vertically. The δ_p remains constant, suggesting that climate models need to treat dust as nonspherical particles in and near source areas.

4) The radiative transfer modeling of regional radiative impacts of dust was performed using the SBDART model, computed dust optical properties (presented in Chapter 3), and representative cases of dust events reconstructed from CALIPSO data. Since the largest heating/cooling rates occurred at the top of the dust layer, CALIPSO vertical profile data provide a key information for their assessment. The increasing dust loadings always result in an increase of radiative heating rate. Examining the effect of solar zenith angle shows that differences in dust radiative heating rates between high and low Sun angle are larger in the case of high albedo (0.3-0.35) than low albedo (~ 0.2). The increase in surface albedo from abot 0.2 to 0.35 causes additional radiative heating of about 1 K/day at AOD=2. The surface albedo difference affects the heating/cooling rate at high Sun angle (31°) but not at low Sun angle (75°). Overall, the dust heating rates depends on the value of AODs and surface albedo.

5) A positive forcing of dust at TOA over dust sources was found at high Sun angle (solar zenith angle=31°) in al regional cases. However, the forcing becomes negative with the increasing Sun angle from 31° to 75°, except for the cases when the surface albedo is high (0.35). This indicates that high surface albedo and AOD at low Sun

angle (75°) may contribute to positive dust radiative forcing. For example, Northern Africa and Arabian Peninsula have a high albedo of around 0.35-0.4 (see Figure 5.16). Thus, region specific surface albedo and dust properties will need to be accounted for in assessments of regional radiative energy balance to improve the global energy balance estimates in climate studies.

.

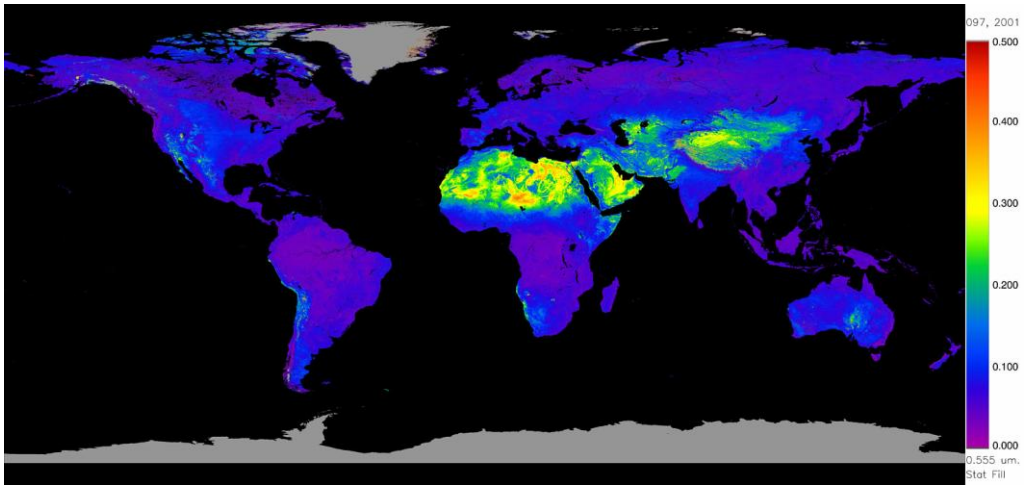

Figure 5.16 The Filled Land Surface Albedo Product in the spring season of 2001, which is generated from MOD43B3 (the official Terra/MODIS-derived Land Surface Albedo Product).

CHAPTER 6

SUMMARY AND CONCLUSIONS

6.1 Conclusions

Since its launch in April 2006, the CALIPSO satellite mission has been providing unique and important observations of aerosols and clouds. The CALIOP (Cloud and Aerosol LIdar with Orthogonal Polarization) on board the CALIPSO platform measures the vertical profiles of atmospheric features' backscatter and polarization, allowing a determination of the vertical distribution of aerosol and clouds on the global scale at night- and day-time over all surface types. Polarization measurements provide an ability to perform height-resolved discrimination of mineral dust aerosol from other aerosol types and most clouds. The very first CALIPSO product (version 2 data) included volume attenuated optical properties while the most recent version 3.03 (released in June 2010) provides aerosol properties (particulate depolarization, extinction, and particle color ration) that can be used directly to study physical and optical properties of dust. However, given the difficulties of performing measurements from space and the complex nature of mineral dust itself, a comprehensive examination of the performance of CALIPSO retrieval algorithms and the realism of aerosol products in the dust-laden conditions must be performed. The dust sources have the heterogeneous spatial distribution around the world, exhibiting various distinct features such as geomorphology, climate, prevailing winds fields, and dust properties. Thus, it is highly desirable to examine CALIPSO products over the major dust source regions that, on the other hand, offer a unique opportunity to characterize the region-specific properties and vertical distribution of dust.

Knowledge of the aerosol vertical profile is particularly important because aerosol residence time, and thus radiative impact, increase significantly when aerosol is lofted high about the boundary layer. Dust vertical profiles formed in dust source regions control where and for how long mineral dust particles will be transported in the atmosphere. In addition, the vertical position of a dust layer is a major factor controlling the radiative heating and hence the dynamics and thermodynamics of the atmosphere. Having CALIPSO flown in formation with several other satellites as part of the A-train constellation permits the acquisition of simultaneous and coincident observations from multiple sensors offering another unique tool for dust studies.

The research presented in this dissertation leverages these new remote sensing capabilities by: 1) examining the retrieval procedure of CALIPSO lidar version 2 and new version 3.01 data and its performances in dust-laden conditions; 2) performing an optical modeling of nonspherical dust particles to aid in the retrievals and interpretation of CALIPSO data and provide the single scattering albedo and asymmetry parameter for the radiative transfer modeling; 3) developing a methodology for examining CALIPSO lidar data of individual dust events on a case-by-case basis; 4) applying this methodology to CALIPSO data from 2006-2010 to determine the spatiotemporal dynamics and physical and optical properties of Asian dust in its source regions in East Asia (China and Mongolia) and downwind, focusing on changes in dust plumes in the sources to mid- and long-range transported dust; 5) computing the radiative forcing and heating rates of Asian dust constrained by CALIPSO lidar data and optical modeling of freshly emitted dust in the sources and aged dust downwind; 6) and determining the region-specific features of dust aerosol in the world's major dust sources in terms of CALIPSO-observed aerosol

characteristics, including assessments of the radiative forcing and heating rates in each dust source region.

An in-depth examination of aerosol retrieval procedures (including SIBYL, SCA, CAD, Aerosol subtyping, and HERA algorithms) presented in Chapter 2 enabled us to identify various problems in the version 2 data in dust-laden conditions. These biases were reported to the CALIPSO Science Team and led to the improvements in the most recent level 2 version 3.01 data. The version 2 data have significant errors in heavy dust-laden conditions in dust sources and in many instances in dust-cloud mixed scenes. In particular, dust layers near the surface were frequently misclassified as clouds. For the same cases, our analyses demonstrated that the new version 3.01 data showed a better discrimination between clouds and aerosols by using 5D PDFs instead of 3D PDFs used in the algorithm of version 2 data. We found that the aerosol optical depth (AOD) of version 3.01 data is more accurate and in better agreement with independent observations. This was achieved by adding the aerosol layer base extension algorithm in the SIBYL algorithm. Another important aspect is that version 3.01 data were retrieved with the different lidar ratios for dust at 1064 nm and polluted dust at 532 nm and 1,064 nm. Overall, based on many improvements in the CALIPSO retrieval algorithm, we believe that version 3.01 data are much better suited for dust studies compared to the previous version 2 data. Our findings question the validity of some results on the dust properties and impacts reported by past studies based on CALIPSO version 2 data.

Despite their significant improvements, detailed analyses of the new CALIPSO level 2 version 3.01 data, however, revealed some remaining biases seen in the version 2 data, as well as some new errors. For example, negative or relatively high values of above

3 of particulate depolarization and color ratios in the version 3.01 data indicate that the new data wrongly discriminate between aerosol and cloud, or use a wrong lidar ratio. In particular, our optical modeling results suggest that a fixed value S_a = 40 sr used for dust in the CALIPSO retrieval algorithm may cause significant biases in the retrieved extinction coefficient and aerosol optical depth, especially in the cases of very dense dust layers and dust-mixed scenes. .

To aid in the retrievals and the interpretation of CALIOP data, intensive optical simulations constrained by recent measurements of dust shape, size distribution, and composition were performed. The goal was to examine the extent to which the microphysical properties of dust particles affect the optical characteristics used in lidar remote sensing (see Chapter 3). We developed a unified technique by merging two different approaches, the T-matrix and IGOM, which enable us to cover the broad range of sizes and composition of nonspherical dust particles in optical modeling. In particular, we examined the effect of the aspect ratio distribution, fine and coarse modes, and composition on δ_p and S_a at the 532 nm lidar wavelength. For the effect of size distribution and composition, when the real part of the refractive index varies from 1.52 to 1.56, δ_p and g at 532 nm decreases down to 0.05 and 0.017, respectively while S_a and ω_0 increase up to 9.7 and 0.0028, respectively. As the imaginary part, which represents the amount of the absorption of the wave as it propagates through the medium, increases from 0.003 to 0.006, S_a and g increase while ω_0 decreases, and there is no special pattern of δ_p. This result implies that the changes in the imaginary part of the refractive index do not have a noticeable impact on the particle depolarization ratio, δ_p.

The results indicate that as the fraction of coarse dust particles decrease, e.g., during the atmospheric transport, the particulate depolarization ratio (δ_p) does not change while the lidar ratio (S_a) at 532 nm decreases significantly. This suggest that using the same lidar ratio (S_a = 40 sr) in the CALIOP algorithm for dust retrievals in dust sources and remote areas downwind is not valid. Furthermore, the regional difference in dust properties may result in different lidar ratio values so that treatments of varying lidar ratio (as a function of dust source and distance from the source) will need to be incorporated in the future CALIPSO retrieval to provide more realistic dust products. This result also suggests that the values of ω_0 and g that are required in the modeling of dust radiative forcing and in many remote sensing applications should be varied depending on the location of dust plumes (source vs. downwind areas), or on the size distribution of dust particles.

We performed a comprehensive analysis of the CALIPSO version 3.01 data with the goal to characterize Asian dust events during the spring seasons of 2007-2010 in the dust sources and downwind areas on a case-by-case basis. We found that during mid- and long-range transport, particulate depolarization ratio of Asian dust remains high (~ 0.3), while the volume depolarization and color ratios continuously decrease along the dust transport route from the deserts to the Pacific Ocean. This indicates that dust particles most likely do not change shapes, but the relative number of coarse dust particles decreases during transport. One important implication is the need for climate and chemical transport models to treat dust as nonspherical particles in both the source regions and remote areas.

In addition to Asian dust, we examined dust episodes in the world's major dust source regions. For this analysis, we identified individual CALIPSO tracks in each region of interest during the spring seasons, selected several representative cases, and then performed detailed examination of CALIPSO data in each case. We also estimated area-mean dust characteristics (i.e., spring mean values over each source region) in order to determine the source-specific dust features. Our results demonstrated that vertical distributions of Asian dust optical properties in the source regions (i.e., the Taklamakan and Gobi Deserts) are highly variable compared to the low variability in the case of Saharan dust reported by Liu et al. (2008). This finding points to some regional differences in dust properties: the existence of a region specific vertical distribution of dust and its optical properties. We also found some similarities in the vertical distribution and properties of dust in the considered regions: $\delta_{p,layer}$ shows little variability vertically and horizontally along the CALIPSO tracks, while $\delta_{v,layer}$ and $\chi_{p,layer}$ decrease from the surface up. Each source region has the certain vertical distribution and values of $\delta_{p,layer}$, $\delta_{v,layer}$, and $\chi_{p,layer}$ of dust. For example, the largest mean value (0.385) of $\delta_{p,\ layer}$ was observed in the Taklamakan Desert. Northern Africa, the Gobi Desert, and Arabian Peninsula had high mean $\delta_{p,\ layer}$ (0.335-0.35), and the Australia Desert had the smallest mean $\delta_{p,\ layer}$ (0.274), although the mean value of $\delta_{p,layer}$ was above 0.3 in most areas except for the Australia Desert. On the contrary, the Taklamakan Desert had the smallest mean value of $\chi_{p,layer}$ (0.899), while the Australia Desert had the largest value ($\chi_{p,layer}$= 1.058)

Based on the vertical distributions and optical properties of dust (presented in Chapters 3, 4, and 5), we computed the radiative forcing and heating/cooling rates caused by dust in each source region as well as in the remote areas affected by transported dust.

The differences in vertical profiles and AODs between dust source regions resulted in a difference of around 5 K/day in the maximum heating rates at the top of the dust layer. The difference in the heating rates of dust affects the temperature profile and thus may contribute to maintaining a warmer and deeper dust air layer or enhancing the strength of the mid-level easterly jet over the dust sources. Examining the effect of the solar zenith angle, the difference of dust radiative heating rates between high and low Sun angles was found to be larger in the case of high surface albedo. The increasing albedo results in increasing radiative heating rates. The results of dust radiative forcing show that a positive forcing of dust occurs at TOA over all dust sources at the high Sun angle (solar zenith angle=31°), but a negative forcing was found over the bright surface when the Sun angle increases from 31° to 75°, except for the case of very high surface albedo (0.3-0.4). This indicates that high surface albedo and AOD at low Sun angle (75°) favor positive dust radiative forcing. Hence, such dust sources like Northern Africa and Arabian Peninsula with very high surface albedo and AOD predominantly have positive dust radiative forcing. During the mid- and long-range transport of dust, AOD and surface albedo decrease, so that dust always cause a negative radiative forcing, unless dust plumes are being transported above cloud layers. In the latter case, the dust forcing will be positive because of high cloud reflectivity.

6.2 Future Work

The results of this study demonstrate that, compared with the previous level 2 version 2 data, the new CALIPSO version 3.01 data can provide important information about the optical and physical characteristics of mineral aerosol and its vertical

distribution in the world's dust sources and downwind. With improved CALIPSO data, we can more accurately assess the impact of dust aerosols on the radiative energy balance and climate. However, the CALIPSO level 2 version 3.01 data still have some errors such as negative values or too high values of particulate depolarization and color ratios in dust laden-conditions.

This study mainly focused on the spring season, especially the year of 2007, since spring is the most active dust season in many dust sources. However, in the Northern Africa, Central Asia and the Arabian Peninsula high dust activity also occurs in the summer season and sometimes in fall and winter. The methodology developed in this dissertation can be applied to CALIPSO lidar data to provide regional dust characterization, and seasonal and interannual variability.

Optical modeling for CALIPSO lidar applications will need to include more realistic shapes of dust particles. Although we demonstrated the capability of spheroidal mixtures to reproduce some lidar measurements, various limitations were also found. Our work stresses the need for more complex optical models (such as the Discrete Dipole Approximation, DDA) that are capable of treating actual dust particle shapes. The combination of CALIPSO data (i.e., vertical distribution and AOD) and the optics modeling (single scattering albedo and asymmetry parameter) enables better assessments of the radiative forcing and heating/cooling rates of dust aerosols. The results suggested that both the vertical distributions of aerosol and their optical properties are important in the calculations of radiative forcing. Unfortunately, CALIPSO has only limited capability in profiling the mixed dust-cloud scenes. Thus, the dust below heavy clouds would be undetected. Nevertheless, analyses of dust-clouds mixed scenes have the potential to shed

new light on the radiative energy balance as well as contribute to improved understanding of dust-cloud interactions.

Future work will benefit from:

1) the analyses of dust plumes combining CALIPSO and MISR. The combination of these two satellite sensors enables reconstruction of a more complete 3D dust plume structure in the dust sources.
2) the integration of the CALIPSO data and regional transport models to improve the treatments of dust in the weather and climate models, ultimately leading to improved understanding of dust aerosols and their impacts on the Erath system.

APPENDIX A

ADDITIONAL TABLES

Table A.1 Comparative Summary of Dust Properties Retrieved from CALIPSO for mid-range transported dust events during May 28-June 1, 2008 (Dust properties means that data retrieved with the lidar ratio of 40 sr).

Date	5/28	5/29	5/30	5/31	6/1
Location (latitude, longitude)	Gobi Desert (35.8N, 112E-44.6N, 109.2E)	Northern China (34.1N, 112.2E-50N, 117.5E)	Korea (31.9N,125.5E-41N, 128.1E)	Eastern Korea (33.5N, 129.7E-41.3N, 127.3E)	Japan (35.2N,143.1E-38.7N,142E)
Vertical extent (km)	0.741-5.232	0.262-10.037	0.023-9.498	0.053-4.274	0.023-3.675
$\delta_{v,layer}$ (average)	0.101-0.416 (0.224)	0.054-0.337 (0.125)	0.050-0.294 (0.117)	0.111-0.732 (0.178)	0.062-0.284 (0.116)
$\delta_{p,layer}$ (average)	0.157-2.051 (0.411)	0.075-1.459 (0.392)	0.086-2.074 (0.343)	0.155-1.305 (0.302)	0.174-0.567 (0.326)
Color ratio	0.540-4.328 (1.479)	0.097-2.421 (0.939)	0.069-2.318 (0.847)	0.122-1.608 (0.896)	0.336-0.972 (0.715)
Dust optical depth	0.021-1.639 (0.545)	0.006-1.244 (0.141)	0.007-0.726 (0.151)	0.014-0.788 (0.260)	0.008-0.155 (0.046)
Aerosol optical depth	0.021-2.852 (0.637)	0.006-1.783 (0.159)	0.007-2.712 (0.271)	0.050-0.788 (0.286)	0.008-0.498 (0.159)

- $\delta_{v,layer}$: The layer integrated volume depolarization ratio
- $\delta_{p,layer}$: The layer integrated particulate depolarization ratio
- Dust optical depth indicates the integrated values of 532 nm feature optical depth with the lidar ratio of 40 sr at each point.
- Aerosol optical depth indicates the integrated values of 532 nm feature optical depth at each point.

Table A.2 Same as Table A.1, but for March 16 - 20, 2009.

Date	3/16	3/17	3/18	3/19	3/20
Location (latitude, longitude)	Gobi Desert (32.8N, 104E-45N, 108E)	Korea (28.5N, 134E-40.1N, 130.8E)	Japan (26.1N,148.5E-38.2N, 145.2E)	Mid-Pacific (28.4N, 169.3E-41.9N, 173.2E)	Eastern Pacific (29N,151.9W-36.8N,149.7W)
Vertical extent (km)	1.00-11.00	0.023-7.926	0.053-8.046	0.023-10.217	0.023-11.893
$\delta_{v,layer}$ (average)	No CALIPSO data	0.082-0.403 (0.153)	0.086-0.267 (0.152)	0.057-0.228 (0.089)	0.050-0.139 (0.073)
$\delta_{p,layer}$ (average)		0.121-1.033 (0.281)	0.063-2.168 (0.288)	0.152-0.495 (0.305)	0.207-0.580 (0.296)
Color ratio		0.362-1.372 (0.835)	0.412-1.383 (0.887)	0.341-1.109 (0.788)	0.436-1.069 (0.702)
Dust optical depth		0.010-1.522 (0.275)	0.030-1.241 (0.319)	0.008-0.240 (0.055)	0.005-0.067 (0.019)
Aerosol optical depth		0.010-1.522 (0.316)	0.035-2.314 (0.401)	0.009-0.771 (0.180)	0.005-2.243 (0.062)

- $\delta_{v,layer}$: The layer integrated volume depolarization ratio
- $\delta_{p,layer}$: The layer integrated particulate depolarization ratio
- Dust optical depth indicates the integrated values of 532 nm feature optical depth with the lidar ratio of 40 sr at each point.
- Aerosol optical depth indicates the integrated values of 532 nm feature optical depth at each point.

Table A.3 Same as Table A.1, but for March 19 - 25, 2010.

Date	3/19	3/20	3/21	3/22
Location (latitude, longitude)	Gobi Desert (27.6N, 102.7E-44.5N, 107.7E)	Northern China (30N, 117.2E-42.7N, 121.7E)	East Sea/Japan Sea (24.6N,129.8E-45.1N, 135.7E)	Western Pacific (22.6N, 143.2E-49.7N, 151.4E)
Vertical extent (km)	0.532-11.414	0.05-10.76	0.023-10.217	0.0-11.06
$\delta_{v,layer}$ (average)	0.025-0.490 (0.128)	0.046-0.687 (0.134)	0.043-0.750 (0.110)	0.025-0.360 (0.106)
$\delta_{p,layer}$ (average)	0.038-4.734 (0.390)	0.126-0.824 (0.315)	0.069-1.982 (0.340)	0.053-3.269 (0.303)
Color ratio	0.167-3.750 (0.982)	0.269-3.184 (0.935)	0.221-2.820 (0.897)	0.254-2.716 (0.914)
Dust optical depth	0.006-4.574 (0.586)	0.009-2.439 (0.490)	0.007-1.970 (0.151)	0.003-1.024 (0.109)
Aerosol optical depth	0.009-4.574 (0.695)	0.015-2.817 (0.481)	0.009-2.986 (0.364)	0.011-3.160 (0.365)

Date	3/23	3/24	3/25
Location (latitude, longitude)	Mid-Pacific (26.5N, 177.2W-39.9N, 173.5W)	Eastern Pacific (32.5N, 137W-39.8N, 134.9W)	Western United States (26.1N,124.8W-39.9N, 121W)
Vertical extent (km)	0.053-13.39	2.897-10.875	0.143-11.474
$\delta_{v,layer}$ (average)	0.015-0.194 (0.102)	0.057-0.126 (0.081)	0.019-0.29 (0.078)
$\delta_{p,layer}$ (average)	0.051-1.18 (0.334)	0.121-0.407 (0.274)	0.051-0.582 (0.281)
Color ratio	0.101-1.916 (0.843)	0.367-0.769 (0.620)	0.372-1.486 (0.771)
Dust optical depth	0.002-0.270 (0.090)	0.005-0.156 (0.033)	0.004-0.161 (0.037)
Aerosol optical depth	0.005-3.220 (0.191)	0.014-0.347 (0.116)	0.004-3.936 (0.102)

- $\delta_{v,layer}$: The layer integrated volume depolarization ratio
- $\delta_{p,layer}$: The layer integrated particulate depolarization ratio
- Dust optical depth indicates the integrated values of 532 nm feature optical depth with the lidar ratio of 40 sr at each point.
- Aerosol optical depth indicates that the integrated values of 532 nm feature optical depth at each point.

APPENDIX B

ADDITIONAL FIGURES

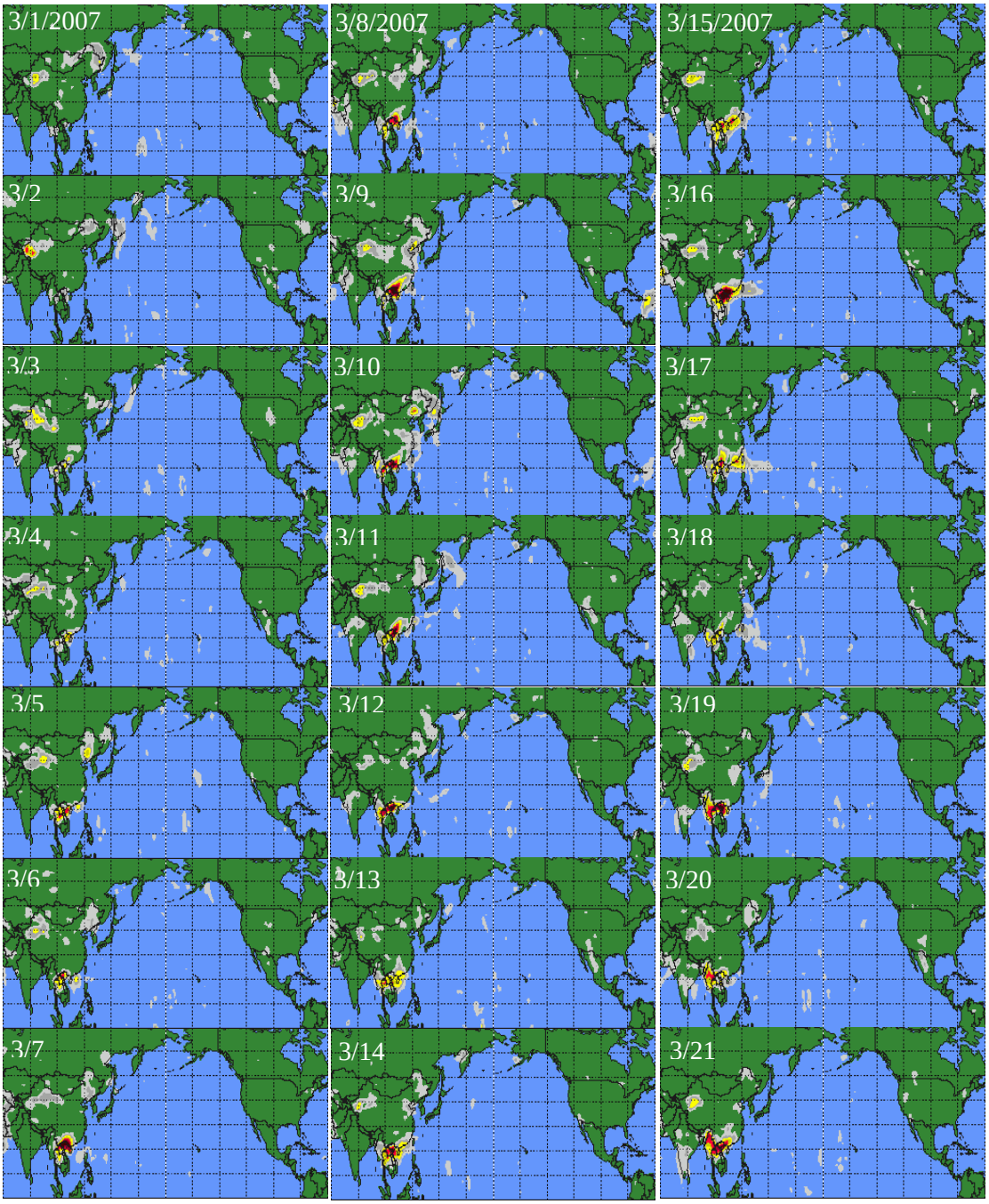

Figure B.1 Aerosol Index from OMI-Aura for the spring season of 2007.

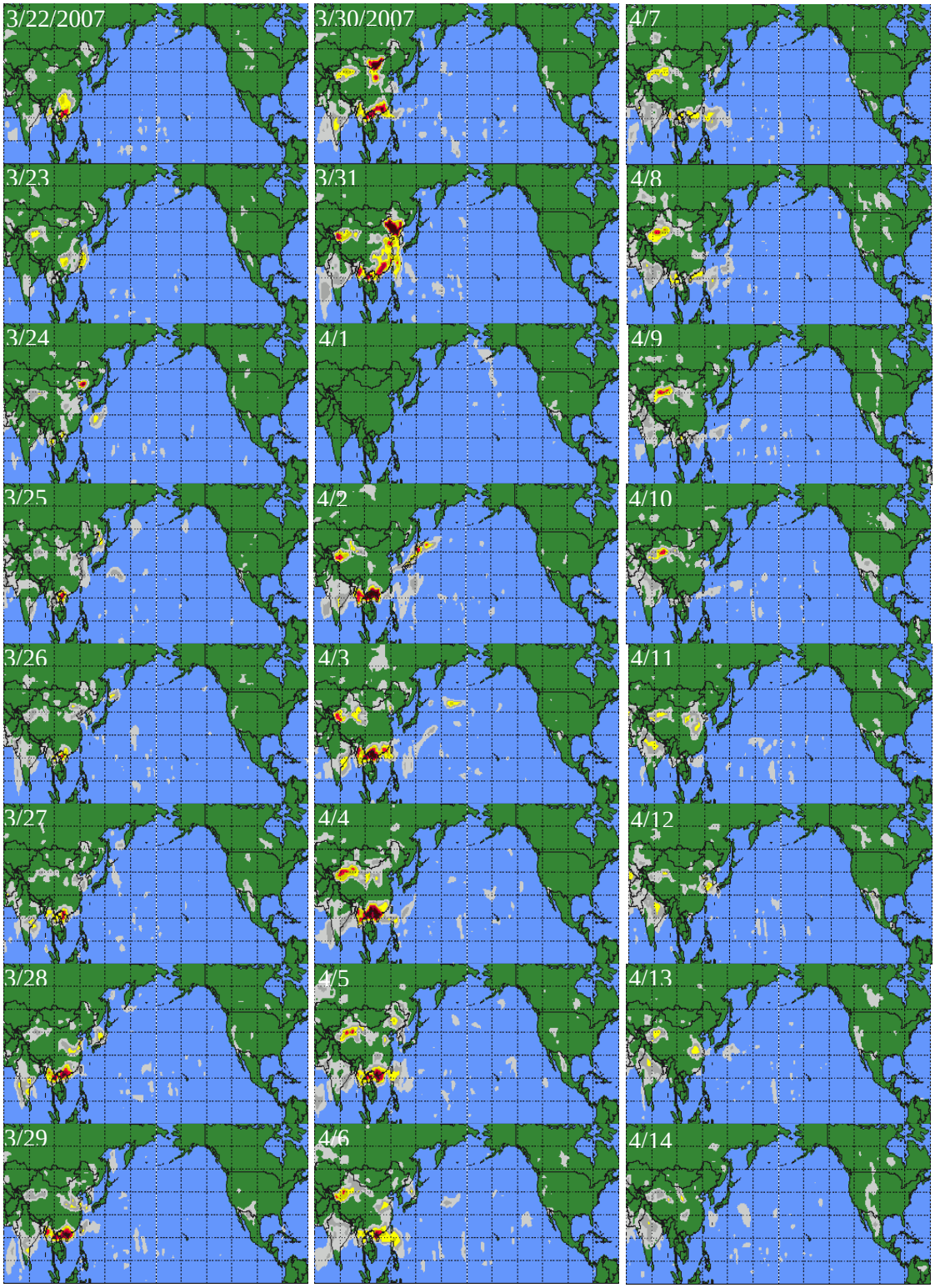

Figure B.1 (continued).

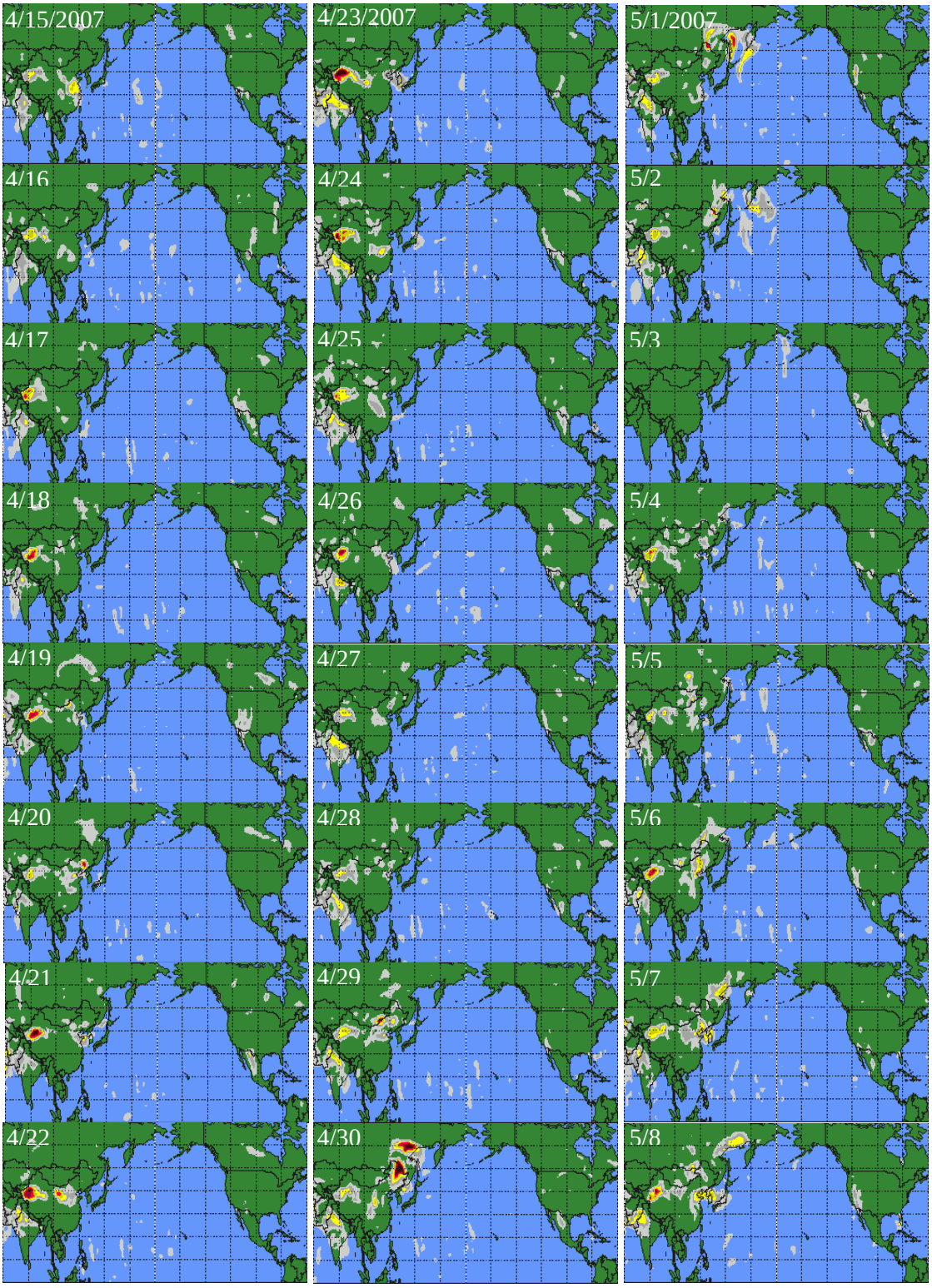

Figure B.1 (continued).

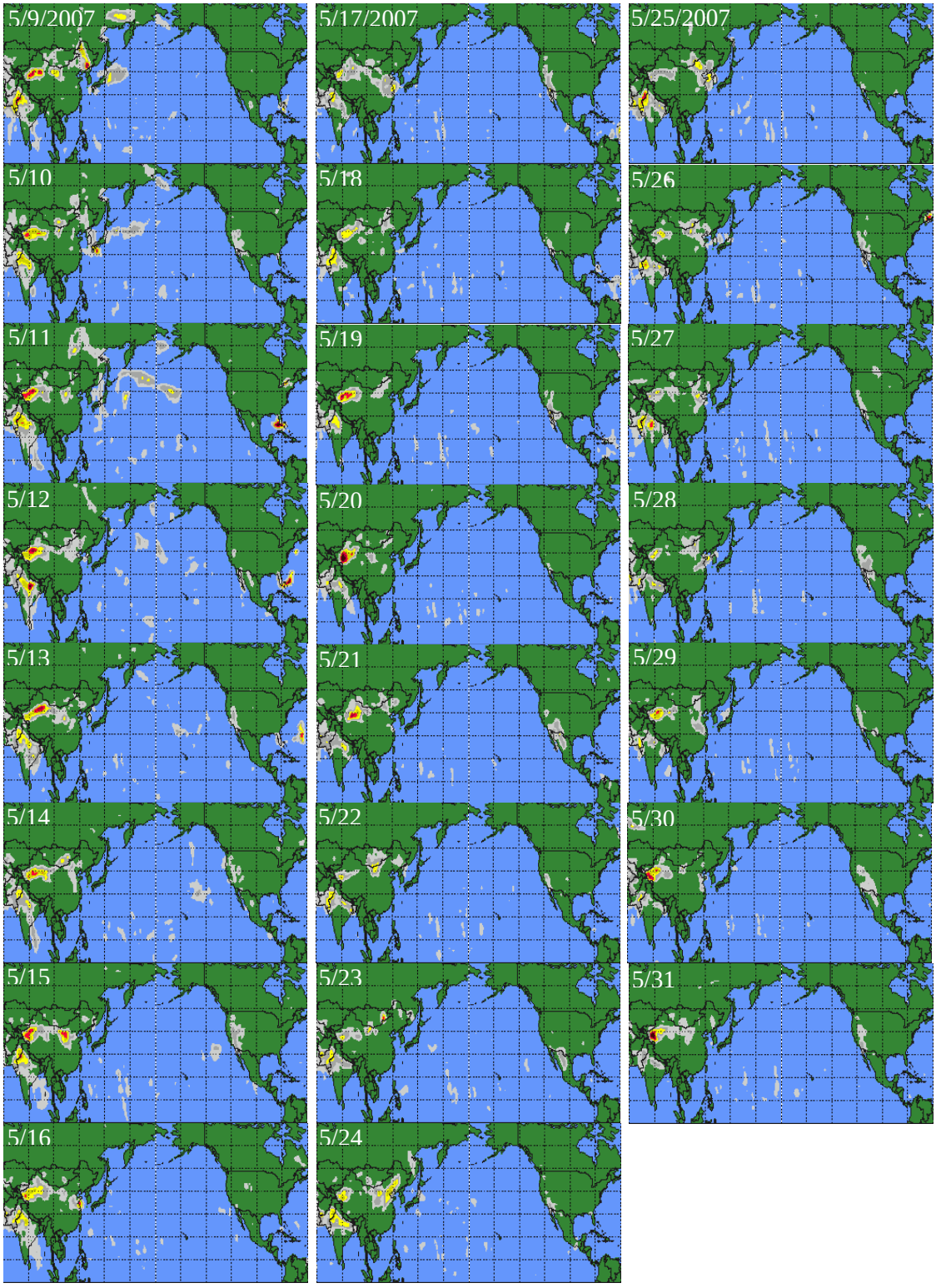

Figure B.1 (continued).

REFERENCES

Alpert, P, Y. J. Kaufman, Y. Shay-El, D. Tanre, A. da Silva, S. Schubert, and Y. H. Joseph (1998), Quantification of dust-forced heating of the lower troposphere, *Nature*, 395, 367-370.

Arimoto, R., Y. J. Kim, Y. P. Kim, P. K.Quinn, T. S. Bates, T. L. Anderson, S. Gong, I. Uno, M. Chin, B. J. Huebert, A. D. Clarke, Y. Shinozuka, R. J. Weber, J. R. Anderson, S. A. Guazzotti, R. C. Sullivan, D. A. Sodeman, K.A. Prather, and I.N. Sokolik (2006), Characterization of Asian Dust during ACE-Asia, *Global and Planetary Change*, 52, 23–56.

Badarinath, K. V. S., S. K. Kharol, D. G. Kaskaoutis, A. R. Sharma, V. Ramaswamy, and H. D. Kambezidis (2010), Long-range transport of dust aerosols over the Arabian Sea and Indian region – A case study using satellite data and ground-based measurements, *Global and Planetary Change*, 72, doi:10.1016/j.gloplacha.2010.02.003.

Ben-Ami, Y., I. Koren, and O. Altaratz, Patterns of North African dust transport over the Atlantic: Winter vs. summer, based on CALIPSO first year data, Atmos. Chem. Phys., 9, 7867–7875,

Bi, L., P. Yang, G. W. Kattawar, B. A. Baum, Y. X. Hu, D. M. Winker, R. S. Brock, and J. Q. Lu (2009), Simulation of the color ratio associated with the backscattering of radiation by ice particles at the wavelengths of 0.532 and 1.064 mm, *J. Geophys. Res.*,114, D00H08, doi:10.1029/2009JD011759.

Chen, B., J. Huang, P. Minnis, Y. Hu, Y. Yi, Z. Liu, D. Zhang, and X. Wang (2010), Detection of dust aerosol by combining CALIPSO active lidar and passive IIR measurements, *Atmos. Chem. Phys*., 10, 4241-4251.

Chen, G., and H. Chen (1987), Study on large-scale feature of duststorm system in East Asia. Papers in Meteorological Research, *Publication of The Meteorology Society of Republic of China,* 10 (1), 57–80.

Chen, S., Y. Kuo, W. Ming, and H. Ying (1994), The effect of dust radiative heating on low-level frontogenesis, *J. Atmos. Sci*., 52, 1414-1420.

Choi, H., I.N. Sokolik, and D. M. Winker (2010),Comparative analyses of Asian and Saharan Dust in source regions and downwind using CALIPSO space lidar data in conjunction with A-Train multi-sensor data and ground-based observations, AMS Annual meeting, Atlanta, GA, USA.

Choi, H., I.N. Sokolik, D. M. Winker, and Y. Kurosaki (2008), Analysis of Asian Dust Events from CALIPSO Space Lidar Data in Conjunction with Passive Remote Sensing and Ground-Based Observations, AGU Joint Assembly, Florida, USA.

Choi, H., I.N. Sokolik, and D. M. Winker (2007), Using CALIPSO space lidar data in conjunction with passive remote sensing for characterization of spatiotemporal distribution of Asian dust outbreaks and their radiative impact, EOS Trans. AGU, Fall Meeting.

Chou, C., P. Formenti, M. Maille, P. Ausset, G. Helas, M. Harrison, and S. Osborne (2008), Size distribution, shape, and composition of mineral dust aerosols collected during the African Monsoon Multidisciplinary Analysis Special Observation Period 0: Dust and Biomass-Burning Experiment field campaign in Niger, January 2006, *J. Geophys. Res*., 113, D00C10, doi:10.1029/2008JD009897.

Darmenov, A. and I. N. Sokolik (2005), Identifying the regional thermal-IR radiative signature of mineral dust with MODIS, Geophys.Res. Lett., 32, L16803, doi:10.1029/2005GL023092.

Dubovik, O., A. Sinyuk, T. Lapyonok, B. N. Holben, M. Mishchenko, P. Yang, T. F. Eck, H. Volten, O. Munoz, B. Veihelmann, W. J. van der Zande, J.-F. Leon, M. Sorokin, and I. Slutsker (2006), Application of spheroid models to account for aerosol particle nonsphericity in remote sensing of desert dust, *J. Geophys, Res*., 111, D11208, doi:10.1029/2005JD006619.

Generoso, S., I. Bey, M. Labonne, and F.-M. Breon (2008), Aerosol vertical distribution in dust outflow over the Atlantic: Comparisons between GEOS-Chem and Cloud-Aerosol Lidar and Infrared Pathfinder Satellite Observation (CALIPSO), *J. Geophys, Res*., 113, D24209, doi:10.1029/2008JD010154.

Guan, H., B. Schmid, A. Bucholtz, and R. Bergstrom (2010), Sensitivity of shortwave radiative flux density, forcing, and heating rate to the aerosol vertical profile, *J. Geophys. Res.*, 115, D06209, doi:10.1029/2009JD012907.

Eguchi, K., I. Uno, K. Yumimoto, T. Takemura, A. Shimizu, N. Sugimoto, and Z. Liu (2009), Trans-pacific dust transport: integrated analysis of NASA/CALIPSO and

a global aerosol transport model, *Atmos. Chem. Phys*., 9, 3137–3145, www.atmos-chem-phys.net/9/3137/2009/.

Elterman, L. (1966), Aerosol measurements in the troposphere and stratosphere. *Appl. Opt.*, 5, 1769–1776.

Esselborn, M., M. Wirth, A. Fix, B. Weinzierl, K. Rasp, M. Tesche, A. Petzold, and G. Ehret (2008), Spatial distribution and optical properties of Saharan dust observed by airborne high spectral resolution lidar during SAMUM 2006, *Tellus Ser. B*, 61, 131– 143.

Fernald, F.G. (1984), Analysis of atmospheric lidar observations: some comments. *Appl. Opt., 23(*5), 652–653.

Fernald, F.G., B. M. Herman, and J. A. Reagan (1972), Determination of aerosol height distributions with lidar. *J. Appl. Meteor*., 11, 482–489.

Forster, P., V. Ramaswamy, P. Artaxo, T. Berntsen, R. Betts, D.W. Fahey, J. Haywood, J. Lean, D.C. Lowe, G. Myhre, J. Nganga, R. Prinn, G. Raga, M. Schulz and R. Van Dorland, 2007: Changes in Atmospheric Constituents and in Radiative Forcing. *In: Climate Change 2007: The Physical Science Basis. Contribution of Working Group I to the Fourth Assessment Report of the Intergovernmental Panel on Climate Change* [Solomon, S., D. Qin, M. Manning, Z. Chen, M. Marquis, K.B. Averyt, M.Tignor and H.L. Miller (eds.)]. *Cambridge University Press*, Cambridge, United Kingdom and New York, NY, USA.

Fournier, G. R. & Evans, B. T. N. (1991), Approximation to extinction efficiency for randomly oriented spheroids, *Applied Optics*, 30, 2042–2048.

Freudenthaler, V., M. Esselborn, M. Wiegner, B. Heese, M. Tesche, and co-authors (2008), Depolarization–ratio profiling at several wavelengths in pure Saharan dust during SAMUM. *Tellus* **61B**, doi: 10.1111/j.1600-0889.2008.00396.x.

Hansen, J.E., and L.D. Travis, 1974: Light scattering in planetary atmospheres. *Space Sci. Rev.*, **16**, 527-610, doi:10.1007/BF00168069.

Hara, Y., K. Yumimoto, I. Uno, A. Shimizu, N. Sugimoto, Z. Liu, and D. Winker (2009), Asian dust outflow in the PBL and free atmosphere retrieved by NASA CALIPSO and an assimilated dust transport model, *Atmos. Chem. Phys*., 9, 1227–1239, http://www.atmos-chem-phys.net/9/1227/2009/.

Hara, Y., I. Uno, K. Yumimoto, M. Tanaka, A. Shimizu, N. Sugimoto, and Z. Liu (2008), Summertime Taklimakan dust structure, *Geophys. Res. Lett.*, 35, L23801, doi:10.1029/2008JD035630.

Heinold, B., I. Tegen, M. Esselborn,K. Kandler, P. Knippertz, and co-authors (2008), Regional Saharan dust modelling during the SAMUM 2006 campaign. *Tellus* 61B, doi:10.1111/j.1600-0889.2008.00387.x.

Hess, M., P. Koepke, and I. Schult (1998), Optical properties of aerosols and clouds: The software package OPAC, *Bull. Am. Meteorol. Soc.*, 79, 831-844.

Huang, J., Q. Fu, J. Su, Q. Tang, P. Minnis, Y. Hu, Y. Yi, and Q. Zhao (2009), Taklmakan dust aerosol radiative heating derived from CALIPSO observations using the Fu-Liou radiation model with CERES constraints, *Atmos. Chem. Phys*., 9, 4011–4021.

Huang, J., P. Minnis, B. Chen, Z. Huang, Z. Liu, Q. Zhao, Y. Yi, and J. Ayers(2008), Long-range transport and vertical structure of Asian dust from CALIPSO and surface, *J. Geophys. Res.*, 113, D23212, doi:10.1029/2008JD010620.

Huang, J., P. Minnis, Y. Yi, Q. Tang, X. Wang, Y. Hu, Z. Liu, K. Ayers, C. Trepte, and D. Winker (2007), Summer dust aerosols detected from CALIPSO over the Tibetan Plateau, *Geophys. Res. Lett*., 34, L18805, doi:10.1029/2007GL029938.

Iwasaka, Y., G.-Y. Shi, Y.S.Kim, A. Matsuki, D. Trochkine, D. Zhang, M. Yamada, T. Nagatani, M. Nagatani, Z. Shen, T. Shibata, and H. Nakata (2004), Pool of dust particles over the Asian continent: Balloon-borne optical particle counter and ground-based Lidar measurements at Dunhuang, China, *Env. Monitoring and Assesment*, 92: 5-24.

Iwasaka, Y., et al. (2003), Large depolarization ratio of free tropospheric aerosols over the Taklamakan desert revealed by lidar measurements: Possible diffusion and transport of dust particles, *J. Geophys. Res*., 108(D23), 8652, doi:10.1029/2002JD003267.

Kandler, K., Sch¨utz, L., Deutscher, C., Hofmann, H., J¨ackel, S. and coauthors (2008), Size distributions, mass concentrations, chemical and mineral composition and optical parameters of the boundary layer aerosol at Tinfou, Morocco, during SAMUM 2006. *Tellus* 61B, doi:10.1111/j.1600-0889.2008.00385.x.

Kalashnikova, O. V., R. Kahn, I. N. Sokolik, and W.-H. Li (2005), Ability of multiangle remote sensing observations to identify and distinguish mineral dust types: Optical models and retrievals of optically thick plumes, *J. Geophys. Res*., 110, D18S14, doi:10.1029/2004JD004550.

Kalashnikova, O.V., and I.N. Sokolik (2004), Modeling the radiative properties of nonspherical soil--derived mineral aerosols, *J. Quant. Specrtrocs. Radiat. Transfer*, 87, 137-166.

Kalashnikova, O.V., and I.N. Sokolik (2002), Importance of shapes and composition of wind-blown dust particles for remote sensing at solar wavelengths. *Geophys. Res. Let*t., 29, No.10, 10.1029/2002GL014947.

Karyampudi, V. M., and T. N. Carlson (1988), Analysis and numerical simulations of the Saharan air layer and its effects on easterly wave disturbances, *J. Atmos. Sci*., 45, 3102-3136.

Kim, S.-W., Berthier, S., Raut, J.-C., Chazette, P., Dulac, F., and Yoon, S.-C. (2008), Validation of aerosol and cloud layer structures from the space-borne lidar CALIOP using a ground-based lidar in Seoul, Korea, Atmos. Chem. Phys., 8, 3705–3720, http://www.atmos-chem-phys.net/8/3705/2008/.

Klett, J. D. (1985), Lidar inversion with variable backscatter/extinction ratios. Appl. Opt., 24, 1638–1643.

Klett, J. D. (1981), Stable analytical inversion for processing lidar returns. Appl. Opt., 20, 211–220.

Lafon, S., I. N. Sokolik, J. L. Rajot, S. Caquineau, and A. Gaudichet (2006), Characterization of iron oxides in mineral dust aerosols: Implications for light absorption, *J. Geophys. Res*., 111, D21207, doi:10.1029/2005JD007016.

Lau, K.-M., M. K. Kim, and K. M. Kim (2006), Asian summer monsoon anomalies induced by aerosol direct forcing: The role of the Tibetan Plateau, *Clim. Dyn*., 26(7-8), 855-864, doi:10.1007/s00382-006-0114-z.

Liu, D., Z. Wang, Z. Liu, D. Winker, and C. Trepte, A height resolved global view of dust aerosols from the first year CALIPSO lidar measurements, *J. Geophys. Res*., 113, D16214, doi:10.1029/2007JD009776.

Liu, Z., R. Kuehn, M. Vaughan, D. Winker, A. Omar, K. Powell, C. Trepte, Y. Hu, and C. Hostetler (2010), The CALIPSO Cloud And Aerosol Discrimination: Version 3 Algorithm and Test Results, 25th International Laser Radar Conference (ILRC), St. Petersburg, Russia, (available at: http://www-calipso.larc.nasa.gov/resources/pdfs/ILRC LaRC 2010/Liu ILRC25 2010.pdf).

Liu, Z., D. Winker, A. Omar, M. Vaughan, C. Trepte, Y. Hu, K. Powell, W. Sun, and B. Lin (2010), Effective lidar ratios of dense dust layers over North Africa derived from the CALIOP measurements, *JQSRT*, doi:10.1016/j.jqsrt.2010.05.006

Liu, Z., M. Vaughan, D. Winker, C. Kittaka, R. Kuehn, B. Getzewich, C. Trepte, and C. Hostetler (2009), The CALIPSO Lidar Cloud and Aerosol Discrimination: Version 2 Algorithm and Initial Assessment of Performance, *J. Atmos. Oceanic Technol.*, 26, 1198–1213, doi:10.1175/2009JTECHA1229.1.

Liu, Z., D. Liu, J. Huang, M. Vaughan, I. Uno, N. Sugimoto, C. Kittaka, C. Trepte, Z. Wang, C. Hostetler, and D. Winker (2008), Airborne dust distributions over the Tibetan Plateau and surrounding areas derived from the first year of CALIPSO lidar observations, *Atmos. Chem. Phys.*, 8, 5045–5060, doi:10.5194/acp-8-5045-2008.

Liu, Z., A. Omar, M. Vaughan, J. Hair, C. Kittaka, Y. Hu, K. Powell (2008), CALIPSO Lidar observations of the optical properties of Saharan dust: a case study of long range transport, *J. Geophys. Res.*, 113, D07207, doi:10.1029/2007JD008878.

Liu Z, N. Sugimoto, and T. Murayama (2002), Extinction-to-backscatter ratio of Asian dust observed with high-spectral-resolution lidar and Raman lidar. *Appl Opt*, 41:2760–7.

Lohmann, U., W. R. Leaitch, L. Barrie, K. Law, Y. Yi, and co-authors (2001), Comparisons of the vertical distribution of sulfur species from models participated in COSAM exercise with observations, Tellus, Ser. B, 53, 646–672.

Maring, H., D. L. Savoie, M. A. Izaguirre, L. Custals, and J. S. Reid (2003), Mineral dust aerosol size distribution change during atmospheric transport, *J. Geophys. Res.*, *108*(D19), 8592, doi:10.1029/2002JD002536.

Merikallio, S., H. Lindqvist, T. Nousiainen, and M. Kahnert (2011), Modelling light scattering by mineral dust using spheroids: assessment of applicability, Atmos. Chem. Phys. Discuss., 11, 3977–4016, www.atmos-chem-phys-discuss.net/11/3977/2011/ doi:10.5194/acpd-11-3977-2011.

Miller, R.L., R.V. Cakmur, Ja. Perlwitz, I.V. Geogdzhayev, P. Ginoux, K.E. Kohfeld, D. Koch, C. Prigent, R. Ruedy, G.A. Schmidt, and I. Tegen (2006), Mineral dust aerosols in the NASA Goddard Institute for Space Sciences ModelE atmospheric general circulation model. *J. Geophys. Res.*, **111**, D06208, doi:10.1029/2005JD005796.

Mishchenko, M. I., I. V. Geogdzhayev, B. Cairns, B. E. Carlson, J. Chowdhary, A. Lacis, L. Liu, W. B. Rossow, and L.D. Travis (2007), Past, present, and future of global aerosol climatologies derived from satellite observations: A perspective, *J. Quant. Specrtrocs. Radiat. Transfer*, 106, 325-347.

Mishchenko, M. I., Cairns, B., Kopp, G., Schueler, C., Fafaul, B. A., Hansen, J. E., Hooker, R. J., Itchkawich, T., Maring, H. B., and Travis, L. D. (2007), Accurate Monitoring of Terrestrial Aerosols and Total Solar Irradiance: Introducing the Glory Mission, *B. Am. Meteorol. Soc.*, 88, 677–691.

Mishchenko, M. I., I. V. Geogdzhayev, L. Liu, J. A. Ogren, A. A. Lacis, W. B. Rossow, J. W. Hovenier, H. Volten, and O. Muñoz (2003), Aerosol retrievals from AVHRR radiances: effects of particle nonsphericity and absorption and an updated long-term global climatology of aerosol properties, *J. Quant. Spectrosc. Radiat. Transfer*, **79/80**, 953–972.

Mishchenko, M. I., J. W. Hovenier, and L. D. Travis (Eds.) (2000), Light Scattering by Nospherical Particles, *Elsevier*, New York.

Mishchenko, M. I., and K. Sassen (1998), Depolarization of lidar returns by small ice crystals: An application to contrails, *Geophys. Res. Lett.*, 25(3), 309-312.

Mishchenko, M. I., L. D. Travis, R. A. Kahn, and R. A. West (1997), Modeling phase functions for dust-like tropospheric aerosols using a shape mixture of randomly oriented polydisperse spheroids. *J. Geophys. Res.*, 102:13543-13553.

Mona, L., G. Pappalardo, A. Amodeo, G. D'Amico, F. Madonna, A. Boselli, A. Giunta, F. Russo, and V. Cuomo (2009), One year of CNR-IMAA multi-wavelength Raman lidar measurements in correspondence of CALIPSO overpass: Level 1 products comparison, Atmos. Chem. Phys. Discuss., 9, 8429-8468, doi:10.5194/acpd-9-8429-2009.

Moulin, C., and I. Chiapello (2004), Evidence of the control of summer atmospheric transport of African dust over the Atlantic by Sahel sources from TOMS satellite (1979-2000), *Geophys. Res. Lett.*, 31, L02107, doi:10.1029/2003GL018931.

Müller, D., B. Weinzierl, A. Petzold, K. Kandler, A. Ansmann, T. Muller, M. Tesche, V. Freudenthaler, M. Esselborn, B. Heese, D. Althausen, A. Schladitz, S. Otto, and P. Knippertz (2010), Mineral dust observed with AERONET Sun photometer, Raman lidar, and in situ instruments during SAMUM 2006: Shape-independent particle properties, *J. Geophys. Res.*, 115, D07202, doi:10.1029/2009JD012520.

Müller, D., A. Ansmann, I. Mattis, M. Tesche, U. Wandinger, D. Althausen, and G. Pisani (2007), Aerosol-type-dependent lidar ratios observed with Raman lidar, *J. Geophys. Res.*, 112, D16202, doi:10.1029/2006JD008292.

Müller, T., A. Schladitz, A. Maßling, N. Kaaden, A. Wiedensohler, and K. Kandler (2009), Spectral absorption coefficients and imaginary parts of refractive indices of Saharan dust during SAMUM-1, *Tellus Ser*. B, 61, 79–95.

Munoz, O., H. Volten, J. W. Hovenier, T. Nousiainen, K. Muinonen, D. Guirado, F. Moreno, and L. B. F. M. Waters (2007), Scattering matrix of large Saharan dust particles: Experiments and computations, *J. Geophys. Res*., 112, D13215, doi:10.1029/2006JD008074.

Murayama, T., et al. (2003), An intercomparison of lidar-derived aerosol optical properties with airborne measurements near Tokyo during ACE-Asia, *J. Geophys. Res*., 108(D23), 8651, doi:10.1029/2002JD003259.

Murayama, T., D. Muller, K. Wada, A. Shimizu, M. Sekigushi, and T. Tsukamato (2004), Characterization of Asian dust and Siberian smoke with multi-wavelength Raman lidar over Tokyo, Japan in spring 2003, *Geophys. Res. Lett*., 31, L23103, doi:10.1029/2004GL021105.

Nousiainen, T., O. Munoz, H. Lindqvist, P. Mauno, and G. Videen (2011), Light scattering by large Saharan dust particles: Comparison of modeling and experimental data for two samples, J. Quant. Spectrosc. Radiat. Transfer., 112:420–433, doi: 10.1016/ j.jqsrt2010.09.003.

Nussenzveig, H. M., and W. J. Wiscombe (1980), Forward optical glory, *Opt. Lett*. 5, 455-457.

Okada, K., J. Heintzenberg, K. Kai, and Y. Qin (2001), Shape of atmopheric mineral particles collected in three Chinese arid-regions, *Geophys. Res. Lett*., 28, 3123-3126.

Otto, S., M. de Reus, T. Trautmann, A. Thomas, M. Wendisch, and S. Borrmann (2007), Atmospheric radiative effects of an in situ measured Saharan dust plume and the role of large particles, *Atmos. Chem. Phys*., 7, 4887-4903.

Patterson, E. M., Gilette, D. A., and B. H. Stockton (1997), Complex index of refraction between 300 and 700 nm for Saharan aerosol, *J. Geophys. Res*., 82, 3153-3160.

Petzold, A., K. Rasp, B. Weinzierl, M. Esselborn, T. Hamburger, and co-authors (2008), Saharan dust refractive index and optical properties from aircract-based observations during SAMUM 2006. *Tellus* 61B, doi:10.1111/j.1600-0889.2008.00383.x.

Platt, C. M. R. (1979), Remote sounding of high clouds: I. Calculation of visible and infrared optical properties for lidar and radiometer measurements. *J. Appl. Meteor.*, 18, 1130–1143.

Platt, C. M. R. (1973), Lidar and radiometer observations of cirrus clouds. *J. Atmos. Sci.*, 30, 1191–1204.

Prospero, J. M., P. Ginoux, O. Torres, and S. E. Nicholson (2002), Environmental characterization of global sources of atmospheric soil dust identified with the Nimbus 7 Total Ozone Mapping Spectrometer (TOMS) absorbing aerosol product, *Rev. Geophys*., 40(3), 1002, doi:10.1029/2000RG000095.

Quijano, A. L., Sokolik, I. N., and O. B. Toon (2000), Radiative heating rates and direct radiative forcing by mineral dust in cloudy atmospheric conditions, *J. Geophys. Res*., 105(D10), 12,207-12,219.

Ramanathan, V., M. Ramana, G. Roberts, D. Kim, C. Corrigan, C. Chung, and D. Winker (2007), Warming trends in Asia amplified by brown cloud solar absorption, Nature, 448, 575– 578.

Ricchiazzi, P, S Yang, C Gautier, and D Sowle (1998), SBDART: A research and teaching software tool for plane-parallel radiative transfer in the Earth's atmosphere, *Bulletin of the American Meteorology Society*, 79(10):2101-2114.

Sakai T, T. Shibata, Y. Iwasaka, T. Nagai, M. Nakazato, T. Matsumura, A. Ichiki, Y-S. Kim, K. Tamura, D. Troshkin, and S. Hamdi (2002), Case study of Raman lidar measurements of Asian dust events in 2000 and 2001 at Nagoya and Tsukuba, Japan. *Atmos. Environ.*, 36:5479–89.

Seinfeld, J. H., G. R. Carmichael, R. Arimoto, W.C. Conant, F. J. Brechtel, T.S. Bates, T. A. Cahill, A. D. Clarke, S. J. Doherty, P. J. Flatau, B. J. Huebert, J. Kim, K. M. Markowicz, P. K. Quinn, L. M. Russell, P. B. Russell, A. Shimizu, Y. Shinozuka, C. H. Song, Y. Tang, I. Uno, A. M. Vogelmann, R. J. Weber, J-H. Woo, and X. Y. Zhang (2004), ACE-ASIA: regional climatic and atmospheric chemical effects of Asian dust and pollution. *Bull. Am. Meteorol. Soc.,* 85, 367–380.

Sokolik I.N. (2002), The spectral radiative signature of wind-blown mineral dust: Implications for remote sensing in the thermal IR region. *Geophys. Res. Lett*. 10.1029/2002GL015910.

Sokolik, I. N., D. Winker, G. Bergametti, D. Gillette, G. Carmichael, Y. Kaufman, L. Gomes, L. Schuetz, and J. Penner (2001), Introduction to special section on mineral dust: Outstanding problems in quantifying the radiative impact of mineral dust, *J. Geophys. Res.*, 106, 18,015-18,028.

Sokolik I.N. , Dust, in *Encyclopedia of Global Environmental Change* . John wiley & Sons Ltd, 2001.

Sokolik I.N. and O.B. Toon. Incorporation of mineralogical composition into models of the radiative properties of mineral aerosol from UV to IR wavelengths. *J. Geophys. Res.*, 104, 9423-9444, 1999.

Sokolik, I. N., O. B. Toon, R. W. Bergstrom (1998), Modeling the radiative characteristics of airborne mineral aerosols at infrared wavelengths, *J. Geophys. Res*., 103, 8813-8826.

Sokolik, I. N., and O. B. Toon (1996), Direct radiative forcing by anthropogenic mineral aerosols, *Nature*, 381, 681-683.

Sugimoto, Nobuo, and Coauthors (2009), Continuous Observations of Aerosol Profiles with a Two-Wavelength Mie-Scattering Lidar in Guangzhou in PRD2006. *J. Appl. Meteor. Climatol.*, **48**, 1822–1830, doi: 10.1175/2009JAMC2089.1.

Takemura, T., T. Nakajima, O. Dubovik, B. N. Holben, and S. Kinne (2002), Single-scattering albedo and radiative forcing of various aerosol species with a global three-dimensional model, *J. Climate*, 15(4), 333-352.

Tegen, I., A. A. Lacis, and I. Fung (1996), The influence on climate forcing of mineral aerosols from distributed soils, *Nature*, 380, 419-422, 1996.

Tesche, M., A. Ansmann, D. Muller, D. Althausen, R. Engelmann, M. Hu, and Y. Zhang (2007), Particle backscatter, extinction, and lidar ratio profiling with Raman lidar in south and north China, *Appl. Opt.*, 46, 6302– 6308.

Textor, C., M. Schulz, S. Guibert, S. Kinne, Y. Balkanski, S. Bauer, and co-authors (2006), Analysis and quantification of the diversities of aerosol life cycles within AeroCom, Atmos. Chem. Phys., 6, 1777–1813, doi:10.5194/acp-6-1777-2006.

Tsai, F., G. T-J. Chen, T-H. Liu, W.-D. Lin, and J.-Y. Tu (2008), Characterizing the transport pathways of Asian dust, *J. Geophys. Res.*, *113*, D17311, doi:10.1029/2007JD009674.

Uno, I., K. Eguchi, K. Yumimoto, T. Takemura, A. Shimizu, M. Uematsu, Z. Liu, Z. Wang, Y. Hara, and N. Sugimoto (2009), Asian dust transported one full circuit around the globe, Nature Geoscience, doi:10.1038/NGEO583.

Uno, I., K. Yumimoto, A. Shimizu, Y. Hara, N. Sugimoto, Z. Wang, Z. Liu, and D. M. Winker (2008), 3D structure of Asian dust transport revealed by CALIPSO lidar and a 4DVAR dust model, *Geophys. Res. Lett.*, 35, L06803, doi:10.1029/2007GL032329.

Van de Hulst, H. C. (1957), Light Scattering by Small Particles, *New York, Wiley*, 470.

Vouk, V. (1948). Projected area of convex bodies. *Nature*, *162*, 330–331.

Wang, W., J. Huang, P. Minnis, Y. Hu, J. Li, Z. Huang, J. K. Ayers, and T. Wang (2010), Dusty cloud properties and radiative forcing over dust source and downwind regions derived from A-Train data during the Pacific Dust Experiment, J. Geophys. Res., 115, D00H35, doi:10.1029/2010JD014109.

Waterman, P. C. (1971), Symmetry, unitarity, and geometry in electromagnetic scattering, *Phys. Rev. D, 3*, 825-839.

Weinzierl, B., A. Petzold, M. Esselborn, M. Wirth, K. Rasp, K. Kandler, L. Schutz, P. Koepke, and M. Fiebig (2009), Airborne measurements of dust layer properties, particle size distribution and mixing state of Saharan dust during SAMUM 2006, *Tellus,Series B: Chemical and Physical Meteorology*, 61B, 96-117.

Wiegner, M., J. Gasteiger, K. Kandler, B. Weinzierl, K. Rasp, M. Esselborn, V.

Freudenthaler, B. Heese, C. Toledano, M. Tesche, and D. Althausen (2009), Numerical simulations of optical properties of Saharan dust aerosols with emphasis on linear depolarization ratio, *Tellus,Series B: Chemical and Physical Meteorology*, 61(1), 180-194.

Winker, D. M., W. H. Hunt, and M. J. McGill (2007), Initial performance assessment of CALIOP, *Geophys. Res. Lett*., 34, L19803, doi:10.1029/2007GL030135.

Winker, D. M., et al.(2006) , The CALIPSO mission and initial results from CALIPSO, *Proc. SPIE, 6409*, 640902, DOI:10.1117/12.698003.

Xie, C., N. Sugimoto, I. Matsui, A. Shimizu, T. Nishizawa, and Z. Wang (2008), An intercomparison of aerosol optical properties between Raman lidar and sun photometer measurements over Beijing, China, http://www-lidar.nies.go.jp/;RSJ/26th_papers/P10_xie.pdf.

Yang, P., and K. N. Liou, (2009), Effective refractive index for determining ray propagation in an absorbing dielectric particle, *J. Quant. Spectrosc. Radiat. Transfer*. 110, 300-306.

Yang P, Q. Feng, G. Hong, G. Kattawar, W. Wiscombe, M. Mishchenko, et al. (2007), Modeling of the scattering and radiative properties of nonspherical dust-like aerosols, *J. Aerosol Sci.*, 38:995–1014.

Yang, P., and K. N. Liou (1996), Geometric-optics – integral-equation method for light scattering by nonspherical ice crystals, *Appl. Opt.*, 35, 6568– 6584, doi:10.1364/AO.35.006568.

Young, S. A., Mark A. Vaughan, (2009), The Retrieval of Profiles of Particulate Extinction from Cloud-Aerosol Lidar Infrared Pathfinder Satellite Observations (CALIPSO) Data: Algorithm Description. *J. Atmos. Oceanic Technol.*, 26, 1105–1119, doi: 10.1175/2008JTECHA1221.1.

Young, S. A. (1995), Lidar analysis of lidar backscatter profiles in optically thin clouds. Appl. Opt., 34, 7019–7031.

Yu, H., M. Chin, D. M. Winker, A. H. Omar, Z. Liu, C. Kittaka, and T. Diehl (2010), Global view of aerosol vertical distributions from CALIPSO lidar measurements and GOCART simulations: Regional and seasonal variations, J. Geophys. Res., 115, D00H30, doi:10.1029/2009JD013364.

Yu, H., Y. J. Kaufman, M. Chin, G. Feingold, L. A. Remer, T. L. Anderson,Y. Balkanski, N. Bellouin, O. Boucher, S. Christopher, P. DeCola, R. Kahn, D. Koch, N. Loeb, M. S. Reddy, M. Schulz, T. Takemura, and M. Zhou (2006), A review of measurement-based assessments of the aerosol direct radiative effect and forcing, *Atmos. Chem. Phys*., 6, 613–666.

VITA

HYUNG JIN CHOI

Hyung Jin was born in Seong-Nam city, South Korea. He attended the Korea military academy (K.M.A.) in South Korea where he received a B.S. in Computer Science in 1997. After graduating from K.M.A., Hyung Jin became an officer of Army in South Korea. In 2000, he attended the Seoul National University in South Korea and received his master's degree in Atmospheric Science in 2002. Hyung Jin returned to the army in 2002 and serviced as a captain by 2004. Hyung Jin moved to the K.M.A. to teach cadets in Environment Science before coming to Georgia Tech to pursue a doctorate in Earth and Atmospheric Sciences in 2006. He is going to return to the K.M.A. after graduating Georgia Tech. His research interests include radiative transfer, remote sensing, and dust aerosol.